

Underlying physics and effects of silicon APD aging in automotive LiDAR applications

Von der Fakultät für Physik und Geowissenschaften
der Universität Leipzig
genehmigte

D I S S E R T A T I O N

zur Erlangung des akademischen Grades

Doctor rerum naturalium

Dr. rer. nat.,

vorgelegt

von M. Sc. Stefan Christoph Kammer

geboren am 09.08.1990 in Gehrden

Gutachter: Prof. Dr. Marius Grundmann (Universität Leipzig)
Prof. Dr. Thomas Dekorsy (Universität Stuttgart)

Tag der Verleihung: 25.04.2022



Bibliographische Beschreibung

Kammer, Stefan Christoph:

Underlying physics and effects of silicon APD aging in automotive LiDAR applications

Universität Leipzig, Dissertation

201 Seiten, 243 Zitate, 72 Abbildungen, 6 Tabellen

Referat:

Ziel dieser Promotion in industriellem Umfeld war es, die zugrundeliegenden physikalischen Alterungsmechanismen von Avalanche Photodioden (APD) und deren Auswirkungen auf die Funktion in der automobilen LIGHT DETECTION AND RANGING (LiDAR) Anwendung zu bestimmen. Es wurde ein neues Degradationsmodell entwickelt, das zahlreiche Aspekte der Generation negativer Oxidladungen und Si:SiO₂ Grenzflächenfallen beinhaltet und an experimentellen Degradationsdaten kalibriert wurde. Die Rückkopplung zwischen Degradationsphänomenen und sensorinternen Feldern und Strömen entspricht einem gekoppelten Problem, das durch einen ausgefeilten, maßgeschneiderten numerischen Iterationsansatz in einem Tandemverfahren der Sensordegradations- und der SILVACO ATLAS Bauteilsimulator selbstkonsistent gelöst wurde. Belastungsexperimente wurden an Testsensoren unter verschiedenen Betriebsbedingungen und an LiDAR-APDs durchgeführt. Der gesamte Satz experimenteller Ergebnisse fand seine vollständige physikalische Interpretation in Verbindung mit dem Degradationsmodell, das eine hervorragende Übereinstimmung erzielte. Dabei wurden zahlreiche neue Erkenntnisse gewonnen: Das Ausmaß der Degradation wird durch die Eigenschaften der Oxidschicht des Sensors bestimmt. Die Degradationsgeschwindigkeit nimmt mit der Temperatur, der Spannung und der Beleuchtungsintensität zu, wobei der Einfluss der Temperatur aufgrund der signifikanten Beteiligung des Dunkelstroms während der Degradation besonders stark ist. Die Generation negativer Oxidladungen führt zu einer Drift der Stoßionisationsrate im Sensorrandbereich. Die Erzeugung von Grenzflächenfallen fördert die Akkumulation negativer Oxidladungen durch die Zufuhr von thermisch erzeugtem Dunkelstrom. Auf diese Weise wird die Degradation um 14% beschleunigt. In einigen Fällen erhöhte sich die Stoßionisationsrate im Sensorrandbereich, was auf ein fundamentales Problem hinweist. Unter erstarkenden Generations-Rekombinationsprozessen im Sensor während der Degradation nimmt das Rauschen zu. Verfügbare Rauschmodelle wurden erweitert, um die Auswirkungen der Degradation zu berücksichtigen. Zusammen mit der Anwendung des kalibrierten APD-Degradationsmodells wurde festgestellt, dass das Rauschen stark beeinflusst wird, was auf einen durch Degradation verursachten Lawinendurchbruch des Randdunkelstroms zurückgeführt wurde. Infolgedessen verschlechtert sich das Signal-Rausch-Verhältnis von kleinen Signalen 100 m entfernter Objekte auf einen Wert unter 1, bei dem selbst theoretisch eine Auflösung unmöglich ist. Die Lebensdauer für die belastendste Bedingung im LiDAR-Betrieb wurde auf nur 1000 h geschätzt, was weit unter den Anforderungen der Automobilindustrie von mehreren Jahrzehnten liegt.

Bibliographic Description

Kammer, Stefan Christoph:

Underlying physics and effects of silicon APD aging in automotive LiDAR applications

Universität Leipzig, Dissertation

201 pages, 243 citation, 72 figures, 6 tables

Abstract:

The aim of this thesis prepared in an industrial environment was to reveal the underlying physical aging mechanisms of avalanche photo diodes (APD) and their effects on the function in automotive LIGHT DETECTION AND RANGING (LiDAR) application. A novel degradation model was developed treating numerous fundamental aspects of negative oxide charge generation and Si:SiO₂ interface trap generation. So far, no model is known covering the kinetics of APD degradation at all. Due to the feedback between degradation phenomena and sensor internal fields and currents, a coupled problem arose, which was solved self-consistently by a sophisticated tailor-made numerical iteration approach in a tandem procedure combining the simulation of sensor degradation and the SILVACO ATLAS device simulator. Therefrom, the generation of negative oxide charges was identified to cause a drift of the impact ionization rate in the sensor edge. The generation of interface traps promotes the accumulation of negative oxide charges by their supply of thermally generated dark current. In this way, degradation is about 14% faster. The model was calibrated on experimental degradation data. Stress experiments have been performed on test sensors under a variation of operation conditions and on APDs. The entire set of experimental results found its complete physical interpretation in conjunction with the degradation model which achieved an excellent agreement. Thereby, numerous novel insights were revealed: The extent of degradation is induced by the properties of the sensor oxide layer. The degradation pace increases with temperature, voltage and intensity of illumination whereas the impact of temperature is particularly strong due to the significant participation of dark current during degradation. The oxygen vacancy was concluded to be the dominant trap in the oxide layer of the studied sensors. An empirical distribution of individual sensor properties was achieved. In some cases, the impact ionization rate in the sensor edge increased which indicates a major problem, as noise increases when the generation-recombination processes in the sensor become more pronounced during degradation. Available noise models were extended to cover the effect of degradation. Together with the application of the calibrated APD degradation model, the noise was revealed to be highly affected, which was ascribed to an avalanche breakdown of the edge dark current caused by degradation. Consequently, the signal-noise-ratio of small signals from 100 m distant objects degrades to a value below 1, where even theoretically a resolution is impossible. A lifetime of only 1000 h was estimated under the most severe automotive LiDAR operation conditions. This falls much below the requirements of the automotive industry of several decades.

Contents

1	Introduction	1
2	Conceptual background	3
2.1	Basic principles of avalanche photo diodes	3
2.1.1	Design basics and internal processes	4
2.1.2	Basic function and parameters	6
2.2	Basic principles of Light Detection And Ranging	11
2.2.1	Basic structure	12
2.2.2	Receiver circuit and time of flight measurement	13
2.3	Basic principles of reliability analysis	15
2.3.1	Concept of aging analysis	16
2.3.2	Generation of interface traps	18
2.3.3	Oxide charge generation	20
2.3.4	Oxide trap generation and oxide conduction	24
2.4	Basics of semiconductor device simulation	25
2.4.1	Basic semiconductor equations	26
2.4.2	Generation and recombination processes	29
2.5	Summary	34
3	Development of an APD degradation model	37
3.1	Degradation processes in LiDAR operation	38
3.2	Energy distribution of electrons at high fields	40
3.3	Injection probability of electrons into the oxide	43
3.3.1	Number of electrons and density of states	44
3.3.2	Injection conditions	45
3.3.3	Amount of injected electrons and injection probability	46
3.4	Generation of oxide charges	49
3.4.1	The origin of electron traps in silicon dioxide	50
3.4.2	Trapping of injected electrons	51

3.4.3	Detrapping of captured electrons	52
3.4.4	Relaxation of trapped electrons from shallow in deep levels	53
3.4.5	Oxide degradation model	54
3.4.6	Positive fixed oxide charges	55
3.5	Generation of interface traps	55
3.5.1	Hydrogen dissociation	55
3.5.2	Diffusion and passivation	59
3.5.3	Interface degradation model	61
3.6	Summary	62
4	Simulation of APD degradation	65
4.1	Oxide degradation	65
4.1.1	Internal drivers of degradation	66
4.1.2	Basic iteration approach	67
4.1.3	The occupation of shallow trap levels	68
4.1.4	Simplified solution	69
4.1.5	Impact of operation conditions	71
4.2	Interface degradation	72
4.2.1	Simplified solution	73
4.2.2	Impact of operation conditions	74
4.3	Self-consistent numerical iteration approach	75
4.3.1	Iteration procedure of the coupled simulation	75
4.3.2	Resolution functions	77
4.3.3	Resulting oxide charge and interface trap densities	79
4.4	Degradation parameter	84
4.5	Simulation of sensor degradation	86
4.6	Summary	89
5	Degradation under varied conditions: Calibration of the model	91
5.1	Design of experiment	91
5.1.1	How to apply stress	92
5.1.2	How to measure degradation	93
5.1.3	Basic device design and applied stress conditions	93
5.2	Degradation behavior under varied conditions	94
5.2.1	General behavior of degrading devices	94
5.2.2	Influence of stress conditions and temporal behavior of degradation	97
5.2.3	Recap	101
5.3	Application of the degradation model	101

5.3.1	Classification of model parameters	101
5.3.2	Simulation vs. experimental data	104
5.3.3	Recap	110
5.4	The individuality of sensors	110
5.4.1	Derivation of an interpolation method	111
5.4.2	Variation between individual sensors	113
5.4.3	The origin of electron traps	115
5.4.4	Recap	116
5.5	Relaxation rate vs. stress conditions	116
5.6	Summary	120
6	Investigation on degrading automotive LiDAR APDs	123
6.1	Degradation behavior of APDs	123
6.1.1	Design of experiment	124
6.1.2	Behaviour of degrading automotive LiDAR APDs	124
6.1.3	Application of the calibrated degradation model	127
6.1.4	Recap	134
6.2	Degradation effect on the APD function in automotive LiDAR systems	135
6.2.1	Extrapolation of sensor properties	135
6.2.2	Impact on device functionality	137
6.2.3	Recap	146
6.3	Degradation mode and estimation of life time	147
6.3.1	Degradation of signal-noise-ratio	147
6.3.2	Estimation of life time for SNR degradation mode	148
6.3.3	Recap	150
6.4	Summary	150
7	Conclusion	153
	List of symbols	157
	Bibliography	159
	Zusammenfassung nach Promotionsordnung §11 (4)	185

Chapter 1

Introduction

Traffic accidents are a negative side effect of modern societies. Especially in big cities, they lead to fatalities every day. Over 90 % of accidents are caused by human error [1]. If technology existed that would allow vehicles to reliably drive autonomously, the number of traffic accidents could be drastically reduced. In addition to saving countless lives, this would also reduce the financial expenses associated with accidents, such as insurance costs, medical treatment costs, and lost work time. Collective behavior of autonomous vehicles would also help avoid traffic jams. This would reduce both, fuel consumption and greenhouse gas emissions [2]. People could work productively or relax while driving. People unable to actively participate in road transportation would be less restricted. Advanced car-sharing approaches could reduce the excessive number of private vehicles in cities and thus increase the quality of life there. Various concepts for autonomous vehicles already exist. For their realization, apart from Tesla¹, all major automobile manufacturers rely on the application of LIGHT DETECTION AND RANGING (LiDAR) [3].

LiDAR is the most precise method to measure distances [4]. Based on the Time of Flight measurement [3, 5-8], LiDAR modules are built of emitting laser diodes and detecting photo sensors. Several techniques are available to scan the space to obtain a high resolution point cloud of distances to surrounding objects [3, 4, 9-17, 17-21]. Currently, more than 95 % of commercial LiDAR systems are based on near-infrared laser wavelengths of mostly 905 nm [4, 22]. Matched to this, silicon-based photo sensors are used. Also higher wavelength are considered [23-25], but corresponding sensors are still under development [26]. Among all employed sensors, avalanche photo diodes (APD) currently possess the advantage of operating reliably despite high background radiation [27] and more efficient than their counterparts [28]. Therefore, they are the only sensor solution in mass production [29]. A major problem APD manufacturers face

¹The car manufacturer Tesla, Inc.

is their comparably high noise level [29]. In the APD, the photogenerated current is multiplied by an internal multiplication mechanism based on impact ionization. As a result, high signal-noise-ratios (SNR) are still achieved to provide the required resolution of high distances above 100 m [4,25,29]. Currently none of the LiDAR technologies meet the reliability requirements of the automotive industry concerning the aging of LiDAR components [17]. So autonomous driving cannot yet be realized for public use. The application in the automotive sector requires the functional parameters of the APD to remain stable for decades. While for APDs from different application areas, a drift of their functional parameters during operation could be observed [30-34], aging under near-application conditions, especially under illumination, has been only sparsely studied. Also, knowledge about failure mechanisms in APDs is meager, so a quantitative understanding of APD aging especially in LiDAR application does currently not exist at all.

In order to establish a fundamental understanding of APD aging in LiDAR application that supports designers to achieve more robust sensors and thus to enable a step closer to the realization of autonomous driving, it is the aim of this thesis prepared in an industrial environment to reveal the underlying physical mechanisms of aging and its effects on the function of APDs in automotive LiDAR application. In chapter 2 the basic principles of APDs, LiDAR modules and aging analysis are introduced. The methods of the employed device simulator and physical degradation mechanisms reported in the field of power devices are presented. In chapter 3 their relevance for APDs in automotive LiDAR operation is examined. Based on that and theoretical high field physics, a novel APD degradation model is developed. Operation conditions produce high fields and currents inside the sensor. These drive the temporal change of internal sensor properties which in turn affect internal fields and currents. This feedback is considered here as a coupled physical problem. Therefore, a sophisticated numerical iteration approach is developed in chapter 4 to solve the coupled degradation problem self-consistently. It is based on a coupled simulation of device simulator and APD degradation model. In chapter 5, aging of test structures is studied under accelerating conditions in stress experiments. By fitting experimental and simulated data, the degradation model from chapter 4 is calibrated. In chapter 6, stress experiments are performed on APDs. Together with simulation results of the calibrated degradation model, new insights into the temporal change of their internal electrical parameters are provided. Based on this, the effect of aging on functional parameters is identified. The APD degradation mode in automotive LiDAR operation is revealed and an estimation of its lifetime under severe LiDAR operation conditions is established. A final conclusion is presented in chapter 7 and an outlook for future APD design optimization is proposed.

Chapter 2

Conceptual background

An overview of the required basic concepts is provided. In section 2.1, the fabrication, design and function of the avalanche photo diode (APD) in the automotive LiDAR application are fundamentally explained. In section 2.2, the structure and function of the rotating LiDAR module is discussed. Section 2.3 gives an introduction to the concept of lifetime determination and explains fundamentally which processes are crucial for the aging of the APD. Some of these are already known from the field of power devices which are also introduced. In the course of this work a model will be developed to simulate the degradation of the APD. Its simulation combines the semiconductor device simulator with the determination of the effects of the degradation. Therefore, section 2.4 gives an overview of semiconductor device simulations and presents the basic physical processes that are crucial in the APD sensor chip.

2.1 Basic principles of avalanche photo diodes

In the following the Avalanche Photo Diode (APD) is introduced. It has a high-speed and high sensitivity operation, which has its origin in the internal multiplication mechanism. In this way the detector multiplies low-level light intensities to large electrical signals. In LiDAR applications, this is particularly important for detecting targets at long distances. Furthermore, in the LiDAR wavelength range of 905 nm, APDs are highly optimized. Their quantum efficiency is very close to 100%. The basic features of the APD are described in sufficient depth in [35,36]. The following is based on these reports and the essential properties of the APD are briefly introduced.

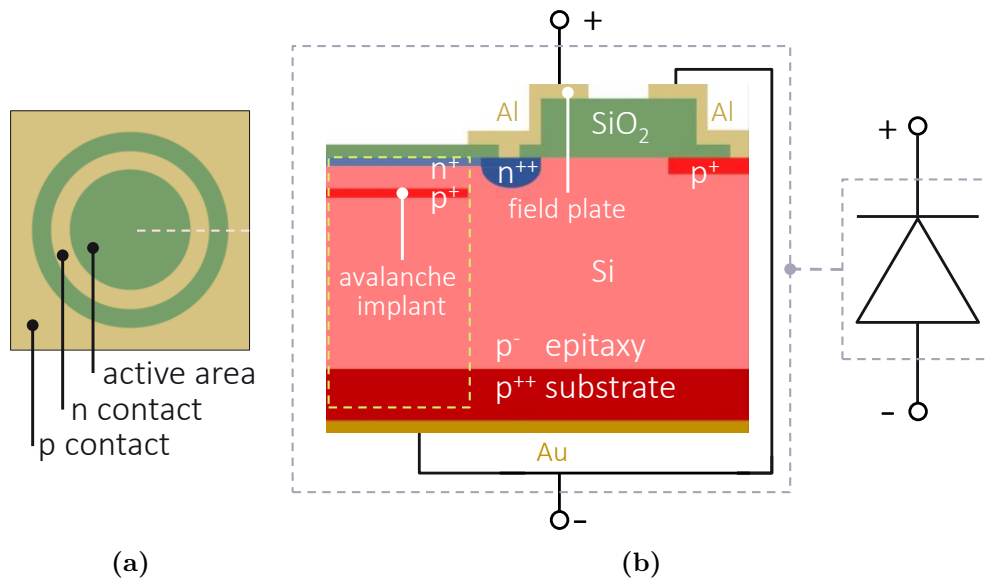


Figure 2.1: Basic structure of APD in topview (a) and cross section of the doping and material profile (b). Also the circuit symbol is shown. APDs are reverse biased.

2.1.1 Design basics and internal processes

Figure 2.1a shows a sketch of the top view on the device. The p contact at the outside, the n contact further inside and in between the underlying silicon dioxide can be seen. The dioxide also covers the active area in the center of the sensor. The regarded device possesses circular symmetry. Its cross section along the dashed line in figure 2.1a is shown in figure 2.1b. The rough process flow for manufacturing is as follows. A very low p doped silicon layer is epitaxied on a high p doped silicon substrate. Subsequently, the surface is oxidized. This is predominantly a wet oxidation, which is much faster compared to the dry version. The resulting oxide layer is about 800 nm thick. The oxide layer is then removed or thinned in some places to process the doping profiles. The central n^+ arsenic and p^+ boron profiles, which are very narrow in depth, are implanted as well as the lateral p^+ boron profile. The former, together with the doping of the epitaxy layer, form the doping profile of the actual APD in the center of the sensor chip. It is outlined in figure 2.1b in dashed lines. The p^+ doping in the center is also called avalanche implant. The lateral p^+ serves as contact doping. The n^{++} doping, which limits the central area, is the so-called guard ring. To process these, the oxide is removed at the intended location and phosphorus chloride (POCl_3) is added to the wafer in the furnace. Phosphor Silicate Glass (PSG) is then deposited on the silicon surface. At high temperatures, phosphorus diffuses from the surface into the silicon. This forms the n^{++} phosphorus doping, which is very inhomogeneous in contrast to the implant profiles. It serves as contact doping and has moreover the effect that the electric field in the chip center is homogeneous and no energetic electrons

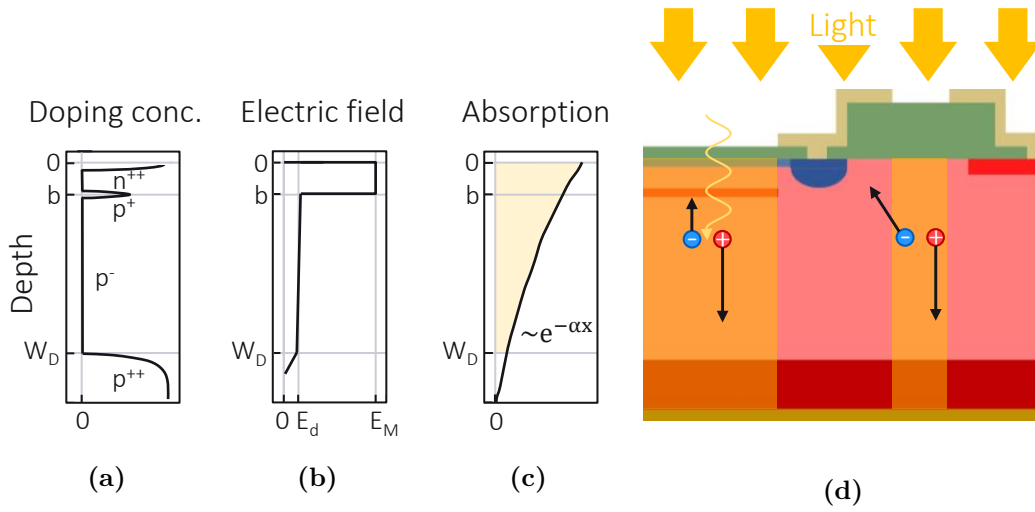


Figure 2.2: Sketch of doping profile (a), electric field profile in operation mode (b) and light absorption (c) in depth of the sensor chip center. Cross section of the sensor with incident light (d).

leak into the edge region. The latter would result in a delayed response behavior. In addition, the impurity gradient must be very low and the radius large to avoid edge breakdown. The anti-reflection coating is then processed. It consists of a thin silicon oxide and silicon nitride layer. The combination of different refractive indices enables one hundred percent transmission of light into the APD. Finally, the oxide is opened at the designated locations and aluminum is deposited as the contact metal. In parts, it overlaps above the oxide. At the n side this overlap is called field plate. Titanium gold is then deposited on the back surface. It serves as the backside contact.

Figure 2.2a illustrates the general doping profile of the investigated APD in the center in a plot of the depth against the doping concentration. This is located in the center of the sensor as outlined in figure 2.1. Directly at the surface there is a rather narrow but very highly concentrated n doping. At a depth of $b \approx 2 \mu\text{m}$ there is a strong and also very narrow p doping. As aforementioned, both are realized by implants. At a depth of $W_D \approx 65 \mu\text{m}$ a very strongly p doped layer follows. It often corresponds to the substrate which is contacted. The region between these three dopants is very weakly p doped and corresponds to the background doping. During operation, a positive voltage is applied to the n side while the p side is grounded. Thus, the diode is operated at reverse voltage. Therefore, the semiconductor can be depleted up to the p^{++} doping and the electric field whose profile is schematically shown in figure 2.2b disappears only beyond the depletion width W_D within the p^{++} doping. However, in the region between the n^{++} and the p^+ doping it obtains high values of around $E_M = 3 \times 10^5 \text{ V/cm}$. Between the p^+ and the p^{++} doping, its magnitude is much smaller with $E_d \approx 10^4 \text{ V/cm}$. In general, the electric field can be determined by the Poisson equation (section 2.4.1),

which relates it to the doping level. Figure 2.2 shows a sketch of the absorption profile in the sensor center. Because the absorption coefficient α of light in the 905 nm region is relatively small, light entering the surface can penetrate deeply into the APD. Therefore, the majority of photo generation occurs in the region below the p^+ layer in the field of E_d . Due to the polarity of the applied voltage, electrons in the electric field are accelerated toward the surface and holes in opposite direction. The drift velocity then depends on the field strength. With increasing field strength, the energy supplied to the charge carriers by the field increases on the one hand. On the other hand, the increase in energy increases the frequency of collisions with lattice atoms. At a field of $E_d = 10^4$ V/cm this leads to saturation of the velocity, so that electrons in the low field range move with saturation drift velocity ($\propto 10^7$ cm/s). In the high field region, a field strength of $E_M > 1.8 \times 10^5$ V/cm is sufficient to enable an additional scattering mechanism: Impact ionization. In this process, very energetic conduction band electrons collide with valence band electrons and thus excite them into the conduction band. These in turn can excite further electrons from the valence band if accelerated long enough in the field. This leads to a multiplication of the original electron entering the high field region. In general, the number of electron-hole pairs generated by this process per unit length is called the ionization rate. It represents a probability for the occurrence of impact ionization and depends on the material and the type of charge carrier. Thus, the ionization rate in silicon is very different for electrons (α_n) and holes (α_p) with $k = \alpha_p/\alpha_n \ll 1$. Its magnitude, and therefore the amount of multiplication, is very strongly dependent on the field strength E_M . At very high operating voltages, a chain reaction is triggered and an avalanche breakdown occurs, corresponding to an infinite multiplication. The voltage at which this occurs is called the breakdown voltage U_{br} .

2.1.2 Basic function and parameters

Electrical properties

The multiplication, also called gain M , is measured as a function of the operating voltage. The resulting gain voltage characteristic is one of the most important sensor properties. It is determined by measuring the photo current at voltage U and relating it to the photo current at a gain of $M = 1$:

$$M = \frac{I_{ph}(U)}{I_{ph}(U_{M=1})} \quad (2.1)$$

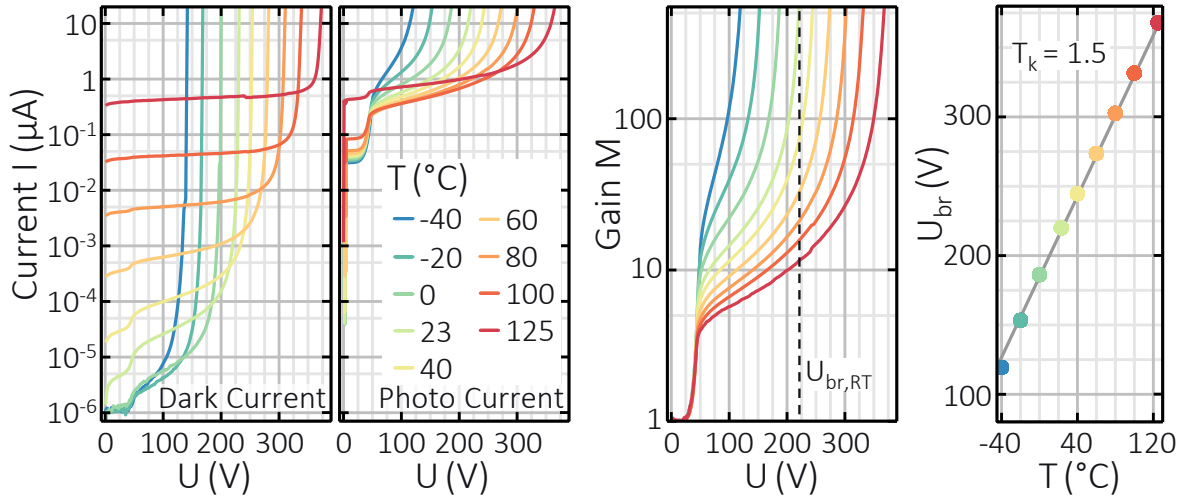


Figure 2.3: Plot of dark current I_d (left), photo current I_{ph} (middle left) and gain M (middle right) against voltage U for a variation of the temperature T . The breakdown voltage U_{br} is plotted against the temperature T (right). Data were provided by the First Sensor metrology group.

Figure 2.3 on the left shows the dark current voltage characteristic $I_d(U)$ in a plot of current I versus voltage U for temperatures $-40^\circ\text{C} < T \leq 125^\circ\text{C}$. As the voltage increases, the dark current increases for each temperature T . The slope is very flat at first. At the breakdown voltage U_{br} the increase becomes abruptly extremely large. This is the avalanche breakdown. The breakdown voltage depends on the temperature and increases with it. Below the breakdown voltage, the dark current is strongly temperature dependent and increases with it. Figure 2.3 on the middle left shows the photo current curves I_{ph} in a plot of current I versus voltage U for the same temperatures as before. The photo current behaves similarly to the dark current. At lower temperatures it runs at much higher values. The I_{ph} curves also increase with voltage rather slowly at first. When the breakdown voltage U_{br} is reached, the slope becomes extremely large. Below the breakdown voltage, the photo current is not as strongly dependent on temperature as the dark current, but still increases with it. From the photo current curves the gain voltage characteristic $M(U)$ can be determined according to equation 2.1. This is shown again for the previous temperatures in figure 2.3 on the middle right. At about 40 V the gain rises sharply within a few volts and reaches values above 4. Thereafter, it increases with voltage. At the breakdown voltage, the slope abruptly becomes extremely large. The gain is then far above 100 and tends towards infinity. The reason for the behavior of these three quantities at about 40 V is that the sensor is depleted to the substrate at this voltage. Thus, electron hole pairs that are generated are separated by the drift field E_d and contribute to the measured current. At the same time E_M becomes large enough for multiplication of the charge carriers.

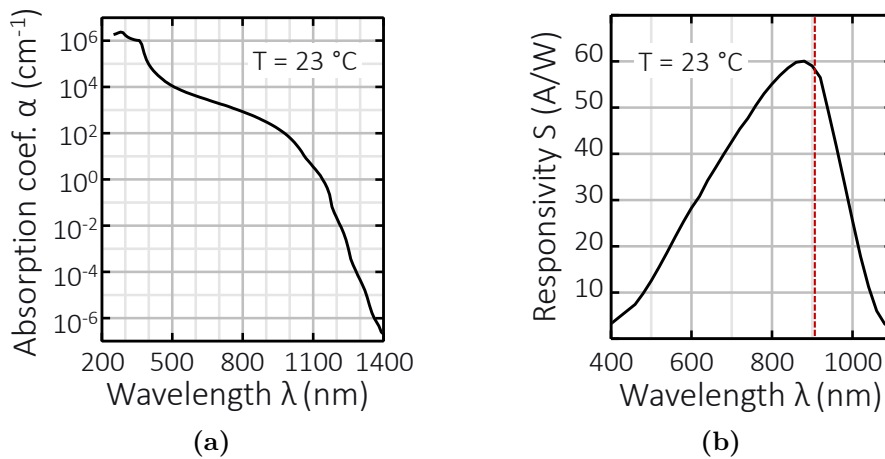


Figure 2.4: a: Absorption coefficient α against the wavelength λ . Data from [37]. b: Responsivity of LiDAR APD against wavelength λ . Data from [38].

In figure 2.3 on the right the breakdown voltage U_{br} is plotted against temperature T . For all curves shown, the breakdown voltage values lie on a straight line with slope $T_K \approx 1.5 \text{ V/K}$. The latter is called the temperature coefficient. It describes how much U_{br} increases per Kelvin. The reason for this behavior of the breakdown voltage is that the number of lattice vibrations increase with temperature. Thus the mean free path of the charge carriers decreases. This leads to an increased rate of collisions with lattice atoms before they have gained enough energy from the field for impact ionization. Therefore, the gain decreases with increasing temperature and higher fields are needed for the same value of the Gain.

Optical properties

The basic physical mechanism of photo detectors is the photoelectric effect. A photon excites a charge carrier into a conductive state, which results in conductivity. The necessary energy for this process is obtained from the energy of the photon E_λ . It is determined from the wavelength by $\lambda = hc/E_\lambda = 1.24/E_\lambda(\text{eV}) \mu\text{m}$. Where h is the Planck constant and c the speed of light. With the transition energy from valence to the conduction band ΔE , photons with $E_\lambda \geq \Delta E$ can excite charge carriers. This corresponds to the lower limit of photon energy. Below this, they cannot be detected. An important measure is the absorption coefficient, which describes the tendency of the semiconductor material to absorb light. Figure 2.4a shows the dependence of the absorption coefficient in silicon on the wavelength of the incident light. It decreases with increasing wavelength until it becomes vanishingly small at about 1100 nm. This corresponds approximately to the wavelength at which photons still have the required

energy of 1.1 eV to lift electrons from the valence band into the conduction band of silicon. Figure 2.2 illustrates the decrease in light intensity with distance x from the surface at $x = 0$ into which the light enters. There is an exponential relationship. Thus, in general, most light is absorbed near the surface. Up to which depth the incident light is absorbed depends strongly on the absorption coefficient. If the value is high, the light is completely absorbed in the first few nm below the surface. This has the disadvantage that the electrons generated there do not pass through the complete area in which multiplication takes place and thus their multiplication factor is lowered. This behavior therefore limits the photon energy. Light with the LiDAR wavelength of 905 nm is absorbed up to a depth of about 65 μm to 90 %. As described, the concept of APD is that the photo generated carriers are generated in the drift field below the $p+$ implant as it is shown in figures 2.1 and 2.2. From there, they drift towards the surface at saturation velocity to be multiplied in the last 2 μm below it. In this process, the field is only present within the depletion zone. Its depth is therefore crucial for the function. This is therefore not guaranteed below 40 V where the depletion width is less than 65 μm . In general, the detector is designed in such a way that the depth of the depletion zone meets this value in the range of the operating voltage.

The quantum efficiency η is a measure that takes all of the above factors into account. It is defined as the ratio of the number of generated electron-hole pairs to the number of incident photons: $\eta = n_{e-h}/n_{ph}$. Ideally, it is $\eta = 1$. Among other factors, reduction occurs due to current loss from recombination of carriers and reflection of light from the surface. Devices with anti-reflective coatings nevertheless achieve quantum efficiencies approaching 100 % in the near-infrared region. Quantum efficiency is the physical measure of responsivity S and thus closely related to it. It is defined as the ratio of the generated photo current to the power of the radiation: $S = I_{ph}/P_{opt}$. It is much easier to measure experimentally than quantum efficiency. Figure 2.4b shows the responsivity S as a function of wavelength λ for the devices studied. Starting at short wavelengths, S increases, reaches its maximum just below 905 nm and drops to zero at 1100 nm. The APD chips are designed such that the depletion width W_D in the range of operating voltages corresponds to a value of $1/\alpha(\lambda = 905 \text{ nm})$ to $2/\alpha(\lambda = 905 \text{ nm})$. Thus the peak of the responsivity curve is set to about 905 nm so that the light signal can be resolved as well as possible.

Functional parameters

The APD transforms an optical into an electrical signal. Figure 2.5 shows schematically the optical input and the electrical output. Mechanisms in the device cause a blurring and delay of the output compared to the input. The rise and fall time correspond to

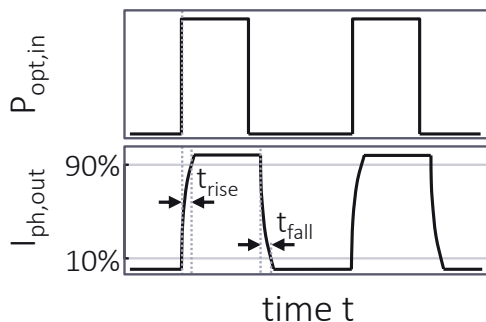


Figure 2.5: Sketch of the optical input signal $P_{opt,in}$ and the electrical output signal $I_{ph,out}$ of the APD.

the delays during the rise and fall of the signal. Both quantities must be minimized. They are significantly influenced by the so-called response speed of the sensor, which is a measure of how quickly generated charge carriers are extracted as output into the external circuit. It is influenced by the following factors. The first is the CR time constant $t_{CR} \propto 1/W_D$, where R and C correspond to the resistance and capacitance of the depletion region. Consequently, the depletion width W_D must be as large as possible. Furthermore, the transit time t_{drift} of the charge carriers in the depletion zone is crucial. This is determined by the drift velocity v_{drift} as $t_{drift} = W_D/v_{drift}$. To minimize it, the depletion zone must become as small as possible and the operation voltage or drift field in the design must be chosen such that the charge carriers move with saturation drift velocity. In addition, very strong generation of charge carriers occurs at very high light intensities. In this case, the attractive force between electrons and holes may cancel out the electric field. A rapid increase of the transit time is the consequence. An increase in multiplication is always accompanied by an increase in lattice collisions, which decelerate the electrons. This leads to an additional delay of the response speed, called multiplication time. Charge carriers generated outside the depletion zone must diffuse into it before they can be accelerated in the drift field. This diffusion process can take up to 1 ns and is called diffusion time. To minimize it, the semiconductor must be depleted as much as possible. Finally, the CR time constant, the drift time and the diffusion time result in an optimum for the depletion width.

In the LiDAR application, the intensities of the signals from distant targets are very low. In order to resolve them, the noise of the sensor must be as low as possible. It is due to spontaneous fluctuations of the current as it flows through the component. There are basically two types of noise sources that cause these fluctuations in the sensor. One is thermal noise, also called Johnson noise. It describes the thermally random motion of the charge carriers. It is frequency independent and therefore corresponds

to white noise. Its noise current $\langle i_{therm}^2 \rangle$ is calculated as:

$$\langle i_{therm}^2 \rangle = 4 k_B T \frac{B}{R} \quad (2.2)$$

Where B is the bandwidth of the readout circuit and R is the sum of all resistors through which current flows. The second noise source is the so-called shot noise. It is caused by the discrete individual events of charge carrier generation and recombination and the statistical fluctuations associated with them. They include thermal and photoelectric generation and recombination and impact ionization. Shot noise is also frequency independent. There is an additional noise factor due to impact ionization which is called excess noise $F(M)$. Its origin is the fact that not every electron experiences the same multiplication. It thus accounts for fluctuations in the process of avalanche multiplication and is dependent on the gain M . Assuming that only electrons enter the multiplication zone, the excess noise can be determined by [39, 40]:

$$F = M[1 - (1 - k)((M - 1)/M)^2] \quad (2.3)$$

Where $k = \alpha_p/\alpha_n$ is the quotient between the field dependent impact ionization rates of holes and electrons (section 2.4). In general, a small value for k is desired to keep the excess noise as low as possible. In silicon $k \ll 1$ since $\alpha_n \gg \alpha_p$. The shot noise is finally determined by [35, 40]:

$$\langle i_{shot}^2 \rangle = 2e (I_d + I_{ph}) MF(M) B \quad (2.4)$$

Here e corresponds to the elementary charge, I_d and I_{photo} to the multiplied dark and photo currents. Thus, $2e I_{d,M=1}$ and $2e I_{ph,M=1}$ are the contributions from thermal and photoelectric generation. The term $MF(M)$ corresponds to the factor by which the noise increases when the noise of the generated carriers is multiplied. Because both, signal and noise are multiplied by M , this results in an optimal value for M regarding the signal-to-noise ratio (SNR) which is defined as the relation of the output signal current to output noise current.

2.2 Basic principles of Light Detection And Ranging

Light Detection And Ranging (LiDAR) is a method to measure distances. It is based on the time of flight measurement. In the following, the basic structure and function of the rotating LiDAR module is summarized.

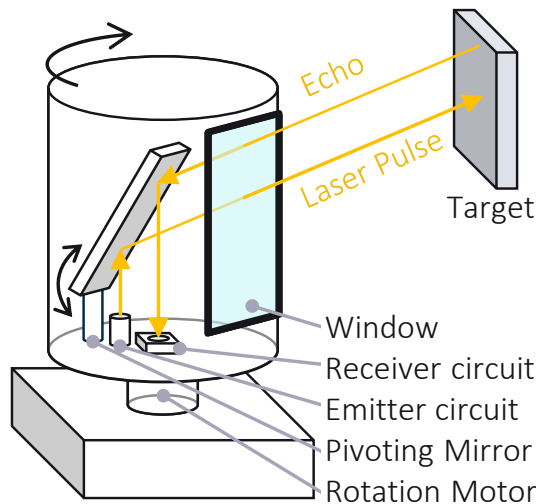


Figure 2.6: Basic structure of a LiDAR module. Its components are labeled. The illustration is inspired by [3, 4, 17, 21, 25]

2.2.1 Basic structure

Figure 2.6 illustrates the basic structure of a LiDAR module. The laser source emits laser pulses which are aligned to the window by a pivoting mirror. They travel at the speed of light, reach the target object and are reflected from it. Part of the reflected light passes through the window into the LiDAR module, where it is aligned with the receiver which detects it as an echo signal. The receiver corresponds to an optical sensor such as an APD or an APD array. During the process, the light travels the distance between the LiDAR module and the target object twice. The distance d can therefore be calculated from the time t_{flight} required to overcome it with $d = t_{flight} c/2$. Due to the rotation around the vertical axis of the module and the pivoting of the mirror, all spatial directions can be scanned. In this way LiDAR provides data of the distances of surrounding objects. Essential is the measurement of the time between emitting the light pulses and detecting the echo pulses. Figure 2.7 shows the output signal of the laser in a plot of signal intensity against time. It corresponds to a rectangular pulse shape. The peak intensity of the output must be maximum to detect remote targets. At the same time, the average output power must be kept as low as possible due to eye safety restrictions. Therefore, the phase of disappearing intensity is kept as long as possible and the high intensity as short as possible. The rectangular pulses are 10 ns long and the signal is modulated with a frequency up to 500 kHz [41, 42]. Figure 2.7 also shows a plot of echo signal intensity $P_{opt,in}$ against time which reaches the APD. Here the time difference t_{flight} corresponds to the time offset due to the time of flight of the light. Extracting this from the data is subject to some challenges. In automotive applications, distances from a few cm up to an order of 100 m must be resolved. To be able to measure small distances, the determination of the time offset between laser output and its echo must be very precise. Time differences must be resolved down

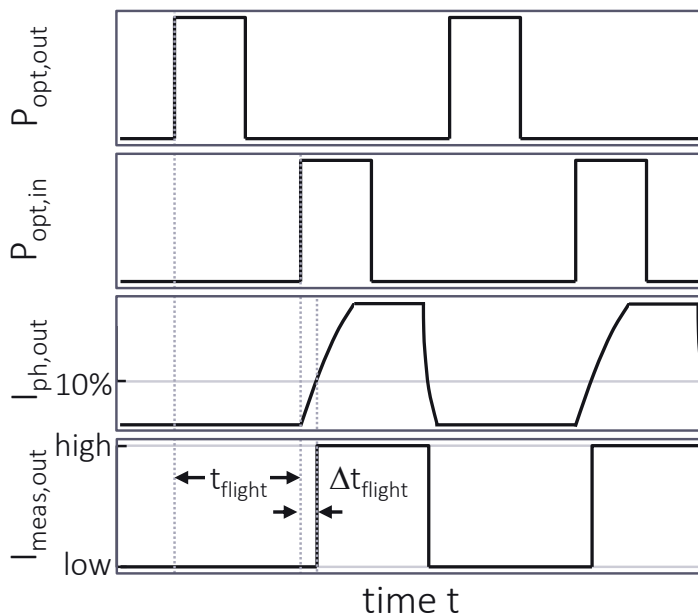


Figure 2.7: Sketch of the optical output signal $P_{opt,out}$ of the laser, the optical echo/input signal to the APD $P_{opt,in}$, the electrical output signal of the APD $I_{ph,out}$ and the resulting output of the voltage comparator $I_{meas,out}$ against time t . The latter is the basis of the measurement of t_{flight} . The time of flight t_{flight} and its error Δt_{flight} are marked.

to the ps range. At large distances, the intensities of the echo signals are very low. Therefore, very low intensities must be resolved at the same time.

2.2.2 Receiver circuit and time of flight measurement

Figure 2.8 shows the basic circuit of the receiver. It consists of a high voltage (HV) contact to which a very high negative voltage is applied. The resistor R is of the order of 10 kOhm and is intended to prevent excessive DC currents from the HV into the circuit if, for example, the APD physically breaks down to prevent further damage in this case. In case of large signal intensities of the optical input, the APD transforms them into large current pulses which should not be suppressed. In this case, the capacitor C and its branch provide the necessary energy for a short time such that the APD can generate the signal without limitation. The capacitor is in the range of 3.3 – 4.7 nF. This is followed by a circuit consisting of APD and transimpedance amplifier (TIA). The APD generates an electrical signal from the optical signal, which is amplified by the TIA for better evaluation. The amplified electrical signal is then passed on to the timing circuit. When using the TIA, it should be noted that in the case of high temperatures or high background radiation, a high DC current is output by the APD. This can cause the TIA to reach its modulation limit and the amplifier closes, so that the signal is not amplified properly and becomes smeared.

There are two ways to prevent DC currents from reaching the amplifier. The circuit of the first one is shown in figure 2.8 on the lower left. The resistor $R_{AC} \propto 1$ kOhm and the contact to ground ensure that ground is applied to the cathode of the APD without

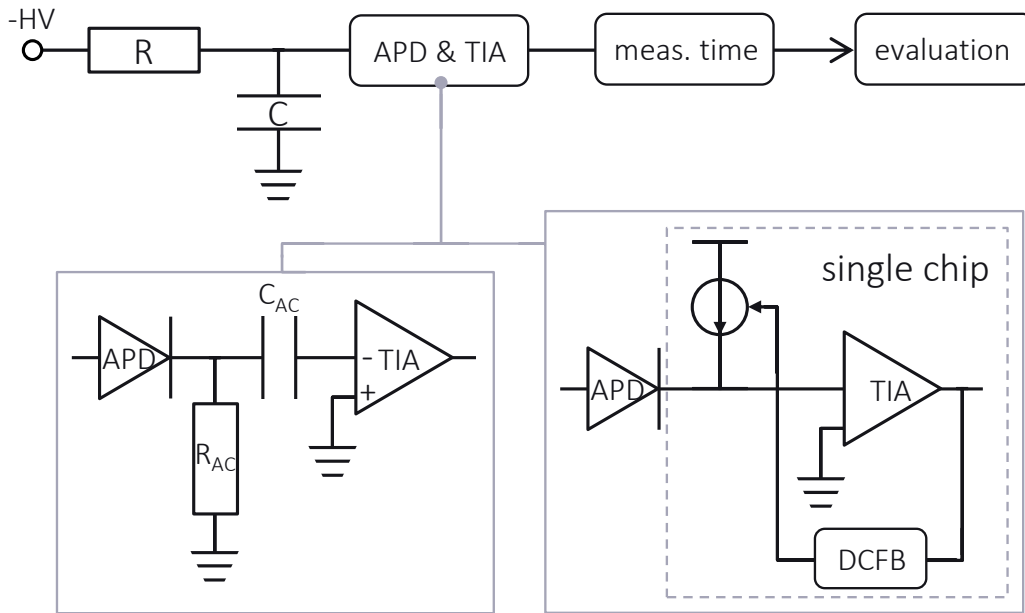


Figure 2.8: Basic receiver circuit of the LiDAR module. Two possible setups of an APD-TIA circuit are shown: the AC coupling (lower left) and the DC feedback loop (lower right).

current passing through. The capacitor $C_{AC} \propto 1 \text{ pF}$ transmits only AC signals to the amplifier and is optimized in size for optimum noise bandwidth. In this way, TIA and APD are AC coupled and the amplifier sees only the AC portion of the current that contains the actual signal. This setup consists of several components. In general, the increase of the number of components leads to an increase the noise of the entire circuit. Therefore, the circuit shown in figure 2.8 on the lower right corresponds to a sufficient alternative. Behind the APD the TIA is connected in a DC feedback loop (DCFB). The DC output from the TIA is branched off and given back into the voltage controlled current source and input back in front of the TIA as a negative current. In this way, up to 2 mA DC component of the APD output can be compensated. The main advantage is that the TIA and the DC feedback loop are fabricated on one chip, so the noise contribution is rather small. In both cases, only the AC portion of the APD output is given to the TIA. This includes not only the signal but also the noise of the APD. In section 2.1 it was shown that all forms of generation and recombination increase the noise current. Therefore, the noise contribution of high background irradiation and temperature which are direct current sources cannot be suppressed. Because of that, the sensor is not exposed to the complete light spectrum. There are always filters in the beam path in front of it, which have a bandwidth of $(905 \pm 50) \text{ nm}$. This keeps the impact of background irradiation as low as possible.

Due to the response behaviour of the APD, the output signal of the APD $I_{ph,out}$ is delayed and smeared compared to the optical input $P_{opt,in}$ as it is shown in figure 2.7.

The output of the APD can now be processed by a voltage comparator. It gives a high output (1) when the output signal of the APD reaches 10 % of its maximum level. Below that it gives a low signal (0). The electrical signal that triggers the laser and the output signal of the voltage comparator $I_{meas,out}$ are now fed into a time-to-digital converter that outputs the time difference of both digitally. Due to the smearing of the APD signal, the time of flight t_{flight} is subject to an error Δt_{flight} . This ultimately determines whether the resolution of the time down to the ps range is possible.

In addition, the light signal must be detectable in the electrical output of the APD. This is not the case if the noise of the APD output is larger than the signal current. Theoretically, signals can only be resolved when the signal-noise-ratio (SNR) is greater than 1. A low SNR can become a problem at high distances when the intensities of the optical echo signal are very small. The gain M of the signal can be controlled by the operation voltage U applied to the APD. However, it also multiplies the noise. That leads to an optimum of the gain M , where the signal is strongly multiplied, but the noise is not. In this optimum weak signals are very well resolved. Therefore, in some concepts it is chosen as the operation point of the APD. Due to the temperature dependence of the M - U characteristic, it must be readjusted in case of temperature fluctuations. This is done according to the temperature coefficient $T_K = 1.5 \text{ V/K}$ introduced in section 2.1. For example, if the optimum is reached at room temperature at $U = 160 \text{ V}$, the voltage must be increased by 30 V for a temperature increase of 20 °C. In this way, the optimum is reached with an accuracy of 5 %. A second concept is to set a limit for the noise level of the APD and increase or decrease the voltage until this limit is reached.

2.3 Basic principles of reliability analysis

In the automotive sector, a very low failure rate of all installed components must be guaranteed for decades. The exact value is demanded from the customer. A value of 1 ppm/h (parts per million) is assumed throughout this work. This also applies to the sensors in the LiDAR module and thus to the APD and its function in the LiDAR application. In order to analyse the reliability of the APD, underlying physical mechanisms governing the aging process need to be known. In the field of reliability physics of power devices, there is a large number of reported mechanisms. Those that can potentially have a large effect on the function of the APD in the automotive LiDAR application are briefly presented. Before, the concept of aging analysis is outlined.

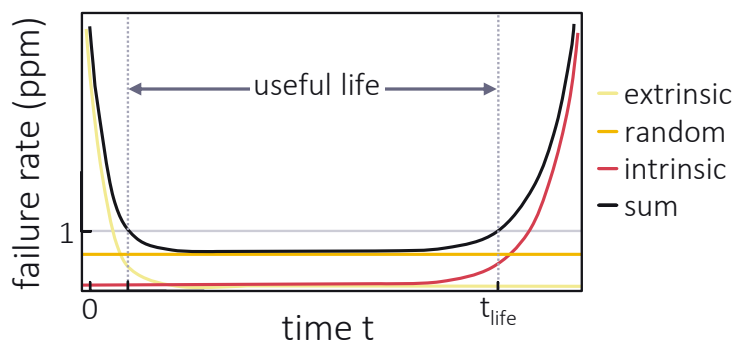


Figure 2.9: The bath tub curve: failure rate as a function of time. Extrinsic, random and intrinsic failures are shown. Their sum corresponds to the overall failure rate. Inspired by [43, 44].

2.3.1 Concept of aging analysis

Failure generally means that the APD does not fulfill its intended function or no longer does so over time. A concept that describes the life cycle of a component is the so-called Bathtub Curve [43, 44] in figure 2.9. It models the failure rate as a function of time and can basically be divided into three phases. The first phase is that of childhood mortality. Due to unintentional failures or deviations during manufacturing, there is an increased failure rate. These so-called extrinsic failures do not originate from inadequate process, design or material planning but are due to the statistically occurring deviations from these. The defective components fail early and the failure rate drops to an ideally moderate level below the 1 ppm/h limit. This is the beginning of the second phase. The failure rate is characterized by a very low rate of random failures. It corresponds to the time when the components are used in the field and function as designed. The processed materials of the components are stressed during their operation and degrade over time. This is due to the choice of materials, design and operating conditions and can have a major impact on function. Therefore, the failure rate increases again over time. This is the third, the wear out phase. It occurs due to physical processes that take place within the component and therefore systematically promote internal degradation. These are so-called intrinsic failures and the physical processes are called intrinsic failure mechanisms. If the failure rate rises above the limit value of 1 ppm/h after a certain time, proper function can no longer be guaranteed. This point in time, which is determined by the intrinsic failure mechanisms, corresponds to the lifetime. The failure rate in the first phase can often be well controlled by process monitoring. In contrast, it is difficult to determine the lifetime.

Similar to the discussion in [45], the APD in the field of lifetime analysis can be understood as a system that transforms optical signals into electrical signal as illustrated in figure 2.10. Moreover, it relates operating conditions, such as operating voltage, intensity of the optical signal, and temperature to properties such as a certain gain M , a noise level, and a response time. As mentioned in section 2.1 and 2.2, these properties have a great influence on how similar optical input and electrical output

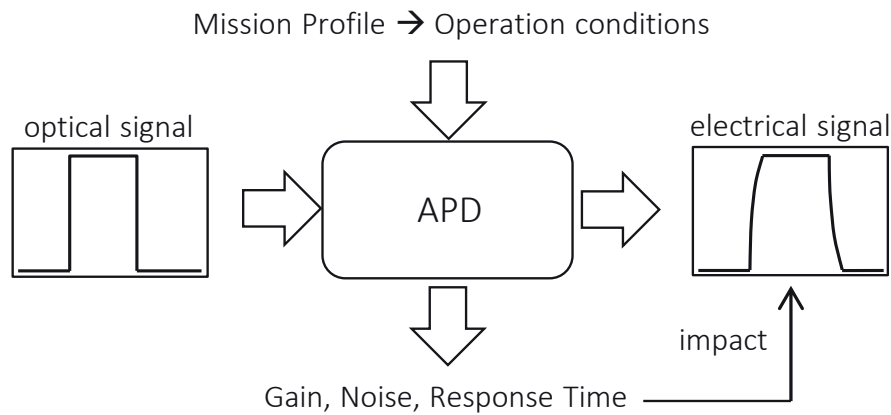


Figure 2.10: The APD as a transformer of optical inputs to electrical outputs. This transformation is impacted by gain M , noise and response time. These are governed by the operation conditions. The operation conditions are defined by the mission profile. Inspired by [45].

are. Ideally, the difference between the two vanishes. The mission profile corresponds to the set of all intended operation conditions [44, 45]. In [46] it is defined as *the simplified representation of all of the relevant conditions to which all of the production devices will be exposed in all of their intended applications throughout the full life cycle of the semiconductor component*. The LiDAR mission profile is defined by the AEC-Q100 standard [47]. Typically, an automotive grade 1 operating temperature range is required, which extends from -40°C to 125°C and is necessary to cover the self-heating of the electronic components inside the LiDAR module and various environmental conditions around the world. Within the mission profile, the sensor must be able to reliably fulfill its intended function. This is defined in the specification. It represents the totality or limits of the properties the APD need to obtain. A sensor is considered robust if its properties lie within the specification. For the noise, for example, in LiDAR operation, this would mean that it must be as low that light intensities from more than 100 m distant objects can still be detected [4, 25, 29]. However, due to the intrinsic failure mechanisms, the characteristics change over time depending on the conditions at which the APD is operated within the mission profile. For example, noise could increase over time and 100 m distant targets could no longer be reliably detected. In this case, the APD can no longer meet the specification and fails by definition. The definition of a failure and thus the lifetime depend on the one hand implicitly on the mission profile and explicitly on the specification.

The content of the following paragraph is based on [43, 44]. The lifetimes of the components are assumed to be in the range of several decades. Therefore, experimental lifetime analyses usually cannot be performed within the mission profile. Instead, the aging mechanisms are accelerated by exposing the sensors under test to elevated oper-

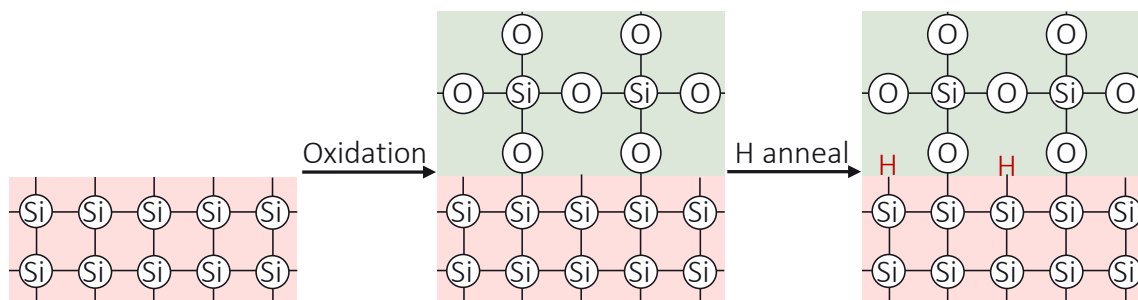


Figure 2.11: Illustration of the oxidation of the silicon surface and the passivation of the resulting Si:SiO₂ interface via hydrogen annealing.

ating conditions, so-called stressors, for a defined period of time. Thus, several decades of continuous operation in the field can be simulated experimentally and the aging effects observed. The rate of degradation depends on how the failure mechanisms depend on the stressors. Since the failure mechanisms occur systematically, a small number of tested components is often sufficient. However, the failure mechanisms may in turn depend on internal properties of the sensors (doping profiles and concentrations, concentration of traps, dislocations, etc.) which may vary for individual sensors. So, it can be important to test a larger number of devices for quantitative lifetime information. In addition to the components in the standard design, test structures can also be used, for example to separately characterize failure mechanisms or to better observe their effects. It is important that no new failure mechanisms occur due to the difference in design. Likewise, the stressors must not differ so much from the mission profile that mechanisms occur that do not play a role in operation within the mission profile. Furthermore, during the stress experiments it is useful to select a parameter on which the degradation is observed. This parameter does not necessarily has to be one of the parameters in the specification pool. For all these considerations, it is important to know in advance about the nature of the failure mechanisms. This can be obtained by preliminary tests or literature research. Countless works in the field of power devices are available. A part of it is presented in the following.

2.3.2 Generation of interface traps

The generation of traps at the Si:SiO₂ interface is a crucial phenomenon in the field of MOSFET reliability physics. In [48] it is proposed to cause 90% of the MOSFET degradation. In order to introduce the underlying concept, a short review of the phenomenology of interface trap generation will be given.

The silicon atom has four valence electrons. So it needs four bonds to be saturated. Silicon has a diamond structure. Thus, each atom in the bulk crystal has four neighbors

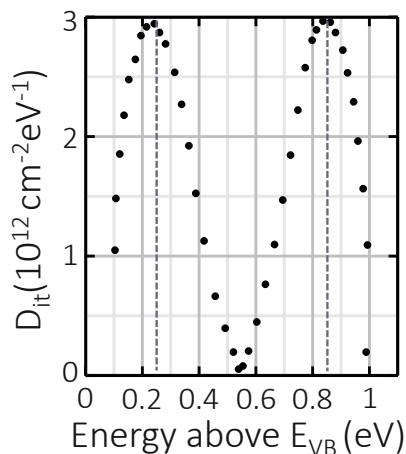


Figure 2.12: Experimentally determined density of states of dangling bonds D_{it} in the silicon band gap. The energy is regarded relative to the valence band edge E_{VB} . Data from [52].

to which it is covalently bonded. This is not true at the surface. As shown in figure 2.11 on the left, the outermost atoms possess dangling bonds - unsaturated valence electrons. There are about 10^{14} cm^{-2} of these Si atoms at the surface [49]. During the process flow of APD fabrication, the surface is oxidized. This reduces the concentration of dangling bonds by two orders of magnitude to 10^{12} cm^{-2} [49]. In the $\langle 111 \rangle$ orientation of the silicon surface, which all studied APDs possess, the dangling bonds are called P_B center. They act as generation-recombination centers in the device [50] and generate dark current. This leads to a lowering of the signal-noise-ratio. Therefore, the Si:SiO₂ interface is passivated with hydrogen during a corresponding annealing at high temperatures (400 °C - 900 °C). As illustrated in figure 2.11 on the right, the dangling bonds are saturated to a large extent. It is shown in [51], that the resulting reduction of the dangling bonds by another two orders of magnitude to 10^{10} cm^{-2} results in a decrease of the dark current by up to two orders of magnitude.

The remaining dangling bonds act electrically as amphoteric traps. This type of traps possesses both donor and acceptor properties. Their density of states in the silicon band gap of 1.1 eV is shown in figure 2.12. All states below the midgap energy E_{midgap} act as donors, all above as acceptors. Thus, the distribution can be considered to be split at E_{midgap} . The distribution of donor states peaks at E_D and that of acceptor states peaks at E_A . In agreement with [52-54], $E_D = 0.25 \text{ eV}$ and $E_A = 0.85 \text{ eV}$ are taken. The effective cross section for electron and hole capture is $\sigma_e \approx 4.4 \times 10^{-15} \text{ cm}^{-2}$ and $\sigma_h \approx 4.4 \times 10^{-17} \text{ cm}^{-2}$ [54-57].

The starting point of degradation is the passivated interface as it is illustrated in figure 2.11 on the right. During operation, the saturated Si-H bonds can interact with electrons on the silicon side. This causes their heating and rupture. The process is shown in figure 2.13. Electrons coming from the silicon crystal to the interface interact with the Si-H bonds - figure 2.13 on the left. It is reported in [58-61] that interface trap generation correlates with high field transport in silicon. This is explained in [62-

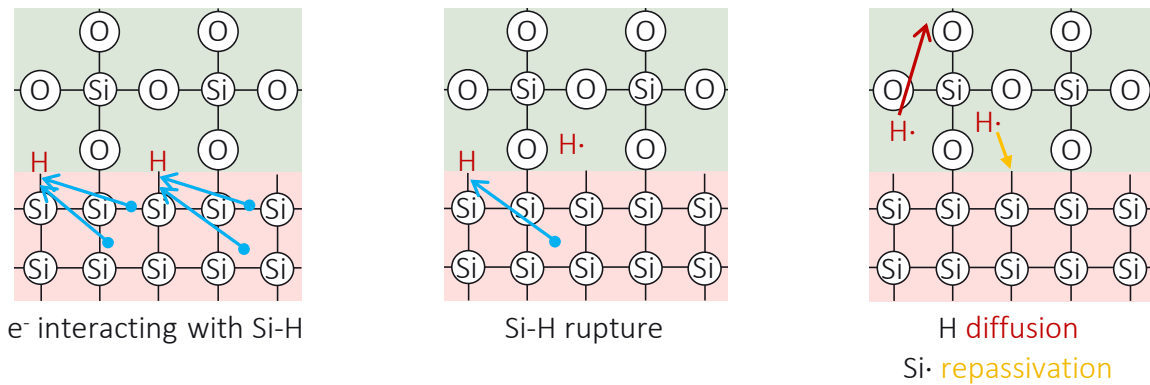


Figure 2.13: Process of dangling bond depassivation at the Si:SiO₂ interface including the interaction of electrons with Si-H bonds (left), the rupture of Si-H bonds (middle) and the diffusion of hydrogen or re-passivation of dangling bonds (right).

66] as the hydrogen desorption depends on the energy distribution of electrons that collide with the interface. The threshold energy for bond breakage varies from 1.5 eV to 3.8 eV. This picture is refined in [64, 67]. Electrons of lower energies heat and thus weaken the Si-H bonds. Single energetic electrons are then able to break the bonds and liberate the hydrogen atoms from their silicon atoms as it is illustrated in figure 2.13 in the middle. These can now either diffuse away from the interface or remain at it and interact with dangling bonds and re-passivate them [68-80]. The diffusing species is assumed to correspond to either atomic or molecular hydrogen. In essence, these processes lead to an increase in the dangling bond concentration at the interface. However, it can be stopped by saturating the interface with deuterium instead of hydrogen. Since deuterium is heavier, its threshold energy for bond breakage is much higher. This so-called isotope effect was observed in [75, 81].

2.3.3 Oxide charge generation

The charging of the device dielectric is also reported as a crucial issue in the field of reliability physics of power devices [59, 82-90]. The following explains the reported behaviour and nature of SiO₂ charging. The basic mechanism is depicted in figure 2.14a. Electrons shown as blue filled circles are injected from the silicon side of the interface into the oxide. There they are captured by electron traps. This generates negative oxide charges, which electrically have an impact on the underlying silicon.

Depending on the process flow, silicon dioxide often possesses an amorphous structure. This leads to defects and stretched bonds. These intrinsic defects can act as electron traps whose density is reported to be determined by the process flow of oxidation [82, 91-96]. One of them is the numerous reported oxygen vacancy [92, 97-103] $O_3 \equiv Si \cdot \cdot Si \equiv O_3$. The origin of its occurrence is the redox reaction [92, 104, 105]: $O_3 \equiv Si-O-Si \equiv O_3 \leftrightarrow$

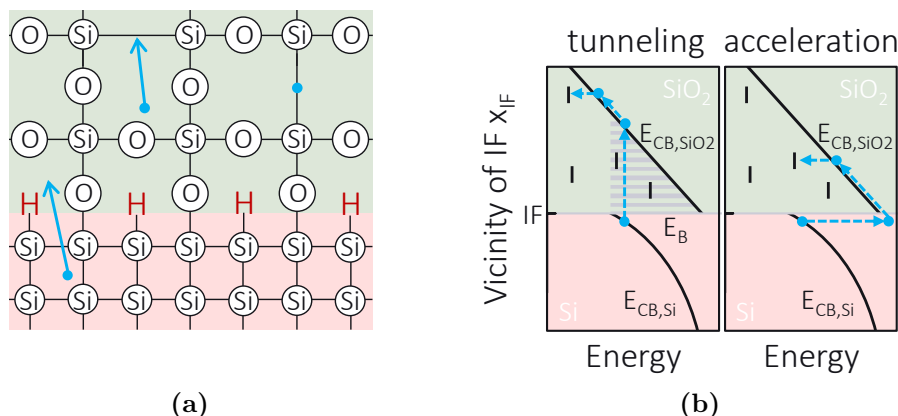


Figure 2.14: Illustration of the process of oxide charging. a: Electrons (blue circles) are injected from silicon into the oxide. There, they get captured by electron traps. b: Illustration of two injection mechanisms. The conduction band edges in silicon $E_{CB,Si}$ and silicon dioxide E_{CB,SiO_2} are shown at the interface. Electron traps are depicted as short lines in the oxide.

$O_3 \equiv Si \cdot \cdot Si \equiv O_3 + O$. An increase of the amount of oxygen during the oxidation and oxygen annealing shifts the equilibrium to the right. Increasing process temperatures shifts it to the left. It was found to have shallow and also deep trap levels. Also, an internal electron transfer, a relaxation from the shallow to the deep level is reported [106, 107]. Very often the process flow is accelerated by wet oxidation where water vapor is added to the oxygen atmosphere. This leads to the formation of water related impurities [82, 108] like interstitial H_2O or $SiOH$ [82, 94, 109, 110]. They act as deep level traps and are very sensitive to heat treatment, which leads to removal and a reduction in the concentration of the traps on one hand [82, 95, 108, 111]. On the other hand, trivalent silicon $O_3 \equiv Si \cdot$ is reported to occur after the removal of water related impurities [92, 110]. It also acts as deep level electron trap [97-103]. It is shown in [97-103] that stretched Si-Si and Si-O bonds introduce a continuum of shallow and deep trap levels. In addition to those mentioned, electron traps can also be formed by phosphorus diffusing from the doped regions in the silicon into the oxide and forming traps there [112]. This is not inconceivable since the $n+$ contact doping shown in figure 2.1 is realized by phosphorus.

In figure 2.14b the evolution of the conduction band edges of silicon $E_{CB,Si}$ and silicon dioxide E_{CB,SiO_2} is shown at the interface during the normal operation of the APD under reverse voltage. A positive voltage is applied above the oxide and a negative voltage below the silicon. This leads to the illustrated curvature of the bands which leads to a kind of potential well formed at the interface on the silicon side. The short lines below the silicon dioxide conduction band edge symbolize traps in the oxide. Electrons are accelerated out of the silicon towards the interface due to the band curvature. At the interface, an energetic barrier E_B exists between silicon and silicon dioxide. The height

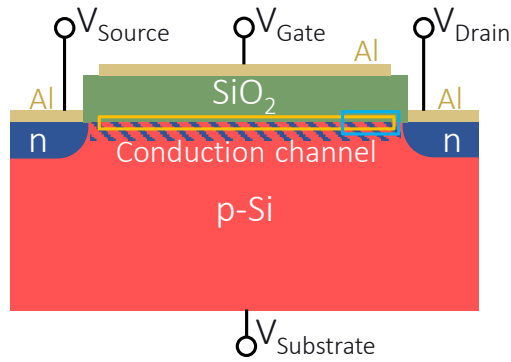


Figure 2.15: Schematic cross section of a MOSFET with doping and material profiles. The conduction channel is laid out and the prominent location of channel hot electron injection (CHEI, blue) and substrate hot electron injection (SHEI, orange) are marked.

of this interface barrier corresponds to the difference in the electro negativities of the two materials. Its value of about 3.25 eV is taken from the literature [35, 112]. Due to image force lowering, also called Schottky lowering, there is a reduction of the barrier proportional to $E_{ox}^{1/2}$ depending on the electric field in the oxide E_{ox} . There are two mechanisms by which electrons can enter the oxide.

The first is a tunneling effect. From the silicon conduction band, electrons can only tunnel directly through oxides with a thickness of less than 3 nm [113]. The standard technology of the considered APDs aims at a thickness of 800 nm. Thus, electrons can not tunnel through the oxide but into its conduction band. This process is shown in figure 2.14b and is called Fowler-Norheim tunneling. The tunneling probability is inversely proportional to the barrier area [114], which is marked by the dashed area below the conduction band edge of the oxide. This is constructed by drawing a horizontal line from the conduction band edge in the silicon at the interface to the conduction band edge of the oxide. The size of the area depends significantly on the curvature of the conduction band. Thus, the area decreases with increasing oxide fields E_{ox} . In conclusion, the tunneling probability increases with increasing oxide field. Therefore, a threshold value can be found below which the tunneling probability becomes negligible. This is $E_{ox} = 6 \text{ MV/cm}$ [113, 115]. The second injection mechanism of electrons into the oxide is also shown in figure 2.14b. Electrons acquire kinetic energy due to the acceleration in the electric field at the silicon side E_{si} . This leads to a heating of the electron population. As a result, electrons have higher energies than the conduction band edge of the silicon. Depending on the field strength E_{si} , a part of the population has an energy higher than the barrier E_B and can therefore overcome it. Corresponding electrons are called hot electrons. There are two hot electron injection methods for MOSFETs, which show a dependence of the injection probability on the angle of the field E_{si} and the interface and its magnitude. These will also be briefly presented. Figure 2.15 shows the basic structure of a silicon MOSFET. As the APD in figure 2.1, it has a p background doping in the illustrated case. On the surface, the n dopants for source and drain are shown laterally. These are each contacted with a contact metal on

the surface to form the contacts of the same name. Between them, the silicon is covered with silicon dioxide, on which the gate contact is located. The gate contact cannot inject charge carriers through the oxide into the device, but can only control the field in the conduction channel underneath and thus its conductivity. In normal operation, a lower voltage is applied to the source than to the drain. This allows electrons to flow from the source to the drain. The current flow can then be controlled by the gate voltage. A high positive voltage leads to a high conductivity in the channel, a high negative voltage leads to a vanishingly low conductivity. In addition to the three contacts mentioned, there is the substrate contact located at the bottom of the chip. The first method of electron injection is channel hot electron injection (CHEI) [81, 113, 116-118]. Here, the source and substrate contacts are grounded ($U = 0$) and the drain contact is slightly higher ($V_{Drain} > 0$ V). A voltage just sufficient for the conduction channel to occur is applied to the gate contact. In this mode, electrons flow mostly parallel to the interface and the angle between the field E_{si} and the interface is very small. When the gate voltage is increased and the angle increases, the injected electrons are measured as gate current. The higher the gate voltage the closer to 90° is the angle of the field E_{si} to the interface. As a result more electrons are injected into the oxide. The injection profile is not homogeneous along the interface, but obtains a peak where the field E_{si} is highest [118]. As shown in figure 2.15, it is located at the channel end near the drain contact.

The second method of electron injection is substrate hot electron injection (SHEI) [81, 113, 118-121]. Here, $V_{Drain} = V_{Source} = 0$ V, $V_{substrate} < 0$ V, and $V_{Gate} > 0$ V. In fact, the substrate voltage is very highly negative. This operation accelerates electrons uniformly from the silicon to the surface. At the surface, the field E_{si} points predominantly perpendicular to the interface and is approximately equal at each location there. As a result, the injection profile is homogeneously distributed along the interface. The injection rate increases with an increase in negative substrate voltage. The results of the two injection methods show that the injection probability of electrons into the oxide is determined by the magnitude of the electric field E_{si} and its angle to the interface. Fields of the order of 10^5 V/cm are sufficient.

If the electrons are in the conduction band of the oxide as shown in figure 2.14a, they can be captured by traps. This generates negative oxide charges [59, 83, 87-90, 122-127]. They can also be released from the traps. This process, called detrapping, was observed in [91, 113, 128, 129]. It was shown that the occupation level saturates at a value corresponding to only a fraction of the concentration of the oxide traps. This saturation value depends on the field E_{ox} and the electron flux in the oxide - the higher both, the stronger is the detrapping. From this it could be concluded that the de-

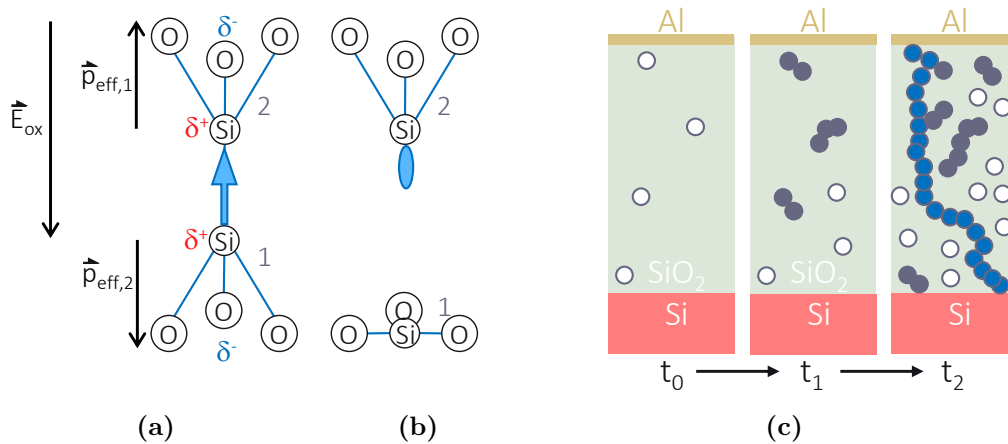


Figure 2.16: a & b: The interaction of the oxide field E_{ox} with the oxygen vacancy leads to a shift of the electron distribution and polarization of the bond (a). Breakage of the Si-Si bond and relaxation of the lower Si atom (b). Inspired by [141-145]. c: Evolution of a conduction path through the oxide. Electron traps (white circles), conducting clusters (grey circles) and the conduction path (blue circles) are shown. Initially, only preexisting traps exist (t_0). After a while additional traps and thus conducting clusters are generated (t_1). Later a conduction path through the oxide is formed (t_2).

trapping process is impact ionization [130, 131]. It was demonstrated for oxide fields $E_{ox} \geq 5 \times 10^5$ V/cm.

2.3.4 Oxide trap generation and oxide conduction

The literature for reliability physics of power devices reports that silicon dioxide becomes conductive during operation. In that case, the APD would no longer be functional. In many cases, reaching a critical concentration of electron traps in the oxide has been associated with conduction occurrence [35, 63, 112, 113, 115, 132, 132-134, 134-140]. In conclusion, this means that electron traps are generated over time during operation. The two most common mechanisms for this and the present conduction mechanism are presented below.

In [113, 145-148] it was found that the generation of electron traps in thick oxides at rather low fields E_{ox} is activated by temperature and driven by the field [149]. This is explained in [141, 142, 145] as the field interacts with all bonds showing dipole character as shown in figure 2.16a. In majority, the participation of the oxygen vacancy $O_3 \equiv Si-Si \equiv O_3$ is accepted [141, 142]. As shown in figure 2.16a, the electron distribution of the Si-Si bond is shifted against the field. The upper O atom is then negatively polarized. Dipole bonds are then stretched and thus excessively weakened. In the previous section, it was explained that stretched bonds can already act as traps. They can interact with phonons [142] and thus become thermally activated, causing them to break with time (figure 2.16b). This process is accelerated in oxides where H annealing has been

performed at high temperatures during the process flow [150]. Likewise in oxides that have a high percentage of water related traps [150-152], which is explained in [132] as all irregularities, defects and impurities lead to mechanical stress within the crystal structure of SiO_2 and bond is already stretched in advance and thus weakened. In this case, the required oxide fields to generate new traps are lower. A threshold value of the field E_{ox} for this process is around $7 \times 10^5 \text{ V/cm}$.

In the second mechanism, trap generation depends on the field E_{ox} and the electron flux in the oxide [48, 48, 63, 128, 153-156] and increases with E_{ox} . The threshold value for this is approximately $E_{ox,thres} = 2 \text{ MV/cm}$, although no generated traps were observed for fields smaller than 1 MV/cm [128, 128, 129, 152, 157-161]. In [115, 115, 128, 153, 160, 162-164] a relation to the energy of the electrons in the oxide could be established and a threshold value for this was determined to be 2 eV . Together with the fact that electron flow is also crucial, it was concluded that above fields of $E_{ox} = 2 \text{ MV/cm}$ impact ionization is responsible for the generation of the traps. In [144], the binding energy of weakly bound oxygen vacancies $\text{O}_3 \equiv \text{Si-Si} \equiv \text{O}_3$ was determined to be approximately 2 eV .

The conduction through the oxide is described mathematically as percolation [113, 145]. The process is illustrated in figure 2.16c. It shows the oxide, the underlying silicon, and the contact metal aluminum processed on top. Traps are shown as dots. The circles drawn around them symbolize their interaction radius. At the beginning of degradation, only traps exist in the oxide, which form during fabrication as described in the previous section. With time, the oxide degrades and new traps increasingly form at random positions. The interaction radii of some begin to overlap. The clusters that form in this way are intrinsically conductive. This is shown by the grey filled circles in figure 2.16c. Further degradation leads to the formation of a single conductive cluster connecting the silicon to the contact. It corresponds to the blue filled circles in the figure. Thus, a conductive path is formed through the oxide. Conduction along this path occurs by localized electrons tunneling or hopping between the traps. This type of conduction is called hopping conduction [165, 166]. Any form of impurity, defect, and mechanical stress weakens the bonding structure in the oxide and accelerates the occurrence of the conductive path [132, 150-152].

2.4 Basics of semiconductor device simulation

In this work, the semiconductor device simulator SILVACO ATLAS [167] is used in a coupled simulation together with a simulation of a novel degradation model. In this framework it delivers the electric fields and current densities inside the studied devices.

The simulator includes the relevant physics in the form of the so-called basic semiconductor equations. It approximates the device on a two-dimensional grid which is defined before the simulation. On this grid, numerical methods solve the implemented equations. This allows the prediction of the electrical and optoelectrical behavior of the semiconductor structure and gives insight into the device internal physical mechanisms associated with its operation. Aside of internal current densities and fields, it determines measurable quantities such as the current voltage characteristics that will be used to compare simulated and experimental data. In this section, the basic function of the simulator SILVACO ATLAS and the physical processes that are crucial in the studied sensors will be outlined. The following is based on the SILVACO ATLAS users manual [167].

2.4.1 Basic semiconductor equations

The basic semiconductor equations are derived from Maxwell's equations [168]:

$$\vec{\nabla} \times \vec{H} = \vec{J} + \frac{\partial \vec{D}}{\partial t} \quad (2.5a)$$

$$\vec{\nabla} \times \vec{E} = -\frac{\partial \vec{B}}{\partial t} \quad (2.5b)$$

$$\vec{\nabla} \cdot \vec{D} = \rho \quad (2.5c)$$

$$\vec{\nabla} \cdot \vec{B} = 0 \quad (2.5d)$$

Where $\vec{D} = \epsilon \vec{E}$ corresponds to electric displacement, ϵ to permittivity tensor, \vec{E} to electric field, \vec{H} to magnetic field, \vec{B} to magnetic flux density, \vec{J} to conduction current density and ρ to electric charge density. Materials such as silicon used in semiconductor devices do not have significant anisotropy or inhomogeneity of ϵ [169]. Thus, the permittivity is assumed to be scalar with:

$$\epsilon \rightarrow \epsilon = \epsilon_r \epsilon_0$$

With the electric field constant $\epsilon_0 = 8.85 \times 10^{-12}$ As/Vm [169] and the relative permittivity ϵ_r possessing a value of 11.7 in silicon and 3.9 in silicon dioxide [169]. Equation 2.5a expresses how an electric current and a change in electric field with time produce a magnetic field. It corresponds to the Ampere-Maxwell law. Equation 2.5b describes how a time-varying magnetic field produces an electric field and thus corresponds to Faraday's law of induction. Equation 2.5c describes the formation of electric fields due to the presence of electric charges and thus corresponds to Gauss's law. Equation 2.5d

formulates the non-existence of magnetic monopoles, sources or sinks.

Poisson equation

From the third Maxwell equation 2.5c the Poisson equation can be derived [167]:

$$\Delta\phi = -\frac{\rho}{\epsilon} \quad (2.6)$$

This involves expressing the electric field \vec{E} as the gradient field of the electric potential ϕ as $\vec{E} = -\vec{\nabla}\phi$. Moreover, ρ here corresponds to the sum of all mobile (n and p) and fixed charges C : $\rho = e(p - n + C)$. Fixed charges can be charged donors N_D and acceptors N_A and trapped electrons ρ_n and holes ρ_h . Image charges are not considered, as their effect turned out to be negligible at the regarded operation conditions in the studied devices. The Poisson equation 2.6 connects variations of the electrostatic potential with local charge densities.

Continuity equation

Applying the divergent operator to Maxwell's equation 2.5a, taking into account that the divergence of the curl from any vector field is zero, and using Maxwell's equation 2.5c, the general continuity equation is obtained:

$$\vec{\nabla} \cdot \vec{J} + \frac{\partial\rho}{\partial t} \quad (2.7)$$

Assuming that fixed charges are invariant in time ($\partial C/\partial t = 0$) and the current can be divided into an electron \vec{J}_n and a hole fraction \vec{J}_p , the continuity equations for electrons and holes follow with the introduction of the quantity R :

$$\frac{\partial n}{\partial t} = \frac{1}{e} \vec{\nabla} \cdot \vec{J}_n - R \quad (2.8a)$$

$$\frac{\partial p}{\partial t} = -\frac{1}{e} \vec{\nabla} \cdot \vec{J}_p - R \quad (2.8b)$$

Here R corresponds to the net recombination rate of electrons and holes. If $R > 0$, it is dominated by recombination. If $R < 0$ generation is dominant. R has to be modeled and depends on the considered generation and recombination mechanisms.

Poisson equation 2.6 and continuity equations 2.8 provide a general framework for semiconductor device simulation. Nevertheless, additional equations for R , \vec{J}_n and \vec{J}_p are needed. The last two can be derived by simplifying the Boltzmann transport equation.

Transport equations

The simplest transport model is the drift-diffusion model. It becomes inaccurate only in cases where the size of the structure under consideration becomes very small. In the present case, the structure sizes are in the μm range. Therefore, it can be used without hesitation. The derivation of the following equations can be found, for example, in [169]. They provide expressions for the current densities:

$$\vec{J}_n = en\mu_n\vec{E} + eD_n\vec{\nabla}n \quad (2.9a)$$

$$\vec{J}_p = en\mu_p\vec{E} + eD_p\vec{\nabla}p \quad (2.9b)$$

The expressions $en\mu_n\vec{E}$ and $ep\mu_p\vec{E}$ with electron and hole mobilities μ_n and μ_p correspond to electron and hole currents due to acceleration in the electric field \vec{E} . Therefore, these terms are called drift currents. They depend strongly on the considered scattering events. The terms $eD_n\vec{\nabla}$ and $eD_p\vec{\nabla}$ correspond to the electron and hole currents due to diffusion processes, which occur when there is a gradient of charge carrier concentrations n or p . The underlying imbalance of their densities is neutralized by diffusion. Here D_n and D_p are the diffusion constants for electrons and holes. They are described by the Einstein relations:

$$D_{n,p} = \frac{k_B T}{e} \mu_{n,p} \begin{cases} 1 & \text{for } |E_{n,p} - E_F| \gg k_B T \\ \frac{F_{1/2}\left[\frac{1}{k_B T}(E_{n,p} - E_{CB,VB})\right]}{F_{-1/2}\left[\frac{1}{k_B T}(E_{n,p} - E_{CB,VB})\right]} & \text{else} \end{cases} \quad (2.10)$$

Here $F_{\pm 1/2}[x]$ correspond to the Fermi-Dirac integral. It was experimentally proven in [170, 171] that the product pn becomes doping dependent in the case of very high dopant concentrations. SILVACO ATLAS includes the associated band gap narrowing for highly doped regions in the device in the calculations. Equations 2.6 (Poisson), 2.8 (Continuity) and 2.9 (Transport) define the required basic semiconductor equations. In this form they were first formulated by Roosbroeck [172]. However, expressions for the mobilities in the transport equations 2.9a and 2.9b are still missing.

Mobility Model

Electrons and holes are accelerated in the electric field, but lose energy due to multiple scattering mechanisms such as lattice vibrations, impurity ions, other carriers, surfaces and lattice imperfections. Therefore, the mobility depends in particular on the field \vec{E} , the temperature T and the dopant concentrations. Therefore, the SILVACO ATLAS simulator proceeds as follows. At $T = 300\text{K}$, it looks up a table that assigns

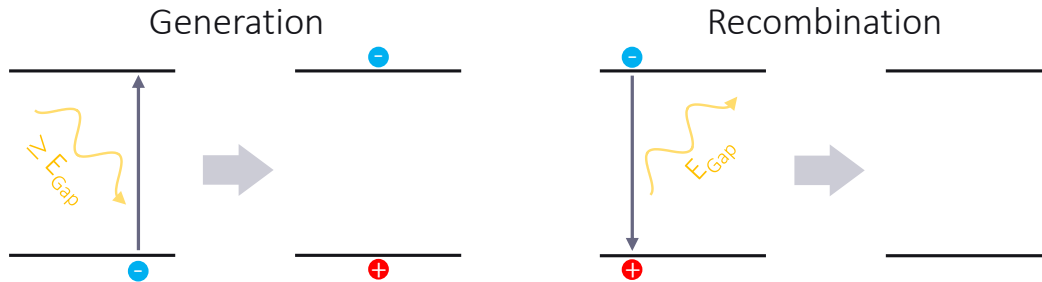


Figure 2.17: The process of photon transition.

the low-field mobility to the dopant concentration. The values contained therein, are experimentally proven [167, table 3-37]. For temperatures different from $T = 300K$, an analytical function from Caughey and Thomas [173] is applied to extrapolate to them. This procedure yields $\mu_n(T)$ and $\mu_p(T)$ and accounts for lattice scattering due to temperature. However, it becomes incorrect if the fields become too large. To include the field dependence as well, a model is used that has been successfully applied in the simulation of MOSFETs [174]. It includes four terms. The bulk semiconductor mobility, surface roughness mobility, surface phonon mobility and coulomb scattering mobility. Here, the bulk mobility is similar to that of Caughey and Thomas. Thus even surface effects are considered. All mentioned terms are combined with Matthiessen's rule:

$$\frac{1}{\mu} = \sum_i \frac{1}{\mu_i} \quad (2.11)$$

Now, only an equation for the generation-recombination rate is missing.

2.4.2 Generation and recombination processes

Mechanisms of generation of electron hole pairs and their recombination are included in the SILVACO ATLAS simulation. The ones used in this work are presented in the following.

Photon transition

The photon transition is a direct transition from valence into conduction band and vice versa [167, 169]. As shown in figure 2.17, recombination consists of an electron from the conduction band emitting a photon with the energy of the bandgap E_{gap} and subsequently falling energetically into the valence band and recombining with a hole. The reversal process is the generation shown in figure 2.17. In this process, an electron from the valence band absorbs a photon with at least the energy of the band

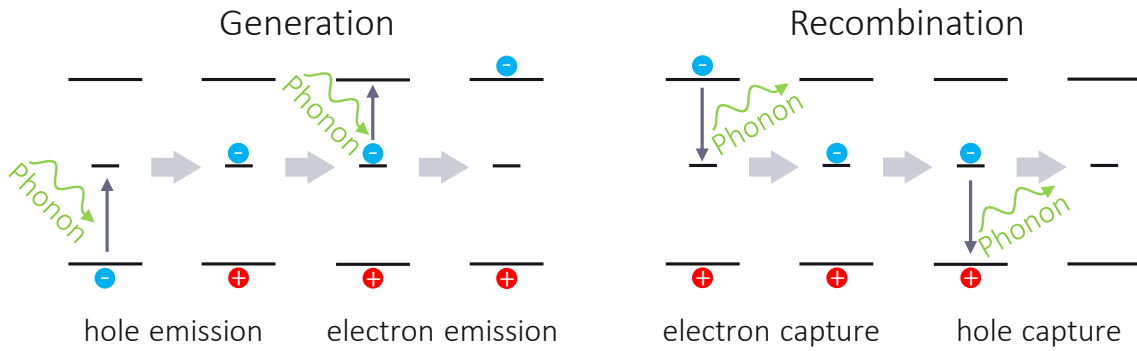


Figure 2.18: The process of trap assisted phonon transition.

gap E_{gap} and is thus energetically lifted into the conduction band. In doing so, it leaves a hole in the valence band. Thereby momentum and energy are conserved, so that the transferred energy ΔE always corresponds to the photon energy $\Delta E = h\nu$. Here ν is the photon frequency and h the Planck quantum of action. Since the momentum of the photon is very small, only negligible momentum can be transferred. Thus, only direct transitions are possible. The generation-recombination rate for the photon transition is:

$$R^{opt} = C_c^{opt}(np - n_i^2)$$

Here C_c^{opt} is the capture rate. If the product of the carrier concentrations is larger than the square of the intrinsic carrier concentration $np > n_i^2$, the recombination process dominates. Conversely, for $np < n_i^2$ the generation of electron hole pairs is dominant.

Phonon transition

Generation and recombination can also take place through the absorption and emission of phonons [167, 169]. This process takes place under the assistance of trap states in the midgap. The energy required during generation and emitted energy during recombination is obtained from and transferred to the lattice. The process was defined by Shockley, Read and Hall in [175, 176] and is therefore known as the Shockley-Read-Hall (SRH) mechanism. The generation is shown in figure 2.18. An electron in the valence band absorbs a phonon from the lattice and thus acquires enough energy to be captured by the trap. In doing so, it leaves a hole in the valence band. Subsequently, the electron absorbs another phonon from the lattice and thus has enough energy to rise into the conduction band. In the first process, hole emission, the emitted phonon has an energy equal to the difference of the valence band to the trap level. In the second process, electron emission, the emitted phonon has an energy equal to the difference of the trap level to the conduction band. Recombination is also shown in figure 2.18. An electron in the conduction band is captured by a midgap trap, emitting energy in the

form of a phonon to the lattice. The electron then falls from the trap into the valence band where it recombines with a hole. In doing so, it emits a phonon to the lattice. In the first process, electron capture, the emitted phonon has an energy equal to the difference between the trap level and the conduction band. In the second process, hole capture, the emitted phonon has an energy equal to the difference of the valence band to the trap level. The generation-recombination rate for this process in the stationary case (DC) corresponds to [167, 169]:

$$R_{SRH} = \frac{pn - n_i^2}{\tau_{p,0} \left[n + n_i \exp\left(\frac{E_t}{k_B T}\right) \right] + \tau_{n,0} \left[p + n_i \exp\left(\frac{-E_t}{k_B T}\right) \right]} \quad (2.12)$$

There E_t is the energy level of the trap. The electron lifetime of $\tau_{n,0} = 13 \times 10^{-6}$ s and the hole lifetime of $\tau_{p,0} = 13 \times 10^{-6}$ s best represent experimental results generated over the years for LiDAR APDs. Moreover, it can be shown by calculation that the SRH mechanism is most effective the closer E_t is to the midgap energy.

Surface recombination

The generation and recombination of electron hole pairs at interfaces is a special case of the SRH process [167, 169]. In this case, the rate of generation and recombination may be increased compared to the bulk. The reason is often a high concentration of interface traps, such as the P_B centers described phenomenologically in section 2.3.2. The generation-recombination rate is calculated according to [167, 169]:

$$R_{surf} = \frac{pn - n_i^2}{\frac{1}{S_p} \left[n + n_i \exp\left(\frac{E_t}{k_B T}\right) \right] + \frac{1}{S_n} \left[p + n_i \exp\left(\frac{-E_t}{k_B T}\right) \right]} \quad (2.13)$$

There S_n and S_p are the surface recombination velocities of electrons and holes, which also increase with an increasing interface trap concentration.

Auger recombination

The Auger generation/recombination mechanism involves three charge carriers. Although the basic physics is still being developed, the corresponding transitions and transition probabilities are known. So that the process can be presented here phenomenologically and a generation/recombination rate determined. There are two ways in which the generation process can occur [167, 169]. The first is the electron emission, shown in figure 2.19. An electron in the conduction band that has a significantly higher energy than the conduction band edge relaxes onto it and transfers the excess energy to an electron in the valence band, which is then excited into the conduction band. This

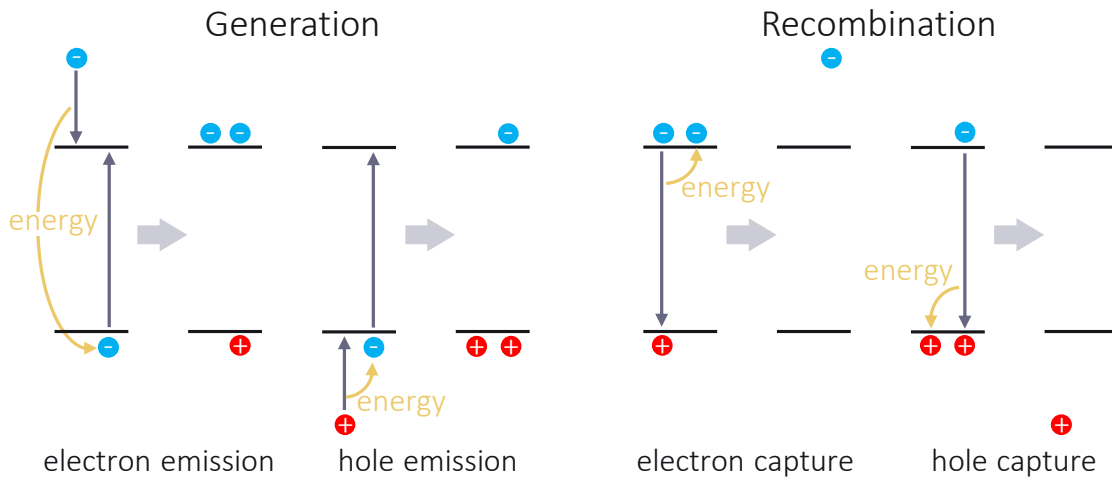


Figure 2.19: The process of Auger transition.

leaves a hole in the valence band. The second is the hole emission. This is shown in figure 2.19. A high-energy hole in the valence band relaxes onto the valence band edge and releases the energy to an electron in the valence band, which is thus lifted into the conduction band. There are also two processes for recombination. The first, electron capture, is schematized in figure 2.19. An electron from the conduction band recombines with a hole from the valence band and transfers the available energy to an electron in the conduction band, which is thus raised energetically within the conduction band. The second process is hole capture, shown in figure 2.19. As before, an electron from the conduction band recombines with a hole in the valence band. This time, however, the available energy is absorbed by a hole in the valence band, which then reaches a higher energy level within the valence band. The generation/recombination rate for the Auger process is [167, 169]:

$$R_{Auger} = \left(C_{cn}^{Auger} n + C_{cp}^{Auger} p \right) \left(np - n_i^2 \right) \quad (2.14)$$

Here $C_{cn}^{Auger} = 2.8 \times 10^{-31} \text{cm}^6/\text{s}$ and $C_{cp}^{Auger} = 9.9 \times 10^{-32} \text{cm}^6/\text{s}$ are the Auger capture rates for electrons and holes, respectively.

Impact ionization

Finally, this section describes the generation mechanism essential for APDs - impact ionization. Due to its importance, the individual aspects are described in more detail. The underlying model for this process originates from Selberherr [169] and is exclusively a generation process. As shown in figure 2.20, a conduction electron moves in the electric field, which is represented by the curvature of the conduction band. The motion is symbolized by the arrow. The electric field accelerates the electron and increases its

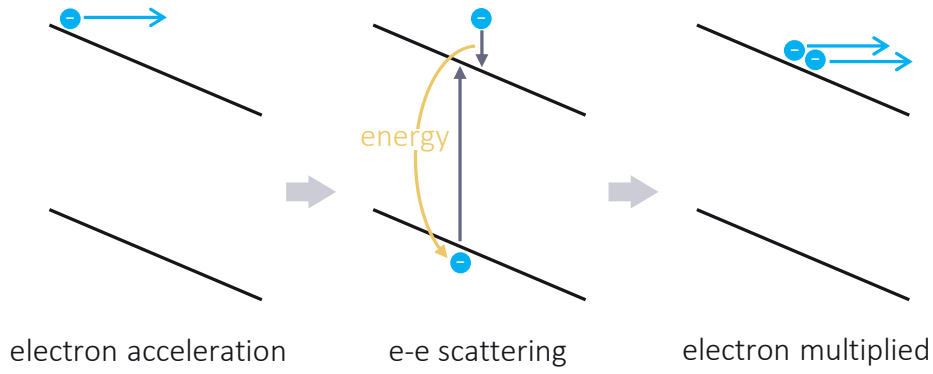


Figure 2.20: The process of impact ionization is only a generation process

energy. This high energetic electron can then scatter at the lattice in such a way that it relaxes onto the conduction band edge and transfers its kinetic energy to an electron in the valence band. This electron is thereby lifted into the conduction band, leaving a hole behind. The process starts again. However, there are twice as many electrons as there were at the beginning. The original electrons have thus been multiplied. This multiplication by the process of impact ionization can propagate like an avalanche. It is the basis of the APD function as described in section 2.1. It seems to be identical to the Auger process of electron emission. The difference however is the energy source. For impact ionization, the energy is drawn from the electric field and thus is most pronounced in areas of high fields. Auger, on the other hand, predominates in areas of high concentration of electrons with negligible currents. Electron currents are as essential to impact ionization as the electric field. Therefore, the generation rates are proportional to the current density:

$$G_n = \alpha_n \frac{|\vec{J}_n|}{e} \quad \text{and} \quad G_p = \alpha_p \frac{|\vec{J}_p|}{e} \quad (2.15)$$

Here α_n and α_p are the ionization rates of electrons and holes. They describe how many electrons and holes are generated per unit length. Theoretical and experimental studies suggest an exponential dependence on the electric field component in the direction of current flow E_J [169]:

$$\alpha_n = \alpha_n^\infty \exp \left[- \left(\frac{E_n^{crit.}}{E_J} \right) \right] \quad \text{and} \quad \alpha_p = \alpha_p^\infty \exp \left[- \left(\frac{E_p^{crit.}}{E_J} \right) \right] \quad (2.16)$$

Here $\alpha_n^\infty \approx 7 \times 10^5 \text{ cm}^{-1}$ and $\alpha_p^\infty \approx 6.7 \times 10^5 \text{ cm}^{-1}$ and threshold fields $E_n^{crit.} = 1.2 \text{ MV/cm}$ and $E_p^{crit.} = 2 \text{ MV/cm}$ at room temperature (300 K) [167]. Basically, they are all temperature dependent. The exact expressions can be found in [167]. All of them increase with temperature, so at higher temperatures higher fields are needed

for impact ionization. This can be explained phenomenologically by the fact that the lattice oscillates more strongly at higher temperatures. Thus, the probability of an energetic electron losing its energy by scattering at phonons increases, rather than ionising an electron.

2.5 Summary

In this chapter, the design and the function of the APD have been fundamentally introduced (sec. 2.1). The physical process of impact ionization leads to a multiplication of generated charge carriers within the sensor. The variation of the gain M with voltage U is an important property of the APD (fig. 2.3). It describes how much the signal is multiplied within the sensor at a certain voltage U . Above 40 V, M increases with voltage. Above the avalanche breakdown voltage U_{br} the gain tends to infinity. Due to the interaction of the charge carriers with the crystal lattice, the M - U characteristic depends on temperature. Above 40 V it is stretched with the temperature coefficient $T_K \approx 1.5 \text{ V/K}$. Therefore, the breakdown voltage depends on temperature and increases with it according to $U_{br}(T_2) = (T_2 - T_1) T_K U_{br}(T_1)$. In addition, the noise behavior of the APD is important. Basically, all generation-recombination processes within the sensor lead to an increase in noise. In section 2.2 the basic structure and function of a rotating LiDAR module was presented. The basis of the function is the time of flight measurement (ToF). A laser emits an optical signal. This signal is reflected by the target and returns to the LiDAR module. There it is detected by the APD. The receiver circuit is designed in such a way that only AC output signals from the APD are evaluated. This includes the optical signal with which the APD is triggered. But also the noise of the APD. Due to the superposition of signal and noise, signals can theoretically only be resolved at signal-noise-ratios of $SNR > 1$. In particular, signals backscattered from distant objects have small signals. In this case, the noise behavior is especially crucial. For LiDAR operation in automotive applications, targets must be reliably detected up to a distance in the order of 100 m. In section 2.3 an introduction to the concept of lifetime analysis was given. Crucial for the aging of the APD are so-called intrinsic failure mechanisms. These are physical processes that occur within every device. Their extent varies between individual sensors due to small deviations from the ideal manufacturing process. Nevertheless, they can be observed in all sensors. In stress experiments, these are investigated under accelerating conditions. Knowledge of the failure mechanisms is then used to describe them quantitatively. By calibrating the corresponding models with experimental data, it is possible to extrapolate to operation conditions. Some of these failure mechanisms are known from the

field of power devices. Potentially crucial for APD are the generation of traps at the Si:SiO₂ interface, the generation of oxide charges and the generation of electron traps in the oxide. In section 2.4, the fundamentals of semiconductor device simulation and the processes that are crucial in APDs were presented. The most important of these is impact ionization which depends on internal fields and current densities.

Chapter 3

Development of an APD degradation model

The aim of this thesis is to provide insights into the APD aging processes in order to enable the development of designs that are robust to degradation in LiDAR operation. Therefore, a novel degradation model is developed in this chapter that includes all important aspects of the aging process. It is concluded from [30-34], that generation of negative charges in SiO_2 and traps at the $\text{Si}:\text{SiO}_2$ interface cause the degradation of APDs. In section 2.3, models reported in literature of power device reliability physics have been presented that produce these phenomena. Crucial processes for APD aging are extracted in section 3.1 by consideration of simulation results for APDs under severe LiDAR operation conditions. Each of these include sub aspects of APD degradation. Due to strong variations of internal electric fields and current densities, they vary in intensity at different locations inside the device. The superposition of all processes leads to the degradation of the sensors, which can be observed experimentally. This introduces the challenge of covering all processes and their interaction as comprehensively and detailed as possible in order to reflect reality accurately.

Therefore, the energy distribution function of electrons under high fields is determined in section 3.2. In section 3.3, the injection probability of electrons into the oxide is determined from it. Electrons in the oxide are captured by electron traps. Trapped electrons in the oxide act as negative oxide charges. The processes involved are discussed and corresponding models presented in section 3.4. Electrons that are not injected into the oxide can interact with Si-H bonds at the $\text{Si}:\text{SiO}_2$ interface, leading to their rupture. Si atoms possessing an unbound valence electron at the interface are called dangling bonds and act as interface traps. Free hydrogen can move away from the interface by diffusion or form bonds with free Si atoms again. These processes are modeled in section 3.5.

3.1 Degradation processes in LiDAR operation

All degradation mechanisms presented in section 2.3 are favored by a high electric field in the vicinity of the Si:SiO₂ interface. High fields throughout the sensor are accompanied by high operating voltages. As mentioned in section 2.1, the operation voltage U of the APD in LiDAR operation is set according the required value of gain M . Often $M = 50$ is chosen. At room temperature, that would lead to $U \approx 190$ (see figure 2.3). It could be seen from figure 2.3 that increasing temperatures stretch the $M-U$ curve to higher voltages. So, a targeted gain M can only be held with an increase in voltage. This increase occurs with the temperature coefficient $T_K = 1.5 \text{ V/K}$ (section 2.1). It is assumed, that the LiDAR system operates at 125°C . This corresponds to the upper limit of the LiDAR mission profile (sec. 2.3.1). Therefore, an operation voltage of 340 V is sufficient in order to estimate the upper limit of occurring fields. The results of a corresponding APD simulation for the distribution of the electric field are shown in figure 3.1. For orientation, the cross section of the circular symmetric APD with doping and material profiles is shown. For more details on that, it is referred to section 2.1. The active area, has a diameter of $230 \mu\text{m}$. The silicon and silicon dioxide layers, the doping and the multiplication region are labeled. The field varies from values below $5 \times 10^3 \text{ V/cm}$ to slightly above $7 \times 10^5 \text{ V/cm}$. No degradation is expected in the multiplication zone, because the flat n doping at the surface leads to a vanishing field at the interface and in the oxide above it. Beside in the multiplication zone, the field is also very large beyond the n^{++} doping in the edge region of the sensor chip. An enlarged section of this region is shown on the right. A local maximum of the field is located at the curvature of the n^{++} doping. The reason for this is precisely this curvature [35]. Although, it has no direct impact on degradation, because for that only fields at the interface are crucial. At the interface, values up to above $2.5 \times 10^5 \text{ V/cm}$ are present on the silicon side. On the oxide side there are values just below $7 \times 10^5 \text{ V/cm}$. In both cases, the maximum values coincide with the end of the field plate. As introduced in section 2.3.2, the generation of traps at the interface is governed by the breaking of Si-H bonds. Their binding energy was reported in section 2.3.2 as at least 1.5 eV . The mean free path length of electrons in silicon is around 70 nm [177-179]. It is sufficient for degradation if only a fraction of the electron population contributes to it. For example, one can consider the upper tail of the free path length distribution, where the path length can be assumed to have values around 130 nm . So, fields in the silicon of at least $E_{si,thres} = 1.2 \times 10^5 \text{ V/cm}$ are necessary to degrade the interface. As shown, the values of the electric field at the interface are higher than $1.2 \times 10^5 \text{ V/cm}$. Thus, its degradation is likely. As discussed in section 2.3.3, electron traps required for the generation of oxide charges are always intrinsically

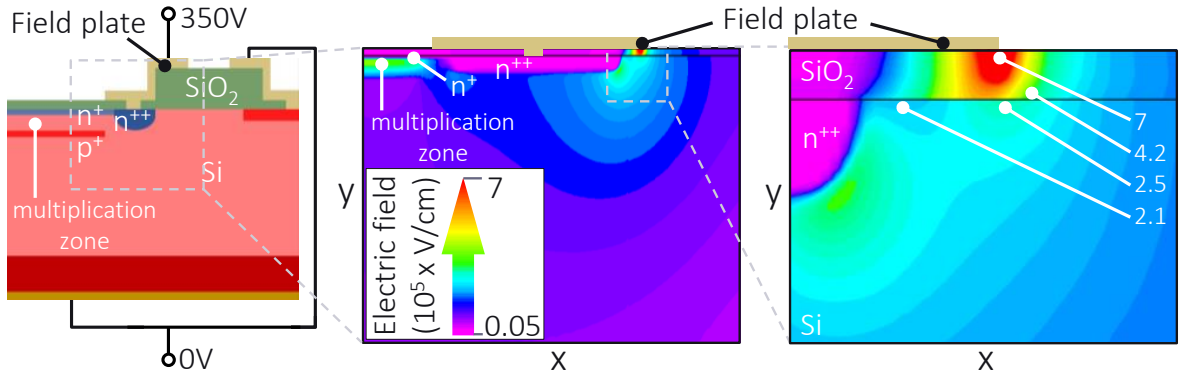


Figure 3.1: Sketch of the APD cross section with doping and material profiles (left). Electric field distributions in the marked areas resulting from simulation are used to estimate the involvement of failure mechanisms in APD degradation. Fields in the enlarged section on the right are in 10^5 V/cm.

present in the oxide due to its amorphous structure. For the injection of electrons from the silicon into the oxide, their energies have to be higher than the interface barrier of $E_B = 3.25$ eV. As before, assuming a free path length of 130 nm, the necessary field is calculated to be $E_{si,thres} = 2.5 \times 10^5$ V/cm. Values of the field in that range are present below the field plate in silicon at the interface. Electrons injected and subsequently trapped in oxide traps can be freed by the detrapping mechanism mentioned in section 2.3.3. Oxide fields of $E_{ox,thres} \approx 5 \times 10^5$ V/cm have been observed during studies of this process. These are present in the oxide below the end of the field plate. The mechanism of oxide conduction, introduced in section 2.3.4, is based on the generation of electron traps in the oxide. It is based on the thermal breaking of bonds, which are strongly weakened by interaction with the oxide field E_{ox} . The process was reported for oxide fields above $E_{ox} \approx 7 \times 10^5$ V/cm. Such values can be observed in the simulation in a small region in the oxide below the field plate. Weak bonds can also be broken by collisions with very energetic electrons, generating electron traps. The threshold value for this has been found to be $E_{ox,thres} = 2 \times 10^6$ V/cm. According to the results in figure 3.1, such values of the oxide field are not present. In conclusion, the generation of oxide traps could be possible by thermal bond breaking. However, the fields in the oxide only just reach the experimentally observed threshold of 7×10^5 V/cm. Moreover, no evidence for this process was found in experiments performed during the course of this work. Therefore, it is excluded. The fields in the oxide are too small for the generation of oxide traps by impact ionization. Nevertheless, the generation of interface traps, the injection of electrons into the oxide, the trapping of the injected electrons in preexisting electron traps in the oxide, and the liberation of the trapped electrons are possible due to sufficiently large fields. In the following, a model is developed that includes all these failure mechanisms and thus can describe the degradation of the LiDAR APD.

3.2 Energy distribution of electrons at high fields

For the case of vanishing electric fields, the lattice and the electron population are in thermal equilibrium and the Fermi distribution function $f(\vec{p})_{fermi}$ with the electron momentum \vec{p} describes the occupation probability of the states in momentum space. Under the influence of an electric field, electrons are accelerated and acquire kinetic energy. By increasing the electron energy, the probability to scatter at the lattice increases. Thus electrons lose energy by the excitation of lattice vibrations. An equilibrium is now established between the energy gain by the field and the loss to the lattice. It does not correspond to thermal equilibrium and the Fermi distribution is not sufficient to describe the occupation probability of the states in momentum space. The objective of this section is to determine the distribution function for fields up to 5×10^5 V/cm. Investigations of high field transport continue to this day and originated several decades ago [180, 181]. The solution of the Boltzmann equation is inevitably the starting point of the derivation, which is formally written as [182, 183]:

$$\frac{\partial f(\vec{p}, t)}{\partial t} = \left[\frac{\partial f(\vec{p}, t)}{\partial t} \right]_{field} + \left[\frac{\partial f(\vec{p}, t)}{\partial t} \right]_{collision} \quad (3.1)$$

In the steady state, as described, an equilibrium is established between the change of the distribution function f due to the field $[\dots]_{field}$ and collisions at the lattice $[\dots]_{collision}$. Therefore, the time dependence t vanishes. The field term can be written as [182, 183]:

$$\left[\frac{\partial f(\vec{p}, t)}{\partial t} \right]_{field} = -e\vec{E} \cdot \nabla_{\vec{p}} f(\vec{p}, t) \quad (3.2)$$

The collision term is determined by interactions between electrons and optical phonons, acoustic phonons, ionized impurities and valence band electrons. The latter corresponds to impact ionization. Depending on the electric field strength, impact ionization and optical-phonon scattering compete. The mean free path for optical-phonon scattering λ_{opt} is independent of the field and varies in the considered temperature range between 52 Å and 65 Å [116]. The for impact ionization λ_{ii} decreases with increasing field. The following values were found for λ_{ii} in the relevant field range: $\lambda_{ii} = 880$ Å at 4×10^5 V/cm [184], $\lambda_{opt}/\lambda_{ii} < 0.1$ at 5×10^5 V/cm [116], $\lambda_{ii} \gg 500$ Å at 2×10^6 V/cm [185]. All literature values found show that the mean free path for impact ionization in the relevant field range of up to 5×10^5 V/cm is more than an order of magnitude larger than that for optical-phonon scattering and suggest that impact ionization can be neglected in the collision term. This is supported by the fact

that the authors in [186] were able to show with Monte Carlo simulations for electric fields $|\vec{E}|$ in the range of 5×10^4 V/cm to 5×10^5 V/cm that optical-phonon scattering determines the collision term. They were also able to show that the deviation from thermal equilibrium in this field range is not large and the distribution function can be expressed as:

$$f(\vec{p}) = f_0(\vec{p}) + f_1(\vec{p}) \quad (3.3)$$

Where $f_0(\vec{p})$ is symmetric and $f_1(\vec{p})$ is antisymmetric about the origin $\vec{p} = \vec{0}$. Thus f_1 describes the current flow and f_0 the occupation of energy states [187, 188]. To solve the Boltzmann equation, a relaxation time approach was used in [186] and the band structure was modeled with:

$$\frac{\vec{p}^2}{2m_e} = xE^y \quad (3.4)$$

Here m_e is the effective mass of electrons in silicon and E the energy. When $x, y \neq 1$ it does not have a parabolic shape, which is reasonable due to the fact that the conduction band at the Si:SiO₂ interface can be assumed to be degenerate due to lattice irregularities and other interface phenomena. Finally, the symmetric part of the distribution function was derived as:

$$f_0(\vec{E}, E, T) = C \exp \left[-\frac{3}{2} \frac{m_e x y^2 E_{opt}}{|\vec{E}| h(\vec{E}) (e \gamma(T))^2} \frac{E^{4y-3}}{4y-3} \right] \quad (3.5)$$

Where C is a constant and $E_{opt} = 0.063$ eV [189] corresponds to the energy electrons give up to or gain from optical phonons. By comparison with other Monte Carlo simulations, field dependence could be determined in [186] to $h(\vec{E}) = |\vec{E}|^{0.5}$ and $y = 1.5$. Using these values, it was shown in [190] that f_0 agrees with Monte Carlo simulations to an accuracy of 4%. For f_1 , a similar approach as in [186] is used in this work and extended to three dimensions in order to enable the study of three dimensional real APDs:

$$f_1(\vec{E}, E, T) = \tau(E, T) e h(\vec{E}) \frac{\vec{E}}{|\vec{E}|} \left[\vec{\nabla}_p f_0 \right](E) \quad (3.6)$$

Here, τ is the relaxation time for optical-phonon scattering, corresponding to the time it takes for the lattice and electron population to reach thermal equilibrium after the field is turned off. Its expression in [186] is extended here by a temperature dependence,

using the relation $\tau \propto \lambda_{opt}$ and the expression for λ_{opt} from [35]:

$$\tau(E, T) = \gamma(T) E^{1-(3/2)y} \text{ with } \gamma(T) = \gamma' x^{-3/2} y^{-1} \frac{\tanh(E_{opt}/2k_B T)}{\tanh(E_{opt}/2k_B 300 \text{ K})} \quad (3.7)$$

Further, it is

$$\vec{\nabla}_p f_0 = \begin{pmatrix} \partial f_0 / \partial p_x \\ \partial f_0 / \partial p_y \\ \partial f_0 / \partial p_z \end{pmatrix} = \begin{pmatrix} \partial E / \partial p_x |\partial f_0 / \partial E| \\ \partial E / \partial p_y |\partial f_0 / \partial E| \\ \partial E / \partial p_z |\partial f_0 / \partial E| \end{pmatrix} = (\vec{\nabla}_p E) \left| \frac{\partial f_0}{\partial E} \right| \quad (3.8)$$

Care must be taken here to ensure that the energy $E \geq 0$ [191]. From the insertion of the dispersion relation (equation 3.4), equation 3.5 and execution of the derivatives it follows:

$$\begin{aligned} \frac{\vec{E}}{|\vec{E}|} \vec{\nabla}_p E &= \frac{\vec{E}}{|\vec{E}|} \vec{\nabla}_p \left[\frac{p_x^2 + p_y^2 + p_z^2}{2m_e x} \right]^{\frac{1}{y}} \\ &= \frac{\vec{E} \cdot \vec{p}}{|\vec{E}|} \frac{1}{m_e x y} \left[\frac{\vec{p}^2}{2m_e} \right]^{\frac{1}{y}-1} \\ &= |\vec{p}| \cos(\theta) \frac{E^{1-y}}{m_e x y} = \frac{\sqrt{2} E^{1-\frac{y}{2}}}{\sqrt{m_e x y}} \cos(\theta) \end{aligned} \quad (3.9)$$

In the last step, the definitions for the dot product were used. Execution of the derivation of the second factor in equation 3.8 on the right yields:

$$\left| \frac{\partial f_0}{\partial E} \right| = \chi(T) (4y - 3) \frac{E^{4y-4}}{|\vec{E}| h(\vec{E})} f_0 \quad (3.10)$$

where

$$\chi(T) = \chi_0 \left[\frac{\tanh(E_{opt}/2k_B 300 \text{ K})}{\tanh(E_{opt}/2k_B T)} \right]^2$$

with

$$\chi_0 = \frac{3}{2} \frac{m_e x y^2 E_{opt}}{(e\gamma' x^{-3/2} y^{-1})^2 (4y - 3)} \quad (3.11)$$

Finally, utilizing equation 3.6 the antisymmetric part f_1 can be determined as:

$$\begin{aligned}
 f_1(\vec{E}, E, T, \theta) &= \gamma(T) E^{1-\frac{3}{2}y} e h(\vec{E}) \frac{\sqrt{2} E^{1-\frac{y}{2}}}{\sqrt{m_e x y}} \cos(\theta) \chi(T) (4y - 3) \frac{E^{4y-4}}{|\vec{E}| h(\vec{E})} f_0(\vec{E}, E, T) \\
 &= \frac{\gamma(T) e \sqrt{2}}{\sqrt{m_e x y}} (4y - 3) \chi(T) \frac{E^{2(y-1)}}{|\vec{E}|} \cos(\theta) f_0(\vec{E}, E, T) \\
 &= \sqrt{\chi(T) 3(4y - 3) E_{opt}} \frac{E^{2(y-1)}}{|\vec{E}|} \cos(\theta) f_0(\vec{E}, E, T)
 \end{aligned} \tag{3.12}$$

With insertion of $y = 1.5$ and using equations 3.5, 3.7 and 3.11, it finally follows:

$$f_0(\vec{E}, E, T) = C \exp \left[-\chi(T) \frac{E^3}{|\vec{E}|^{1.5}} \right] \tag{3.13}$$

and

$$f_1(\vec{E}, E, T, \theta) = f'_1(\vec{E}, E, T) \cos(\theta) \text{ where } f'_1(E, T, \vec{E}) = 3\sqrt{\chi(T) E_{opt}} \frac{E}{|\vec{E}|} f_0(\vec{E}, E, T) \tag{3.14}$$

Here, x is determined from the dispersion relation and as such it is implied by χ_0 . Utilizing equation 3.3 finally yields:

$$f(\vec{p}) = f(\vec{E}, E, T, \theta) = f_0(\vec{E}, E, T) + f_1(\vec{E}, E, T, \theta) \tag{3.15}$$

3.3 Injection probability of electrons into the oxide

In the following, the injection probability of electrons into the oxide will be determined. This is done on the basis of the previously determined probability distribution of the occupation of states $f(\vec{p}) = f(\vec{E}, E, T, \theta)$ at energy E for electric field \vec{E} , angle θ between momentum and field and temperature T . The injection probability P_{inj} is supposed to indicate what fraction of the total electron population at the Si:SiO₂ interface is injected into the oxide. Using the number of injected electrons n_{inj} and the total number of electrons n , this can be written as [191]:

$$P_{inj} = \frac{n_{inj}}{n} = \frac{j_{inj}}{j} \tag{3.16}$$

In equation 3.16, the injection probability is also related to the total electron current density j at the Si:SiO₂ interface and the part of it that gets injected j_{inj} . This relation

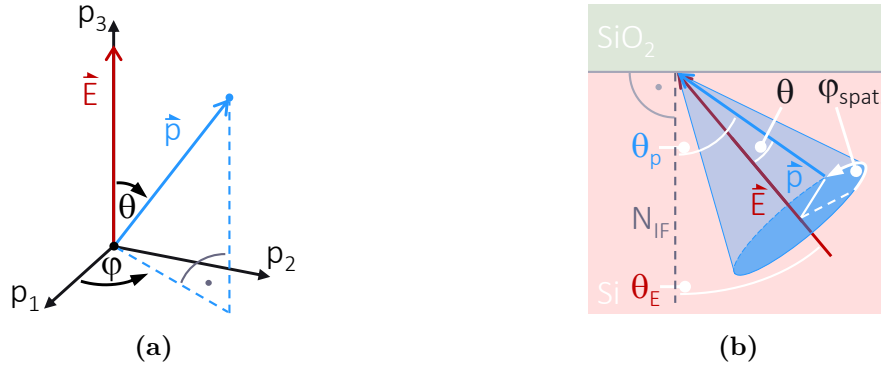


Figure 3.2: Representation of the electron momentum \vec{p} and electric field \vec{E} , the respective angles θ_p and θ_E between them and the interface normal N_{IF} , the angle θ between \vec{p} and \vec{E} and the azimuthal angles φ and $\varphi_{\text{spat.}}$ where $\varphi = \varphi_{\text{spat.}} - \pi$. a: Representation in momentum space. b: Spatial representation at the Si:SiO₂ interface.

is later used to determine j_{inj} . In the following, P_{inj} will be determined via n_{inj} and n . Therefore, an expression for the number of electrons will be derived.

3.3.1 Number of electrons and density of states

In the absence of magnetic fields, there is no spin degeneracy and a state in momentum space occupies a volume of $(h/L)^3/2$ [192]. Here h and L^3 correspond to the Planck quantum of action and the volume of the considered region of the crystal. Thus, in an infinitesimal part of the momentum space dV_p there are $2(L/h)^3 dV_p$ states and the distribution function $f(\vec{p})$ determines how many of these states are occupied by electrons, i.e. how many electrons are in dV_p :

$$dn(\vec{p}) = 2 \left(\frac{L}{h}\right)^3 f(\vec{p}) dV_p = 2 \left(\frac{L}{h}\right)^3 f(p, \theta) p^2 \sin(\theta) dp d\theta d\phi \quad (3.17)$$

Here, spherical coordinates in momentum space relative to the electric field \vec{E} were used, as shown in figure 3.2a. This is reasonable due to the fact that the momentum aligns parallel to the field, since the latter determines in particular the direction of acceleration of the electrons and thus the change of direction of the momentum. So, the p_z axis is chosen along the field \vec{E} . In spherical coordinates, the polar angle θ corresponds to the angle between field and momentum \vec{p} . The azimuthal angle φ gives the angle between the projection of the momentum in the p_x - p_y plane and the p_x axis. When $L = 1 \text{ cm}$, n corresponds to the electron concentration per cm^3 . Integration over the momentum space element V_{p_0} using the dispersion relation in equation 3.4

then gives the number of electrons in it:

$$n(V_{p0}) = \iiint_{V_{p0}} f(\vec{E}, E, T, \theta) \left(\frac{2m_e x}{h^2} \right)^{3/2} y E^{(3/2)y-1} \sin(\theta) \, dE d\theta d\phi \quad (3.18)$$

Here, x and y correspond to the meanings in equation 3.4. It is now possible to determine the total concentration of electrons by evaluating the integral over the complete momentum space so that $E \in [0, \infty[$, $\theta \in [0, \pi]$ and $\phi \in [0, 2\pi]$. Using $f = f_0 + f_1$ and $\int_{\theta \in [0, \pi]} f_1 \sin(\theta) d\theta = 0$ it follows:

$$n = \int_0^\infty n(E) \, dE \quad \text{with} \quad n(E) = f_0(\vec{E}, E, T) g(E) \quad (3.19)$$

Here f_0 and f_1 are defined in section 3.2. As a by-product, the density of states comes out:

$$g(E) = 4\pi \left(\frac{2m_e x}{h^2} \right)^{3/2} y E^{(3/2)y-1} \quad (3.20)$$

Thus, the required total concentration of electrons n and the concentration of electrons in an arbitrary momentum space volume V_{p0} are determined. From the latter, the concentration of injected electrons n_{inj} can be determined later. For this purpose, the conditions for the injection of electrons must first be established, which define the momentum space volume over which is integrated.

3.3.2 Injection conditions

In order to be injected into the oxide, the energy of the electrons, as described in section 2.3, must be greater than the energy barrier of the interface E_B and an energy condition results:

$$E \geq E_B \quad (3.21)$$

Better agreement of model and experiment is obtained if the reflection of electrons at the interface due to their direction of motion is taken into account [189, 191]. How this is done is illustrated in figure 3.3. Electrons approaching the interface from the silicon side obtain momentum \vec{p} represented by the blue solid arrow. The interface normal and \vec{p} enclose an angle θ_p . The electron momentum can be divided into a part parallel p_{\parallel} and perpendicular p_{\perp} to the interface, both shown in blue dashed lines. The barrier energy E_B can be translated into a momentum $p(E_B)$ using the dispersion relation in

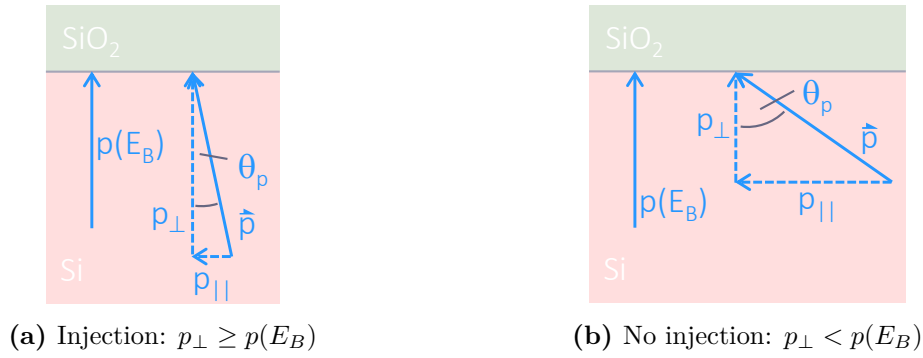


Figure 3.3: Illustration of the injection condition of the angle between the electron momentum and the interface θ_p .

equation 3.4. It is represented perpendicular to the interface, which serves the following purpose. The perpendicular part of the electron momentum is now compared with it. For injection to take place it has to be $p_{\perp} \geq p(E_B)$. In figure 3.3a the case is shown where this condition is fulfilled. So, the perpendicular part p_{\perp} is sufficient for the electron to be injected. In contrast, in figure 3.3b it is not strong enough and the electron is scattered back at the interface. Mathematically this is expressed as follows:

$$p_{\perp} = |\vec{p}| \cos(\theta_p) \geq p(E_B) \Rightarrow \sqrt{E^y} \cos(\theta_p) \geq \sqrt{E_B^y} \Rightarrow \cos(\theta_p) \geq \sqrt{\left(\frac{E_B}{E}\right)^y} \quad (3.22)$$

Where in the last step the dispersion relation (eq. 3.4) was used as described. With $0 \leq \theta_p < \pi$ [182] the injection condition for the momentum angle θ_p can be derived:

$$\theta_p \leq \theta_{p,0} = \arccos \left[\sqrt{\left(\frac{E_B}{E}\right)^y} \right] \quad (3.23)$$

With these conditions finally the concentration of injected electrons and the injection probability can be determined.

3.3.3 Amount of injected electrons and injection probability

With equation 3.18 the concentration of the injected electrons n_{inj} can be calculated with the same procedure as the total concentration n . For this, the momentum space volume V_{p_0} must be chosen to satisfy the injection conditions. The energy condition in equation 3.21 is satisfied with integration over $E \in [E_B, \infty[$. In order to solve the integral in equation 3.18 for injected electrons, the condition in equation 3.23 need to be transformed to momentum space, i.e. an expression depending on θ is needed. Its derivation is outlined in the following. For clarity, the region around the interface is shown in figure 3.2b. The silicon side is highlighted in red and the oxide in green.

The interface normal N_{IF} is perpendicular to it. The electric field \vec{E} is shown as a red vector. The electron momentum \vec{p} corresponds to the blue vector. The angle θ corresponds to the angle between field and momentum as in momentum space. The distribution function $f(\vec{p}) = f(E, T, \vec{E}, \theta)$ does not determine the azimuthal angle φ . Thus, it and its spatial counterpart $\varphi_{spat.} = \varphi + \pi$ are indeterminate, i.e. quantum mechanically degenerated. This means that a certain state in momentum space (p, θ) corresponds not only to one momentum, but to all momentums possessing a magnitude p on the blue cone around the field vector \vec{E} , which enclose an angle θ with it. Due to the fact that the angle θ_E between the field and the interface normal N_{IF} is mostly nonzero, the angle θ_p between a given momentum on the cone and N_{IF} depends in a very complex way on θ , θ_E and $\varphi_{spat.}$. The corresponding functional relation is written here as $\theta_p = u(\theta, \theta_E, \varphi_{spat.})$ and is not explicitly derived. Now the limit $\theta_{p,0}$ can be substituted for θ_p from the angle condition and converted to θ . This gives an expression $\theta_0 = v(\theta_{p,0}, \theta_E, \varphi)$. The intergral 3.18 must then be evaluated for $\theta \in [0, \theta_0]$. An approximation for a similar problem was found in [191]. Fields perpendicular to the interface are considered there. In this case $\theta_E = 0$ and thus $\theta_p = \theta$ holds. Thus the angle condition can be explicitly applied to θ :

$$\theta \leq \theta_0 = \arccos \left[\sqrt{\left(\frac{E_B}{E} \right)^y} \right] \quad (3.24)$$

It also follows that there is no limit to φ . Finally, the energy condition and the angle condition are satisfied when the intergral 3.18 is solved for $E \in [E_B, \infty[$, $\theta \in [0, \theta_0]$ and $\phi \in [0, 2\pi]$. The generalization to arbitrary angles θ_E is obtained by multiplying the integrand by a correction factor $C_0(\vec{E}, E, T, \theta)$:

$$n_{inj} = \int_{\infty}^{E_B} \int_0^{\theta_0} \int_0^{2\pi} f(E, \theta) \frac{g(E)}{4\pi} \sin(\theta) C_0(\vec{E}, E, T, \theta) d\phi d\theta dE \quad (3.25)$$

The correction factor is determined by [191]:

$$C_0(\vec{E}, E, T, \theta) = \frac{1 + \frac{f'_1(\vec{E}, E, T)}{f_0(\vec{E}, E, T)} \cos(\theta_E)}{1 + \frac{f'_1(\vec{E}, E, T)}{f_0(\vec{E}, E, T)}} \quad (3.26)$$

With equation 3.24 it follows:

$$n_{inj} = \int_{\infty}^{E_B} n(E, T) S(E, T) dE \quad (3.27)$$

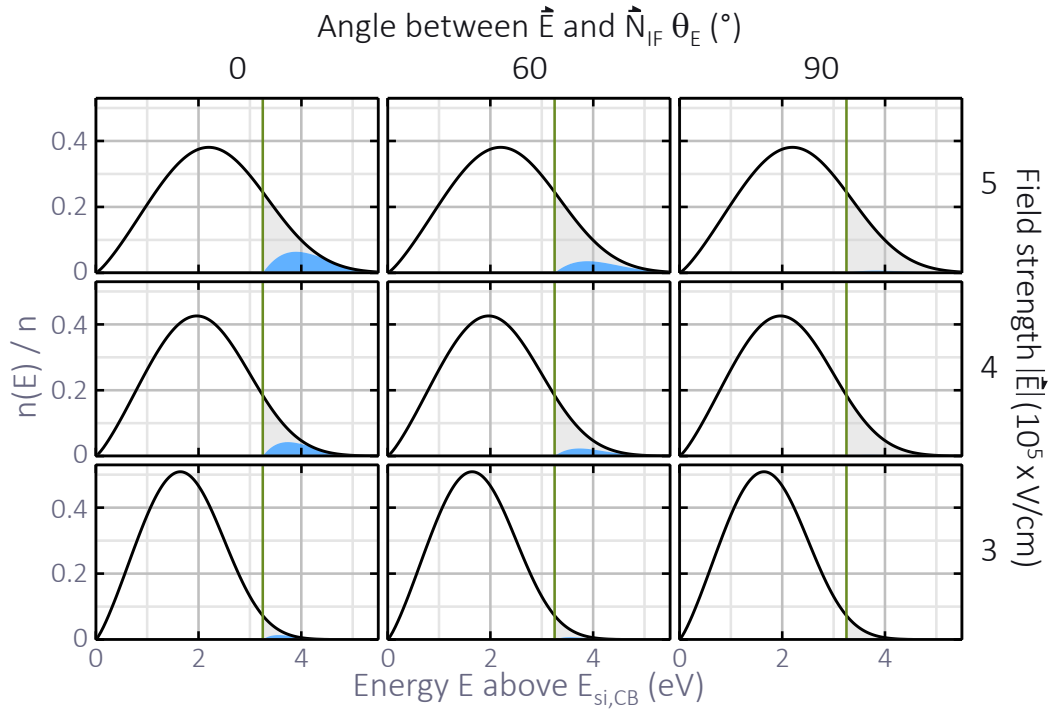


Figure 3.4: Plot of the density of occupied conduction band states $n(E)$ at the interface on the Si side normalized to the total density of electrons n against the energy of electrons above the conduction band edge $E_{si,CB}$ (black curve). The interface barrier $E_B = 3.25$ eV is shown in green. The colored areas below the curves corresponding to the fraction of electrons possessing at least an energy of E_B . Some of them satisfy (blue) and do not satisfy (gray) the angular condition of the orientation of their momentum. The curves for a variation of three different field angles θ_E and field strengths $|\vec{E}|$ are shown.

with

$$S(\vec{E}, E, T, \theta) = \left[\frac{1}{2} \left(1 - \sqrt{\frac{E_B}{E}} \right) + \frac{1}{4} \left(1 - \left[\frac{E_B}{E} \right]^y \right) \frac{f'_1(\vec{E}, E, T)}{f_0(\vec{E}, E, T)} \right] C_0(\vec{E}, E, T, \theta)$$

The quantity $S(E, T)$ can be understood as an energy dependent scattering factor describing the probability that electrons with an energy E are not backscattered at the interface at an angle θ_E of the electric field. It is used to weight the concentration of electrons of energy E . The integral then provides the injected fraction of the electron population n_{inj} . Figure 3.4 shows the energy dependent electron concentration normalized to the total concentration $n(E)/n$ versus the energy above the silicon conduction band. The interface barrier energy E_B is drawn. All electrons with energies above it satisfy the energy condition for injection. They are represented by the entire colored area under the black curve. Only a portion of them satisfies the angle condition. This part is colored blue. The orientations of the electric field are varied from perpendicular to the interface ($\theta_E = 0$) to parallel to it ($\theta_E = 90^\circ$). For energies rather close to

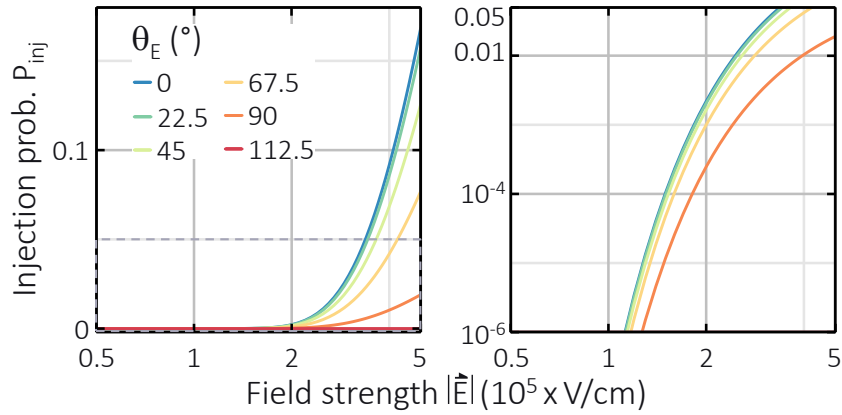


Figure 3.5: Injection probability P_{inj} as a function of the electric field strength $|\vec{E}|$ for various orientations of the electric field θ_E . $\theta_E = 0$ and $\theta_E = 90^\circ$ correspond to the field perpendicular and parallel to the interface.

the barrier energy E_B , the fraction satisfying the angular condition is rather small. It increases with increasing energy, so that at high energies above E_B all electrons are injected. The reason for this is the angular distribution of the electron momentum. At rather low energies, the component perpendicular to the interface is usually too small. Therefore the backscattering is relatively strong as shown in figure 3.3. At higher energies, the momentum and thus its perpendicular component is larger. This leads to a decrease in the influence of the angle. In general, however, the fraction satisfying the angle condition decreases with increasing angle between field and interface normal θ_E . Therefore, the injected fraction (blue) decreases with increasing angle θ_E and almost disappears for fields parallel to the interface in figure 3.4. It is now also possible to determine the injection probability, which corresponds to the integral over the injected fraction of the electron population and thus to the blue area in figure 3.4. This is shown in figure 3.5 as a function of the electric field strength $|\vec{E}|$ for various angles θ_E . For increasing fields, in particular above $2 \times 10^5 \text{ V/cm}$, the injection probability P_{inj} increases and reaches a value close to 0.2 in the considered field range. For fields of around $1 \times 10^5 \text{ V/cm}$, an injection probability of 10^{-6} can be expected. Furthermore, it can be seen that as the angle θ_E increases, the injection probability generally decreases. For values above 90° , electrons are no longer injected.

3.4 Generation of oxide charges

In this section, the rate of oxide charge generation will be modeled. Their generation can have several origins. Among others, it is the injection of charge carriers from silicon into the oxide where they get captured by oxide traps. Due to the operation and design of the LiDAR APDs studied here, these can only be electrons. It was

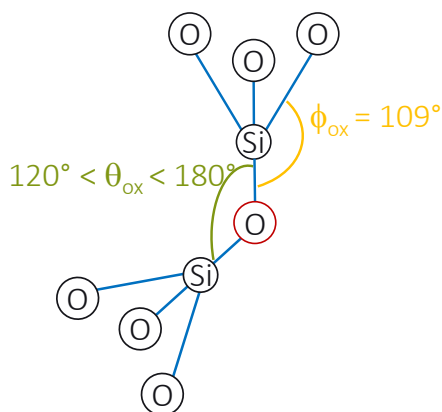


Figure 3.6: The structural unit of SiO_2 is the SiO_4 tetrahedron. The bond of two of them is shown and the ideal bond angles θ_{ox} and ϕ_{ox} are drawn. Deviations from them promote the occurrence of the oxygen vacancy, a formation acting as electron trap where the red marked O atom is missing.

mentioned in paragraph 2.3.3 that electron traps in silicon dioxide are formed due to its amorphous crystal structure. Those and the physical processes involved that lead to the generation of oxide charges are presented. These are the capture of electrons from the conduction band by the traps (trapping), the release of trapped electrons (detrapping) and the relaxation of trapped electrons from shallow to deep energy levels. For the latter, an entirely new model needed to be developed. Finally, the models of the three mechanisms and the previously developed injection probability are united to the oxide degradation model

3.4.1 The origin of electron traps in silicon dioxide

The structural unit of SiO_2 is the SiO_4 tetrahedron. In figure 3.6 the bond of two of them is illustrated. A silicon atom saturates its four valence electrons each with covalent bonds to neighboring oxygen atoms. The resulting local tetrahedral ordering is found in all forms of silicon dioxide. During the process of oxidation, it usually grows in an amorphous structure that has only local tetrahedral ordering. The bond angles within the tetrahedron are $\phi_{ox} = 109^\circ$ [144]. In the perfect lattice the bond angle with neighboring tetrahedra would be $\theta_{ox} = 150^\circ$. Due to amorphous growth however, these can deviate significantly. Deviations from the ideal bond angle cause the bond to be strongly stretched and distorted, and thus weakened. For bond angles above 180° and below 120° , the O-vacancy occurs [193]. The oxygen atom marked in red in the figure then does not exist and the Si-O-Si structure is replaced by a Si-Si bond. In addition, the Si-O bond can also break. This was shown in figure 2.16a. One of the two silicon atoms is then bonded to only three oxygen atoms. This arrangement is called trivalent Si ($\cdot\text{SiO}_3$). Stretched and distorted bonds, trivalent Si atoms and Si-Si bonds act as electron traps [92, 97-103, 115, 194-198]. Obviously, electron traps are already preexisting in the oxide due to the processing of the oxide layer. Oxidation rate and temperature play an important role for their concentration.

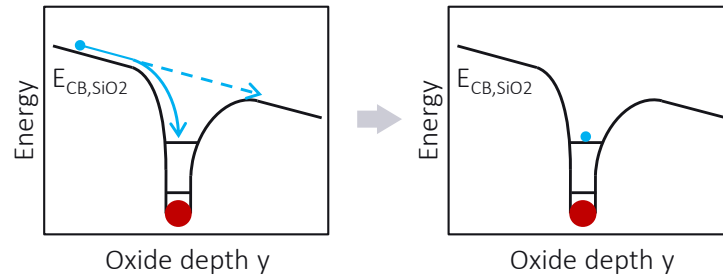


Figure 3.7: Trapping of electrons in shallow trap levels in the oxide.

In addition to these intrinsic traps, impurities can occur that also capture electrons. Adding water vapor during oxidation accelerates the process but incorporates water into the oxide in addition to the amorphous growth of SiO_2 . This increases the disorder of the lattice and impurities such as Si-O-H and Si-H appear, which interact as electron traps [82, 150, 151, 153, 198]. In this process, the concentration of traps increases with the amount of added water vapor. Presumably, Si-H bonds are also formed during hydrogen annealing, which corresponds to the passivation of the interface [150]. The increased disorder due to these impurities leads to increased distortion and stretching of the SiO_2 lattice. Moreover, the intrinsic Si-O bond is very polar [144]. All polar bonds can be further stretched and distorted by the application of an electric field [141]. The density of the resulting initiated traps is then field dependent.

3.4.2 Trapping of injected electrons

Electrons that have overcome the interface barrier can subsequently be captured in the oxide by electron traps. This process is illustrated in figure 3.7. It generates negative oxide charges. Here $N_{ox,max}$ corresponds to the concentration of electron traps and thus to the maximum possible concentration of trapped electrons in the oxide. The concentration of trapped electrons in the oxide $N_{ox}(t)$ is then determined by [91, 93, 199]:

$$\left. \frac{\partial N_{ox}}{\partial t} \right|_{\text{trapping}} = \frac{j_{inj}}{e} \sigma (N_{ox,max} - N_{ox}(t)) \quad (3.28)$$

Here j_{inj} is the current density of injected electrons, which can be determined by equation 3.16 via the injection probability and the current density of electrons at the interface on the silicon side. The term j_{inj}/e therefore describes how many electrons per second are injected into the oxide and are available for capture. The effective cross section σ describes the strength with which they are attracted by traps. It is a property of the traps. In general, $N_{ox,max}$ is time dependent as more traps could be generated as a result of the sensor degradation during the operation. However, in the course of

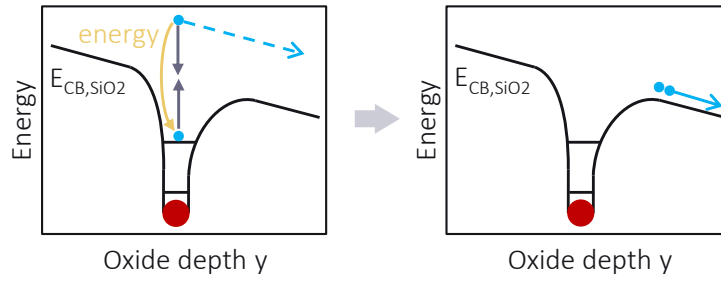


Figure 3.8: Detrapping - the liberation of trapped electrons from shallow trap levels via impact ionization.

this work no indication for it was found.

3.4.3 Detrapping of captured electrons

The concentration of occupied electron traps $N_{ox}(t)$ is determined from equation 3.28. Since the injection probability P_{inj} and hence the injection current j_{inj} (section 3.3) increase with field, the generation of oxide charges $N_{ox}(t)$ is expected to be accelerated under increased fields. However, it was observed in [91] during experiments of oxide charging that the negative charge in the oxide saturates after a while and that the particular saturated charge concentration decreases with increasing field. The higher the field, the lower the oxide charge concentration that is reached. It was found that the occupation level of traps in the oxide is field dependent [91, 129]. The reason for this is a detrapping mechanism, whereby trapped electrons are released from the traps. Depending on the field, an equilibrium between trapping and detrapping is established. This corresponds to a certain occupation level of the traps, i.e. a certain amount of oxide charges. It could be shown that the underlying physical process is impact ionization [91, 129-131]. As illustrated in figure 3.8, electrons from the conduction band of the oxide scatter at trapped electrons and thus excite them into the conduction band. The temporal change of the occupation is thereby described by [91, 135, 200, 201]:

$$\left. \frac{\partial N_{ox}}{\partial t} \right|_{\text{detrapping}} = -\frac{j_{inj}}{e} \alpha(E_{ox}) N_{ox}(t) \quad (3.29)$$

The detrapping via impact ionization depends on the current density of injected electrons j_{inj} into the conduction band of SiO_2 . The effective cross section $\alpha(E_{ox})$ contains the field dependence and can be empirically modeled as [135]:

$$\alpha(E_{ox}) = \alpha_0 \exp\left(-\frac{B}{E_{ox}}\right) \quad (3.30)$$

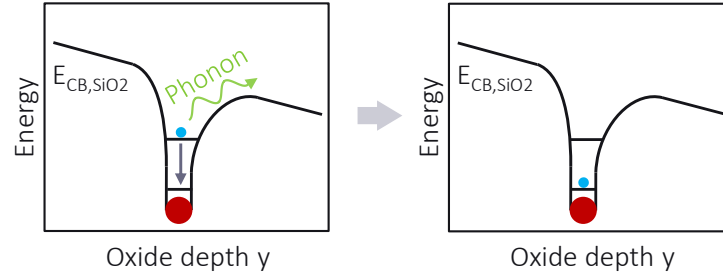


Figure 3.9: Relaxation of trapped electrons from shallow into deep levels.

Here α_0 corresponds to a constant prefactor and B describes the threshold oxide field for impact ionization, which is determined by the energy levels from which the trapped electrons are excited [159, 200]. Of course, these levels correspond to the energy levels of the traps. As the oxide field E_{ox} increases, the probability of detrapping by impact ionization also increases. Monte Carlo simulations of the rate of this process, taking into account intervalley and umklapp scattering, have shown very good agreement with equation 3.30 [200]. In addition, good agreement with experimental data has been demonstrated in [91, 201].

3.4.4 Relaxation of trapped electrons from shallow in deep levels

In [92, 107, 202] it was found that the oxygen vacancy Si-Si, has at least two trap levels. It was further observed experimentally that electrons trapped in the shallow level can relax into the deep level by a relaxation mechanism. The process is illustrated in figure 3.9. The Si-Si bond is under high tension due to the absence of an oxygen atom. In this respect, the relaxation of a trapped electron could correspond to a relaxation of the Si-Si bond. The relaxation mechanism is not determined quantitatively in literature. In this work, the relaxation of trapped electrons from the shallow into the deep trap level is modeled as a rate equation:

$$-\frac{\partial N_{ox,shallow}}{\partial t} = \frac{\partial N_{ox,deep}}{\partial t} = \gamma_0 N_{ox,shallow}(t) \quad (3.31)$$

Here, $N_{ox,shallow}$ and $N_{ox,deep}(t)$ are the concentrations of trapped electrons in shallow levels and those that are already relaxed into deep levels. The relaxation rate γ_0 determines how many electrons per time relax from shallow levels to deep levels. The total concentration of trapped electrons and thus the negative oxide charge $N_{ox}(t)$ does not change. It is the sum of both: $N_{ox}(t) = N_{ox,shallow}(t) + N_{ox,deep}(t)$. This implies the assumption that only one electron can be trapped per trap no matter if in a shallow or deep level. Furthermore, if an electron is trapped in a deep level, it stays there.

3.4.5 Oxide degradation model

The mechanisms for oxide charge generation from the last three sections will now be synthesized into one expression of the generation rate of oxide charges. As already illustrated in figure 3.7, it is assumed that after electrons are captured they first occupy shallow levels. Thus, they can only get into deep levels via the relaxation from shallow levels. From this, it follows that the increase in oxide charges N_{ox} due to the trapping of electrons corresponds to the increase in occupied shallow trap levels $N_{ox,shallow}$ due to electron trapping:

$$\left. \frac{\partial N_{ox}}{\partial t} \right|_{\text{trapping}} = \left. \frac{\partial N_{ox,shallow}}{\partial t} \right|_{\text{trapping}} \quad (3.32)$$

The concentration of electrons in shallow traps can be written as:

$$N_{ox,shallow}(t) = \Gamma_0(t) N_{ox}(t) \quad (3.33)$$

where $\Gamma_0(t)$ is the fraction of the total oxide charge that is determined by electrons occupying shallow levels. It is time dependent and describes at any time t how many electrons are in shallow and deep levels. Its value ranges between 0 and 1. With time, all electrons relax into deep levels. Therefore, $\Gamma_0(t \rightarrow \infty) \rightarrow 0$. It was already illustrated in figure 3.8, that it is assumed further that only electrons from shallow levels can be liberated by impact ionization. Thus, the change in oxide charge N_{ox} due to detrapping corresponds to the change in occupied shallow levels $N_{ox,shallow}$ due to detrapping. This results in a modified detrapping term:

$$\begin{aligned} \left. \frac{\partial N_{ox}}{\partial t} \right|_{\text{detrapping}} &= \left. \frac{\partial N_{ox,shallow}}{\partial t} \right|_{\text{detrapping}} \\ &= -\frac{j_{inj}}{e} \alpha(E_{ox}) N_{ox,shallow}(t) \\ &= -\frac{j_{inj}}{e} \alpha(E_{ox}) \Gamma_0(t) N_{ox}(t) \end{aligned} \quad (3.34)$$

Here it can already be seen that the relaxation process from shallow to deep levels weakens the detrapping mechanism with time. From the equations for trapping 3.28 and detrapping 3.34 the rate equation for oxide charges N_{ox} is determined:

$$\frac{\partial N_{ox}}{\partial t} = \frac{j_{inj}}{e} \sigma [N_{ox,max} - N_{ox}(t)] - \frac{j_{inj}}{e} \alpha(E_{ox}) \Gamma_0(t) N_{ox}(t) \quad (3.35)$$

Every electron trapped in an oxide trap corresponds to a negative oxide charge no matter if in a shallow or deep trap level. Equations 3.31, 3.32, and 3.34 can now be

used to determine the rate of change of the occupied shallow traps:

$$\frac{\partial N_{ox,shallow}(t)}{\partial t} = \frac{\partial N_{ox}(t)}{\partial t} - \gamma_0 N_{ox,shallow}(t) \quad (3.36)$$

Equation 3.36 describes how the occupation of shallow levels increases by electron trapping and decreases by detrapping (first term) and relaxation (last term). It is used in chapter 4 to numerically determine the ratio $\Gamma_0(t)$.

3.4.6 Positive fixed oxide charges

After the sensors come out of production, they already have positive oxide charges (fixed charges). Their concentration is determined by the oxidation conditions of the silicon surface. They are located approximately within the first 3 nm in the oxide from the interface [203]. They are generated as a consequence of the lattice strain near the interface due to the lattice mismatch between Si and SiO₂. Electrically, they compensate the generated negative oxide charges in parts.

3.5 Generation of interface traps

In the literature of the reliability physics of power devices, models are reported covering the generation of electron traps at the Si:SiO₂ interface. However, these models usually focus only on certain aspects of the overall process. In this section, a model is developed that describes the overall process in all its sub-aspects by melting a wide range of models together and in parts extending these. As mentioned in chapter 2.3.2, these are the breaking of the Si-H bond at the interface and the subsequent diffusion of the hydrogen species or the re-formation of Si-H bonds by the reaction of free hydrogen with unpassivated dangling bonds. These processes are described in the following quantitatively by their microscopic physics and combined together in order to reliably model the degradation of the interface. In this respect the following model is the first of its kind which describes the mentioned aspects comprehensively.

3.5.1 Hydrogen dissociation

In order to describe the dissociation of hydrogen from the Si-H bond microscopically, the truncated oscillator was introduced in [67, 204-209]. It is illustrated in figure 3.10a and describes the Si-H bond energetically. The ground state E_0 corresponds to the energetic minimum of the bonding state of the Si-H bond. The energy E_{SiH} is the Si-H

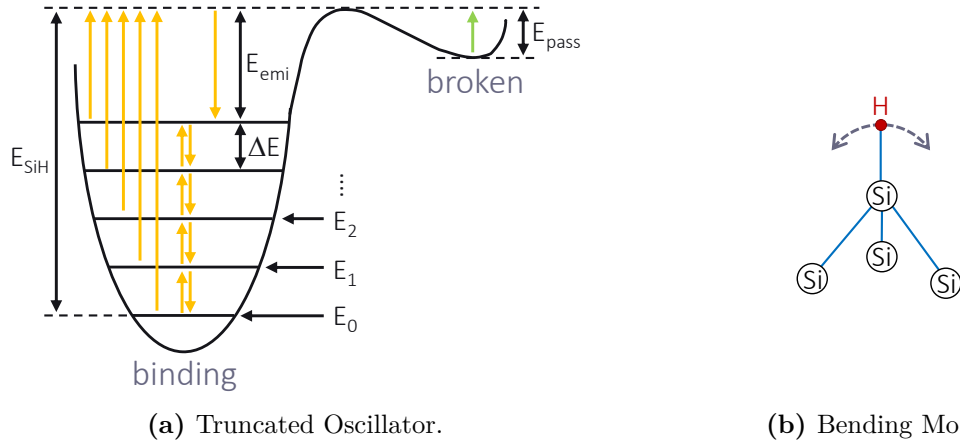


Figure 3.10: a: The Si-H bond described by the truncated oscillator is shown with its levels E_n and its thermal equilibrium binding state E_0 . E_{SiH} corresponds to the binding energy of the Si-H bond. The energetic difference from one bond state to the next is ΔE . By drawing/transferring energy from/to electrons and the lattice, the bond moves up/down the levels E_n . Arrived at the top it breaks. Then, it is in the broken state. b: The bending mode is shown schematically. Each excited bond oscillates accordingly. Both inspired by [67, 204-209]

energy of the bond in the ground state. There are some energy levels it can climb which corresponds to the excitation of vibrations of the bond. In this way, its binding energy is lowered and the bond is weakened. The difference between the levels is equal to ΔE . E_{emi} corresponds to the energy difference of the highest level and the emission barrier. By overcoming it, the bond runs into the second minimum which corresponds to the anti-bonding state. That means the Si-H bond is broken and hydrogen released. Here E_{pass} corresponds to the energy that has to be supplied to the bond in order to move it from anti-bonding back to the bonding state. The number of levels is calculated according to:

$$N = \frac{E_{SiH} - E_{emi}}{\Delta E} \quad (3.37)$$

Between them, the bond can jump up and down by drawing thermal energy from or giving it to the lattice [204, 205, 208]. This corresponds to the creation ($n \rightarrow n + 1$) and annihilation ($n \rightarrow n - 1$) of local phonons, namely the oscillation of the Si-H bond. The thermal creation rate is:

$$\omega'_{+,th} = \omega'_0 \exp\left(-\frac{\Delta E}{k_B T_{lattice}}\right) \quad (3.38)$$

Here ω'_0 corresponds to a characteristic rate. It simply corresponds to the rate of annihilation:

$$\omega'_{-,th} = \omega'_0 \quad (3.39)$$

The process described corresponds to heating or cooling of the bond, which seeks thermal equilibrium with the lattice. Electrons possessing energies greater than the level difference ΔE can scatter at the bond and also excite local vibrational states ($n \rightarrow n + 1$). Likewise, electrons can absorb a vibrational quantum from the bond ($n \rightarrow n - 1$). This creation and annihilation by interaction with electrons corresponds to heating or cooling of the bond by multiple collisions with electrons [210, 211] and is determined by a characteristic energy-dependent interaction frequency of electrons with the Si-H bond γ . In [207, 212-216] it was found to be the determining quantity in the generation of interface traps. It describes how likely an interaction of electron and Si-H bond is per unit time. In [204-207] the explicit expressions differ strongly. However, the qualitative approach is always the same - how many times per unit time does an electron with sufficient energy move past the bond and how likely is their interaction then. In the following, the interaction rate γ is determined based on the quantities derived in section 3.2 and 3.3. First, the portion $\hat{n}(E)$ of the electron population at the interface in silicon possessing some energy E is needed. It is determined by the energy distribution of the electrons concentration $n(E)$:

$$\hat{n}(E) = \frac{n(E)}{\int_0^\infty n(E') dE'} \quad (3.40)$$

From this, the concentration of electrons of a certain energy per time is obtained by multiplying $\hat{n}(E)$ by the total concentration of electrons per time. This is modeled here with the electron current density at the interface $j_{e,IF}/e$. Not every electron that moves past the bond and has sufficient energy will interact with it. The probability of an interaction to occur is measured by an effective cross section σ_{SiH-e} [205-207, 217]:

$$\sigma(E, E_{thres}) = \sigma_0 \left[\frac{E - E_{thres}}{E_{ref}} \right]^p \quad (3.41)$$

Here E_{thres} corresponds to the threshold energy of the regarded interaction. The reference energy is $E_{ref} = 1\text{eV}$ [205] and the exponent p depends on the type of interaction. The interaction frequency is then expressed as:

$$\gamma(E_{thres}) = \frac{j_{IF}}{e} \int_{E_{thres}}^\infty \hat{n}(E) \sigma(E) dE \quad (3.42)$$

From equations 3.38, 3.39 and 3.42, the creation and annihilation rates for the heating and cooling of the bond can be determined. For that the threshold energy corresponds to the difference of vibrational levels ΔE . This yields:

$$k_{\uparrow} = \gamma(\Delta E) + \omega'_0 \exp\left(-\frac{\Delta E}{k_B T_{lattice}}\right) \quad (3.43)$$

$$k_{\downarrow} = \gamma(\Delta E) + \omega'_0 \quad (3.44)$$

There are two main local vibrational modes of the Si-H bond: Stretching and bending modes. The first corresponds to oscillations in the H atoms distance from its Si atom [218]. The second, illustrated in figure 3.10b, corresponds to a deflection of the bond from its rest position by a certain angle, as in a pendulum. Thus, it is a rotation of the Si-H bond around the Si atom [219, 220]. In [67, 204, 207, 208, 220, 221] the authors achieved good agreement with experimental data by taking into account only the bending mode.

In addition to heating, the bond can also be directly broken from the ground state and any excited level E_n [205,222]. In this case, the energy difference $\Delta E_n = E_{SiH} - E_n$ from the start level E_n to the emission barrier must be overcome. This can be supplied to the bond by very energetic electrons. For this to happen, the threshold energy of ΔE_n has to be supplied to the bond. The interaction frequency $\gamma(\Delta E_n)$ then determines how likely per unit time this interaction is. Moreover, the required energy can also be supplied thermally by the lattice. Analogous to the creation rate for the local oscillation k_{\uparrow} , the rupture rate is obtained from the i -th level:

$$r_n = \gamma(\Delta E_n) + \gamma_{rupture} \exp\left(-\frac{\Delta E_n}{k_B T}\right) \quad (3.45)$$

Here $\gamma_{rupture}$ corresponds to the frequency at which phonons with sufficient energy are transferred from the lattice to the bond. Using the expressions from equations 3.43 and 3.45, the cumulative Si-H rupture rate corresponds to [205]:

$$R = C \sum_{m=0}^N r_m \left(\frac{k_{\uparrow}}{k_{\downarrow}}\right)^m \quad \text{with } C = \sum_{m=0}^N \left(\frac{k_{\downarrow}}{k_{\uparrow}}\right)^m \quad (3.46)$$

This in turn can be used to derive the generation rate of interface traps:

$$\left. \frac{\partial N_{it}}{\partial t} \right|_{\text{SiH rupture}} = (N_{it,max} - N_{it}) R \quad (3.47)$$

3.5.2 Diffusion and passivation

Passivation of dangling bonds corresponds the transition from the anti-bonding state in figure 3.10a to the binding state. The passivation rate is modeled as Boltzmann thermal activation:

$$P = \gamma_{pass} \exp\left(-\frac{E_{pass}}{k_B T}\right) \quad (3.48)$$

It is given by the passivation frequency γ_{pass} and the passivation barrier E_{pass} . Of course free hydrogen needs to be present for this process. Thus, the passivation is also governed by the concentration of atomic hydrogen at the interface $N_{H,IF}$. It is determined by the diffusion of free hydrogen away from the interface [68, 70-80, 211, 222]. Atomic [76, 123, 223-227] and molecular hydrogen [228-230] were found to be the diffusing species. An exact description of diffusion is possible by means of a system of coupled differential equations [79, 167]:

$$\frac{\partial N_H}{\partial t} = D_H \frac{\partial^2 N_H}{\partial x^2} - k_{H \rightarrow H_2} N_H^2 + k_{H_2 \rightarrow H} N_{H_2} \quad (3.49)$$

$$\frac{\partial N_{H_2}}{\partial t} = D_{H_2} \frac{\partial^2 N_{H_2}}{\partial x^2} - 0.5 k_{H_2 \rightarrow H} N_{H_2} + 0.5 k_{H \rightarrow H_2} N_H^2 \quad (3.50)$$

D_i corresponds to the diffusion coefficient of the species i and describes, as a function of temperature, how fast its concentration front propagates with time:

$$D_i = D_{i0} \exp(-E_i/k_B T) \quad (3.51)$$

Here, D_{i0} and E_i correspond to a constant prefactor and thermal activation energy for the diffusion of species i . The process is shown in figure 3.11a. Once atomic hydrogen is generated at the interface, it can react to molecular hydrogen and vice versa. This process is described by the terms with factors $k_{H_i \rightarrow H_j}$. In addition, both hydrogen species diffuse through the oxide and silicon. The terms $D_i \partial N_i / \partial t$ describe this diffusion process. The differential equation 3.49 would have to be solved to determine the hydrogen concentration at the interface $N_{H,IF}$. However, this is a very complex task and can only be done numerically. Therefore, some simplifications are made. The diffusion coefficient of atomic as well as molecular hydrogen at a temperature of 125°C in silicon dioxide ($D_H \propto 10^{-7} \text{cm}^2/\text{s}$, $D_{H_2} \propto 10^{-10} \text{cm}^2/\text{s}$) is up to three orders of magnitude larger than that in silicon ($D_H \propto 10^{-5} \text{cm}^2/\text{s}$, $D_{H_2} \propto 10^{-7} \text{cm}^2/\text{s}$) [231]. Therefore, in agreement with literature, diffusion is assumed to occur exclusively through the oxide [68, 70-80]. For thicknesses greater than 100nm, it can be assumed to be infinitely thick [232]. Under these assumptions, according to [73, 74, 79] the shape of the hydro-

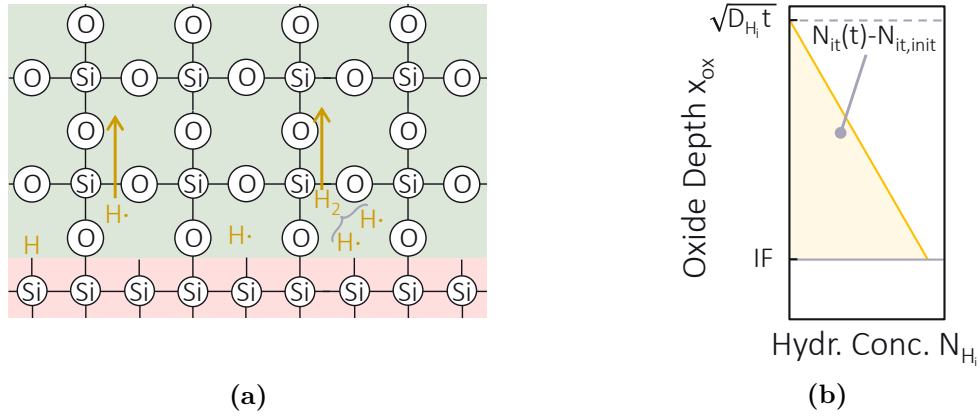


Figure 3.11: Reaction-diffusion process of hydrogen at the Si:SiO₂ interface (a). Concentration of H_i in the depth of the oxide after the triangular approximation (b).

gen species diffusion profile can be approximated as a triangle. This is illustrated in figure 3.11b. Here, the distance of the diffusion front from the interface corresponds to $\sqrt{D_H t}$ and increases with increasing time t . Considering diffusion exclusively by atomic hydrogen, its concentration at a certain distance from the interface x_{ox} is consequently

$$N_H(x_{ox}) = N_{H,IF} - \frac{N_{H,IF}}{\sqrt{D_H t}} x_{ox} \quad (3.52)$$

where the total amount of hydrogen in the oxide corresponds to the integral of $N_H(x_{ox})$ over the oxide depth x_{ox} . Moreover, this must correspond to the generated interface traps. From this the concentration of hydrogen at the interface is determined:

$$\begin{aligned} N_{it} - N_{it,init} &= \int_0^{\sqrt{D_H t}} N_H(x_{ox}) dx_{ox} = \frac{\sqrt{D_H t}}{2} N_{H,IF} \\ \Rightarrow N_{H,IF} &= \frac{2}{\sqrt{D_H t}} (N_{it} - N_{it,init}) \end{aligned} \quad (3.53)$$

Above, $N_{it,init}$ corresponds to the concentration of interface traps prior their generation during degradation. Similarly, diffusion can be considered which takes place exclusively by molecular hydrogen. Only a relation between the atomic and diffusing molecular hydrogen formed is needed. This is provided in [79] as:

$$\begin{aligned} \frac{N_{H,eff,IF}^2}{N_{H_2,IF}} &= n_0 = const. \\ \Rightarrow N_{H,eff,IF} &= \sqrt{N_{H_2,IF} n_0} \end{aligned} \quad (3.54)$$

Using this, and following an analogous procedure as before, the concentration of atomic hydrogen at the interface for diffusion of molecular hydrogen is obtained to be:

$$N_{H,IF} = \sqrt{\frac{n_0}{\sqrt{D_{H_2}t}} (N_{it} - N_{it,init})} \quad (3.55)$$

It was found in the course of this work, that good agreement with experimental data is achieved by using $n_0 = 2$, which corresponds to the obvious meaning that one hydrogen molecule decays into two hydrogen atoms.

In reality, the removal of hydrogen from the interface is accomplished by a combination of diffusion of atomic and molecular hydrogen, as schematized in figure 3.11a. Thus, the corresponding results for $N_{H,IF}$ are considered here as the upper and lower limits within the true solution is found:

$$N_{H,it} = \left[\frac{2}{\sqrt{Dt}} (N_{it} - N_{it,init}) \right]^a \quad \text{with } D = b D_{H_2} + (1 - b) D_H \quad (3.56)$$

$$a = \frac{b}{2} + (1 - b)$$

Here $b = 0$ and $b = 1$ correspond to the limiting cases where only atomic (H) or molecular hydrogen (H_2) is involved in the diffusion process. Substitution into equation 3.48 now yields the determination of the repassivation rate. Considering equations 3.43 and 3.56, the rate of change of interface traps can now be written as [76, 79]:

$$\left. \frac{\partial N_{it}}{\partial t} \right|_{\text{passivation}} = -P N_{H,it}(t) N_{it}(t) \quad (3.57)$$

3.5.3 Interface degradation model

Finally, from equation 3.47, 3.57 and comparison of [67, 68, 73, 76, 77, 79, 205, 206] and section 4.1.2 in [167], a differential equation can now be set up, which describes both the rupture of Si-H bonds, the diffusion of hydrogen atoms and the passivation of dangling bonds (Si·):

$$\begin{aligned} \frac{\partial N_{it}}{\partial t} &= \left. \frac{\partial N_{it}}{\partial t} \right|_{\text{SiH rupture}} + \left. \frac{\partial N_{it}}{\partial t} \right|_{(\text{re})\text{passivation}} \\ &= (N_{it,max} - N_{it}) R - P N_{H,it}(t) N_{it}(t) \end{aligned} \quad (3.58)$$

Equation 3.58 determines the generation rate of interface traps $\frac{\partial N_{it}}{\partial t}$. It will be solved in chapter 4 numerically.

3.6 Summary

Crucial processes for APD degradation were extracted from the consideration of simulation results of an APD under severe LiDAR operation conditions. Due to strong variations of internal electric fields and current densities, they vary in intensity at different locations inside the device. The superposition of all processes causes the degradation of the sensors. In order to obtain a model that reflects reality accurately enough, each of the processes involved is represented comprehensively and in detail.

At first the electron distribution function was determined. It expresses the likelihood of electron state occupation in momentum space. A literature review on the strength of scattering mechanisms at relevant electric fields in silicon below 5×10^5 V/cm identified electron phonon scattering as the most prominent in the collision term of the Boltzmann transport equation. A solution approach to the latter was found in literature and extended by temperature dependency and to the three dimensional case in order to be applicable to 3d real APDs in the full LiDAR temperature range. Taking into account the electron distribution function, the occupation of states in momentum space was derived. The corresponding integrals were solved in order to fulfill previously defined injection conditions for the electric field strength and the orientation of electron momentum. Consequently, the energy dependent electron concentration at elevated fields and the injection probability of electrons into the oxide were established. The latter over proportionally increases with the electric field strength and decrease the more parallel the electric field is oriented towards the interface.

From this, the current density of electrons injected into the oxide was determined. In the oxide, electrons are captured in preexistent electron traps. Electrons drawn sufficient energy from the oxide field tend to liberate trapped electrons via impact ionization which is covered by an empirical detrapping model reported in literature. However, by supposing oxygen vacancies as the dominant trap, the liberation is mitigated by relaxation of trapped electrons from shallow into deep trap levels. For this process only its presence was proven experimentally in literature without underlying mathematics. In conjunction with aging phenomena the mechanism is first expressed quantitatively in this work. Its temporal evolution runs in parallel to the generation of negative oxide charges. Therefore, its solution needs to be embedded into the simulation of the entire degradation model. The mentioned mechanisms of electron injection, trapping, detrapping and relaxation are melt together into a novel oxide degradation model expressed as a time differential equation. No model found in literature covers the kinetics of negative oxide charge generation in such deep detail. Negative oxide charges are partially compensated by preexistent positive oxide charges. They occur as a consequence of lattice strain in the first few nm from the interface and will be

incorporated into the simulation of the oxide degradation model.

At the Si:SiO₂ interface, most of the dangling bonds are passivated with hydrogen. However, interaction with electrons and lattice vibrations induce heating and rupture of the Si-H bonds. The corresponding rupture rate is assembled from different models found in literature and the previously achieved energy dependent electron concentration. It is opposed by the repassivation of dangling bonds, which depends on the availability of free hydrogen at the interface. The latter is governed by its generation due to Si-H bond rupture and its diffusion through the oxide away from the interface. In order to approximate the diffusion process, a triangular approximation for the profile of hydrogen concentration within the oxide is applied. Union of rupture, repassivation and diffusion forms the interface degradation model which also correspond to a time differential equation. No model could be found in literature which is as comprehensive and detailed.

In order to model APD degradation, the differential equations of the oxide and interface degradation need to be solved in parallel.

Chapter 4

Simulation of APD degradation

In the previous chapter, novel degradation models of the oxide and the Si:SiO₂ interface were established. They are expressed by the differential equations 3.35 and 3.58. Both of the generation processes are promoted by electron currents and electric fields inside the device. In turn, oxide charges and interface traps affect internal currents and fields. A coupled problem arises, which cannot be solved analytically. In order to tackle this challenge, a sophisticated numerical iteration approach is established in this chapter, that simulates APD degradation in a tandem procedure incorporating the device simulator.

Section 4.1 first defines the stressors of degradation within the device. Then, the basic solution approach is developed. This is then applied to solve the differential equation of the oxide charges generation in the simplified case of constant fields and currents. Similarly it is used to solve the differential equation of interface trap generation in section 4.2. In section 4.3, a method is developed to solve both differential equations self-consistently in parallel on sensor level using the aforementioned tandem procedure. It can be used to calculate the profiles of oxide charges and interface traps within the device. In section 4.4, a parameter is defined to measure the degradation of the sensor. Finally, in section 4.5, the degradation of real sensors is simulated and discussed.

4.1 Oxide degradation

In chapter 3 a model was established, which covers the degradation of silicon dioxide by generation of negative oxide charges. Thereby, the differential equation 3.35 determines the increase of their concentration N_{ox} with time. Negative oxide charges correspond to the concentration of electrons trapped in the oxide. Their generation rate can be abstracted by a function of all internal quantities $Q(t)$, the concentration

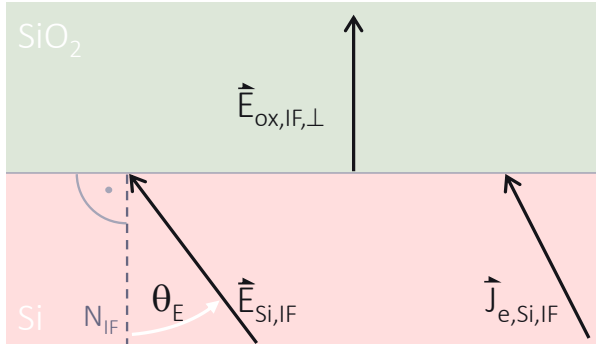


Figure 4.1: Sensor internal drivers of degradation at the interface: The electric field strength in silicon $E_{si} := |\vec{E}_{si,IF}|$, the component perpendicular to the interface in the oxide $E_{ox} := |\vec{E}_{ox,IF,\perp}|$ and the electron current density in silicon $j_e := |\vec{j}_{e,Si,IF}|$. The angle θ_E between $\vec{E}_{si,IF}$ and the interface normal N_{IF} .

$N_{ox}(t)$ itself, and its fraction of occupied shallow trap levels $\Gamma_0(t)$:

$$\frac{\partial N_{ox}}{\partial t} = \mathbf{F}_{ox} [\mathbf{Q}(t), N_{ox}(t), \Gamma_0(t)] \quad (4.1)$$

The rate of change \mathbf{F}_{ox} is determined by equation 3.35.

4.1.1 Internal drivers of degradation

The device internal quantities $\mathbf{Q}(t)$ are the drivers of degradation. They are illustrated in figure 4.1 and include the electric field at the interface in silicon $E_{si} := |\vec{E}_{si,IF}|$ and the angle $\theta_{E,si}$ between the field $\vec{E}_{si,IF}$ and the interface normal N_{IF} . It is calculated from the components of the field perpendicular and parallel to the interface according to $\theta_E = \arccos(-E_{\perp}/\sqrt{E_{\parallel}^2 + E_{\perp}^2})$. Furthermore, the electron current density at the interface in silicon $j_e := |\vec{j}_{e,si,IF}|$, the component of the field perpendicular to the interface in the oxide $E_{ox} := |\vec{E}_{ox,IF,\perp}|$ and the temperature of the crystal lattice at the interface in silicon T_L are included. Heating of the lattice by electron-phonon scattering is not considered here. Therefore, the latter corresponds to the temperature of the environment $T_L = T$. The choice of these quantities is justified by their influence on components of the model: The injected electron current is explicitly determined by the electron current at the interface $j_{inj} = j_e P_{inj}$. The injection probability P_{inj} is determined by the field in silicon E_{si} , the angle θ_E and the temperature T (section 3.3). In addition, the detrapping process is caused by the oxide field E_{ox} . Charges in the oxide act on the underlying silicon as an applied gate voltage in MOSFETs. Therefore, the $\mathbf{Q}(t)$ are in turn affected by the degradation phenomenon $N_{ox}(t)$, so they are themselves time dependent. For reasons of self-consistency, this feedback of the effect $N_{ox}(t)$ to its cause $\mathbf{Q}(t)$ must be taken into account in order to provide a self-consistent solution of equation 3.35.

4.1.2 Basic iteration approach

There is no information in analytical form about the feedback. Therefore, no analytical solution for equation 3.35 can be given. Therefore, a numerical method is established, which allows a solution taking into account the feedback. The first and also basic part of it will now be presented. For the time being, the feedback is disregarded and introduced at a later point in section 4.3. The procedure is illustrated in a N_{ox} vs. t plot in figure 4.2a. The solid curve corresponds to the solution of N_{ox} that is to be determined. It increases with time and slowly approaches the limit concentration of available preexisting oxide traps $N_{ox,max}$. The procedure to determine it is as follows. At first, the slope F_i at time t_i is determined according to equations 3.35 and 4.1 by

$$F_i = \mathbf{F}_{ox} [\mathbf{Q}(t_i), N_{ox}(t_i), \Gamma_0(t_i)] \quad (4.2)$$

In the figure it is shown as a tangent to the curve at $t = t_i$. In the second step, the size of the valid time step must be determined. If it is too large, the true solution will be greatly overestimated. If it is too small the solution algorithm would be very slow in the end and thus useless, because too much computing time would be consumed. The ideal step size depends on the curvature of the $N_{ox}(t)$ curve and thus also on time. An empirical function $\Delta_{N_{ox}}(t)$ is used for its determination. It will be defined below. It corresponds to the maximum valid change in the concentration of oxide charges at time t_i . This yields the allowed time step at time t_i :

$$\Delta t_i = \frac{\Delta_{N_{ox}}(t_i)}{F_i} \quad (4.3)$$

The step Δt_i is taken as illustrated in figure 4.2a which is accompanied by a change in the oxide charge:

$$\Delta N_{ox}(t_i) = F_i \Delta t_i \quad (4.4)$$

In the third and final step, the next moment in time t_{i+1} and the corresponding concentration of the oxide charge $N_{ox}(t_{i+1})$ are determined:

$$\begin{aligned} N_{ox}(t_{i+1}) &= N_{ox}(t_i) + \Delta N_{ox}(t_i) \\ t_{i+1} &= t_i + \Delta t_i \end{aligned} \quad (4.5)$$

Executing the procedure, the time t is discretized. Iteration over the time windows $[t_i, t_i + \Delta t_i[$ yield an piecewise approximation of the $N_{ox}(t)$ curve. It is then piecewise linear with slope F_i . Essential to this procedure is the function $\Delta_{N_{ox}}(t)$, which

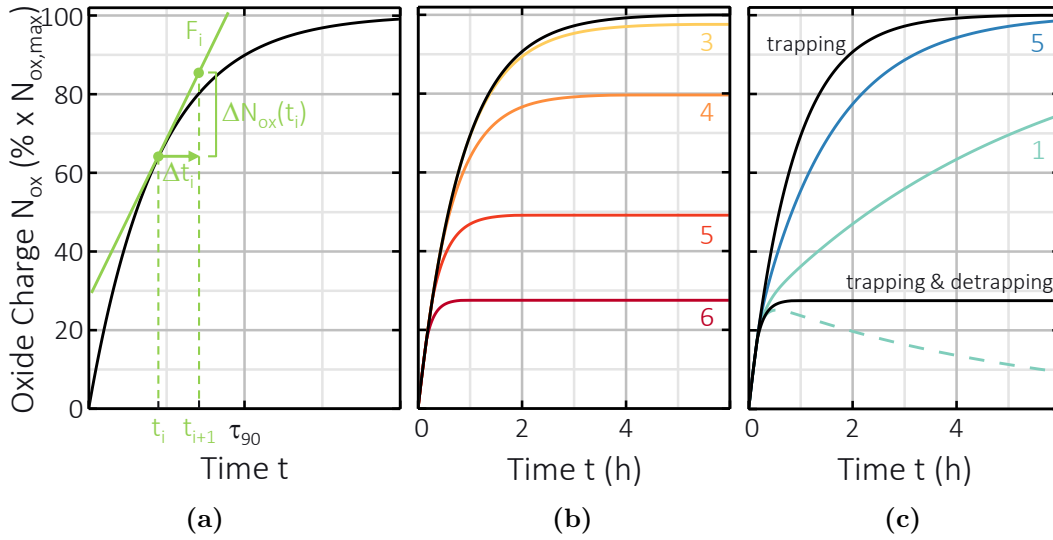


Figure 4.2: a: Illustration of the step wise approach to solve the differential equation of oxide degradation (eq. 3.35). This leads to the time dependent concentration of electrons trapped in the oxide $N_{ox}(t)$. Solutions for $N_{ox}(t)$ as determined via the simplified approach in case of b: only trapping (black) and additional detrapping for four values of the oxide field E_{ox} (10^5 V/cm). And c: only trapping (black), trapping and detrapping (γ_0) and the entire model (trapping, detrapping, relaxation) (blues). The relaxation rate γ_0 (10^{-4} s $^{-1}$) is varied as labeled and the concentration of electrons occupying shallow trap levels $N_{ox,shallow}$ is plotted for $\gamma_0 = 10^{-4}$ s $^{-1}$ (dashed). Here, the concentration of available preexisting oxide traps $N_{ox,max}$ is set equal to 10^{12} cm $^{-2}$.

ensures that the true solution $N_{ox}(t)$ is not overestimated. In order to compute $F_i = \mathbf{F}_{ox}[\mathbf{Q}(t_i), N_{ox}(t_i), \Gamma_0(t_i)]$, the fraction of occupied shallow trap levels $\Gamma_0(t)$ needs to be known. This is the subject of the next paragraph.

4.1.3 The occupation of shallow trap levels

In paragraph 3.4.4 a model was developed which captures the relaxation of electrons from shallow to deep trap levels in the oxide. The fraction Γ_0 of the total concentration of oxide charges N_{ox} which corresponds to electrons in shallow states $N_{ox,shallow}$ is determined by equation 3.33. It enters explicitly into the differential equation of oxide degradation and thus into $\mathbf{F}_{ox}[\mathbf{Q}(t_i), N_{ox}(t_i), \Gamma_0(t_i)]$. An approach is developed that allows its determination. It is embedded into the procedure of the previous paragraph 4.1.2. Discrete time windows at time t_i with a length of Δt_i are considered. Both quantities t_i and Δt_i are determined following the procedure there. Time t_0 corresponds to $t = 0$. Initially, no electrons are trapped in the oxide. For this, they have to be injected into the oxide in time window $i = 0$ and trapped there. Therefore, at time t_1 , there are $N_{ox}(t_1) = \Delta N_{ox}(t_0)$. It is assumed that trapped electrons can occupy deep states only by relaxation. Therefore $\Gamma_0(t_1) = 1$. In general, the concentration of

occupied shallow traps at time t_i is determined by:

$$N_{ox,shallow}(t_i) = N_{ox}(t_i) \Gamma_0(t_i) \quad (4.6)$$

As described in paragraph 3.4.4, relaxation is determined by a constant rate γ_0 . Electrons can only get trapped in shallow levels. From there they relax to deep states within $[t_i, t_i + \Delta t_i]$. But only as many can relax as are in shallow states at time t_i . This gives the change due to relaxation:

$$\Delta N_{ox,shallow}(t_i)|_{\text{relaxation}} = -\min [N_{ox,shallow}(t_i) \gamma_0 \Delta t_i ; N_{ox,shallow}(t_i)] \quad (4.7)$$

From this the net change is obtained:

$$\Delta N_{ox,shallow} = \Delta N_{ox}(t_i) + \Delta N_{ox,shallow}(t_i)|_{\text{relaxation}} \quad (4.8)$$

Finally, from this $\Gamma_0(t_{i+1})$ is determined:

$$\Gamma_0(t_{i+1}) = \frac{N_{ox,shallow}(t_i) + \Delta N_{ox,shallow}(t_i)}{N_{ox}(t_i) + \Delta N_{ox}(t_i)} \quad (4.9)$$

The numerator corresponds to the concentration of occupied shallow states $N_{ox}(t_{i+1})$ and the denominator to the total concentration of oxide charges $N_{ox}(t_{i+1})$ at time t_{i+1} . Within one iteration step, this procedure is performed after that in the previous paragraph. Both are then iterated over together yielding the piecewise linear approximation of the $N_{ox}(t)$ and $\Gamma_0(t)$ curves. With this sophisticated tool at hand, the interaction of the processes involved in negative oxide charge generation is now examined.

4.1.4 Simplified solution

If the feedback between the drivers $\mathbf{Q}(t)$ and the degradation $N_{ox}(t)$ is initially disregarded, equation 3.35 can now be solved numerically for time invariant $\mathbf{Q}(t)$. Within the model of oxide degradation, electrons in the conduction band of the oxide tend to excite electrons from shallow trap states into the conduction band by impact ionization via the detrapping mechanism (paragraph 3.4.3). The necessary energy for this is provided by their acceleration in the oxide field E_{ox} . Figure 4.2b shows the solutions for a variation of the oxide field considering trapping and detrapping in an N_{ox} vs. t plot. All remaining model parameters were chosen identically. If only trapping is considered (black curve), the concentration N_{ox} increases relatively strongly at small times t , passes through a kink, and converges to the maximum value of $N_{ox,max}$. The influence of the detrapping mechanism is regarded by the variation of the oxide field

E_{ox} (colored curves) while the relaxation mechanism is turned off. At early times, the curves increase equally regardless of the field E_{ox} . However, the larger E_{ox} , the earlier the curves saturated. The saturation concentration $N_{ox,sat}$ is smaller than $N_{ox,max}$ and decreases with increasing field E_{ox} . Within the model, this can be explained by the fact that as the field increases, an increasing number of electrons in the conduction band of the oxide have enough energy to excite electrons from shallow trap states. Therefore, equilibrium between trapping and detrapping occurs at a decreasing concentration of trapped electrons. For the stationary case $\partial N_{ox}(t)/\partial t = 0$, the saturation concentration can be derived:

$$N_{ox,sat}(t) = \left[\frac{\Gamma_0(t) \alpha(E_{ox})}{\sigma} + 1 \right]^{-1} N_{ox,max} \quad (4.10)$$

Considering equation 3.30, it follows that $\alpha(E_{ox})$ increases with increasing field. Thus, equation 4.10 states a decrease of the saturation concentration with increasing field E_{ox} . The more pronounced the detrapping process, the lower is the concentration of oxide charges that is reached. Now, the relaxation process is turned on. In figure 4.2c the $N_{ox}(t)$ curves corresponding to the full set of processes (trapping, detrapping and relaxation) are shown where the relaxation rate γ_0 is varied and the oxide field is fixed. Also the already discussed curves of only trapping and only trapping and detrapping are shown. Furthermore, the concentration of electrons in shallow trap states for one value of γ_0 is plotted. At early times t , all curves increase equally. The larger the value of γ_0 , the more the solution of $N_{ox}(t)$ deviates from that considering trapping and detrapping, and the closer it is to that considering only trapping. Thus, for the curve with the lower relaxation rate, the kink can be seen where the detrapping curve enters its saturation. In the case of the curve with the higher relaxation rate, this kink is not visible. At late times t both relaxation curves approach the maximum value $N_{ox,max}$. The concentration of electrons in shallow trap states increases with time in the same way as all other curves, then passes through a maximum and thereafter decreases with time and approaches 0. Thus, at the beginning, all electrons are trapped in shallow states from which they can be released via impact ionization. With time, they relax into deep states from which they can not be released by impact ionization. Thus, the influence of detrapping decreases with time. The larger the relaxation γ_0 , the stronger is this decrease and the faster is the approach to the solution for exclusively trapping. So, the relaxation mechanism affects the detrapping mechanism by allowing the amount of trapped electrons that can be liberated from the shallow levels to decrease with time. The oxide field E_{ox} primarily influences the strength of the detrapping mechanism. Together with the relaxation it delays the generation of oxide charges compared to the case where only electron trapping is considered.

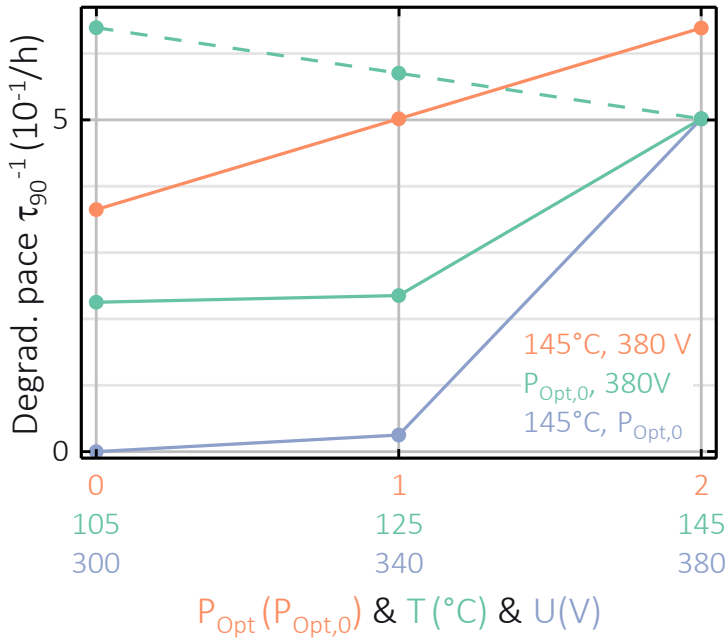


Figure 4.3: solid: Influence of the external stressors U , T and P_{opt} on oxide degradation. The belonging of the x-axis labels to the stressors is assigned by color. The degradation pace is measured by τ_{90}^{-1} . For each stressor variation, the remaining stressors are kept constant. P_{opt} variation (red): $T = 145^\circ\text{C}$, $U = 380\text{ V}$; T variation (green): $P_{opt} = P_{opt,0} = 20\text{ mW/cm}$, $U = 380\text{ V}$; U variation (blue): $P_{opt} = P_{opt,0}$, $T = 145^\circ\text{C}$. dashed: Without temperature induced generation of dark current. Current density is fixed at its value at $T = 145^\circ\text{C}$.

4.1.5 Impact of operation conditions

With the application of the previously developed approach, the influence of the external stressors is investigated. These are the intensity of the incident light P_{opt} , the operation voltage U and the temperature T . In order to measure the impact of the stressors on the aging process, a degradation pace is defined. Here, it corresponds to the reciprocal time at which 90% of the maximum oxide charge density $N_{ox,max}$ is reached. It is exemplarily marked in figure 4.2a. In figure 4.3 the degradation pace t_{90}^{-1} is plotted (solid) against a variation of the illumination intensity P_{opt} in multiples of $P_{opt,0} = 20\text{ mW/cm}$, voltage U and temperature T . For these, the values of the device internal parameters of current density j_e and electric field E_{si} are extracted from the device simulation and given into the simulation of the model, while all remaining model parameters are held constant. The intensity of incident light and the photo-generated electron current are linearly related. Temperature affects the generation of the dark current in the device. Therefore, the total electron current varies with both. As the illumination intensity increases, t_{90}^{-1} increases. With voltage and temperature, t_{90}^{-1} increases slowly for small values and rapidly for larger values. This means that the rate of degradation and hence the stress on the device increases with the operating voltage U , temperature T , and illumination intensity P_{opt} . The increase with voltage can be explained as follows. The fields inside the sensor increase with increasing voltage. In paragraph 3.3.1 and 3.3.3, it was quantitatively concluded that the mean energy of electrons and

thus the injection probability increase with increasing fields. So, an increased number of electrons has sufficient energy to overcome the interface barrier and is injected into the oxide. Increasing illumination intensity P_{opt} or temperature increase the amount of photo or thermally generated electrons in silicon. As higher electron currents are available in both cases, more electrons are injected into the oxide. Finally, an increase of all stressors lead to an increased amount of electrons involved in trapping. This corresponds to a higher amount of oxide charges generated with time. The dashed curve in figure 4.3 corresponds to the case without temperature induced generation of dark current. Instead, the current density is fixed at its value at $T = 145^\circ\text{C}$. So, the impact of the temperature on the current density is turned off and the pure temperature dependence of the injection process is regarded. It turns out that in this case the degradation pace decreases with temperature. In the framework of the discussion in paragraph 3.2 this behavior is explained as follows. An increase of the temperature leads to an increase of the optical phonons present in the lattice. Therefore, the electron mean energy is reduced due to the promotion of scattering events where electrons lose their energy to the lattice and only a decreased amount is energetic enough to overcome the interface. Obviously, this effect is outweighed by the thermal generation of dark current.

4.2 Interface degradation

The differential equation of the interface degradation model equation 3.58 is composed of two competing terms. The rupture rate (equation 3.47) drives the degradation of the interface. The passivation rate (equation 3.57) counteracts the degradation. In its form equation 3.58 is similar to equation 3.35 describing oxide degradation. For this reason, the basic solution approach from paragraph 4.1.2 is adopted. In this case, the rate of change is written as:

$$\frac{\partial N_{it}}{\partial t} = \mathbf{F}_{it}[\mathbf{Q}(t), N_{it}(t), N_{H,IF}] \quad (4.11)$$

It is determined by equation 3.58. The quantity $N_{H,IF}$ corresponds to the hydrogen concentration at the interface and $\mathbf{Q}(t)$ to the internal stressors introduced in section 4.1.1. As discussed in paragraph 3.5.1, the electric field in silicon E_{si} and the current density j_e enter the interaction frequency $\gamma(E)$ (equation 3.42). The temperature T influences all rates in their Boltzmann-like exponential factors.

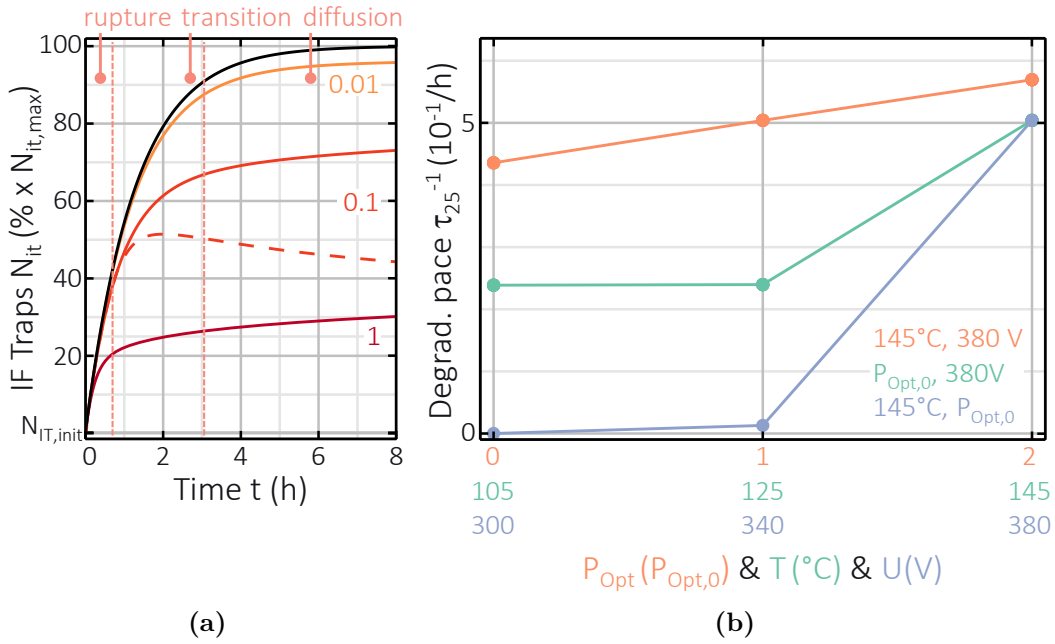


Figure 4.4: a: Solution for the concentration of interface traps $N_{it}(t)$ resulting from equation 3.58. The strength of passivation is varied via a variation of the passivation rate γ_{pass} (colored). Labels of the curves correspond to the quotient $\gamma_{pass}/\gamma_{rupture}$ with $\gamma_{rupture} = 10^{12} s^{-1}$. For $\gamma_{pass}/\gamma_{rupture} = 0.1$ the hydrogen concentration at the interface is shown (dashed). The solution for the case of vanishing passivation is also shown (black). Also the periods of dominant rupture and passivation and the transition period are marked. b: Influence of the external stressors U , T and P_{opt} on interface degradation. The belonging of the x-axis labels to the stressors is assigned by color. The degradation rate is measured by τ_{25}^{-1} . Stressor variations as in figure 4.3

4.2.1 Simplified solution

Figure 4.4a shows the solutions for the concentration of interface traps $N_{it}(t)$ in an N_{it} vs. t plot for the case of vanishing passivation ($\gamma_{pass} \rightarrow 0$) and a variation of the passivation frequency γ_{pass} . Also shown is the concentration of hydrogen at the interface $N_{H,IF}(t)$ for one of the N_{it} curves. This is determined by the diffusion of the hydrogen in the oxide away from the interface as explained in paragraph 3.5.2. The solution of $N_{it}(t)$ without passivation increases rapidly at early times starting from its initial value $N_{it,init}$ and then slowly converges to the limit of $N_{it,max}$ at late times. Similarly, the curves of the solutions taking passivation into account increase at early times t . However, they kink earlier and run below the curve of vanishing passivation. The difference between every curve with $\gamma_{pass} \neq 0$ and the one with $\gamma_{pass} \rightarrow 0$ increases and the time of kink decreases with increasing γ_{pass} . The hydrogen concentration at the interface $N_{H,IF}$ increases at early times t along with the associated $N_{it}(t)$ curve, moves away from it after the kink, passes through a maximum, and then slowly decreases. In conclusion, the process of Si-H bond rupture is dominant at early

times. Therefore, the passivation curves initially follow the course without passivation. New interface traps are quickly generated. Similarly, hydrogen is generated at the interface. Both concentrations are therefore initially the same. The availability of hydrogen at the interface in the early stage of degradation increases with time. This is why passivation is becoming more pronounced with time. An equilibrium is established between the generation of dangling bonds and their passivation. This would lead to a steady state ($\partial N_{it}/\partial t = 0$) and a saturation of the concentration at $N_{it} < N_{it,max}$. At the same time however, hydrogen is removed from the interface and distributed in the oxide due to the diffusion process introduced in paragraph 3.5.2. Consequently, its concentration at the interface decreases with time and the equilibrium shifts toward increasing concentrations N_{it} until $N_{it,max}$ is reached. Therefore, the slow increase of N_{it} at the late stage of degradation is due to diffusion of the hydrogen away from the interface. So, the diffusion process dominates. In the transition from the rupture to the diffusion dominance, the N_{it} curve passes through its kink and the $N_{H,IF}$ curve through its maximum. At this moment the equilibrium of generation and passivation would form if there would be no diffusion.

4.2.2 Impact of operation conditions

The influence of the external stressors, i.e. the intensity of the incident light P_{opt} , the voltage U and the temperature T , is investigated in the following. As in paragraph 4.1.5, the reciprocal time is chosen as a measure of the degradation pace. Here, the time τ_{25} is chosen which is when 25% of $N_{it,max}$ is generated. In figure 4.4b the degradation pace t_{25}^{-1} is plotted against a variation of the illumination intensity P_{opt} in multiples of $P_{opt,0} = 20 \text{ mW/cm}$, voltage U and temperature T . For these, the values of the component internal parameters of current density j_e and electric field E_{si} are extracted from device simulation results and given to the simulation of the model, while all remaining model parameters are kept constant. As the illumination power increases, t_{25}^{-1} increases. With voltage and temperature, t_{25}^{-1} increases slowly for small values and rapidly for larger values. As discussed in section 3.3, the average energy of electrons increases with electric field and thus with voltage. In that case, the Si-H bonds are weakened more due to the heating process described in paragraph 3.5.1. Also, the number of electrons that can directly break the bond is increased. So, the interface trap generation rate increases with increasing voltage. An increased illumination intensity P_{opt} means an increased generation rate of photo generated electrons and electron current density. This also increases the number of electrons that can heat and directly break the bonds. Increased temperature T increases the number of phonons in the lattice and also the availability of electrons that can interact with the bond

and heat it up. In addition, the diffusion of hydrogen is accelerated. The equilibrium between rupture and passivation is therefore shifted in favor of rupture. Finally, due to these processes, N_{it} increases faster, reaching the 25 % mark more quickly, and the degradation pace increases.

4.3 Self-consistent numerical iteration approach

In this section, the solution approach for the oxide and interface degradation differential equations (eq. 3.35 and 3.58) is completed. Self-consistency is achieved by the incorporation of the feedback between internal stressors \mathbf{Q} and degradation phenomena N_{ox} and N_{it} . This is done on device level by a tandem procedure including the device simulator (sec. 2.4) and the parallel simulation of oxide and interface degradation. The latter two and the procedure outlined in the following are implemented in the R PROGRAMMING LANGUAGE.

4.3.1 Iteration procedure of the coupled simulation

In order to incorporate the feedback between internal stressors \mathbf{Q} and degradation phenomena N_{ox} and N_{it} during sensor aging, a coupled simulation approach is developed. Its procedure is illustrated in figure 4.5. During its initialization, sensor design and internal properties are defined. Only circular symmetric sensors are considered. Therefore, it is sufficient to regard a 2d cross section of the simulation domain. As discussed in section 3.1, the degradation is supposed to occur in the edge region of the APD. There it is both, a temporal and spatial physical process. Therefore, the edge region is spatially discretized. This is done by dividing sections along the interface over the distance between n and p contacts. In the three dimensional sensor, the sections correspond to rings drawn around the active area. Within the sections, the initial values of N_{ox} and N_{it} are defined. On the resulting structure, the device simulator then determines the internal stressors \mathbf{Q} by solving the Poisson and continuity equations. They are output as illustrated by the drawn curve and discretized by averaging their values in each section. The discretization is shown as bars within each section. The discretized internal stressors $\mathbf{Q}(t_i, x_j)$ serve as input to the simulation of the degradation model.

According to equation 3.35, 4.1 and 4.2, the generation rate of oxide charges $F_{ox,i,j} = F_{ox}[\mathbf{Q}(t_i, x_j), N_{ox}(t_i, x_j), \Gamma_0(t_i, x_j)]$ for each section j along the interface at time t_i of iteration step i is determined from $\mathbf{Q}(t_i, x_j)$. Similar to the discussion in section 4.1, the resolution function $\Delta_{N_{ox},i,j}$ gives the allowed maximum change in the concentration of oxide charges $N_{ox}(t_i, x_j)$ at time t_i and in section x_j at the interface. As discussed

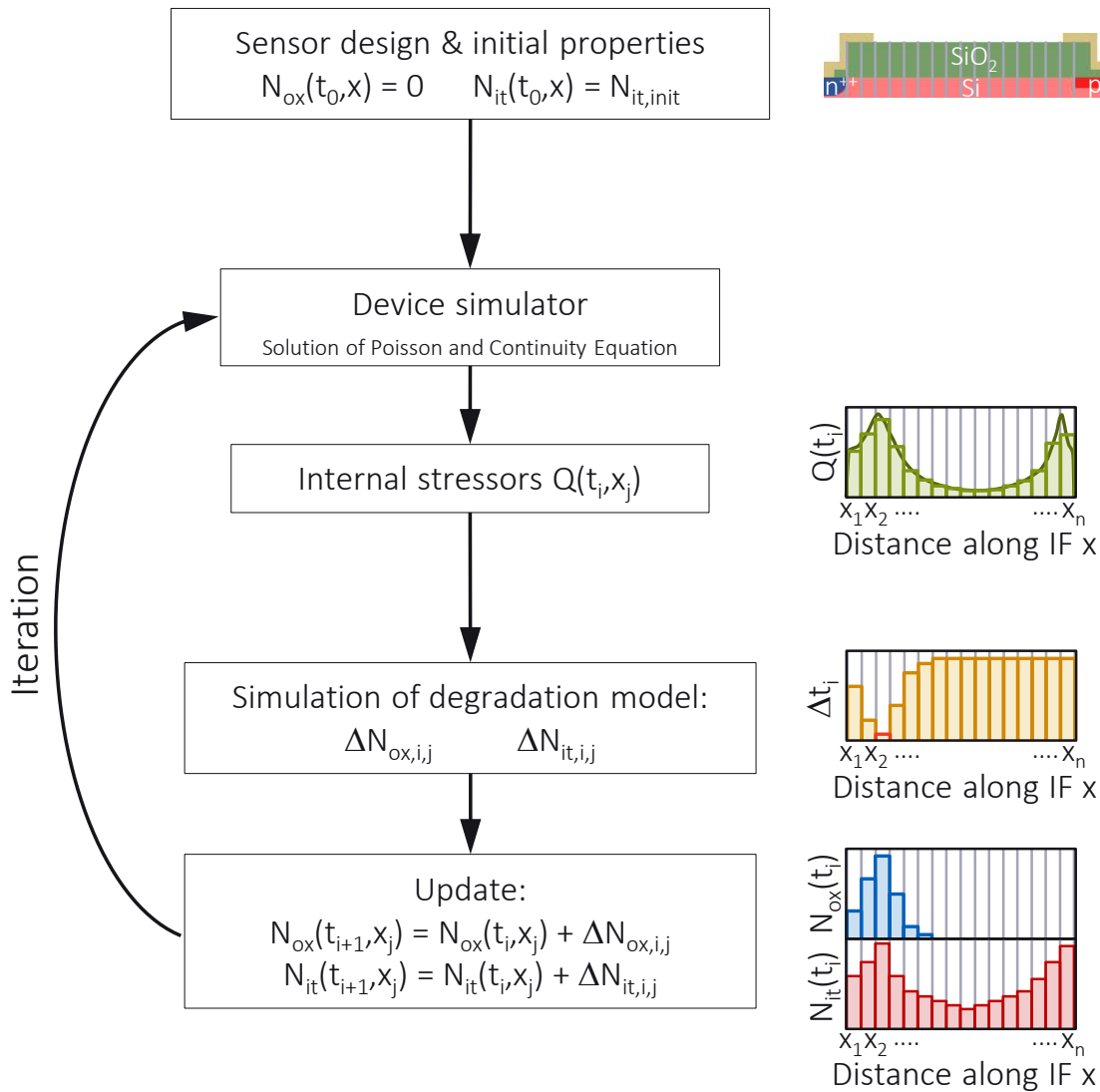


Figure 4.5: Illustration of the numerical iteration procedure that is developed for the self-consistent simulation of APD degradation.

in paragraph 4.1.2, the permitted time step $\Delta t_{i,j}$ at time t_i and location x_j follows according to equation 4.3. In the figure it is illustrated by the yellow bars. Of course, the same time step must be taken in all sections. As $\Delta N_{ox,i,j}$ must not be exceeded per section, the minimum of all sections $\Delta t_i = \min(\Delta t_{i,j})$ is taken forward in time and $\Delta N_{ox,i,j} = F_{ox,i,j} \cdot \Delta t_i$ gives the change per section j for iteration step i . During initial investigations of the presented solution approach, it was found that the time steps in the solution of the equation of the interface traps are very small and thus the solution requires many iterations and thus a lot of computation time. However, it was also found that the influence of the oxide charges on the internal stressors is much larger than that of the interface traps. This will be discussed in more detail in the end of this chapter. The discrete time windows $[t_i, t_i + \Delta t_i[$ are therefore determined by

the generation of oxide charges as described. Within these windows, the generation of interface traps is determined as discussed in section 4.2 under the action of $Q(t_i)$. By doing so, for interface generation the feedback for the duration of Δt_i is disregarded. From this, the change of the interface trap concentration $\Delta N_{it,i,j}$ follows.

According to equations 4.4 and 4.5, the concentration of oxide charges is updated $N_{ox}(t_{i+1}, x_j) = N_{ox}(t_i, x_j) + \Delta N_{ox,i,j}$. Subsequently, the amount of occupied shallow oxide traps is determined according to paragraph 4.1.3. This yields the portion of occupied shallow trap levels $\Gamma_0(t_{i+1}, x_j)$. In same way the concentration of interface traps is updated $N_{it}(t_{i+1}, x_j) = N_{it}(t_i, x_j) + \Delta N_{it,i,j}$. These are then given as input into the device simulator in order to determine the internal stressors for the next time step.

Iteration over the described procedure provides the self-consistent solution of the APD degradation model. Next, the empirical resolution functions $\Delta_{N_{ox,i,j}}$ and $\Delta_{N_{it,i,j}}$ are defined.

4.3.2 Resolution functions

In this paragraph, the resolution functions for oxide charge and interface trap generation will be given by means of pseudo code.

Oxide charge resolution function

Positive oxide charges $N_{ox,init}$ are present in the oxide of the sensor after production due to technology. Although these are assumed to be uncorrelated to the degradation, they still enter the resolution function $\Delta_{N_{ox}}(N_{ox}(t_i, x_j), N_{ox,max}, N_{ox,init}, N_{ox,sat})$. Also the saturation concentration $N_{ox,sat}$ under detrapping enters (equation 4.10). The pseudo code is:

Pseudo Code 4.3.2.1

- (i) $\Delta N_{ox} = 2 N_{ox}$
- (ii) $\Delta_{min} N_{ox} = 0.5 N_{ox,sat}$
- (iii) if $(N_{ox,init} < 0.5 N_{ox,sat}) \& (N_{ox} = 0)$:
 if $(\Delta N_{ox} < N_{ox,init})$: $\Delta N_{ox} = N_{ox,init}$
 elseif $(\Delta N_{ox} < \Delta_{min} N_{ox})$: $\Delta N_{ox} = \Delta_{min} N_{ox}$
- (iv) if $(\Delta N_{ox} > 0.9 [N_{ox,sat} - N_{ox}])$: $\Delta N_{ox} = 0.9 [N_{ox,sat} - N_{ox}]$
- (v) if $(\Delta N_{ox} < 0.025 N_{ox,max})$: $\Delta N_{ox} = 0$
- (vi) if $(N_{ox} \geq 0.97 N_{ox,sat})$: $\Delta N_{ox} = 0$

The basic rule of change is pseudo code 4.3.2.1 (i). Thus, the current oxide charge concentration is doubled. This is especially important for the start of the simulation to avoid too small steps in $N_{ox}(t_i, x_j)$, which unnecessarily lengthen the calculation. Small concentration does not have a large impact. Therefore, a minimum change is defined in pseudo code 4.3.2.1 (ii). It corresponds to 50 % of the saturation concentration $N_{ox,sat}$. If the simulation is still at the beginning ($N_{ox}(t_i, x_j) = 0$) and the concentration of initial positive oxide charges $\Delta N_{ox,init}$ is smaller than the minimum change $\Delta_{min} N_{ox,i,j}$, $\Delta N_{ox,i,j}$ must be determined according to a different rule. That is pseudo code 4.3.2.1 (iii). If $\Delta N_{ox,i,j}$ is smaller than $\Delta N_{ox,init}$, it is set equal to it. If $\Delta N_{ox,i,j}$ is smaller than the minimum change $\Delta_{min} N_{ox,i,j}$, it is set equal to it. This seems like a lot because in this case all positive charges would be compensated and/or already 50 % of the saturation concentration would be reached. However, it must be noted that the time step Δt ends up being the minimum of all columns. Thus, only the section with the maximum degradation rate, i.e. the one exposed to the maximum stress, would take this initial step. It was found that everything that happens before that does not have a big influence on the degradation itself but only costs computing time. On the one hand, if the simulation is no longer at the beginning ($N_{ox}(t_i, x_j) > 0$), it must be ensured that no steps are taken that are so large that $N_{ox,sat}$ is exceeded. This is checked by pseudo code 4.3.2.1 (iv). If this is the case, the step size $\Delta N_{ox,i,j}$ is set to 90 % of the difference of the current value and the saturation concentration. As mentioned, small step sizes decelerate the simulation. Therefore, on the other hand, it is checked if the step size is smaller than 2.5 % from the maximum value $N_{ox,max}$. In that case it is set equal to zero (pseudo code 4.3.2.1 (v)). This procedure is important in areas where the detrapping influence slowly fades due to relaxation. There, very small step sizes were observed, which unnecessarily delay the simulation. Illustratively, in this case, we wait until a single large step $> 2.5\%$ of $N_{ox,max}$ is taken instead of many small ones. A similar case occurs when the oxide charge concentration approaches its saturation value. Therefore, the step size is also set to zero when 97 % of the saturation concentration is already reached (pseudo code 4.3.2.1 (vi)). The presented determination rule for ΔN_{ox} is only the basis. In a lot of cases it was needed to be adjusted in order to meet the requirement of keeping the computing time as low and the accuracy of the results as high as possible.

Interface trap resolution function

The empirical resolution function for the generation of interface traps is defined by its pseudo code as:

Pseudo Code 4.3.2.2

- (i) $\Delta N_{it} = N_{it}$
- (ii) if $(\Delta N_{it} > 0.5 [N_{it,max} - N_{it}])$: $\Delta N_{it} = 0.5 [N_{it,max} - N_{it}]$
- (iii) if $(\Delta N_{it} \geq 0.97 N_{it,max})$: $\Delta N_{it} = 0$

Here the initial value $N_{it,init}$ corresponds to the concentration of dangling bonds after passivation with hydrogen. In paragraph 2.3.2 it was mentioned that $N_{it,init} = 10^{10} \text{ cm}^{-2}$. The basic rule for the step size of the resolution function for the generation of interface traps is pseudo code 4.3.2.2 (i). Thus, unlike before, this is chosen to be the current concentration $N_{it}(t_i, x_j)$. As before, it must be ensured that by some step size, the saturation concentration $N_{it,max}$ is not exceeded (pseudo code 4.3.2.2 (ii)). Moreover, small steps are to be avoided if the concentration N_{it} strives towards its saturation value (pseudo code 4.3.2.2 (iii)), in order to prevent unnecessary small steps that would lengthen the computation time.

4.3.3 Resulting oxide charge and interface trap densities

The coupled simulation approach developed previously is now applied to the degradation model developed in chapter 3 in order to determine the oxide charge and interface trap distributions and their temporal fluctuations inside the APD. The external stressors correspond to a temperature of $T = 145^\circ\text{C}$, an operating voltage of $U = 380 \text{ V}$, and an intensity of the incident light of $P_{opt} = 20 \text{ mW/cm}^2$. Model parameters are listed in table 4.1. Figure 4.6 shows a cross-section of the localization of the degradation in the sensor. The active area is on the left of the n^{++} layer. For more details on that it is referred to section 2.1. The degradation is supposed to occur at the interface below the field plate and extends there into the gap between the p and n contact metals. The spatial distributions of the internal stressors $\mathbf{Q}(x,t) = \{E_{si}(x,t), j_e(x,t), \theta_E(x,t), E_{ox}(x,t)\}$ at the interface are plotted as a function of distance x from the center of the device. The simulated sensor has an active area with a diameter of 1 mm and circular symmetry. The time under stress t_{stress} is assigned by color. The initial state before degradation $t = 0$ corresponds to the black line in each case. Starting at the end of the n contact doping at $x = 589 \mu\text{m}$, the electric field on the silicon side of the interface $E_{si}(x,t)$ increases strongly in the initial state of the device ($t = 0$), reaches its maximum below the end of the field plate at $x = 595 \mu\text{m}$ and then decreases with increasing distance x to about $x = 610 \mu\text{m}$, increases slightly and passes through a local maximum just at the overlap of the p side contact over the oxide. With time, no serious change is detected at $x > 600 \mu\text{m}$. Significant is the time variation below and in the vicinity of

Table 4.1: Applied model parameters.

Parameter	Value	Unit	Reference
Injection model			
χ_0	1.7×10^7		
Generation of oxide charges Trapping of injected electrons			
σ_{ox}	10^{-15}	cm^2	
Detrapping of captured electrons			
α_0	$280 \sigma_{ox}$	cm^2	
B	1.4×10^6	V/cm	
Relaxation of captured electrons			
γ_0	3×10^{-4}	s^{-1}	
Generation of interface traps Hydrogen dissociation			
$\sigma_{mp,0}$	10^{-13}	cm^2	
$p_{\sigma_{mp}}$	1		[205, 206]
$\sigma_{sp,0}$	10^{-13}	cm^2	
$p_{\sigma_{sp}}$	11		[205-207]
E_{SiH}	1.5	eV	[67, 167, 205, 207, 218-220]
E_{emi}	0.8	eV	[167]
$\gamma_{rupture}$	10^{12}	s^{-1}	[167]
ΔE	0.075	eV	[67, 167, 207]
ω'_0	10^{11}	s^{-1}	[67, 167, 207]
Diffusion and (re)passivation			
E_{pass}	0.8	eV	[167]
γ_{pass}	10^{12}	s^{-1}	[167]
$D_{H,0}$	8.1×10^{-3}	cm^2/s	[167, 231]
$D_{H_2,0}$	8.1×10^{-5}	cm^2/s	[167, 231]
E_H	0.2	eV	[167, 231]
E_{H_2}	0.2	eV	[167, 231]
x	0.5		

the field plate ($589 \mu\text{m} < x < 600 \mu\text{m}$). In the vicinity of the location of the initial peak at $x = 595 \mu\text{m}$, it increases with time and then decreases again. At $x = 590 \mu\text{m}$ it also increases sharply with time.

The electron current density $j_e(x,t)$ on the silicon side at the interface increases in the initial state ($t = 0$) starting at $x = 589.5 \mu\text{m}$ and passes through its peak just before the end of the field plate at about $x = 594 \mu\text{m}$. Thereafter, it decreases with increasing x toward the p side contact doping. It also exhibits the most significant variation with time in the region below the field plate ($589 \mu\text{m} < x < 600 \mu\text{m}$). With time, the peak at $x = 594 \mu\text{m}$ increases and becomes somewhat broader. Then, the peak decreases to below its initial shape and becomes narrower than it. Above $x = 595 \mu\text{m}$ $j_e(x,t)$

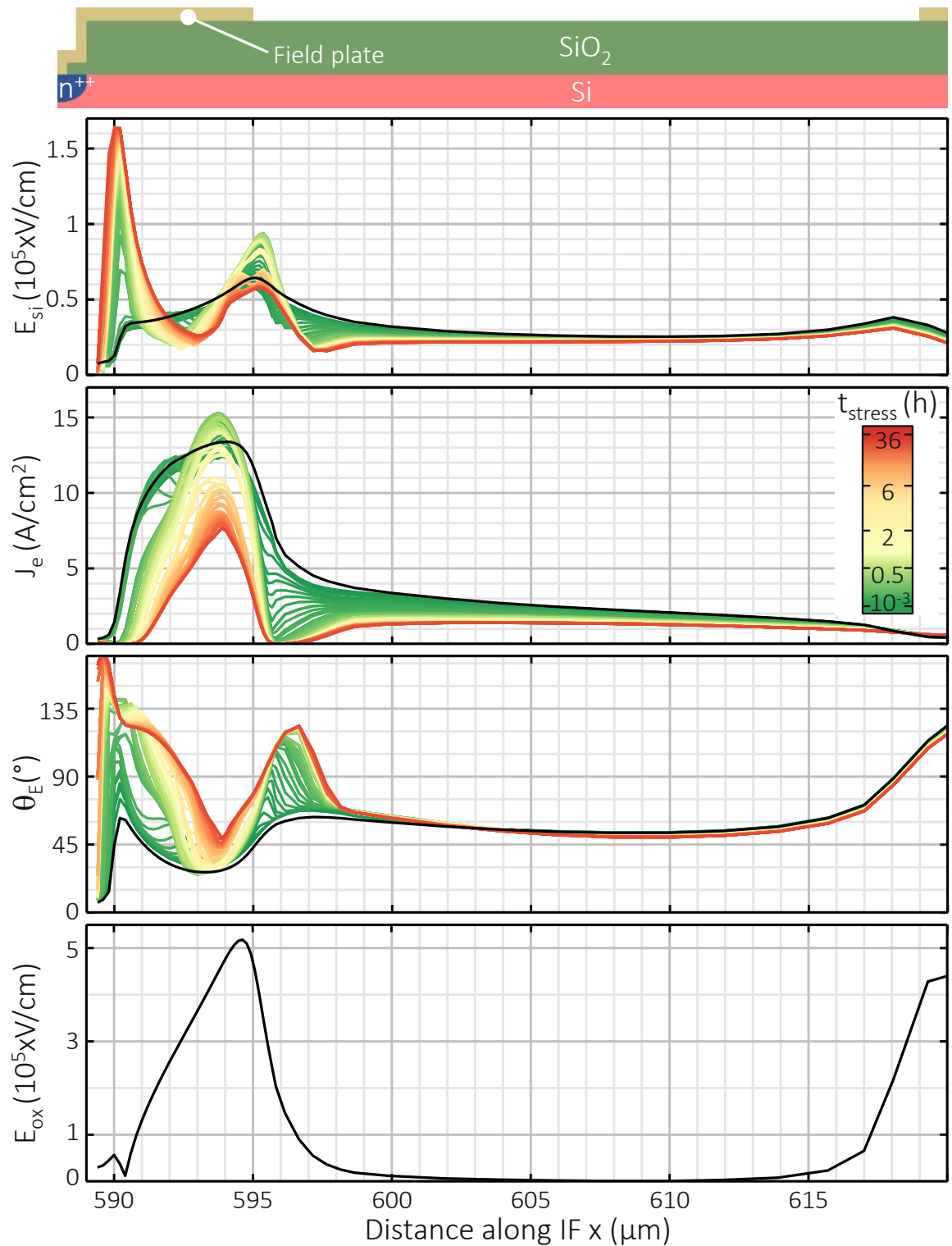


Figure 4.6: Sketch of the sensor edge cross section (above). Profile along the interface of the electric field in silicon E_{si} , the electron current density in silicon j_e , the angle θ_E between E_{si} and interface normal and the electric field in the oxide E_{ox} for a variation of time under stress t_{stress} .

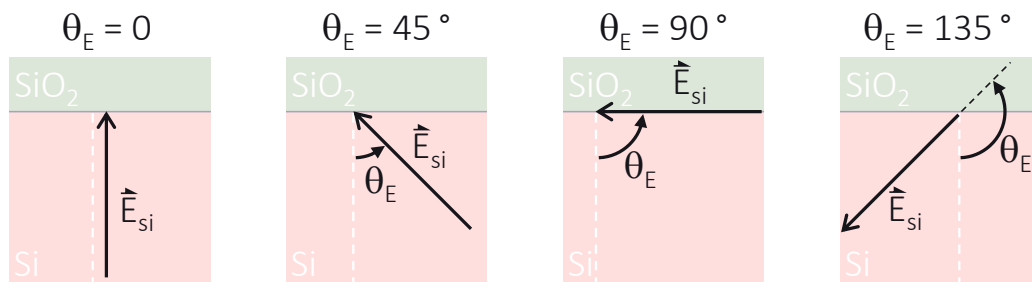


Figure 4.7: Orientations of the field E_{si} for different angles θ_E .

decreases steadily with time.

The angle $\theta_E(x,t)$ between interface normal and electric field $E_{si}(x,t)$ increases sharply in the initial state ($t = 0$), passes through a maximum of 60° at $x = 590.5 \mu\text{m}$, then decreases to 30° at approximately $x = 593 \mu\text{m}$, increases again, passes through a maximum of 60° again at approximately $x = 597 \mu\text{m}$ and then decreases until approximately $x = 610 \mu\text{m}$. At $x = 610 \mu\text{m}$ it increases again. As before, $\theta_E(x,t)$ varies most with time below $x = 600 \mu\text{m}$ and increases there. The maximum at $x = 590.5 \mu\text{m}$ increases to 165° and that at $x = 597 \mu\text{m}$ to 120° . For clarity, the orientations of the field E_{si} for different angles are shown in figure 4.7. It is responsible for the direction of the acceleration of the electrons. For $\theta_E(x,t) = 0$ it is perpendicular to the interface, so electrons are accelerated directly towards the interface. Likewise for $\theta_E(x,t) = 45^\circ$. But, not the hole magnitude of the field contributes in the latter case. When $\theta_E(x,t) = 90^\circ$ the field is parallel to the interface and electrons are accelerated in the direction parallel to the interface. For $\theta_E(x,t) > 90^\circ$ the field points away from the interface into the silicon and they are moved away from the interface. Thus, electrons are displaced from the IF in regions where $\theta_E > 90^\circ$. Therefore, the current density $j_e(x,t)$ decreases there.

The feedback of the trapped charges in the oxide to the field in the oxide E_{ox} depends on their distribution into the depth of the oxide. This is not considered by the derived model in chapter 3. The variation of E_{ox} with time is not considered. So, its profile is fixed to that of $t = 0$. Starting at $x = 589.5 \mu\text{m}$, this increases and passes through a maximum of more than $5 \times 10^5 \text{ V/cm}$ at $x = 594.5 \mu\text{m}$. After that it decreases to 0 at $x = 607 \mu\text{m}$ and then increases again.

Figure 4.8 shows the spatial distribution of the concentration of oxide charges $N_{ox}(x,t)$ and interface traps $N_{it}(x,t)$. As with figure 4.6, the cross section of the localization of degradation is shown here. The distance x is measured starting at the center of the active area and moving outward. The variation over time is assigned by color. In the early stage of degradation, the concentration of negative oxide charges $N_{ox}(x,t)$ increases in the vicinity of the end of the field plate at $x = 595 \mu\text{m}$. From there, it spreads out with

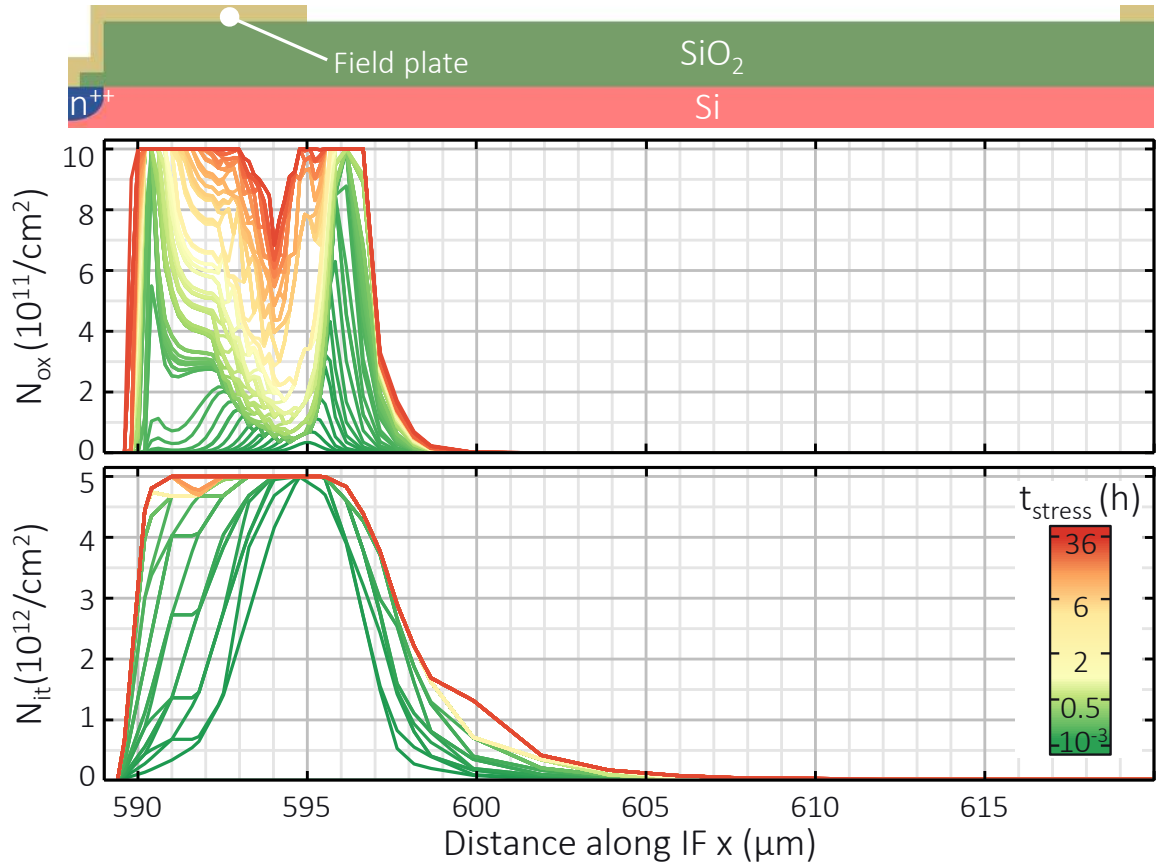


Figure 4.8: Profiles of generated concentration of negative oxide charges N_{ox} and interface traps N_{it} along the interface in the sensor after different times under stress t_{stress} .

time to higher and lower values of x with generation tending to stagnate at $x = 595 \mu\text{m}$. In this fashion two local maxima accumulate at around $590.5 \mu\text{m}$ and $596 \mu\text{m}$. In between, and especially at $592 \mu\text{m} < x < 595.5 \mu\text{m}$, the generation proceeds much more slowly. So that $N_{ox,max}$ is reached later there. Above $x = 597 \mu\text{m}$, $N_{ox}(x,t) < 10^{11} \mu\text{m}^{-2}$ for the simulated stress time of 72 h and even $N_{ox}(x > 600 \mu\text{m}, t) = 0$.

The concentration of interface traps $N_{it}(x,t)$ first increases sharply in the vicinity of the ending of the field plate at $x = 595 \mu\text{m}$. Already within the first 30 min $N_{it}(x,t)$ increases at $589.5 \mu\text{m} < x < 596 \mu\text{m}$ to more than 80% of the maximum concentration $N_{it,max}$. Even for high stress times of $t > 3$ d, the concentration profile remains negligible at $x > 610 \mu\text{m}$. By $t = 1$ d, $N_{it}(x,t)$ is saturated below the field plate and beyond at $x < 596 \mu\text{m}$. Compared to the generation of oxide charges, it can be seen that the saturation of $N_{it}(x,t)$ occurs more than three times faster in the region of $589.5 \mu\text{m} < x < 596 \mu\text{m}$. Thus, the generation of oxide charges occurs significantly slower than that of interface traps.

Comparison with figure 4.6 reveals the effect of the feedback of oxide charges and interface traps on the internal stressors. An increase in oxide charges causes a change in

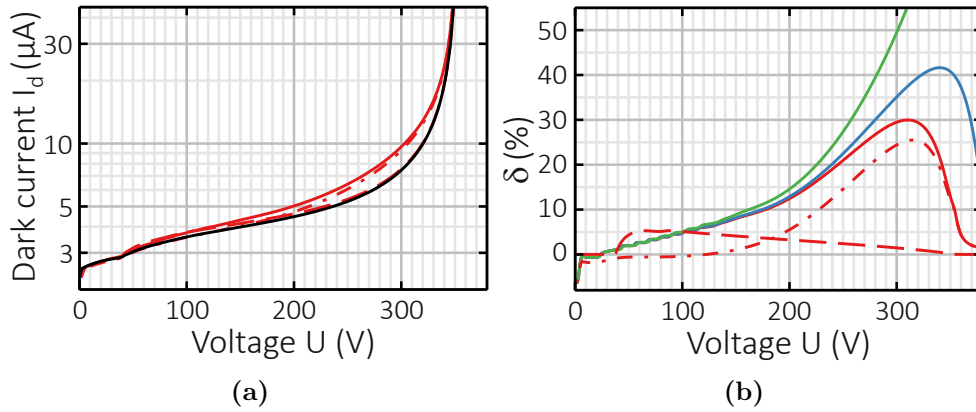


Figure 4.9: Simulation study on a: The effect of degradation phenomena on the I_d - U curve for $U_{br,RT} = 200 \text{ V}$. black: no degradation ($N_{ox} = 0, N_{it} = 0$). red and dashed: $N_{ox} = 0, N_{it} = 5 \times 10^{12} \text{ cm}^{-2}$. red and dot-dashed: $N_{ox} = 10^{12} \text{ cm}^{-2}, N_{it} = 0$. red and solid: $N_{ox} = 10^{12} \text{ cm}^{-2}, N_{it} = 5 \times 10^{12} \text{ cm}^{-2}$. b: The effect of degradation on the δ - U curve for $N_{ox} = 10^{12} \text{ cm}^{-2}$ and $N_{it} = 5 \times 10^{12} \text{ cm}^{-2}$. red: $U_{br,RT} = 200 \text{ V}$ (as in (a)). blue: $U_{br,RT} = 240 \text{ V}$. green: no avalanche implant ($U_{br,RT} \rightarrow \infty$).

the electric field E_{si} and its orientation θ_E . This leads to a redirection of electron flow in silicon, changing the current density j_e . It is increased by the increase in interface traps due to the promoted generation of dark current.

4.4 Degradation parameter

Both in simulation and later in experiment, the question arises how to measure the degradation. A quantity that can be easily simulated and measured is the voltage dependent dark current $I_d(U)$. This has already been presented in section 2.1 and figure 2.3. In the previous section it was presented that the degradation model from chapter 3 predicts the generation of oxide charges and interface traps predominantly below the field plate and in the vicinity of its ending. It is verified in the following from results of the device simulator that these phenomena of degradation are fundamentally reflected in the I_d - U characteristic of the APD. The concentration of the avalanche implant was chosen such that the breakdown voltage at room temperature is $U_{br,RT} = 200 \text{ V}$. Accordingly, at 125°C it is $U_{br,125} \approx 350 \text{ V}$. The concentration of oxide charges due to trapped electrons N_{ox} and the concentration of interface traps N_{it} were varied in the area below the field plate. In both cases their values were spatially constant. Figure 4.9a shows the resulting I_d - U curves for the case of no degradation ($N_{ox} = 0, N_{it} = 0$), exclusively interface traps ($N_{ox} = 0, N_{it} = 5 \times 10^{12} \text{ cm}^{-2}$), exclusively oxide charges ($N_{ox} = 10^{12} \text{ cm}^{-2}, N_{it} = 0$) and both ($N_{ox} = 10^{12} \text{ cm}^{-2}, N_{it} = 5 \times 10^{12} \text{ cm}^{-2}$). In the case of no degradation, the dark current I_d increases with voltage. At low voltages,

the increase is rather weak. From about 250 V the increase increases. From about 340 V I_d increases so fast that the curve is almost vertical. The curve for the case of exclusively interface traps is similar to the one without degradation. It is only slightly above it at voltages between 50 V and 200 V. The curve for the case of exclusively oxide charges is also very similar to that without degradation. However, it runs above it between about 170 V and 350 V. The difference is higher than before for the case of exclusively interface traps. The curve of both, interface traps and oxide charges, is also very similar to one without degradation. It runs above it between about 50 V and 350 V. Their difference gets even higher than in the aforementioned cases. In general, the effects of degradation can be seen only weakly in this plot. The I_d - U characteristic basically measures the overall state of the sensor. Degradation changes this compared to the initial unstressed state. However, for the investigation of the aging behavior, the difference between the initial and the degraded state is crucial. To be able to measure this, the relative deviation of the current from the initial state δ is defined as:

$$\delta(U,t) = \frac{I_d(U,t) - I_d(U,t=0)}{I_d(U,t=0)} \quad (4.12)$$

Thus, for each voltage, the difference between the current and the initial dark current is determined and normalized to the latter. Figure 4.9b shows the relative deviation for the data from figure 4.9a in an δ vs. U plot (red curves). In the case of exclusive generation of interface traps, the relative deviation is significant at $U > 40$ V and reaches a maximum value of 5% at about $U = 75$ V and then decreases with increasing voltage U . In the case of exclusive oxide charge generation, $\delta(U)$ increases with voltage, reaches its maximum at 25% at $U = 315$ V, and then decreases again. When oxide charges and interface traps are assumed, the $\delta(U)$ curve for $40 \text{ V} < U < 100 \text{ V}$ runs below that of exclusive generation of interface traps. Otherwise it runs above both curves. It increases with increasing voltage, reaches its maximum of 30% at $U = 315$ V and then decreases again. In general, its trend most resembles that of exclusive oxide charge concentration, but runs up to 8% above it. Thus, it can be concluded that the generation of oxide charges has a dominant influence on the δ - U characteristics. Except for the simulation results for the APD with $U_{br,RT} = 200$ V, the δ - U characteristics for $U_{br,RT} = 240$ V and $U_{br,RT} = \infty$ at maximum oxide charge and interface traps concentrations ($N_{it} = N_{it,max} = 5 \times 10^{12} \text{ cm}^{-2}$, $N_{ox} = N_{ox,max} = 10^{12} \text{ cm}^{-2}$) are shown only. For $U_{br,RT} = 240$ V, the δ - U curve follows that of $U_{br,RT} = 200$ V and increases with voltage to its maximum of 36% at $U = 340$ V and then decreases again. An APD with $U_{br,RT} = \infty$ corresponds to an APD in which the avalanche implant has a vanishing doping concentration. Thus, it is a simple PIN photo diode. In this case, the

δ - U curve increases with voltage reaching values of over 50 % in the considered voltage range of $0 \leq U < 380$ V. Obviously, the effects of degradation are much more visible in the δ - U characteristic than in the I_d - U characteristic. Moreover, at constant oxide charge and interface state concentration, i.e., the same state of degradation, these are more pronounced the higher the breakdown voltage U_{br} is. This increases with temperature as described in section 2.1 and decreases with increasing avalanche implant concentration. In conclusion, the relative deviation $\delta(U)$ is chosen as degradation parameter. Furthermore, in order to investigate the temporal degradation behavior an APD with a vanishing avalanche implant, i.e., a PIN diode, is first investigated at elevated temperature in the following. For the case of the PIN diode at voltages $U > 150$ V, compared to APDs δ is larger for the same values of N_{ox} , N_{it} and U and thus the degradation is best measurable.

4.5 Simulation of sensor degradation

In the previous section it was shown that the degradation is most clearly measurable on PIN diodes. In order to investigate the effect of degradation on the δ - U characteristic, the degradation of a PIN photo diode is simulated. The same stress and model parameters as in section 4.3 are used. Figure 4.10a shows the dark current voltage characteristic. The I_d - U curve of the sensor in the initial unstressed state corresponds to the black line. The dark current I_d increases saddle-shaped with voltage U . The curves in the stressed states are also shown. Each curve is assigned to a time t_{stress} by color. At high voltages $U > 130$ V the values of $I_d(U)$ increase with time. At voltages $U < 130$ V $I_d(U)$ slightly decreases with time. The behavior of the I_d - U curves with t_{stress} is similar to a rotation of them around the point $P = (130 \text{ V}, I_d(U = 130 \text{ V}, t = 0))$. With time the curves rotate away from the initial course. After $t_{stress} \approx 3.5$ h they rotate back towards the initial course. This backward motion saturates after $t_{stress} \approx 9$ h before the initial course is reached. In figure 4.10b the degradation parameter δ is plotted against the voltage U . The time under stress t_{stress} is assigned by color as before. After each t_{stress} , δ increases with voltage. For $U < 130$ V $\delta < 0$, above that $\delta > 0$. This is consistent with the observation in figure 4.10a that the stressed characteristics drift away from the initial characteristic at $U < 130$ V below and at $U > 130$ V with time. The values of δ at voltage $U > 130$ V increase with time. In particular, for voltages $U > 300$ V, this trend reverses after a certain time and the values of δ become smaller again with time and then saturate. With the simulation results in figure 4.10b, it could be shown that both the effect of generation of interface traps and oxide charges are more visible at high voltages. Finally, $\delta(U = 380 \text{ V})$ is plotted in figure 4.10c against

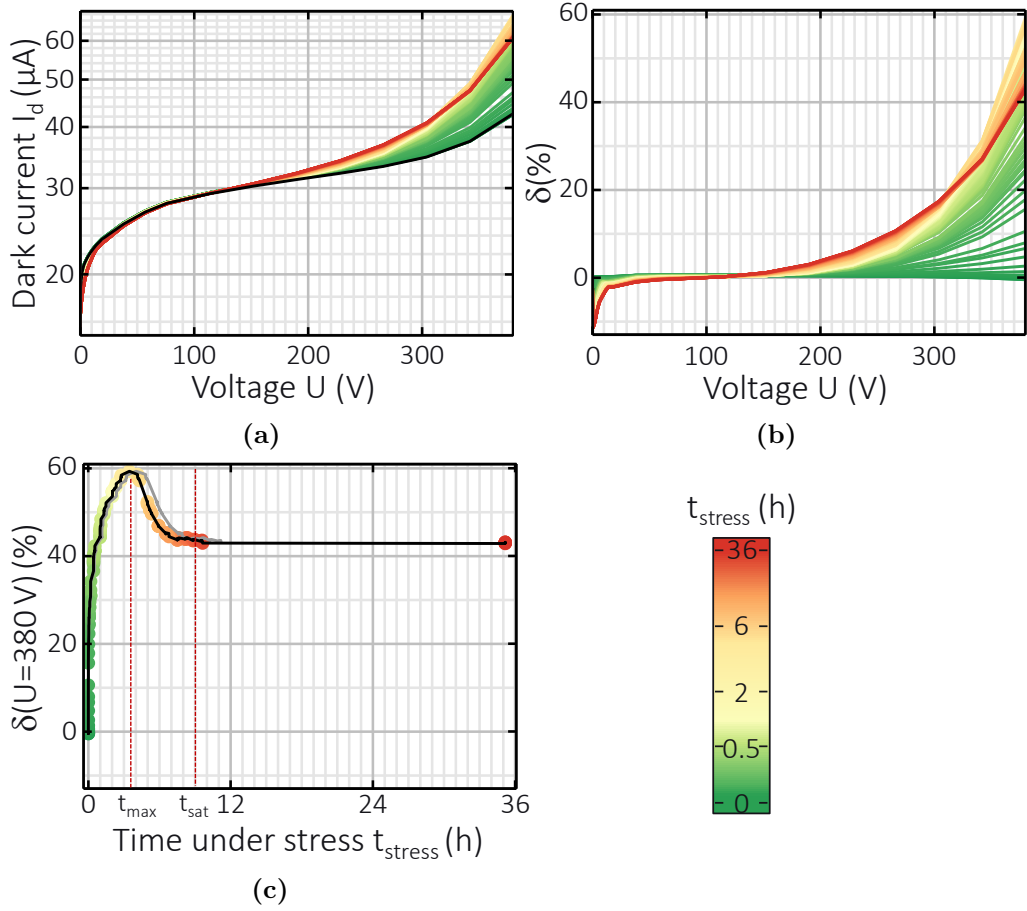


Figure 4.10: Results of the simulation of the degradation of a PIN photo diode. I_d - U (a) and δ - U (b) characteristics for a variation of stress time t_{stress} . c: Course of degradation in a plot of $\delta(U = 380 \text{ V})$ against t_{stress} . Points are assigned to curves in (a) and (b) by color and connected with the black curve. Also the case of no generation of interface traps is shown (gray).

t_{stress} . A value of $\delta(U = 380 \text{ V}, t_{\text{stress}}) = 0$ corresponds to the initial state of the sensor. With time $\delta(U = 380 \text{ V})$ increases, reaching its maximum of 60% at $t_{\text{stress}} \approx 3.5 \text{ h}$ and then decreases within another 6 h to the saturation value of about 43%. Comparing with figure 4.8, it is noticeable that the time of the maximum coincides with the moment when the oxide charge reaches the limit value of $N_{\text{ox}} = N_{\text{ox,max}}$ in the regions around $590.5 \mu\text{m}$ and $596 \mu\text{m}$. At the same time, the generation between these two regions starts. It is thus the moment when the N_{ox} profile is most inhomogeneous.

To understand the cause of this behavior, the cross section of the sensor in figure 4.11 shows the distribution of the electric field strength at different times. In the initial state ($t_0 = 0$), in the state of maximum ($t_{\text{max}} = 3.5 \text{ h}$) and in the saturated state ($t_{\text{sat}} = 35 \text{ h}$). Two areas are distinguished where the field strength is particularly high. Area 1 is located at the pn junction, where the n contact doping has its strongest curvature. Area 2 is located immediately below the end of the field plate below the interface.

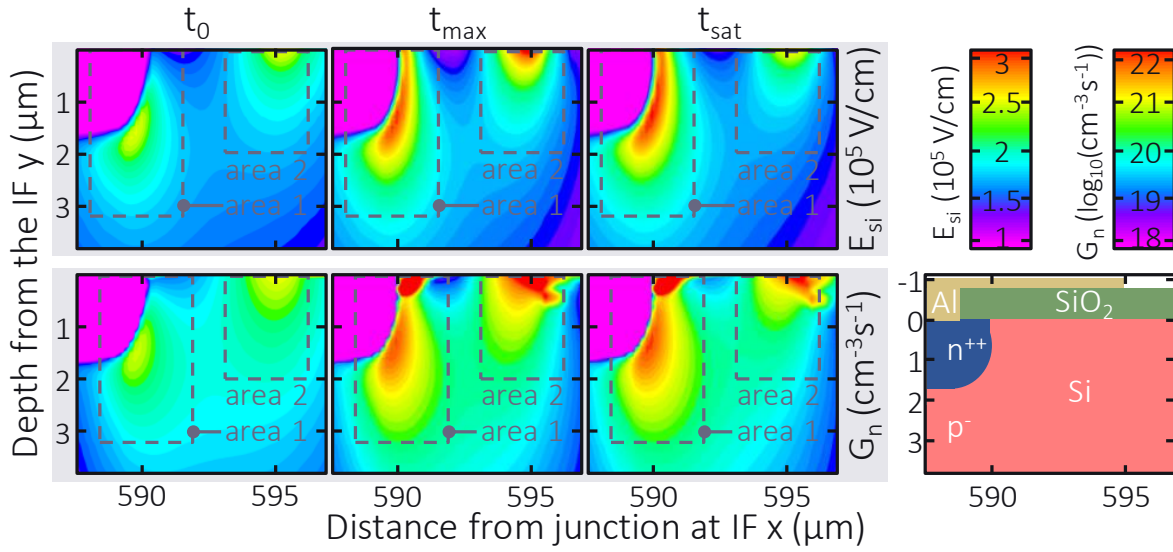


Figure 4.11: Cross section of the edge area of the simulated PIN photo diode. For clarity its structure with doping and material profiles is shown (lower right). The spatial distribution of the electric field strength $E = |\vec{E}|$ and the impact ionization rate extracted from simulation results are shown for the times t_0 , t_{max} and t_{sat} .

Comparing t_0 and t_{max} , it is noticeable that the field strength in both areas increases from about 2.5×10^5 V/cm at the maximum at t_0 to over 3×10^5 V/cm at t_{max} . The field increases, especially in both of the areas. At the transition of t_{max} to t_{sat} , in area 1 the region with a field above 3×10^5 V/cm expands somewhat. However, the field in area 2 decreases again and has again a maximum value of about 2.5×10^5 V/cm. As mentioned above, t_{max} coincides with the moment when the profile of oxide charges is most inhomogeneous such that the limit of $N_{ox,max}$ is already reached at around $590.5 \mu\text{m}$ and $596 \mu\text{m}$ but N_{ox} in between is rather low. Obviously, area 2 is well below the region of low N_{ox} . Also the field in this area obtains a maximum at t_{max} . Then the concentration of oxide charges increases between $590.5 \mu\text{m}$ and $596 \mu\text{m}$, δ is going down and also the field in area 2 decreases. The fact that an increase and decrease of the field strength lead to an increases and decreases of the current suggests, that impact ionization is the cause of up-down trend in figure 4.10. In order to verify that, the distribution of the impact ionization rate G_n is also shown in figure 4.11. At time t_0 , its maximum value in area 1 and 2 is about 10^{20} /cm²s. By time t_{max} , this increases and is above 3×10^{21} /cm²s in both areas. By time t_{sat} , the generation rate decreases again in area 2. Whereas in area 1 it stays constant. Thus, the reason for the increase of $\delta(U = 380 \text{ V}, t_{stress})$ with time is an increase in the impact ionization rate, which is primarily caused by the increase in negative oxide charges. The maximum in $\delta(U = 380 \text{ V}, t_{stress})$ is caused by a maximum inhomogeneity of the N_{ox} profile leading to a maximum in the impact ionization rate. So far, the temporal degradation

behavior is explained by means of the generation of negative oxide charges. In order to investigate the role of the generation of interface traps, the $\delta(U = 380 \text{ V})-t_{stress}$ curve for the case of exclusive generation of oxide charges is shown in figure 4.10c. It increases with time, reaching its maximum of 60 % at about $t_{stress} = 4 \text{ h}$ and decreasing to its saturation value of 43 % after a little more than 6 h. Obviously, it takes the same course as the curve assuming both, the generation of oxide charges and interface traps. The only difference is that it is around 14 % slower in time. Thus, the generation of interface traps seems to accelerate the degradation. As discussed in paragraph 2.3.2, an increase in interface traps increases the SRH generation and recombination rate. This allows more electron-hole pairs to be generated, leading to an increase in current density. As discussed in section 4.1, the generation rate of oxide charges increases with current density j_e . Which in turn accelerates the degradation.

4.6 Summary

The feedback between internal stressors and the generation of negative oxide charges and interface traps poses a problem. Due to its complexity, it cannot be represented analytically. However, a sophisticated numerical iteration approach was tailor-made and solved this coupled problem self-consistently. Its application provided new insights into the degradation kinetics of APDs.

Each of the processes of negative oxide charge and interface trap generation is expressed as time differential equation. A basic numerical iteration approach was developed that provides piecewise linear approximations for them. In detail, in the process of oxide charge generation a second temporal process, the relaxation of electrons from shallow into deep trap levels, is involved which runs in parallel and is coupled to it. Its incorporation was another hurdle, which was overcome via the elaboration of a refined extension that allows to embed the solution of this second process into the solution of the main process. No comparable approach is found in the literature, neither in the field of power devices nor in degradation modeling of APDs. Application of the basic approach already led to important insights into the kinetics of each generation process. It indicates the increase of their pace with increasing external stressors, i.e. temperature T , voltage U and intensity of incident light P_{opt} .

In order to involve the feedback between internal stressors and the generation processes in the solution of their differential equations, the basic approach was completed by a tandem procedure. In a coupled simulation, the device simulator determines internal stressors by solving the Poisson and continuity equations. These serve as input to the simulation of the degradation model. It determines the generated oxide charges and

interface traps within a defined time window and updates their concentrations. These are then passed to the device simulator to determine the resulting internal stressors. Iteration over this procedure led to a self-consistent numerical solution for the time course of degradation. As a novel result, time dependent profiles of negative oxide charges and interface traps inside the sensor were provided. Also their impact on the temporal change of the internal stressors were determined. The devices exclusively degrade inside their edge region starting below the field plate.

Furthermore, a degradation parameter δ was defined, which reflects the relative change of the degrading sensor with respect to its initial state. It is based on the dark current characteristic I_d-U , which is easy to measure and simulate. It was revealed, that the higher the breakdown voltage U_{br} , the more pronounced the effect of degradation phenomena on δ . The breakdown voltage increases with temperature (fig. 2.3) and decreases with increasing concentration of the avalanche implant.

The simulation of degradation effects provided additional new insights into the APD degradation behavior. The generation of negative oxide charges was identified to cause a drift of the impact ionization rate in the edge region of the sensor. The generation of interface traps promotes the accumulation of negative oxide charges by their supply of thermally generated dark current. In this way, degradation is about 14 % faster.

Chapter 5

Degradation under varied conditions: Calibration of the model

In order to provide insights into the aging of APDs in automotive LiDAR applications, the model developed in chapter 3 covers the intended crucial degradation mechanisms that promote the aging process. In chapter 4, a numerical iteration approach was tailor-made to enable the self-consistent simulation of the degradation model. Although, it already reflects the causal relations of APD degradation, the model cannot capture reality. For this purpose, it needs to be calibrated on real world data. Stress experiments under severe operation conditions are conducted to provide the necessary data. It was shown in chapter 4, that degradation is best measurable at PIN photo diodes.

First the design of experiment, i.e. stress conditions, stress routine and the design of PIN test structures, is introduced in section 5.1. Then stress experiments are performed on the sensors and the influence of operation conditions on their degradation is investigated (sec. 5.2). Thereafter, the degradation model will be applied in order to fit the experimental data (sec. 5.3). This provides new insights into the variation of the degradation behavior between individual sensors and the origin of oxide electron traps (sec. 5.4). In the end of this chapter the calibrated degradation model is achieved.

5.1 Design of experiment

It is presented in paragraph 5.1.1, how stress is applied to the sensors in order to meet the requirements mentioned in paragraph 2.3.1. Furthermore, a stress routine is introduced in paragraph 5.1.2 enabling the characterization of the tested sensors during the stress experiments. These concepts are adopted to all stress experiments

in this work. In the end, paragraph 5.1.3 illustrates the basic design of the sensors investigated in this chapter.

5.1.1 How to apply stress

In section 4.2 and 4.1, it was shown that the pace of negative oxide charge and interface trap generation increase with temperature T , operating voltage U , and illumination intensity P_{opt} . In order to accelerate aging as much as possible, these would have to be selected as high as possible. However, stress conditions must be avoided that cause failure mechanisms or a function of the APD that cannot occur in the APD mission profile in LiDAR operation (sec. 2.3.1).

Above $E_{ox} = 2 \times 10^6$ V/cm oxide trap generation via impact ionization and for $E_{ox} > 5 \times 10^6$ V/cm tunneling processes of electrons into the oxide occur. Both were excluded for normal operation in section 3.1. Moreover, an operation voltage of $U > 400$ V causes the sensor to physically break through due to a flashover from the n to the p contact. As a result, the APD will no longer function properly. A failure that is impossible within the LiDAR mission profile. It is extracted from device simulations, that the oxide field is smaller than 1×10^6 V/cm for an operation voltage of 380 V. This value differs also enough from 400 V to prevent flashovers and is therefore chosen as upper limit. At operation voltages above the breakdown voltage $U > U_{br}$, the conductivity of the APD approaches infinity. Accordingly, its resistance drops to almost zero. In this case, the series resistance R_S , i.e. the resistance of all cables, measuring devices, etc. connected before and after the sensor, is greater than its own resistance. As a result, any voltage applied to the test setup in addition to U_{br} no longer drops across the APD but across R_S . Therefore, above $U = U_{br}$, the signal is primarily generated by R_S and not by the APD. So, high operation voltages can only be realized for high breakdown voltages U_{br} , which increase with temperature (fig. 2.3) and decreasing concentration of the avalanche implant.

The temperature is only limited by experimental setup, i.e. the cables and the optical fiber used in the experiments. These can withstand only up to $T = 150^\circ\text{C}$. Therefore, 145°C was chosen as the maximum applied temperature.

When the intensity of the incident light is large, large amounts of charge carriers are generated which can lead to partial shielding of areas inside the device from the electric field induced by the external voltage U . This excess radiation must be prevented. Moreover, Si-H bonds at the interface can be broken by energetic radiation in the UV range or higher. Therefore, the wavelength must not deviate much from the LiDAR mission profile wavelength of 905nm. At the maximum illumination intensity during the stress experiment of 40 mW/cm^2 , no radiation excess was detected. This corresponds

to about a quarter of the maximum intensity of the entire solar spectrum on earth of 150 mW/cm^2 [233]. The LEDs used provide a peak at 940 nm.

5.1.2 How to measure degradation

The characterization during the stress experiment is possible only by alternating stress and characterization phases. In section 4.4 it was shown that all information about the degradation is contained in the degradation parameter $\delta(U)$. It is based on the dark current characteristic I_d-U . The corresponding routine of the stress experiment is as follows. At the beginning, the sensor is characterized by means of a dark current curve $I_d(U)$. In terms of the degradation parameter δ , this is the necessary reference for the time course of the degradation. Then the stress loop starts. The following steps are repeated until the end of the experiment. For a predefined time Δt_{stress} the sensor is stressed at constant voltage U , constant temperature T and constant illumination intensity P_{opt} . The stress strongly drives the sensor from thermal to an equilibrium characterized by high fields and high current densities. In order to perform meaningful characterizations, the sensor must physically relax to an equilibrium closer to the thermal one. Thus, after stressing, the sensor is given the time Δt_{relax} to relax into thermal equilibrium. After that, the characterization is done by measuring a dark current curve $I_d(U)$. With this procedure, the sensor is repeatedly subjected to the same stress for the time Δt_{stress} and then characterized. The result is a time history of dark current curves, as already shown as a result of the simulation of the degradation model in section 4.5. The elapsed time under stress t_{stress} is calculated from the number of iterations n and the duration of the stress periods according to: $t_{stress} = n \Delta t_{stress}$.

5.1.3 Basic device design and applied stress conditions

Figure 5.1 illustrates the basic design of the investigated PIN test sensors. The difference to the APD as presented in section 2.1, is that the avalanche implant is missing. The top view on the device (figure 5.1a) shows the circular active area. It has a diameter of 1 mm. All the sensors exhibit circular symmetry. Figure 5.1b shows the cross section along the straight line in figure 5.1a of the sensor edge region. The essential dimensions are shown. The field plate has a length of $6 \mu\text{m}$. The gap between the n and p contact metals has a length of $24 \mu\text{m}$. As discussed in sections 4.1 and 4.2, the oxide charge and interface trap generation models predict an increase in degradation pace with all external stressors U , T , and P_{opt} . In agreement with the maximum values defined in section 5.1.1, the stressors were varied as noted in table 5.1. In order to be able to make statistically significant statements, five devices are examined per stress

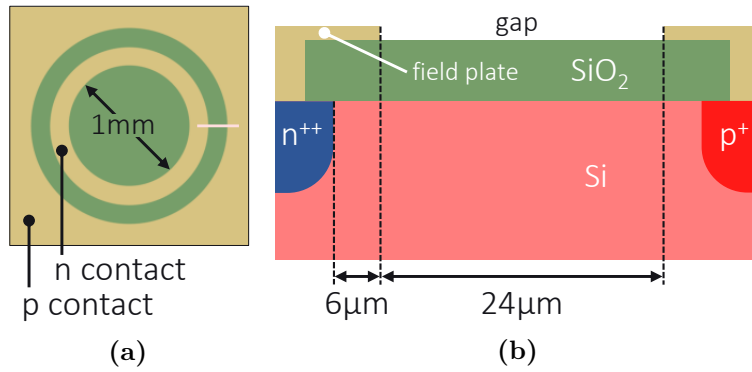


Figure 5.1: Illustration of the basic device design. a: Top view. b: Cross section of the edge area with material and doping profiles with dimension of the field plate and gap between n and p contact.

Table 5.1: Applied stress levels.

U in V	T in $^{\circ}\text{C}$	P_{opt} in mW/cm^2	level no
380	105	20	1
380	125	20	2
300	145	20	3
340	145	20	4
380	145	0	5
380	145	20	6
380	145	40	7

level. In section 4.4 it was shown by simulations that the signal of degradation effects in the dark current I_d and the degradation parameter δ increases with increasing operating voltage. In order to characterize the state of the sensors, a characteristic curve of the dark current up to a voltage of $U = 380 \text{ V}$ was regularly recorded after $\Delta t_{stress} = 30 \text{ min}$ of constant stress and subsequent relaxation of the sensor to thermal equilibrium (sec. 5.1.2).

5.2 Degradation behavior under varied conditions

Stress experiments were performed according to the previous section. In this section the general behavior of degrading sensors will be discussed. After that the impact of the applied stress conditions on their degradation is investigated.

5.2.1 General behavior of degrading devices

Figure 5.2a shows the dark current voltage curves of a sensor stressed at level 6. The total time under stress t_{stress} is assigned by color. The initial characteristic curve

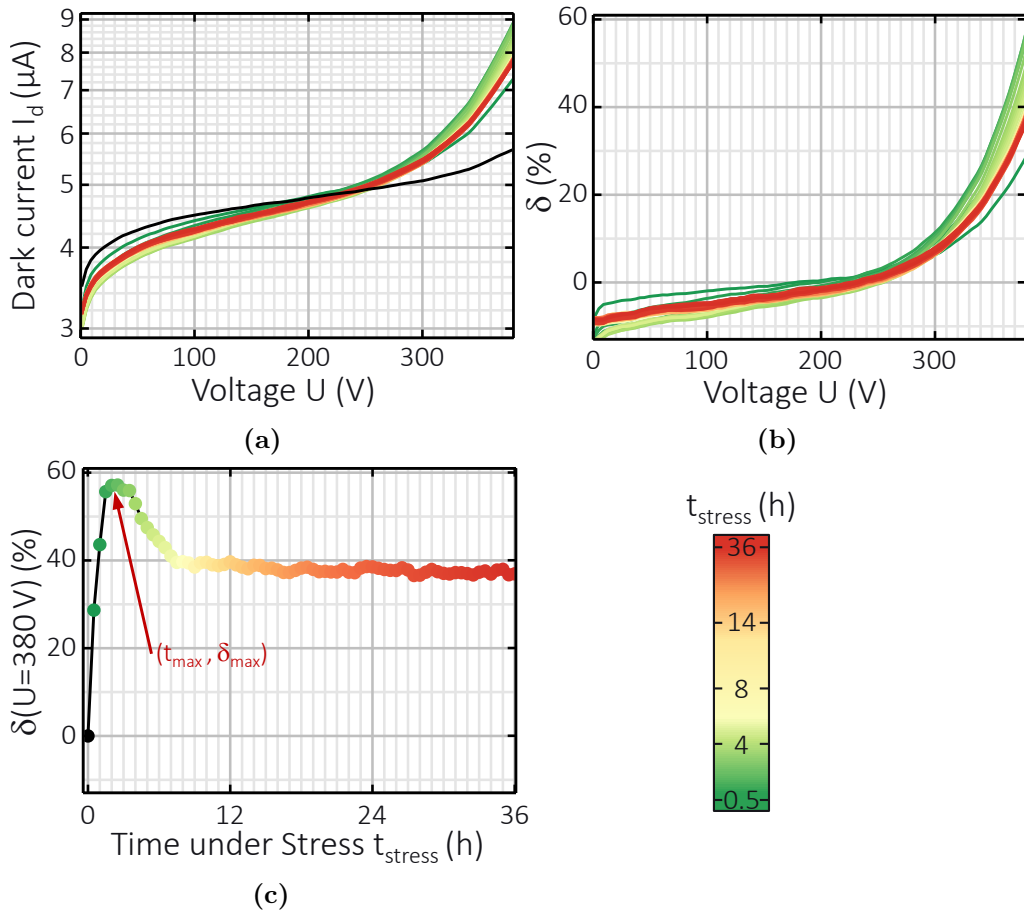


Figure 5.2: Results of the stress experiment under the conditions of level 6 on a PIN test sensor. I_d - U (a) and δ - U (b) characteristics for the variation of stress time t_{stress} . c: Course of degradation in a plot of $\delta(U = 380 \text{ V})$ vs. t_{stress} . Points are assigned to curves in (a) and (b) by color and connected with a black curve.

shows a saddle-shaped course. The dark current I_d increases strongly with voltage U at lower voltages, then somewhat weaker for $U > 40 \text{ V}$ and again more strongly at higher voltages $U > 300 \text{ V}$. Already after the first half hour the I_d - U curve differs quite strongly from its initial course. It seems to have rotated out of the initial orientation around a point around $U = 240 \text{ V}$ counterclockwise. This rotation progresses with time. So, the dark current values at low voltages $U < 240 \text{ V}$ decrease and at voltages $U > 240 \text{ V}$ they increase. After $t_{\text{stress}} \approx 2.5 \text{ h}$ it rotates back. The backward motion saturates before the initial curve is reached. This behavior can be seen more clearly when considering the δ - U curves shown in figure 5.2b. A value of $\delta(U_0) = 0$ means that at a voltage of U_0 the dark current is the same as in the beginning ($t = 0$). All $\delta(U)$ curves increase with voltage. At voltages $U > 240 \text{ V}$ their course resembles an exponential one. This exponential like trend at $U > 240 \text{ V}$ becomes steeper with time t_{stress} . With time the slope of the $\delta(U)$ with U increases. After about $t_{\text{stress}} = 2.5 \text{ h}$ the curve becomes flatter again and goes down with time. For $U < 240 \text{ V}$ the dark

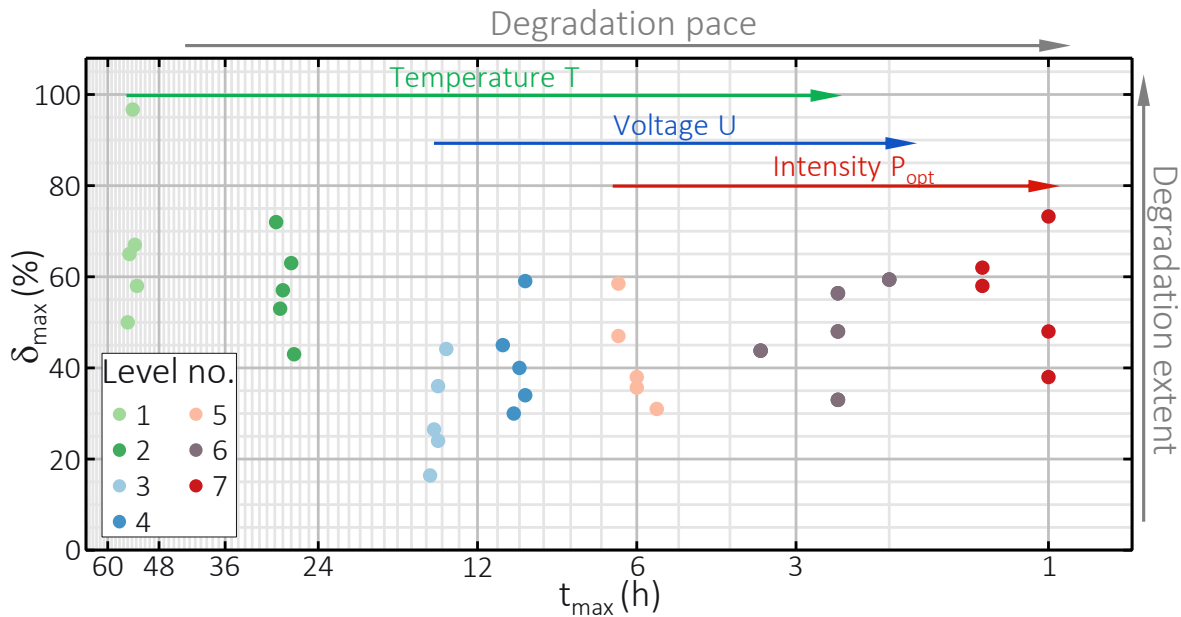


Figure 5.3: Results of all stress experiments on PIN photo sensors. The maximum reached degradation parameter δ_{max} is plotted against the time t_{max} when it occurs. Stress levels are assigned to their conditions in table 5.1 by color. Temperature variation: 1, 2, 6. Voltage variation: 3, 4, 6. Intensity variation: 5, 6, 7.

current decreases with time such that the decrease is higher for lower voltages. At $U \approx 240$ V $\delta = 0$ for all times. This behavior is similar to a rotation of the $\delta(U)$ curves around $(240$ V, 0) out of the zero position of $\delta(U) = 0$ for all regarded voltages U . At about $t_{stress} \approx 2.5$ h this motion inverts. The backward motion stops before the zero position is reached again. In section 4.4, the value of the degradation parameter δ at $U = 380$ V, was chosen as measure of the course of degradation. The same is done here. The resulting curve is shown in a plot of $\delta(U = 380$ V) against t_{stress} in figure 5.2c. It increases very sharply at early times, passes through a maximum of almost 60% at $t_{stress} = t_{max} = 2.5$ h and then decreases again. At $t_{stress} = t_{sat} \approx 7$ h it reaches a value of 40% and decreases only very weakly thereafter, so that at $t_{stress} = 36$ h it reaches a value of 35%.

The deviation of the curve from its initial course increases with time, is the highest at t_{max} , then decreases and saturates before the initial course is reached again. All sensors that were investigated at all of the stress levels in table 5.1 qualitatively showed the same degradation behavior as the one discussed. The only difference is, that their time scales and magnitude of δ varied.

5.2.2 Influence of stress conditions and temporal behavior of degradation

Previously, the degradation behavior of one sensor during the stress experiment was discussed as an example. All remaining sensors showed the same trend in all stress levels, although their respective time scale and the magnitude of δ varied. For the course of the degradation as shown in figure 5.2c, it is decisive on the one hand how fast it proceeds and on the other hand how strong the deviation from the initial state is. In order to represent the course of the degradation of all experiments as compressed as possible, the time t_{max} is chosen, at which the maximum deviation from the initial course, i.e. the maximum in $\delta(U = 380 \text{ V})$ is reached. Moreover, the value of the maximum $\delta_{max} = \max[\delta(U = 380 \text{ V})]$ itself is suitable to measure how strong the deviation from the initial state is after this time. Regarding the simulation results in section 4.5, it is clear that t_{max} is a characteristic value for the time course of the degradation, because the moment when the maximum occurs in $\delta(U = 380 \text{ V})$, the distribution of oxide charges N_{ox} is maximum inhomogeneous. As discussed in section 4.5, t_{max} is not only affected by the generation of oxide charges but also by generation of interface traps. As it impacts the speed of degradation. Thus, t_{max} contains information about the course of both failure mechanisms, oxide charge and interface trap generation. In figure 5.3 the experimental results for all levels and sensors in a plot of δ_{max} against t_{max} is shown. Here, the t_{max} axis is reciprocal and logarithmically scaled. Thus, the x axis reflects the degradation pace. The stress levels investigated, are assigned by color. At first glance, it can be seen that the data points of the different stress levels form separate clusters from each other. Furthermore, degradation pace increases with an increase of temperature, voltage and intensity of the incident light. For a better overview, the individual clusters are shown in figure 5.4, 5.5 and 5.6 according to the stressor variations.

In the temperature variation (figure 5.4), the sensors are exposed to an operation voltage of $U = 380 \text{ V}$, an illumination intensity of $P_{opt} = 20 \text{ mW/cm}^2$ and the temperature is varied. Stress level 1 has the lowest temperature with $T = 105^\circ\text{C}$. Thereby, the maximum for the five investigated sensors scatters between 50% and almost 100% deviation δ_{max} from the initial state. It occurs between almost 53 h and 55 h. At the next higher temperature of $T = 125^\circ\text{C}$ at level 2, δ_{max} varies between 43% and 73% deviation from the initial state after a stress time of approximately 27.25 h to slightly more than 29 h. The sensors are exposed to the highest temperature of $T = 145^\circ\text{C}$ at stress level 6. They reach the maximum deviation from the initial state after 2 h to 3.5 h. It varies between 33% and 60%.

In voltage variation (figure 5.5), the sensors are subjected to a temperature of $T =$

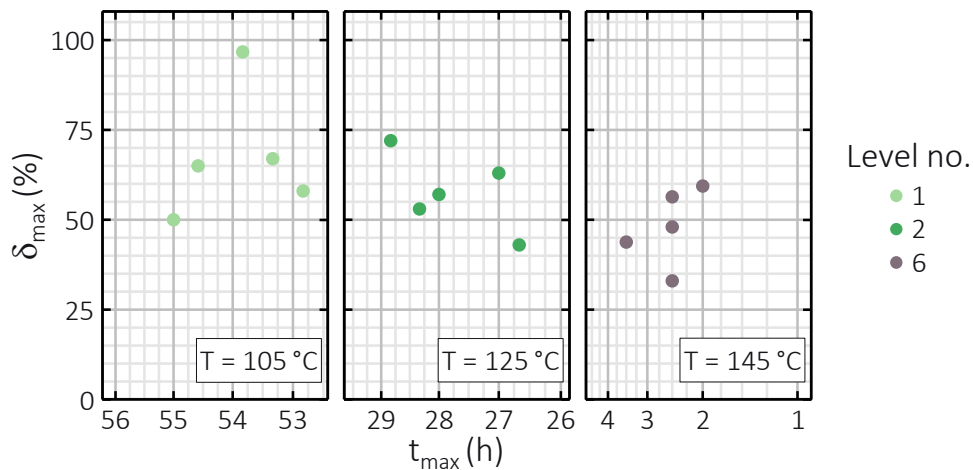


Figure 5.4: Data from figure 5.3 for the variation of temperature T .

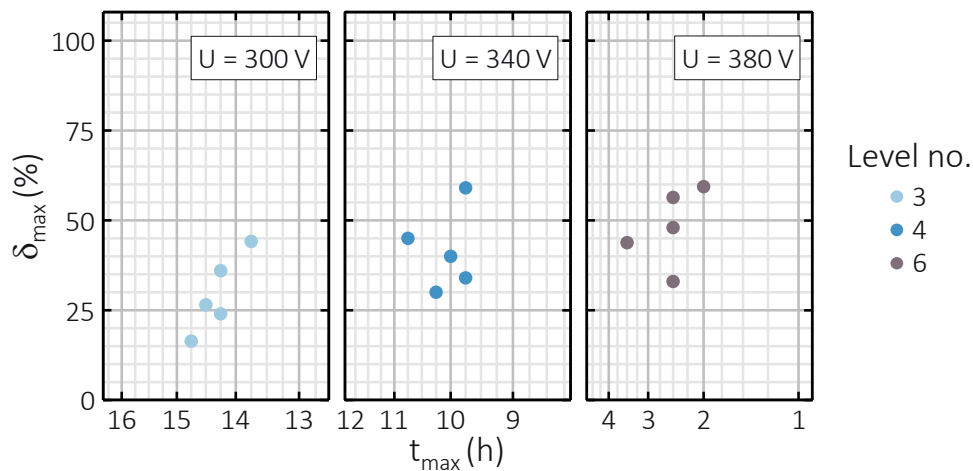


Figure 5.5: Data from figure 5.3 for the variation of voltage U .

145 °C, an illumination intensity of $P_{opt} = 20 \text{ mW/cm}$, and the operation voltage U is varied. Stress level 3 corresponds to the stress with the lowest voltage of $U = 300 \text{ V}$. Thereby, the maximum δ_{max} for the five studied sensors varies between 15 % and almost 45 %. It occurs between 13.75 h and 14.75 h. At level 4, the tested sensors are subjected to a stress of $U = 340 \text{ V}$. The maximum δ_{max} occurs after a stress time of about 9.75 h to 10.75 h with a value of 30 % to 60 %. The highest voltage of $U = 380 \text{ V}$ is applied at level 6, the investigated sensors reach a maximum deviation from the initial state δ_{max} of 33 % to 60 % after between 2 h and 3.5 h.

In variation of the illumination intensity (figure 5.6), the sensors are exposed to a temperature of $T = 145 \text{ °C}$, a voltage of $U = 380 \text{ V}$, and the illumination intensity P_{opt} is varied. Stress level 5 corresponds to the stress with the lowest illumination intensity of $P_{opt} = 0$. So, it corresponds to stress in the dark. Here, the maximum δ for the five sensors studied varies between 30 % and almost 60 % deviation from the initial

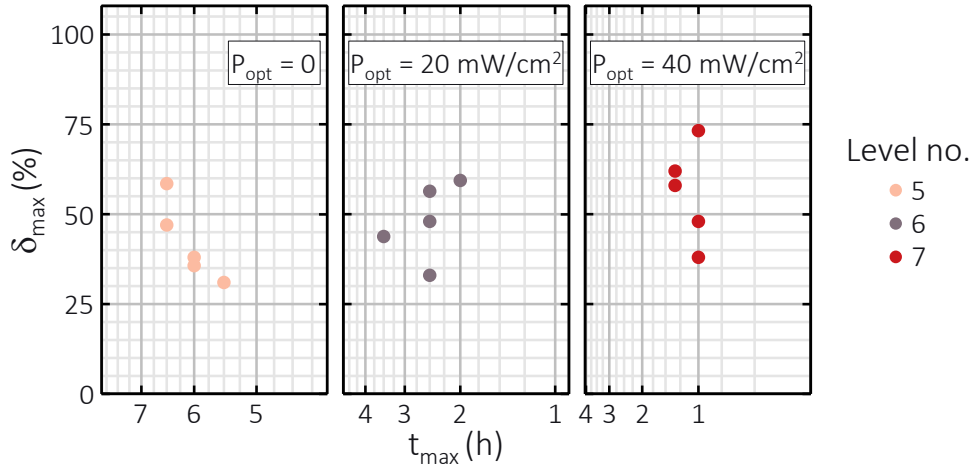


Figure 5.6: Data from figure 5.3 for the variation of intensity P_{opt} .

condition. It occurs between 5.5 h and 6.5 h under stress. At level 6, the investigated sensors are exposed to an illumination of $P_{\text{opt}} = 20 \text{ mW/cm}$. The maximum δ occurs after a stress time of 2 h to 3.5 h with a value of 33 % to 60 % deviation from the initial state. Under stress of the highest illumination intensity $P_{\text{opt}} = 40 \text{ mW/cm}^2$ at level 7, the investigated sensors reach a maximum deviation from the initial state of 38 % to almost 75 % after already 1 h to 1.5 h.

Each of the plots in figure 5.4, 5.5 and 5.6 covers 3.8 h on time scale. Thus, it is easy to see that for all stress levels, the maximum for all sensors occurs in a time window smaller than this 3.8 h. At levels 1 and 2, the range is slightly more than 2 h. The largest scatter in the deviation from the initial state occurs at level 1 with almost 50 %. It is also noticeable that per stressor variation, the time after the maximum deviation occurs decreases with the increase of the respective stressor. There is also a slight trend that the clusters of data points shifts towards smaller values of δ_{\max} with a temperature increase. With voltage variation, the cluster shifts slightly towards larger values of δ_{\max} with increasing voltage U . Thus, larger deviations δ_{\max} from the initial state are achieved on average with a decrease in temperature and an increase in voltage. In particular, on the time scale, the clusters of data points of each stress level are clearly separated. This demonstrates that each stress level corresponds to its own degradation pace. To examine this behavior in more detail, the mean of t_{\max} per stress level $\langle t_{\max} \rangle$ is plotted against the stress level in figure 5.7 for every stressor variation.

When varying the illumination intensity P_{opt} at constant voltage $U = 380 \text{ V}$ and temperature $T = 145^\circ\text{C}$, the maximum deviation from the initial state occurs for $P_{\text{opt}} = 0$ after 6 h, for $P_{\text{opt}} = 20 \text{ mW/cm}^2$ after 2.6 h, and for $P_{\text{opt}} = 40 \text{ mW/cm}^2$ after about 1 h and 10 min. Thus, with an increase in P_{opt} , the degradation pace $\propto \langle t_{\max} \rangle_{\text{level}}^{-1}$ increases slightly over proportionally. When varying the operation voltage U at constant

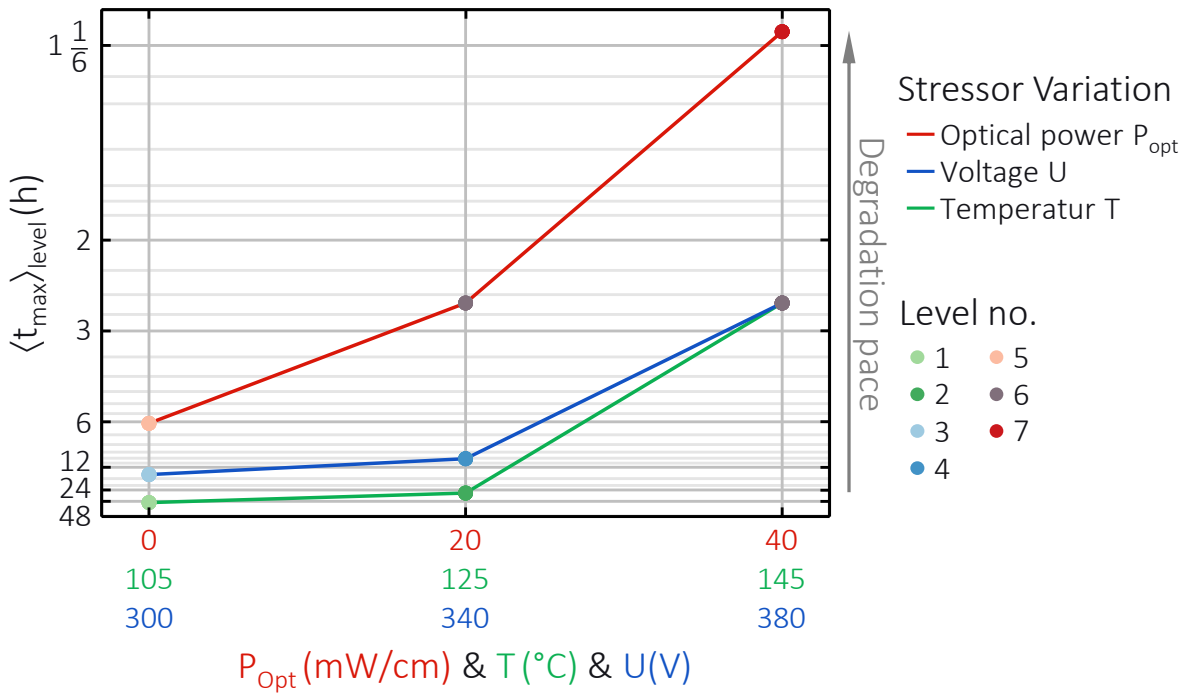


Figure 5.7: Variation of $\langle t_{max} \rangle$ with stress level for the variation of illumination intensity P_{opt} ($U = 380$ V, $T = 145$ °C), voltage U ($P_{opt} = 20$ mW/cm², $T = 145$ °C) and temperature T ($U = 380$ V, $P_{opt} = 20$ mW/cm²). The x -axis labels are assigned to the stressor variations by color.

illumination intensity $P_{opt} = 20$ mW/cm² and temperature $T = 145$ °C, the maximum deviation from the initial state occurs at $U = 300$ after about 14 h, at $U = 340$ V after 10 h, and at $U = 380$ V after 2.6 h. With an increase in the operation voltage U the degradation pace also increases over proportionally. When varying the temperature T at constant illumination intensity $P_{opt} = 20$ mW/cm² and voltage $U = 380$ V, the maximum deviation from the initial state occurs at $T = 105$ °C after about 48 h, at $T = 125$ °C after about 24 h, and at $T = 145$ °C after 2.6 h. With an increase in temperature T the degradation pace increases over proportionally. In conclusion, the degradation pace increases over proportionally with all stressors U , T , and P_{opt} .

Level 6 is shared by every stressor variation. From level 6, a decrease in temperature of about 14% (20 °C) to level 2 leads to almost a tenfold increase in time t_{max} . A decrease of the intensity by 100% (20 mW/cm²) to level 5 leads to a little more than a doubling of t_{max} . A decrease of the voltage by 10% (40 V) leads to a fourfold increase of t_{max} . Especially at high temperatures, the temperature appears to have the greatest influence on the degradation pace. This suggests that the dark current provides a significant contribution to the degradation. To further support this proposition, figure 5.7 can be compared with figure 4.3. There, the generation pace of oxide charges was plotted for the temperature variation. The solid curve corresponds to the case where

the increase of the dark current due to the temperature increase was included. The dashed curve reflects a temperature independent dark current. The curve from the stress experiments in figure 5.7 corresponds qualitatively to the first case. Thus, the dark current actually provides a very large contribution to sensor degradation.

5.2.3 Recap

Stress experiments on PIN test diodes have been conducted. Every device on every stress level obtains qualitatively the same degradation course. A maximum deviation from their initial state δ_{max} is observed. In comparison with simulation results in chapter 4 the moment when the maximum occurs is assigned to the appearance of the maximum inhomogeneous negative oxide charge profile. It is thus a characteristic moment in the course of degradation. Therefore, the values of the maximum δ_{max} and the time t_{max} after which it occurs are chosen in order to characterize the extent and time scale of the degradation course of every device. In a plot of δ_{max} against t_{max} , the data points form clusters on the time axis per stress level. Thus, the stress level governs the time scale of degradation. The degradation pace increases over proportionally with temperature, voltage and intensity of the incident light. Moreover, the data points of individual sensors scatter much in extent and slightly in time per stress level. Finally, it was concluded, that the dark current provides an outstanding contribution to the degradation of the devices.

5.3 Application of the degradation model

The comparison of the plots in figures 4.10 and 5.2 reveals that the degradation behavior resulting from simulation and those observed in the stress experiment are very similar. So, the experimental trend is fit by the simulation of the degradation model at least qualitatively. In the following simulation results are generated in order to fit the experimental results quantitatively. Doing so, the model parameters should be calibrated on the totality of all experimental data and varied in the smallest possible extent in favor of agreement between simulation and experiment.

5.3.1 Classification of model parameters

The varied parameters are shown in table 5.2. They can be differentiated according to what they are predominantly determined by. There are those that are predominantly determined by the technology. The technology includes all processes used in general

Table 5.2: Varied model parameters.

Symbol	Context	Main cause
Injection model		
χ_0	Determines the shape of the silicon band structure at the Si/SiO ₂ interface.	
Generation of oxide charges		
$N_{ox,init}$	Initial positive oxide charge concentration.	Process flow
$N_{ox,max}$	Concentration of preexisting electrons traps in the oxide. Corresponding to the maximum concentration of negative oxide charge in addition to $N_{ox,init}$.	Process flow
σ_{ox}	Oxide electron trap capture cross section.	Technology
α_0	Prefactor of detrapping rate of electrons in shallow oxide trap levels.	Technology
B	Critical field of detrapping rate of electrons in shallow oxide trap levels.	Technology.
γ_0	Relaxation rate of electrons from shallow into deep oxide trap levels.	operation conditions
Generation of interface traps		
σ_0	Prefactor of the cross section of electron Si-H interaction.	Technology
x	Contribution of H ₂ to hydrogen diffusion	Technology

for the production of the investigated sensors. The technology is the same for all investigated sensors. Therefore, the corresponding parameters should be also the same for all sensors. As described in section 3.2, the shape of the band structure of silicon at the Si:SiO₂ interface is modeled according to equation 3.4. Among other things, this depends, on the parameter x , which is determined by χ_0 according to equation 3.11. Therefore, the parameter χ_0 determines the modeled shape of the band structure of the silicon at the interface. It depends on the orientation of the silicon surface and the process flow of oxidation. In all the devices studied, the silicon at the interface has $\langle 111 \rangle$ orientation and the oxidation has the same process flow. Using $\chi_0 = 1.7 \times 10^7$ good agreement between simulated and experimental data was obtained. The authors in [190] were able to obtain good agreement with their data with $\chi_0 = 1 \times 10^8$. Both values are less than one order of magnitude apart and thus comparable.

Another parameter is the capture cross section of electron traps in the oxide σ_{ox} . With a value of $\sigma_{ox} = 10^{-15} \text{ cm}^2$ good agreement between simulated and experimental data could be achieved. This value corresponds to the cross section of the dominant trap.

The authors in [92] were able to assign a value between 10^{-16}cm^2 and 10^{-15}cm^2 to the shallow trap level of the oxygen vacancy. So, there is also good agreement with literature. As discussed in chapter 3.4.1, the amorphous growth of silicon dioxide leads to the appearance of stretched and distorted Si-O bonds. If the deviation from the ideal structure is too strong, oxygen vacancies occur. In the present case, the process of oxide growth is the same in the production of each sensor and thus leads to the same type of oxide trap and the same value of its cross section for all sensors.

In section 3.4.3, a detrapping model was introduced that describes the impact ionization of electrons from shallow electron trap levels in the oxide. This process is considered to be mostly determined by the properties of the dominant electron trap in the oxide. These in turn are assumed to be determined by the technology of oxidation. The detrapping rate is empirically described by the expression in equation 3.29 and 3.30. Good agreement of the degradation model with the experimental data could be achieved assuming the exponential prefactor of $\alpha_0 = 2.8 \times 10^{-13}\text{cm}^2$. In [201], good agreement could be obtained between the simulated data there and the experimental data from [91] using a value of $\alpha_0 = 8 \times 10^{-13}\text{cm}^2$. Using the same value, agreement with Monte Carlo simulations was obtained in [200]. For the critical oxide field B a value of $B = 1.4\text{MV/cm}$ was found in this work. In [113] detrapping of shallow electron traps in the oxide was experimentally detected at 1.2MV/cm . In [129], the threshold value of the oxide field E_{ox} for detrapping was determined to be of the order MV/cm . In [129] it was shown that all trapped electrons in the oxide are liberated at a field of 6MV/cm . Thus, the two parameters of the detrapping model α_0 and B found in this work are in good agreement with literature values.

For the cross section of the interaction of electrons with the Si-H bonds at the interface σ_0 (sec. 3.5.1), the experimental results could be met with a value of $\sigma_0 = 10^{-13}\text{cm}^2$. The authors in [205,206] were already able to show that this parameter is the same for the scattering of multiple electrons of low energy and single electrons of high energies. In [167,208] a value of $\sigma_0 = 10^{-14}\text{cm}^2$ was adopted to successfully fit experimental data. So the value found in this work differs by an order of magnitude from the literature value.

The parameter x corresponds to the fraction of molecular hydrogen (H_2) in the diffusion mechanism of hydrogen away from the interface as described in section 3.5.2. In this work, $x = 0.5$ turned out to be appropriate. According to this parameter, atomic and molecular hydrogen are equally involved. No literature values could be found for this parameter. In [71-73] models for hydrogen diffusion were also developed. Good agreement with the experimental data from the references of these works could be obtained only under the assumption that both molecular and atomic hydrogen are

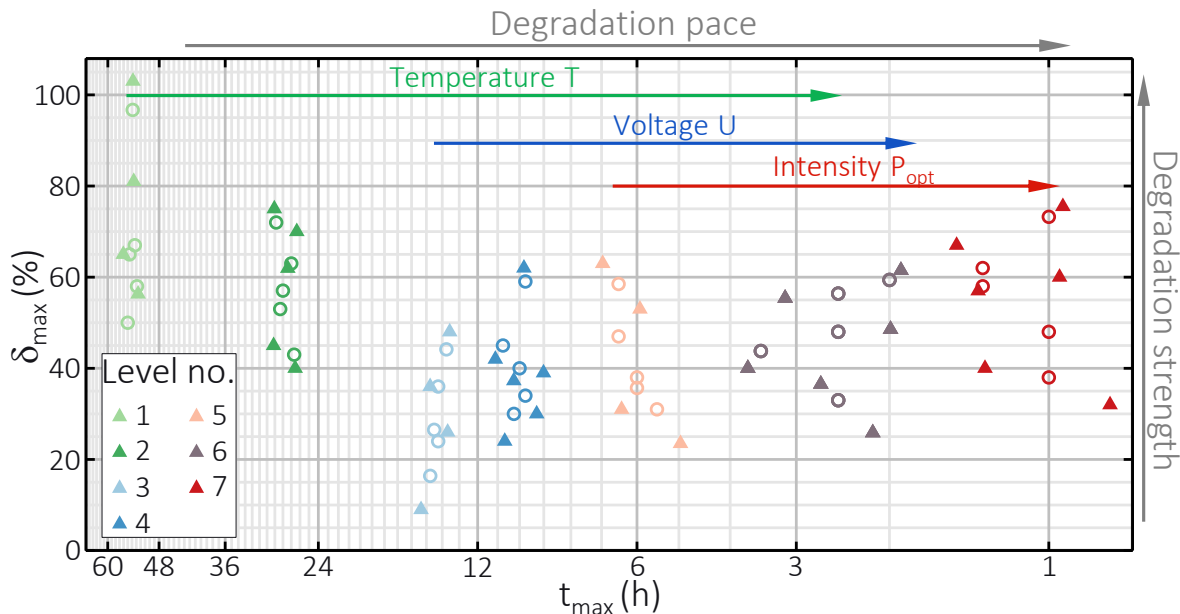


Figure 5.8: Results of experiment (empty circles) and simulation (triangles) of the degradation of PIN test sensors. The maximum deviation δ_{max} from the initial state of the sensors is plotted against the time t_{max} when it occurs. Stress levels are assigned to their conditions in table 5.1 by color.

involved in the diffusion process. So there is good qualitative agreement with the results in the literature.

As described in section 3.4.4, the relaxation rate γ_0 determines the amount of electrons in shallow trap levels in the oxide that relax per unit time into the deep levels. This physical mechanism is believed to vary in extent with both field and temperature.

It is further hypothesized that the parameters of the available electron traps in the oxide $N_{ox,max}$ and that of the initial positive oxide charges $N_{ox,init}$ vary due to process fluctuations across the wafer but also between batches and thus from device to device. The last three mentioned will be discussed in the following. All remaining model parameters correspond to their values in table 4.1.

5.3.2 Simulation vs. experimental data

The attempt to fit the model to experimental I_d-U curves as shown in figure 5.2a turns out to be unnecessarily complicated. Due to the complexity of the devices, even small deviations from the ideal process flow during their fabrication, which occur naturally in reality, can lead to significant deviations from the ideal dark current curve as it is determined in the semiconductor device simulation. In terms of the informative value of the model with respect to degradation, it is more important whether the extent of the degradation and its time scale in the simulation match those in the experiment.

As before, this is examined using the maximum deviation δ_{max} and the time t_{max} after which it occurs. Figure 5.8 shows the experimental data previously discussed in section 5.2.2 in a δ_{max} vs t_{max} plot. The resulting data points from the simulation are also shown. Model parameters are varied such that the experimental clusters are met by the simulated data points at each stress level. Doing so, the relaxation rate γ_0 is varied between stress levels depending on voltage and temperature. The parameters of $N_{ox,max}$ and $N_{ox,init}$ were varied to obtain the individual data points per stress level. It can be seen that the clusters of experimental data of each stress level coincide with the clusters formed by the simulated data points at each stress level. Furthermore, the simulated clusters surround the experimental ones for each stress level. As in the previous section, the data are shown separately in figures 5.9, 5.10, and 5.11 for the variation of temperature T , operation voltage U , and illumination intensity P_{opt} . The values for the relaxation rate γ_0 per stress level are noted in table 5.3. The data points

Table 5.3: Relaxation rate parameter γ_0 per Stresslevel.

Stress level no.	γ_0 in s^{-1}
1	8×10^{-6}
2	3×10^{-5}
3	1×10^{-5}
4	5×10^{-5}
5	3×10^{-4}
6	3×10^{-4}
7	3×10^{-4}

from the simulation are labeled for each stress level separately and assigned to a pair of values $N_{ox,max}$ and $N_{ox,init}$ as listed in table 5.4.

The simulation data of stress level 1 in figure 5.9, are close to the experimental data. To achieve this agreement, a relaxation rate of $\gamma_0 = 8 \times 10^{-6}$ was found and the concentration of initially present positive oxide charges $N_{ox,init}$ was varied between 10^{11} cm^{-2} and $1.5 \times 10^{11} \text{ cm}^{-2}$. The concentration of electron traps in the oxide $N_{ox,max}$ varies between $8 \times 10^{11} \text{ cm}^{-2}$ and $20 \times 10^{11} \text{ cm}^{-2}$. For simulated data points 3 and 4, $N_{ox,max} = 10 \times 10^{11} \text{ cm}^{-2}$ and only the values of $N_{ox,init}$ differ. For data point 3, it is $N_{ox,init} = 1 \times 10^{11} \text{ cm}^{-2}$. In the plot in figure 5.9, it is at $\delta_{max} = 65\%$ and $t_{max} \approx 56 \text{ h}$. For data point 4, $N_{ox,init} = 1.5 \times 10^{11} \text{ cm}^{-2}$. In the plot, it is at $\delta_{max} \approx 55\%$ and $t_{max} \approx 52.5 \text{ h}$. Thus, as $N_{ox,init}$ increases, the time t_{max} and δ_{max} decrease. Starting at data point 4 with $N_{ox,init} = 1.5 \times 10^{11} \text{ cm}^{-2}$ and $N_{ox,max} = 10 \times 10^{11} \text{ cm}^{-2}$, $N_{ox,max}$ increases with constant $N_{ox,init}$ at points 2 with $N_{ox,max} = 14 \times 10^{11} \text{ cm}^{-2}$ and 1 with $N_{ox,max} = 20 \times 10^{11} \text{ cm}^{-2}$ an. Data point 2 is at $\delta_{max} \approx 80\%$ and $t_{max} \approx 53.5 \text{ h}$, data point 1 is at $\delta_{max} \approx 103\%$ and $t_{max} \approx 53.75 \text{ h}$. So, δ_{max} and t_{max} increase with

Table 5.4: Parameter values of the initial positive oxide charge concentration $N_{ox,init}$ and the concentration of electron traps in the oxide $N_{ox,max}$ of simulated data points (triangles) in figures 5.9, 5.10, and 5.11.

Level no	data point no	$N_{ox,init}$ in 10^{11} cm^{-2}	$N_{ox,max}$ in 10^{11} cm^{-2}
1	1	1.5	20
1	2	1.5	14
1	3	1	10
1	4	1.5	10
1	5	1	8
2	1	1	14
2	2	1.5	12
2	3	1	10
2	4	0.1	8
2	5	1	8
3	1	1.8	12
3	2	1	10
3	3	1.5	10
3	4	0.8	6
4	1	1.8	16
4	2	0.1	10
4	3	1.8	12
4	4	1	10
4	5	1.5	10
4	6	0.5	8
5	1	1	14
5	2	1	10
5	3	0.5	8
5	4	1	6
6	1	1.5	12
6	2	1	10
6	3	1.5	10
6	4	0.1	8
6	5	1	8
6	6	1	6
7	1	1.5	15
7	2	1	12
7	3	1.5	12
7	4	1	10
7	5	0.5	8
7	6	1.5	9

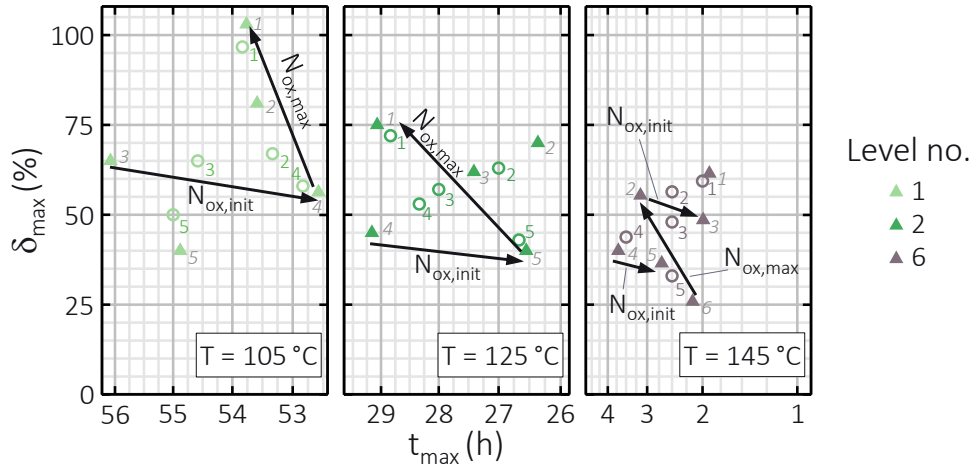


Figure 5.9: Data from figure 5.8 for the variation of temperature T . Italic numbers at triangles assign the particular data point to the parameters of $N_{\text{ox},\text{max}}$ and $N_{\text{ox},\text{init}}$ listed in table 5.4. Non-italic numbers at empty circles assign the particular data point to the parameters of $N_{\text{ox},\text{max}}$ and $N_{\text{ox},\text{init}}$ listed in table 5.5. Their values are obtained by the interpolation procedure (paragraph 5.4.1). Variations with the values of $N_{\text{ox},\text{max}}$ and $N_{\text{ox},\text{init}}$ are drawn.

$N_{\text{ox},\text{max}}$. Thereby, the increase in δ_{\max} and t_{\max} with $N_{\text{ox},\text{max}}$ is stronger than with their decrease with $N_{\text{ox},\text{init}}$.

The simulation data of stress level 2 in figure 5.9, are close to the experimental data. For this match, a relaxation rate of $\gamma_0 = 2 \times 10^{-5}$ was found and the concentration of initially present positive oxide charges $N_{\text{ox},\text{init}}$ varies between $0.1 \times 10^{11} \text{ cm}^{-2}$ and $1.5 \times 10^{11} \text{ cm}^{-2}$. The concentration of electron traps in the oxide $N_{\text{ox},\text{max}}$ varies between $8 \times 10^{11} \text{ cm}^{-2}$ and $14 \times 10^{11} \text{ cm}^{-2}$. For simulated data points 4 and 5, it is $N_{\text{ox},\text{max}} = 8 \times 10^{11} \text{ cm}^{-2}$ and the values of $N_{\text{ox},\text{init}}$ vary. At data point 4, $N_{\text{ox},\text{init}} = 0.1 \times 10^{11} \text{ cm}^{-2}$. In the plot in figure 5.9, it is at $\delta_{\max} \approx 45\%$ and $t_{\max} \approx 29.25 \text{ h}$. For data point 5, $N_{\text{ox},\text{init}} = 1 \times 10^{11} \text{ cm}^{-2}$. In the plot, it is at $\delta_{\max} \approx 40\%$ and $t_{\max} \approx 26.5 \text{ h}$. Thus, as $N_{\text{ox},\text{init}}$ increases, the time t_{\max} and δ_{\max} decrease. Starting at data point 5 with $N_{\text{ox},\text{init}} = 1 \times 10^{11} \text{ cm}^{-2}$ and $N_{\text{ox},\text{max}} = 8 \times 10^{11} \text{ cm}^{-2}$. $N_{\text{ox},\text{max}}$ increases with constant $N_{\text{ox},\text{init}}$ for points 3 with $N_{\text{ox},\text{max}} = 10 \times 10^{11} \text{ cm}^{-2}$ and 1 with $N_{\text{ox},\text{max}} = 14 \times 10^{11} \text{ cm}^{-2}$ an. Data point 3 is at $\delta_{\max} \approx 63\%$ and $t_{\max} \approx 27.3 \text{ h}$, data point 1 is at $\delta_{\max} \approx 75\%$ and $t_{\max} \approx 29.1 \text{ h}$. So δ_{\max} and t_{\max} increase with $N_{\text{ox},\text{max}}$ also in this case. Here again, the increase in δ_{\max} with $N_{\text{ox},\text{max}}$ is stronger than with their decrease with $N_{\text{ox},\text{init}}$.

The simulation data of stress level 3 in figure 5.10, are also close to the experimental data. For this, a relaxation rate of $\gamma_0 = 1 \times 10^{-5}$ was set and the concentration of initially present positive oxide charges $N_{\text{ox},\text{init}}$ varies between $0.8 \times 10^{11} \text{ cm}^{-2}$ and $1.8 \times 10^{11} \text{ cm}^{-2}$. The concentration of electron traps in the oxide $N_{\text{ox},\text{max}}$ varies between $6 \times 10^{11} \text{ cm}^{-2}$ and $12 \times 10^{11} \text{ cm}^{-2}$. For simulated data points 2 and 3, it is $N_{\text{ox},\text{max}} =$

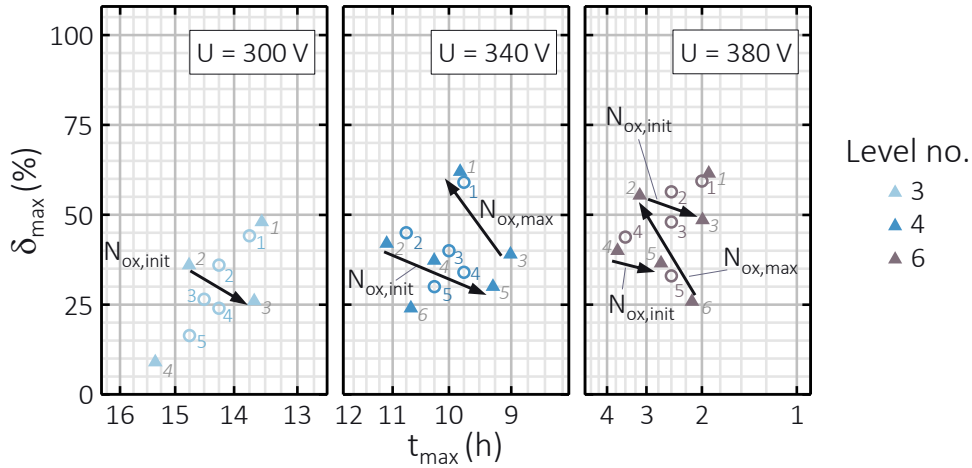


Figure 5.10: Data from figure 5.8 for the variation of voltage U . Italic numbers at triangles assign the particular data point to the parameters of $N_{ox,max}$ and $N_{ox,init}$ listed in table 5.4. Non-italic numbers at empty circles assign the particular data point to the parameters of $N_{ox,max}$ and $N_{ox,init}$ listed in table 5.5. Their values are obtained by the interpolation procedure (paragraph 5.4.1). Variations with the values of $N_{ox,max}$ and $N_{ox,init}$ are drawn.

$10 \times 10^{11}\text{ cm}^{-2}$ and the values of $N_{ox,init}$ vary. At data point 2, $N_{ox,init} = 1 \times 10^{11}\text{ cm}^{-2}$. In the plot in figure 5.10, it is at $\delta_{max} \approx 36\%$ and $t_{max} = 14.75\text{ h}$. At data point 3, $N_{ox,init} = 1.5 \times 10^{11}\text{ cm}^{-2}$. In the plot, it is at $\delta_{max} \approx 26\%$ and $t_{max} \approx 13.7\text{ h}$. So, the time t_{max} and δ_{max} decrease with increasing $N_{ox,init}$.

At stress level 4, it was also possible that the simulated data points in figure 5.10 were close to the experimental data. Here, the relaxation rate was $\gamma_0 = 5 \times 10^{-5}$. The concentration of initially present positive oxide charges $N_{ox,init}$ varies here between $0.1 \times 10^{11}\text{ cm}^{-2}$ and $1.8 \times 10^{11}\text{ cm}^{-2}$ and the concentration of electron traps in the oxide $N_{ox,max}$ varies between $8 \times 10^{11}\text{ cm}^{-2}$ and $16 \times 10^{11}\text{ cm}^{-2}$. A trio of points can be found to study the effect of varying $N_{ox,init}$ on the degradation parameters δ_{max} and t_{max} . At points 2, 4, and 5, $N_{ox,init}$ varies at constant $N_{ox,max} = 10 \times 10^{11}\text{ cm}^{-2}$ with $0.1 \times 10^{11}\text{ cm}^{-2}$, $1 \times 10^{11}\text{ cm}^{-2}$ and $1.5 \times 10^{11}\text{ cm}^{-2}$. The values of 11.15 h, 10.25 h, and 9.25 h are obtained for the time t_{max} , and the values of 42 %, 37 %, and 30 % are obtained for the deviation δ_{max} . So both degradation parameters decrease with $N_{ox,init}$. The effect of varying $N_{ox,max}$ can be analyzed on the pair of points 1 and 3. Here $N_{ox,init} = 1.8 \times 10^{11}\text{ cm}^{-2}$ and $N_{ox,init} = 16 \times 10^{11}\text{ cm}^{-2}$ and $N_{ox,max} = 12 \times 10^{11}\text{ cm}^{-2}$. This leads to values for t_{max} of 9.8 h and 9 h and for δ_{max} of 62 % and 39 %. So both degradation parameters increase with the limit concentration $N_{ox,max}$.

At stress level 5, the simulated data points in figure 5.11 are close to the experimental data. For this, the relaxation rate is $\gamma_0 = 5 \times 10^{-4}$ and the concentration of initially present positive oxide charges varies $N_{ox,init}$ between $0.5 \times 10^{11}\text{ cm}^{-2}$ and $1 \times 10^{11}\text{ cm}^{-2}$. The concentration of electron traps in the oxide varies $N_{ox,max}$ between $6 \times 10^{11}\text{ cm}^{-2}$

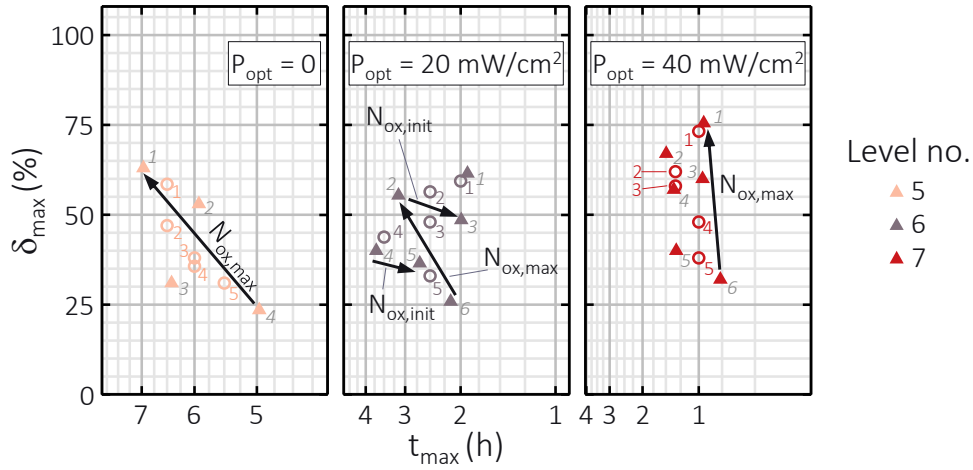


Figure 5.11: Data from figure 5.8 for the variation of intensity P_{opt} . Italic numbers at triangles assign the particular data point to the parameters of $N_{ox,max}$ and $N_{ox,init}$ listed in table 5.4. Non-italic numbers at empty circles assign the particular data point to the parameters of $N_{ox,max}$ and $N_{ox,init}$ listed in table 5.5. Their values are obtained by the interpolation procedure (paragraph 5.4.1). Variations with the values of $N_{ox,max}$ and $N_{ox,init}$ are drawn.

and $10 \times 10^{11} \text{ cm}^{-2}$. The influence of $N_{ox,max}$ can be studied using the trio of points 1, 2 and 4. With constant $N_{ox,init} = 1 \times 10^{11} \text{ cm}^{-2}$, $N_{ox,max}$ varies with $14 \times 10^{11} \text{ cm}^{-2}$, $10 \times 10^{11} \text{ cm}^{-2}$ and $6 \times 10^{11} \text{ cm}^{-2}$. For the degradation parameters, the values for t_{max} are 7 h, 5.9 h and 4.9 h and for δ_{max} 63 %, 53 % and 24 %, respectively. As the limiting concentration of trapped electrons in the oxide increases, both degradation parameters increase.

The simulation data of stress level 6 in figures 5.9, 5.10 and 5.11, are close to the experimental data. Here, a relaxation rate of $\gamma_0 = 2 \times 10^{-5}$ was set and the concentration of initially present positive oxide charges $N_{ox,init}$ varies between $0.1 \times 10^{11} \text{ cm}^{-2}$ and $1.5 \times 10^{11} \text{ cm}^{-2}$. The concentration of electron traps in the oxide $N_{ox,max}$ varies between $6 \times 10^{11} \text{ cm}^{-2}$ and $12 \times 10^{11} \text{ cm}^{-2}$. For simulated data points 2 and 3, it is $N_{ox,max} = 10 \times 10^{11} \text{ cm}^{-2}$ and the values of $N_{ox,init}$ vary. At data point 2, it is $N_{ox,init} = 1 \times 10^{11} \text{ cm}^{-2}$. In the plot, it is at $\delta_{max} \approx 55 \%$ and $t_{max} \approx 3.3$ h. At data point 3, it is $N_{ox,init} = 1.5 \times 10^{11} \text{ cm}^{-2}$. In the plot, point 3 is at $\delta_{max} \approx 58 \%$ and $t_{max} = 2$ h. For simulated data points 4 and 5, it is $N_{ox,max} = 8 \times 10^{11} \text{ cm}^{-2}$. For data point 4, it is $N_{ox,init} = 0.1 \times 10^{11} \text{ cm}^{-2}$. In the plot, it is at $\delta_{max} = 40 \%$ and $t_{max} \approx 3.75$ h. For data point 5, it is $N_{ox,init} = 1 \times 10^{11} \text{ cm}^{-2}$. In the plot, it is at $\delta_{max} \approx 37 \%$ and $t_{max} = 2.75$ h. So the time t_{max} and δ_{max} decrease with increasing $N_{ox,init}$ in both examples. Starting at data point 6 with $N_{ox,init} = 1 \times 10^{11} \text{ cm}^{-2}$ and $N_{ox,max} = 6 \times 10^{11} \text{ cm}^{-2}$, $N_{ox,max}$ increases with constant $N_{ox,init}$ at points 5 with $N_{ox,max} = 8 \times 10^{11} \text{ cm}^{-2}$ and 2 with $N_{ox,max} = 10 \times 10^{11} \text{ cm}^{-2}$. Data point 6 is at

$\delta_{max} \approx 26\%$ and $t_{max} \approx 2.3$ h, point 5 at $\delta_{max} \approx 36\%$ and $t_{max} \approx 2.7$ h and point 2 at $\delta_{max} \approx 55\%$ and $t_{max} \approx 3.2$ h. In this example δ_{max} and t_{max} increase with $N_{ox,max}$. Thereby, the increase in δ_{max} and t_{max} with $N_{ox,max}$ is stronger than with their decrease with $N_{ox,init}$.

At stress level 7 shown in figure 5.11, the simulated data points are close to the experimental data. The relaxation rate of $\gamma_0 = 1 \times 10^{-4}$ was found. The value for the concentration of initially present positive oxide charges $N_{ox,init}$ varies between $0.5 \times 10^{11} \text{ cm}^{-2}$ and $1.5 \times 10^{11} \text{ cm}^{-2}$ and the concentration of oxide traps $N_{ox,max}$ varies between $8 \times 10^{11} \text{ cm}^{-2}$ and $15 \times 10^{11} \text{ cm}^{-2}$. A trio of points can be found to study the effect of varying $N_{ox,max}$ on the degradation parameters. For points 1, 3, and 6, $N_{ox,max}$ varies at constant $N_{ox,init} = 1.5 \times 10^{11} \text{ cm}^{-2}$ with $15 \times 10^{11} \text{ cm}^{-2}$, $12 \times 10^{11} \text{ cm}^{-2}$ and $9 \times 10^{11} \text{ cm}^{-2}$. The values 0.95 h, 0.94 h and 0.8 h are obtained for the time t_{max} and the values 42%, 37% and 30% are obtained for the deviation δ_{max} . So both of the parameters increase with $N_{ox,max}$.

5.3.3 Recap

With the self-consistent simulation of the degradation model it is possible to generate data which is very close to the data of the stress experiments. Model parameters are in good agreement with their literature values. The relaxation rate γ_0 increases with voltage U and temperature T . It is independent of the illumination intensity P_{opt} . Thereby, the variation of the experimental data points between individual sensors at each stress level can be captured by a variation of the model parameters $N_{ox,max}$ and $N_{ox,init}$. In this context, δ_{max} and t_{max} increase with $N_{ox,max}$ and decrease with $N_{ox,init}$. Although, the increase with $N_{ox,max}$ is stronger than the decrease with $N_{ox,init}$. In general, the variation of $N_{ox,max}$ or $N_{ox,init}$ impacts δ_{max} more than t_{max} . It is also seen, that the stress level has a much more significant impact on t_{max} . Regarding a constant stress level, the difference of an individual sensor in t_{max} from the average is in the range of 1% and thus negligible.

5.4 The individuality of sensors

The natural fluctuation within the process flow leads to fluctuations of device properties across a single wafer but also between individual runs. This results in slight fluctuations in the properties between individual sensors. In the previous section it could be seen, that the model parameters of the initial concentration of positive oxide charges $N_{ox,init}$ and the concentration of oxide traps $N_{ox,max}$ allowed to capture the

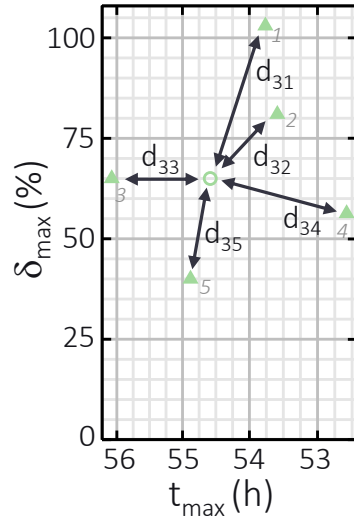


Figure 5.12: In the case of stress level 3, maximum deviation from the initial state of the sensor δ_{max} is plotted against time t_{max} at which it occurs. Experimental data point 3 and all simulated data points are shown. Distances d_{3j} between between them are drawn.

variation of experimental data points that occurred for each stress level. In this section, an interpolation procedure will be derived that allow the determination of the parameters $N_{ox,init}$ and $N_{ox,max}$ for the experimental data points and the corresponding sensors. Thus, the fluctuations between the sensors concerning their degradation behavior will be modeled via the variation of $N_{ox,init}$ and $N_{ox,max}$.

5.4.1 Derivation of an interpolation method

The simulated and experimental data in figure 5.8 are close. But they do not match perfectly. In order to determine the parameters of $N_{ox,init}$ and $N_{ox,max}$ for the experimental data points, an interpolation procedure is derived. Following the k-nearest-neighbor algorithm [234], the experimental data are considered separately. Figure 5.12 illustrates the procedure. Exemplary the experimental and simulated data points of stress level 3 are shown in a plot of δ_{max} against t_{max} . The distances d_{3j} between the experimental point 3 and all simulated data points j are illustrated. The assumption is that the experimental data point corresponds to a pair of values $(N_{ox,init}, N_{ox,max})$. Furthermore, it is assumed that the difference between the values of $N_{ox,init}$ and $N_{ox,max}$ of two points is less, the closer the points are located in the δ_{max} - t_{max} space. So, similarity is measured by their distance in the δ_{max} vs. t_{max} plot. Because the δ_{max} axis and the t_{max} axis are at two different scales and dimensions, the Euclidean distance measure cannot be used to calculate the distance here. Instead, the *Mahalanobis Distance* [235] is used, which is unitless and scale invariant. It incorporates the correlations of the parameters of the data set and is defined as [235] :

$$d(x,y) = \sqrt{(x-y)^T S^{-1} (x-y)} \quad (5.1)$$

Where x and y are the two points between which the distance is determined and S corresponds to the covariance matrix of the entire data set. It is determined here separately for each stress level. Experimental and simulated data are included in the calculation of the covariance matrix. The points considered here are two dimensional. This results in the form of S :

$$S = \begin{pmatrix} s_{\delta}^2 & s_{\delta t} \\ s_{t\delta} & s_t^2 \end{pmatrix} \quad (5.2)$$

Where $s_{\delta} = \sigma_{\delta}$ and $s_t = \sigma_t$ are the standard deviations of the data in δ_{max} and t_{max} , and the correlation of the n data points of the data on the δ_{max} and t_{max} axis:

$$s_{\delta t} = s_{t\delta} = \frac{1}{n-1} \sum_{i=1}^n (x_{i\delta} - \bar{x}_{\delta}) (x_{it} - \bar{x}_t) \quad (5.3)$$

The quantities \bar{x}_{δ} and \bar{x}_t correspond to the arithmetic mean of the data in δ_{max} and t_{max} . Thus, the *Mahalanobis Distance* in equation 5.1 can be simplified to:

$$d(x,y) = s_{\delta}^2(x_{\delta} - y_{\delta})^2 + s_t^2(x_t - y_t)^2 - 2s_{\delta t}(x_{\delta} - y_{\delta})(x_t - y_t) \quad (5.4)$$

The distances in figure 5.11 $d_{ij} = d(x_{exp i}, x_{simu j})$ correspond to the distance between the i th experimental data point $x_{exp i}$ and the j th simulated data point $x_{simu j}$.

With the distance of two points, now a parameter α_{ij} can be defined, which describes the similarity of the points $x_{exp i}$ and $x_{simu j}$. Using the softmax function [236, 237] it is defined as:

$$\alpha_{ij} = \frac{\exp(d_{ij}^{-1})}{\sum_j d_{ij}^{-1}} \quad (5.5)$$

On a scale from 0 to 1, its value indicates how similar the points are to each other. The smaller the distance, the more similar they are. The sum of the values of the similarity parameter of a single experimental point to all simulated points gives 1:

$$\sum_j \alpha_{ij} = 1 \quad (5.6)$$

This can now be used to determine the pair of values $(N_{ox,init}, N_{ox,max})$ of an experimental data point $x_{exp i}$:

$$\begin{pmatrix} N_{ox,init} \\ N_{ox,max} \end{pmatrix}_{x_{exp i}} = \sum_j \alpha_{ij} \begin{pmatrix} N_{ox,init} \\ N_{ox,max} \end{pmatrix}_{x_{simu j}} \quad (5.7)$$

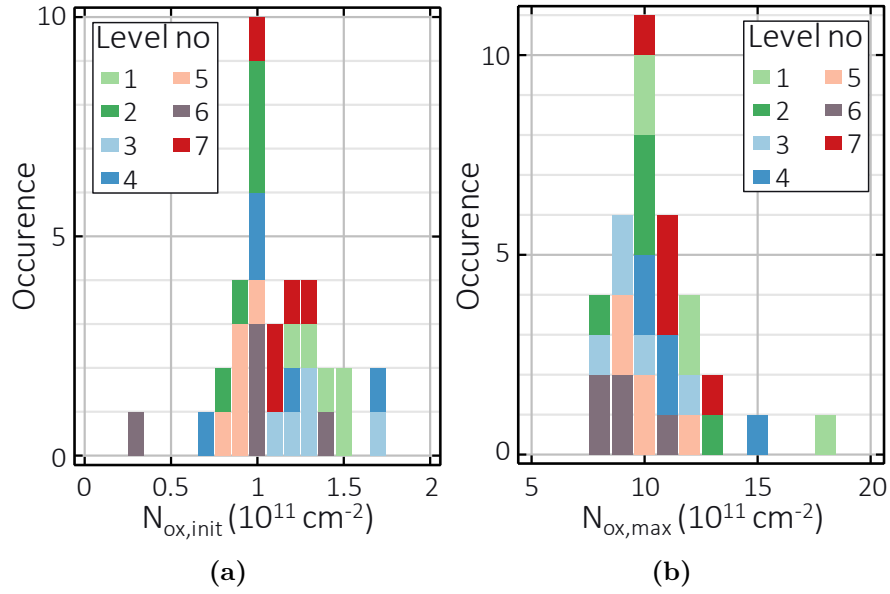


Figure 5.13: Distribution of occurrence of $N_{ox,max}$ (a) and $N_{ox,init}$ (b) values of the studied PIN test sensors resulting from the interpolation procedure derived in paragraph 5.4.1.

In this way, the $(N_{ox,init}, N_{ox,max})$ pair of the simulated data point closest to the respective experimental point is weighted most heavily in the calculation of the experimental $(N_{ox,init}, N_{ox,max})$ pair. This procedure can now be performed for each experimental data point of each stress level to finally obtain an estimate of the concentration of electron traps in the oxide $N_{ox,max}$ and initial positive oxide charges $N_{ox,init}$ for the experimental data points. The resulting values of $N_{ox,max}$ and $N_{ox,init}$ for each experimental data point are listed in table 5.5. The numbering of the data points corresponds to that in figures 5.9, 5.10 and 5.11.

5.4.2 Variation between individual sensors

Figure 5.13 shows the occurrences of values of $N_{ox,init}$ and $N_{ox,max}$ in a plot of the number of occurrences against the concentration. The contributions of each stress level are assigned by color. As can be seen from figure 5.13a, $N_{ox,init} = 10^{11} \text{ cm}^{-2}$ occurs most frequently. There, the distribution of $N_{ox,init}$ values has a peak. Overall, this value was determined for 10 of the 35 sensors studied. Starting from the peak, $N_{ox,init}$ decreases with increasing values $N_{ox,init} > 10^{11} \text{ cm}^{-2}$ and decreasing values $N_{ox,init} < 10^{11} \text{ cm}^{-2}$. Values were found between approximately $0.3 \times 10^{11} \text{ cm}^{-2}$ and $1.7 \times 10^{11} \text{ cm}^{-2}$. The peak is exactly central in this range. However, values $N_{ox,init} > 10^{11} \text{ cm}^{-2}$ occur more frequently. Moreover, no clear correlation can be seen between the stress level and the value of $N_{ox,init}$. Thus, it does not depend on the voltage U , temperature T , or illumination intensity P_{opt} . The occurrence of the concentration of electron traps in the oxide

Table 5.5: Initial positive oxide charge concentration $N_{ox,init}$ and concentration of electron traps in the oxide $N_{ox,max}$ of experimental data points (circles) in figure 5.9,5.10 and 5.11 determined by the derived interpolation procedure as described in paragraph 5.4.1.

Level no	data point no	$N_{ox,init}$ in 10^{11} cm^{-2}	$N_{ox,max}$ in 10^{11} cm^{-2}
1	1	1.47	18.4
1	2	1.36	12.5
1	3	1.28	12.2
1	4	1.47	10.3
1	5	1.16	10.4
2	1	0.99	13.5
2	2	1.01	10.3
2	3	0.92	10.3
2	4	0.84	10.1
2	5	0.99	8.2
3	1	1.74	11.7
3	2	1.3	9.9
3	3	1.24	9.3
3	4	1.3	9.5
3	5	1.14	8.5
4	1	1.72	15.4
4	2	0.68	10.5
4	3	1.05	10.4
4	4	1.16	10.7
4	5	0.97	10.2
5	1	0.96	12
5	2	0.87	10.2
5	3	0.86	9.5
5	4	0.83	9.4
5	5	0.9	8.9
6	1	1.42	11.5
6	2	1.04	9.3
6	3	1.03	9.1
6	4	0.34	8.3
6	5	1.01	8.4
7	1	1.34	12.9
7	2	1.06	10.8
7	3	1	10
7	4	1.18	11
7	5	1.14	10.7

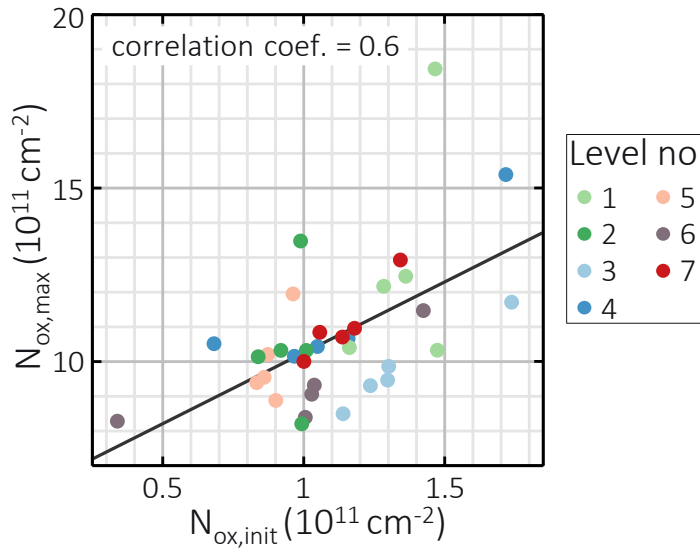


Figure 5.14: Correlation between $N_{ox,max}$ and $N_{ox,init}$. The correlation coefficient is 0.6, which indicates a moderate correlation. It was determined by the *cor*-function in the *R* programming language. Also shown is the linear regression.

$N_{ox,max}$ in figure 5.13b has a peak at $N_{ox,max} = 10 \times 10^{11} \text{ cm}^{-2}$. Overall, this value occurred in 12 of the 35 sensors studied. In [93], this value was used to fit degradation data from oxide charging experiments of MOSFETs. On the right $N_{ox,max} > 10^{11} \text{ cm}^{-2}$ and on the left $N_{ox,max} < 10^{11} \text{ cm}^{-2}$ of the peak, the number of occurrences decreases. Values occur between approximately $8 \times 10^{11} \text{ cm}^{-2}$ and $18 \times 10^{11} \text{ cm}^{-2}$. The location of the peak in this region is shifted from the central position to lower values of $N_{ox,max}$. No clear correlation can be seen between the stress level and the value of $N_{ox,max}$.

5.4.3 The origin of electron traps

It is investigated whether the initial positive charges and the electron traps in the oxide have a common origin. If this were the case, $N_{ox,init}$ and $N_{ox,max}$ should show a correlation. In figure 5.14, the results of the values of both parameters from the interpolation approach from paragraph 5.4.1 for the tested sensors are plotted against each other. The correlation coefficient was determined using the *cor*-function in the *R* programming language. It is 0.6 which indicates a moderate correlation between $N_{ox,init}$ and $N_{ox,max}$. Also the linear regression is shown. Especially those points around $N_{ox,init} = 1 \times 10^{11} \text{ cm}^{-2}$ and $N_{ox,max} = 10 \times 10^{11} \text{ cm}^{-2}$ are very close to the corresponding line. Generally, the increase of $N_{ox,max}$ with $N_{ox,init}$ is seen. This allows the interpretation that the occurrence of at least some of the electron traps in the oxide can be traced to the same origin as the positive oxide charges. As discussed in section 3.4, the positive oxide charges occur due to distortion of the oxide lattice at the interface with silicon. In section 2.3.4 and 3.4 it was discussed that the occurrence of oxygen vacancies is also due to the distortion of the lattice. The reason for the

correlation between $N_{ox,max}$ and $N_{ox,init}$ is therefore the distortion of the lattice at the interface. It follows that the majority of the electron traps in the oxide are located close to the interface. This result is consistent with the authors' findings in [238] that the majority of the electron traps in the oxide are localized less than 200 \AA from the interface.

5.4.4 Recap

An interpolation procedure has been derived. With the *Mahalanobis Distance* a similarity measure was defined that allowed the interpolation between simulated data points. It enabled the determination of the concentrations of initially presented positive oxide charges $N_{ox,init}$ and electron traps in the oxide $N_{ox,max}$ for the experimental data points. The number occurrences of $N_{ox,init}$ and $N_{ox,max}$ was determined. This provides new insights into the variation of individual sensors concerning their degradation behavior. The value of $N_{ox,max} = 10 \times 10^{11} \text{ cm}^{-2}$ occurred most frequently and corresponds to the value reported in literature. To larger and smaller values the number of occurrence decreases continuously. This distribution is used later in this work to provide an estimation on the lifetime of APDs in automotive LiDAR application. A correlation of 0.6 between $N_{ox,init}$ and $N_{ox,max}$ was determined indicating a moderate correlation. This points to a common origin, which are the first 200 \AA from the interface where lattice distortion is very high. This provides a perfect environment for the formation of oxygen vacancies. Therefore, the oxygen vacancy is concluded to be the dominant trap in the oxide layers of the investigated sensors. This is also new information about the properties of the studied APDs.

5.5 Relaxation rate vs. stress conditions

In the previous section it was finally concluded that the oxygen vacancy is the dominant trap dominant electron trap in the silicon dioxide layers of the studied sensors. In section 3.4.4 a mechanism was presented which assumes the existence of two energy levels in this trap and describes an electron transfer from the shallow to the deep state by means of a relaxation rate. According to [106], the origin of the existence of the two trap levels is an asymmetric relaxation, of the two neighboring silicon atoms of the oxygen vacancy. As soon as an electron is captured by one silicon atom (Si^1) of the vacancy, the second one (Si^2) relaxes into the plane of its bound oxygen atoms. This creates a two-level system that can be described schematically as shown in figure 5.15 [106, 239-241]. The potential of the oxygen vacancy has two local minima at the positions of silicon atoms Si^1 and Si^2 . Initially, the trapped electron is located

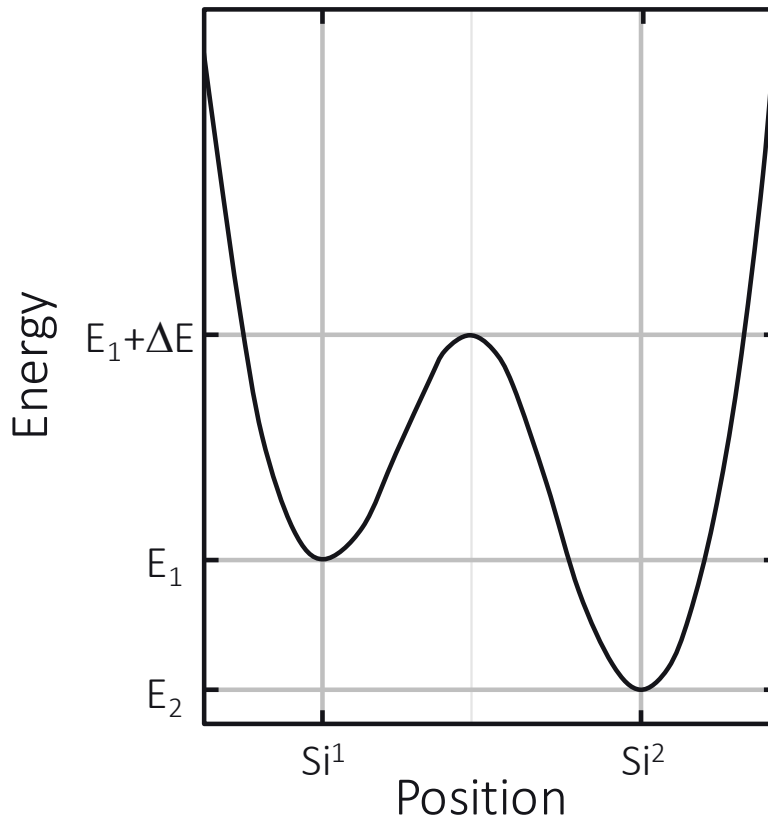


Figure 5.15: Illustration of the energetic structure of the two level system. Inspired by [106, 239-241].

in the minimum of higher energy at Si^1 . To get to the lower energy minimum, i.e., the deep trap level, it must either overcome the barrier ΔE , or tunnel through it. At elevated temperatures, quantum effects play an increasingly minor role. Therefore, in the present case, the electron is more likely to overcome it at high temperatures above 100°C by thermal excitation [239-241]. For this, the transition rate between the minimum at Si^1 to that at Si^2 , i.e., the relaxation rate of the electron, can be described by an Arrhenius dependence [240]:

$$\gamma_0 \propto \exp\left(\frac{\Delta E}{k_B T}\right). \quad (5.8)$$

The relaxation of the oxygen vacancy leads to an electric dipole μ [239]. This interacts with an external electric field E_{ox} , resulting in a net lowering of the barrier by $\mu E_{ox}/2$. This yields the barrier energy [239]:

$$\Delta E = \Delta E_0 - \frac{\mu}{2} E_{ox} \quad (5.9)$$

Where ΔE_0 corresponds to the barrier energy without an external field. From this, the following dependence of the relaxation rate γ_0 on the oxide field E_{ox} and temperature

T can be derived:

$$\gamma_0(E_{ox},T) = \gamma_a \exp\left(-\gamma_b \frac{\gamma_c - E_{ox}}{k_B T}\right) \quad (5.10)$$

Here γ_a , γ_b and γ_c are constants. No values could be found for them in the literature. Therefore, an absolute comparison of the relaxation rate values in table 5.3 is not possible. However, it is investigated in the following whether the dependences on the temperature T and the oxide field E_{ox} agree with equation 5.10. The oxide field E_{ox} varies with the operation voltage U . This relationship must first be quantified. However, in addition to the voltage U , E_{ox} also varies spatially. The spatial $E_{ox}(x)$ profile is shown in figure 4.6. During device degradation, the relaxation rate has a significant effect on sensor properties in the regions where detrapping is most pronounced. There is an exponential relationship between the detrapping rate and the oxide field (eq. 3.29 and 3.30). Therefore, for a fixed value of U , a mean value $\langle E_{ox} \rangle_x(U)$ is taken from all values of the spatial E_{ox} profile that are greater than or equal to 90% of the maximum value. Moreover, for a fixed voltage U , the field in the oxide E_{ox} increases with a decreasing concentration of initial positive charges $N_{ox,init}$. Using the distribution of $N_{ox,init}$ from figure 5.13a, a statistically significant expected value for $\langle E_{ox} \rangle_x(U)$ and an upper and lower bound can be specified. The expected value is defined as the value for E_{ox} at the peak value of $N_{ox,init} = 10^{11} \text{ cm}^{-2}$: $\overline{E_{ox}}(U) = \langle E_{ox} \rangle_x(U, N_{ox,init} = 10^{11} \text{ cm}^{-2})$. Similarly, the upper ($E_{ox,+}(U)$) and lower ($E_{ox,-}(U)$) limits for $\langle E_{ox} \rangle_x(U)$ defined at the values of $N_{ox,init}$ corresponding to the median of all values of the distribution in figure 5.13a that are smaller (for $E_{ox,+}(U)$) or larger (for $E_{ox,-}(U)$) than $N_{ox,init} = 10^{11} \text{ cm}^{-2}$. Substituting these values into equation 5.10 allows to find the voltage dependent expectation value of the relaxation rate $\overline{\gamma_0}(U,T) = \gamma_0(\overline{E_{ox}}(U),T)$ and correspondingly a range between resulting upper ($\gamma_{0,+}(U,T) = \gamma_0(E_{ox,+}(U),T)$) and lower limit ($\gamma_{0,-}(U,T) = \gamma_0(E_{ox,-}(U),T)$) that corresponds to the statistical dispersion of the theoretical relaxation rate from equation 5.10.

Figure 5.16 shows the results of the relaxation rate of the fit from subsection 5.3 which are shown in table 5.3. Also shown is the previously derived theoretical expected value $\overline{\gamma_0}(U,T)$ and the associated scatter. Here, γ_a in equation 5.10 was chosen to match the value from the fit and the theoretical expected value at $U = 380 \text{ V}$ and $T = 145^\circ \text{C}$. Also, $\gamma_b = 1.11 \times 10^{-6} \text{ ecm}$ and $\gamma_c = 1.73 \times 10^6 \text{ V/cm}$ were set. Where e corresponds to the elementary charge.

Figure 5.16a shows the variation of the relaxation rate at a temperature $T = 145^\circ \text{C}$ with stress. On the $\log \gamma_0$ axis, the straight line corresponds to the theoretical expected value $\overline{\gamma_0}(U, T = 145^\circ \text{C})$ and the shaded region corresponds to the associated scatter of

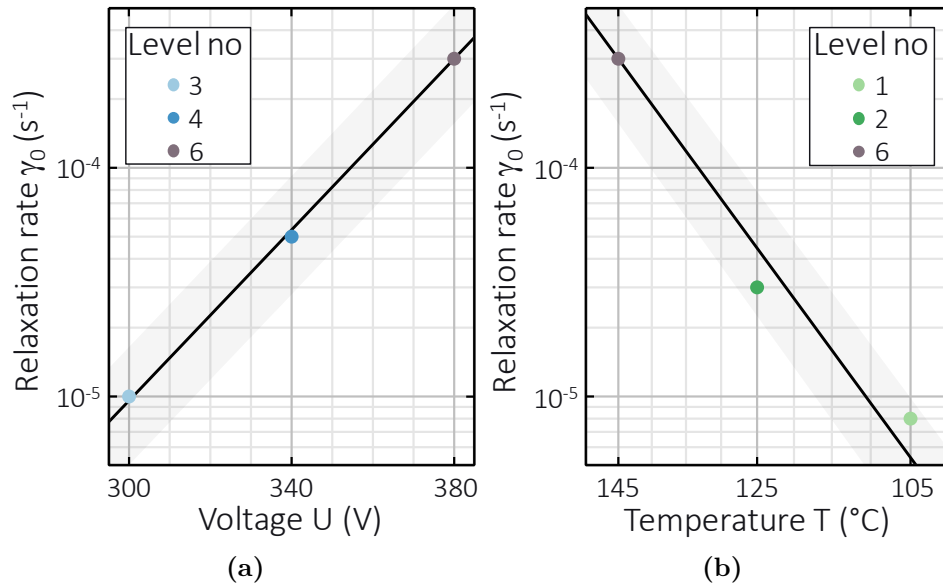


Figure 5.16: Dependence of relaxation rate γ_0 on voltage U (a) and temperature T (b). Values for γ_0 are obtained by the fit of the degradation model to the experimental data in section 5.3. The expected theoretical value of γ_0 from equation 5.10 (black line) and its tolerance (shaded area) are also plotted. The latter are determined following the approach discussed in the text.

the theoretical value for γ_0 . The values from the fit in section 5.3 are shown, which belong to the variation of the voltage U . These are stress levels 3, 4 and 6. Both the theoretical value and the fitted value of the relaxation rate increase with increasing stress. The values from the fit are very close to the straight line of the theoretical expected value. Obviously, the trend from the fit of the experimental data agrees well with the theoretically expected one from equation 5.10. Figure 5.16b shows the variation of the relaxation rate at a voltage $U = 380$ V with temperature in an Arrhenius plot. On the reciprocally scaled T axis and the logarithmically scaled γ_0 axis, the theoretical expected value $\bar{\gamma}_0(U = 380 \text{ V}, T)$ corresponds to a straight line. The shaded area corresponds to the expected deviation of γ_0 from the line. The values from the fit of the experimental degradation data are shown, which belong to the temperature variation. These are stress levels 1, 2 and 6. Both the values from the fit and the theoretical ones increase with increasing temperature. The fitted values are close to the theoretical straight line that passes through the fitted data point at $T = 145$ °C. However, at $T = 125$ °C the data point is about 25% below the straight line and at $T = 105$ °C it is about 60% above the straight line. Nevertheless, the fitted values are within the expected deviation of the theoretical values. Overall, there is good agreement with the fitted values for the relaxation rate γ_0 within the tolerance of the theoretical values. Thus good agreement with literature is obtained.

5.6 Summary

Stress experiments have been conducted under seven stress conditions on five PIN test sensors each. The deviation of the sensors from their initial state $\delta(U = 380 \text{ V})$ increased during stress action, reached a maximum δ_{max} after a time t_{max} , decreased and saturated before the initial state was reached again. Self-consistent simulation results of the degradation model in chapter 4 yielded a similar behavior. It was distilled there that t_{max} corresponds to a characteristic value of the time course of degradation. Therefore, the extent of degradation δ_{max} and its time scale t_{max} are predestined to represent the experimental results. In this way, the essential information of degradation data consisting of hundreds of dark current curves are extracted and compressed into a scatter plot of δ_{max} against t_{max} . In this framework, the degradation course of one sensor corresponds to a single point. Thus, a novel representation of APD degradation data is found, whose efficiency outshines everything known in literature.

Data points of every stress level form clusters on time scale. Thus, the stress level governs the time scale of degradation. The degradation pace increases over proportionally with temperature, voltage and intensity of the incident light. Moreover, the data points of individual sensors scatter much in degradation extent and slightly in time around the average per stress level. It was also concluded, that the dark current provides an outstanding contribution to the degradation of the devices. This is a very important new result.

With the self-consistent simulation of the degradation model it is possible to generate data which is very close to the data of the stress experiments. All model parameters are in good agreement with their literature values. Thereby, the variation of the experimental data points between individual sensors at each stress level can be captured by a variation of the model parameters $N_{ox,max}$ and $N_{ox,init}$. In this context, δ_{max} and t_{max} increase with $N_{ox,max}$ and decrease with $N_{ox,init}$. Although, the increase with $N_{ox,max}$ is stronger than the decrease with $N_{ox,init}$. In general, the variation of $N_{ox,max}$ or $N_{ox,init}$ impacts δ_{max} more than t_{max} . It is also seen, that the stress level has a much more significant impact on t_{max} . Regarding a constant stress level, the difference of an individual sensor in t_{max} from the average is in the range of 1% and thus negligible. These are new results never been achieved before in this condensed quantitative manner.

An interpolation procedure has been derived. With the *Mahalanobis Distance* a similarity measure was defined that allowed the interpolation between simulated data points. It enabled the determination of the concentrations of initially presented positive oxide charges $N_{ox,init}$ and electron traps in the oxide $N_{ox,max}$ for the experimental data points. The distribution of the number of occurrences of $N_{ox,init}$ and $N_{ox,max}$ was determined, which reflects the distribution of degradation related properties of individual

devices. It provides new insights into the variation of individual sensors. The value of $N_{ox,max} = 10 \times 10^{11} \text{ cm}^{-2}$ occurred most frequently and corresponds to the value reported in literature. To larger and smaller values the number of occurrence decreases continuously. This distribution is used later in this work to provide an estimation on the lifetime of APDs in automotive LiDAR application. A correlation of 0.6 between $N_{ox,init}$ and $N_{ox,max}$ was determined indicating a moderate correlation. This points to a common origin, which are the first 200 Å from the interface where lattice distortion is very high. That provides a perfect environment for the formation of oxygen vacancies. Therefore, the oxygen vacancy is concluded to be the dominant trap in the oxide layers of the investigated sensors. This is also new information about the properties of the studied APDs. The relaxation of trapped electrons from shallow into deep trap levels is a idiosyncrasy of the oxygen vacancy. The corresponding relaxation rate introduced in section 3.4 obtained a dependency from temperature and voltage that is also in very good agreement with literature. Aside of the mentioned new insights and extraordinary results, the degradation model was calibrated by the fit on the experimental data.

Chapter 6

Investigation on degrading automotive LiDAR APDs

A lot of new knowledge concerning the degradation behavior in general was gained in the previous chapters. A novel APD degradation model was developed in chapter 3. In chapter 4, a numerical iteration approach was tailor-made to enable the self-consistent simulation of the model. In the previous chapter 5, the model was calibrated and proven to fit experimental degradation data in excellent agreement. With this powerful tool at hand, the question of how APDs degrade and what consequences the degradation has for the function of the sensors in LiDAR operation will be answered in this chapter. First, stress experiments are performed on APDs. The calibrated degradation model from chapter 5 is used to provide insight into how the internal properties of the sensor changes during its degradation (sec. 6.1). Next, the impact of degradation on the APD function in automotive LiDAR application is investigated in section 6.2. Finally, the failure mode is identified in section 6.3 and its lifetime is estimated under the most severe condition within the mission profile for automotive LiDAR.

6.1 Degradation behavior of APDs

The degradation of automotive LiDAR APDs is investigated experimentally. After that the calibrated APD degradation model is used in order to simulate the observed degradation behavior. The obtained simulation results are then used to provide insights into the internal state of the sensor during degradation.

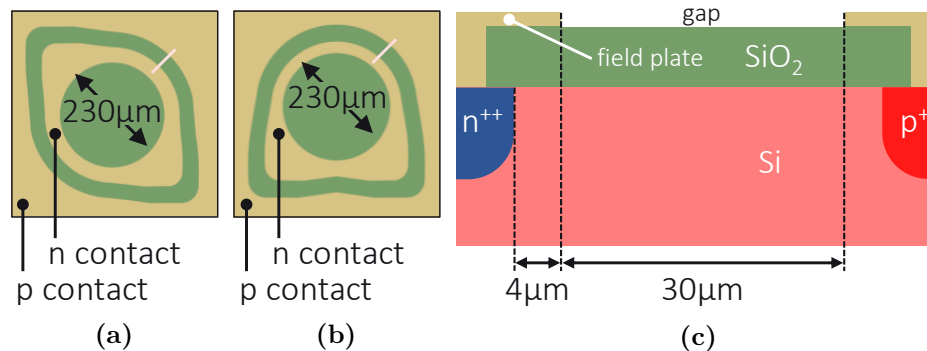


Figure 6.1: Schematic top view on automotive LiDAR APD of the two investigated designs (a,b). Cross section of their edge region with schematic doping and material profile (c).

6.1.1 Design of experiment

Degradation is studied on APDs. Sensors of their design are currently tested and installed in LiDAR systems used in automotive applications. The design of these APDs is shown in figure 6.1. The active area has a diameter of $230\ \mu\text{m}$. For more details on the basic design, it is referred to the discussion in section 2.1. The investigated sensors obtain two slightly different designs. The top view in figures 6.1a and 6.1b reveal the differences. The shape of the n contact differs. In the first case (fig. 6.1a), the two bond pads are opposite each other. In the second case (fig. 6.1b), they are next to each other. Figure 6.1c shows a cross-section of the edge region of the sensors. The n^{++} contact doping of the n side and the p^+ contact doping of the p side are shown. Silicon dioxide is on top of the silicon. Aluminum is used as the contact metal. The field plate which is the extension of the n contact across the oxide has a length of $4\ \mu\text{m}$ beyond the pn junction. The gap between the n and p contact is $30\ \mu\text{m}$. For the investigated sensors, the doping concentration of the avalanche implant varies, which leads to different avalanche breakdown voltages U_{br} . In this respect, five groups can be distinguished possessing a breakdown voltage $U_{br,RT}$ of 220 V, 240 V, 275 V, 295 V and ∞ at room temperature. The last one corresponds to PIN photo diodes. All degradation experiments are performed at a temperature of $145\ ^\circ\text{C}$, an operation voltage of 380 V and an illumination intensity of $P_{opt} = 20\ \text{mW}/\text{cm}^2$. This stress condition corresponds to that of stress level 6 in section 5.1.3 listed in table 5.1.

6.1.2 Behaviour of degrading automotive LiDAR APDs

In the stress experiments more than 30 sensors were tested. Basically, two different degradation trends are observed.

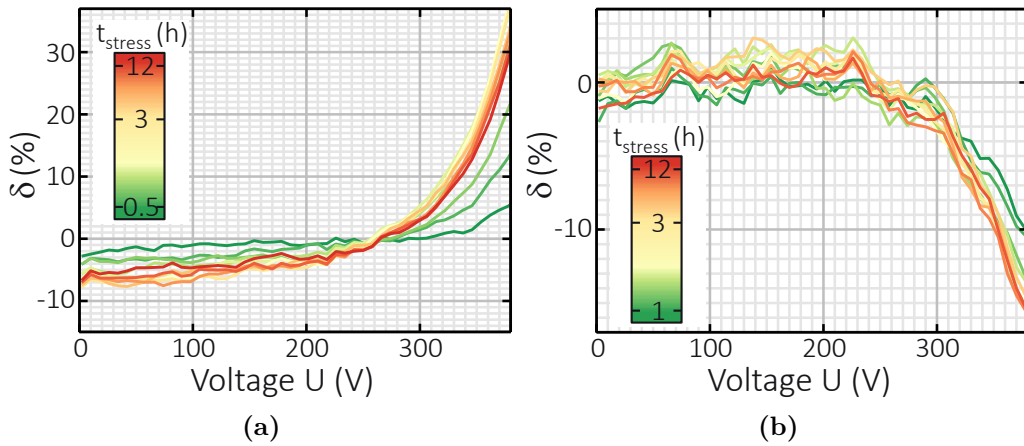


Figure 6.2: Observed degradation trends of automotive LiDAR APDs in a plot of the degradation parameter δ against the operation voltage U . The time under stress t_{stress} is assigned by color. a: The up-down trend. b: The down trend.

Occuring degradation trends

Figure 6.2 shows the two occurring degradation trends in a plot of the degradation parameter δ against the operation voltage U . The temperature during the corresponding measurements corresponds to the stress temperature of $T = 145^\circ\text{C}$. The time under action of stress t_{stress} is assigned by color.

For the degradation trend in figure 6.2a, the degradation parameter is less than zero at voltages below approximately $U = 265\text{ V}$. In this voltage range, δ increases with voltage for every t_{stress} , reaching a value of $\delta = 0$ at approximately 265 V and increase further above 265 V at values $\delta > 0$. In this range, the progression with voltage resembles an exponential relationship. With time, δ becomes smaller at voltages of $U < 265\text{ V}$. At voltages $U > 265$, δ becomes larger with time and the curve becomes steeper. Therefore, the behavior of the δ - U curve with time is similar a rotation of the curve from the zero position ($\delta = 0$ for all U) around the point of $\delta = 0$ and $U = 265\text{ V}$. After a time of $t_{stress} \approx 2.5\text{ h}$ this behavior reverses and the curve begins to rotate back towards the zero position. At this time the deviation of the sensor from its initial course ($t_0 = 0$) is maximum in magnitude. At a voltage of $U = 380\text{ V}$ the maximum value of δ is approximately 36% . After $t_{sat} \approx 10\text{ h}$ this backward rotation saturates before the zero position is reached. Then there is no significant change with time. The discussed behavior is referred to in this work as the up-down trend. It is similar to the behavior observed in chapter 5 on PIN test sensors.

The second degradation trend is shown in figure 6.2b. At voltages of approximately $U < 200\text{ V}$ the δ - U characteristic fluctuates around a value of $\delta = 0$. Above $U = 200\text{ V}$ the deviation from the initial state δ decreases with voltage. In that range the curve is similar to an exponential decrease. With time, the values of δ decrease at voltages

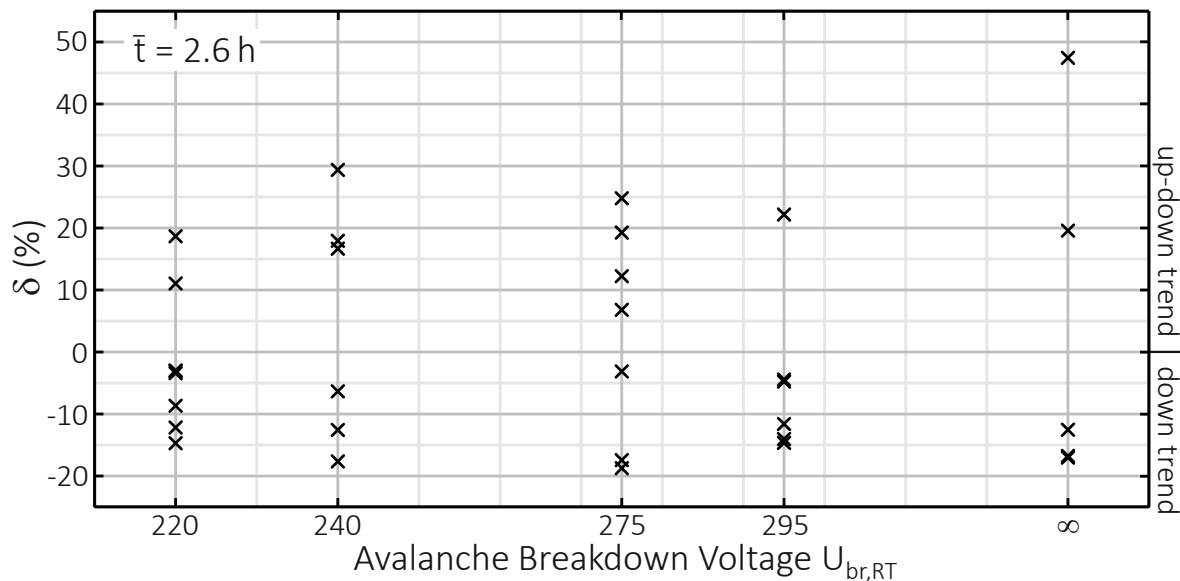


Figure 6.3: Distribution of extent and occurrence of the degradation trends in dependence on the breakdown voltage $U_{br,RT}$ in a plot of the degradation parameter δ against $U_{br,RT}$. A positive value of δ corresponds to δ_{max} of the occurred up-down trend. A negative value of δ corresponds to δ_{85} of the occurred down trend.

of $U > 200$ V. This motion saturates with time. So after a saturation time t_{sat} the δ - U characteristic does not change significantly with time. For example, at a voltage of $U = 380$ V, a value of $\delta \approx -15\%$ is reached after about 10.5 h. This behavior will be referred to as down trend in the following.

Distribution of extent and occurrence of the degradation trends

The extent and number of occurrences of the previously discussed trends in correlation with the breakdown voltage $U_{br,RT}$ will be investigated. In order to represent the degradation data as compressed as possible, the procedure is similar to that in chapter 5. For each sensor which degraded with an up-down trend, the time t_{max} when δ is maximum at a voltage of $U = 360$ V and the corresponding value $\delta_{max} = \max[\delta(U = 360 \text{ V}, t)]$ is determined. In case of the down trend the following procedure is executed. First, δ at a voltage of $U = 360$ V is determined. Then, the time $t_{stress} = t_{85}$ when $\delta(U = 360 \text{ V}, t)$ corresponds to 85% of the saturation value $\delta(U = 360 \text{ V}, t \rightarrow \infty)$ is determined. The value of 85% is chosen such that t_{85} coincides on average with the time t_{max} of the up-down trends. Accordingly, $\delta_{85} = \delta(U = 360 \text{ V}, t = t_{85})$ is the analogon of δ_{max} .

In figure 6.3, δ_{max} in case of an up-down and δ_{85} in case of a down trend are plotted against the breakdown voltage at room temperature $U_{br,RT}$. Therefore, a negative value

of $\delta < 0$ corresponds to the determined value of δ_{85} if the respective sensor degraded in a down trend. Vice versa, a positive value of $\delta > 0$ corresponds to the determined value of δ_{max} if it was an up-down trend. A breakdown voltage of $U_{br,RT} = \infty$ corresponds to a PIN photo diode. All sensors possessing the design in figure 6.1b are PIN photo diodes. Of the eight devices tested possessing a breakdown voltage of $U_{br,RT} = 220$ V, two show an up-down and six a down trend. The upper value of δ_{max} which was reached is almost 20 %, and the lower value is just above 10 %. The upper value of δ_{85} of the down trend sensors is about -3 % and the lower almost -15 %. For the six sensors studied with breakdown voltage of $U_{br,RT} = 240$ V, the up-down and down trends were observed three times each. The upper value of δ_{max} of the up-down sensors is 30 %, and the lower value is approximately 17 %. The upper value of δ_{85} of the down trend sensors is about -6 %, the lower about -18 %. Furthermore, seven devices with breakdown voltage $U_{br,RT} = 275$ V were studied. Of these, four exhibit an up-down trend and three a down trend. The upper value of δ_{max} of the up-down sensors which was reached is about 25 %, and the lower value is just above 6 %. The upper value of δ_{85} of the down trend sensors is about -4 %, the lower nearly -20 %. Of the six devices tested with a breakdown voltage of $U_{br,RT} = 295$ V, one sensor degrades with an up-down trend and five sensors with a down trend. For the up-down trend sensor, it is $\delta_{max} = 23$ %. The upper value of δ_{85} of the down trend sensors is approximately -5 %, and the lower value is approximately -15 %. Moreover, five PIN photo diodes ($U_{br,RT} = \infty$) were tested. Two degraded with an up-down and three with a down trend during degradation. The upper value of δ_{max} of the up-down sensors which was reached is approximately 58 %, and the lower value is just 20 %. The upper value of δ_{85} of the down trend sensors is about -3 %, the lower about -17 %. Of the 32 sensors studied here, in total 63 % exhibit the down trend. The rest of the devices degraded with the up-down trend. For all breakdown voltages, both trends occur. Neither the extent nor the number of occurrence show any correlation with it. Therefore, no clear relationship can be established between the occurrence of a trend and its extent and the breakdown voltage $U_{br,RT}$.

The median of the times t_{max} and t_{85} of all studied sensors is $\bar{t} = 2.6$ h. This agrees well with the experimental results in section 5.2.2. There, the median of the values of t_{max} of the sensors stressed under level 6 is 2.5 h. So under stress level 6 the PIN test sensors and the APD degrade at the same pace.

6.1.3 Application of the calibrated degradation model

The degradation model developed in chapter 3 and calibrated in chapter 5 will be applied in order to investigate the degradation of APDs. For this purpose, it is simulated

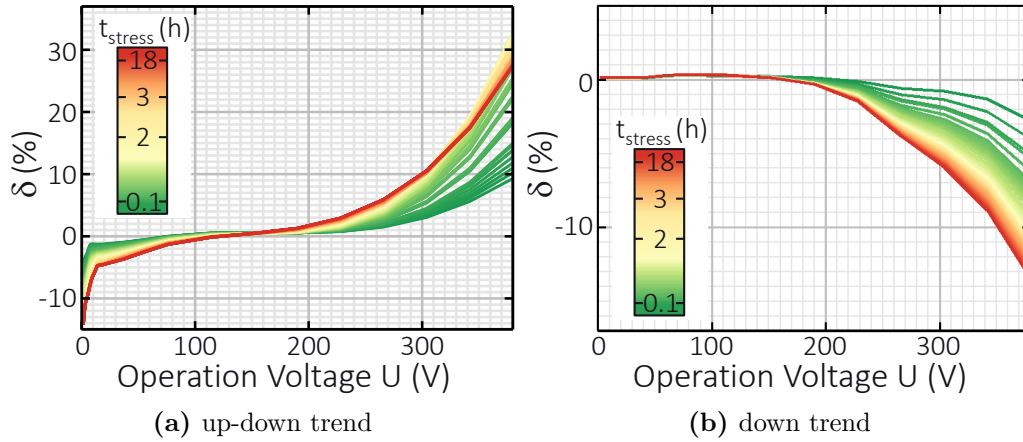


Figure 6.4: Simulation results for up-down (a) and down (b) degradation trends of APDs. The time under stress t_{stress} is assigned by color.

after the procedure described in chapter 4. In the previous section, the sensors were stressed under stress level 6 (tab. 5.1). Under the corresponding conditions, it was found in section 5.3 that the relaxation rate is $\gamma_0 = 3 \times 10^4 \text{ s}^{-1}$. As in section 5.3, the parameters of the concentration of electron traps in the oxide $N_{ox,max}$ and the concentration of initially present positive oxide charges $N_{ox,init}$ are varied in order to fit the previously discussed degradation trends. All remaining parameters correspond to the values given in section 5.3 and 4.3.

Simulation of APD degradation trends

The simulated δ - U characteristics are shown in figure 6.4. The time under stress is assigned by color. As in section 5.3, the up-down trend is obtained with the choice of $N_{ox,max} > N_{ox,init}$. This is exemplified in figure 6.4a for $N_{ox,max} = 8 \times 10^{11} \text{ cm}^{-2}$ and $N_{ox,init} = 2 \times 10^{11} \text{ cm}^{-2}$. Starting at values smaller than zero the degradation parameter δ increases with voltage, reaches a value of $\delta = 0$ at about 150 V and increases sharply above 150 V with values $\delta > 0$. In this range, the variation with voltage resembles an exponential relationship. With time, δ becomes smaller at voltages of $U < 150$ V. At voltages $U > 150$ V, δ becomes larger with time and the curve in this voltage range becomes steeper. Therefore, the behavior of the δ - U curve with time is similar to a counterclockwise rotation of the curve from the zero position ($\delta = 0$ for all U) around $\delta = 0$ and $U = 150$ V. After a time of $t_{stress} = t_{max} \approx 2.5$ h this behavior reverses and the curve begins to rotate back towards the zero position. At this time the deviation of the curve from its initial course ($t_0 = 0$) is maximum in magnitude. For example, at a voltage of $U = 380$ V, it is $\delta \approx 33\%$ at this time. Subsequently, the reverse motion stops before reaching the zero position. From this moment t_{sat} , the δ - U curve does not change significantly with time.

In section 5.3, it was shown that δ_{max} decreases with increasing $N_{ox,init}$ and decreasing $N_{ox,max}$. Following this relationship, the down trend was achieved for values $N_{ox,max} < N_{ox,init}$. Figure 6.4b shows simulation results for $N_{ox,max} = 6 \times 10^{11} \text{ cm}^{-2}$ and $N_{ox,init} = 10^{12} \text{ cm}^{-2}$. Starting at low voltages, δ equals zero until it slightly increases at $U = 50 \text{ V}$. At around 100 V it reaches a maximum of under 1% and decreases. Between 160 V and 230 V it falls below zero and decreases further with voltage. The decrease follows a steep curve that resembles an exponential decrease. The voltage when $\delta = 0$ decreases with increasing time. With increasing time, the values of δ for $U > 160 \text{ V}$ decrease. This behavior saturates. For example, at a voltage of $U = 380 \text{ V}$, a value of $\delta \approx -13\%$ is reached after about 10 h . Subsequently, the δ - U curve does not change significantly with time.

In comparison, the discussed simulated and experimental trends in figure 6.2 are similar. For the up-down trend, the maximum deviation from the initial state in experiment and simulation is reached after approximately $t_{max} = 2.5 \text{ h}$. In the down trend, the values for the time t_{sat} after which the characteristics do not change significantly in the experiment ($t_{sat,exp} \approx 10.5 \text{ h}$) and the simulation ($t_{sat,simu} \approx 10 \text{ h}$) are close to each other. Thus, an excellent agreement is established on time scale of degradation. The extent of degradation is measured by the value of the degradation parameter δ . At a voltage of $U = 380 \text{ V}$, the maximum for the up-down trend is approximately 36% for the experimental curve in figure 6.2a. For the simulated up-down trend, it is about 33% . For the experimental down trend (fig. 6.2b), the saturation value at 380 V is about 15% and for the simulated down trend it is about 13% . So, an excellent agreement is also demonstrated for the extent of degradation. In the following, the results of the simulation are used to provide insights into the internal state of the APD during degradation.

Drift of internal parameters during up-down degradation

The drift of sensor internal parameters during the up-down degradation trend of LiDAR APDs is investigated in the following. Insight is provided by the simulation results of the calibrated degradation model. Figure 6.5 shows the spatial distribution of the concentration of negative oxide charges $N_{ox}(x,t)$ and interface traps $N_{it}(x,t)$. The distance x is measured from the center of the active area. The variation over time is assigned by color.

Initially, the concentration of negative oxide charges $N_{ox}(x,t)$ increases in the vicinity of the field plate ending at $x = 155 \mu\text{m}$. From there, $N_{ox}(x,t)$ propagates with time to higher and lower values of x with generation tending to stagnate between $153 \mu\text{m}$ and $155.5 \mu\text{m}$. Thereby, maxima at $151.5 \mu\text{m}$ and $156 \mu\text{m}$ arise in the first 2.5 h obtaining

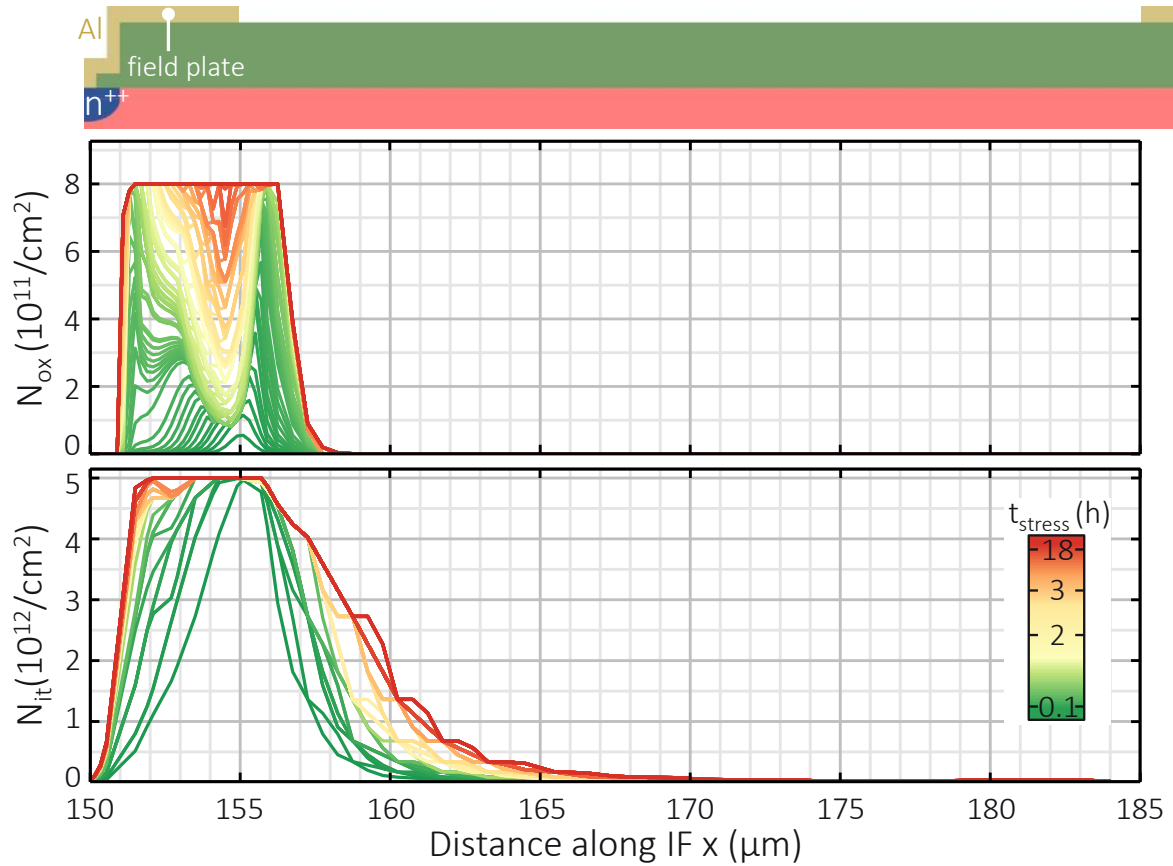


Figure 6.5: Concentration profiles of negative oxide charge N_{ox} and interface traps N_{it} along the interface in the APD edge extracted from simulation results. The time under stress influence t_{stress} is assigned by color.

values of the concentration limit $N_{ox,max} = 8 \times 10^{11} \text{ cm}^{-2}$. In between and especially around $154.5 \mu\text{m}$ the generation proceeds much slower and $N_{ox,max}$ is reached only after 16 h. Above $x = 159 \mu\text{m}$, the concentration of negative oxide charges remains vanishingly small for the simulated degradation time of 18 h.

The concentration of interface traps $N_{it}(x,t)$ initially increases rapidly in the vicinity of the field plate ending at $x = 155 \mu\text{m}$. Already within the first 6 min $N_{it}(x,t)$ increases at $154.5 \mu\text{m} < x < 156 \mu\text{m}$ to over 80% of the maximum concentration $N_{it,max} = 5 \times 10^{12} \text{ cm}^{-2}$. After a stress time of $t > 3 \text{ h}$, the concentration profile is less than 20% of the concentration limit $N_{it,max}$ only at $x > 161 \mu\text{m}$ and below $x = 151 \mu\text{m}$. After about 3 h, $N_{it}(x,t)$ is almost completely saturated below the field plate from $x = 151 \mu\text{m}$ to $x = 155 \mu\text{m}$. In comparison, the generation of oxide charges proceeds much more slowly than the generation of interface traps.

In comparison with figure 6.4a, it is noticeable that the moment of maximum deviation from the initial state t_{max} coincides with the moment when the two maxima in the profile of negative oxide charges at $151.5 \mu\text{m}$ and $156 \mu\text{m}$ have already imposed

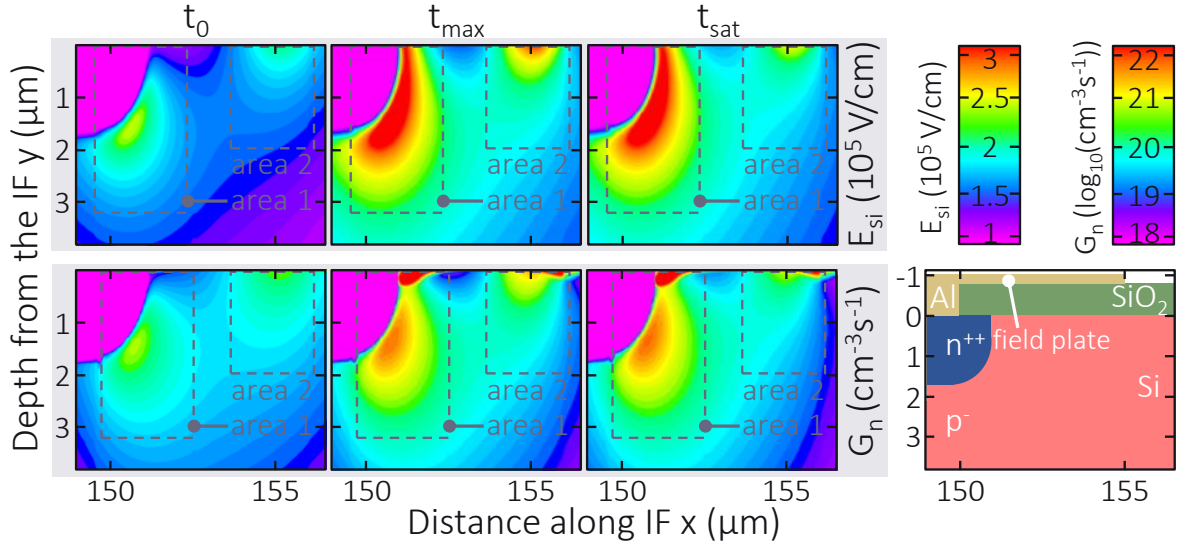


Figure 6.6: Profile of the electric field and the impact ionization rate in the cross section through the edge region of the simulated APD for three different times t_0 , t_{max} and t_{sat} . Also, a sketch of the doping profile is shown for clarity.

themselves, but the concentration in between is still rather low. Thus, the N_{ox} profile is maximally inhomogeneous at that time. These results are completely similar to the findings from simulation results of PIN test sensors in chapter 4.

The electric field and the impact ionization rate are shown in figure 6.6 in a cross section of the sensor edge region for three different times $t_0 = 0$, t_{max} and t_{sat} . These correspond to the time before stress, when the maximum deviation from the initial course of the $\delta-U$ curve occurs and the time after which the $\delta-U$ curve remains constant in time. The coordinates x and y correspond to the distances from the center of the active area along the interface and from the interface into the depth of the sensor. To facilitate understanding, two areas are drawn and a schematic cross section with the doping and material profiles is shown. For more details on the latter, it is referred here to section 2.1. Area 1 is located at the pn junction, where the n contact doping has its strongest curvature. Area 2 is located near the Si:SiO₂ interface below the field plate ending. Comparing the field distribution of times t_0 and t_{max} , it is noticeable that the field strength in both areas increases from around 2.3×10^5 V/cm at the maximum at t_0 to over 3×10^5 V/cm after t_{max} . In general, the field increases. During the transition from t_{max} to t_{sat} , the field in area 1 marginally increases. In contrast, the field in area 2 decreases from above 3×10^5 V/cm at its maximum to below 2.5×10^5 V/cm. Previously, it was found that the time of the maximum deviation in the up-down trend coincides with the moment when the oxide charge profile around $151.5 \mu\text{m}$ and $156 \mu\text{m}$ reaches the limit of $N_{ox} = N_{ox,max}$ and is still relatively low between these areas. Area 2 lies roughly between $151.5 \mu\text{m}$ and $156 \mu\text{m}$. Reaching the maximum concentration of

oxide charges at $151.5 \mu\text{m}$ and $156 \mu\text{m}$, thus leads to the high field in area 2 after t_{max} . The subsequent increase of negative oxide charges in between $151.5 \mu\text{m}$ and $156 \mu\text{m}$ then displaces the field and leads to its decrease. At time t_0 , the impact ionization rate obtains local maximum values in area 1 and 2 which are approximately $10^{20} / \text{cm}^2\text{s}$. Until t_{max} , it increases above $3 \times 10^{21} / \text{cm}^2\text{s}$ in both areas. Subsequently, the generation rate in area 2 decreases again to below $1 \times 10^{21} / \text{cm}^2\text{s}$ after t_{sat} . Thus, reaching the maximum deviation from the initial curve in the up-down trend can be associated with reaching a maximum impact ionization rate in area 2. At the same time, it increases in area 1, so that the initial state of the device is not reached again during the back rotation in figures 6.2 and 6.4. The drift of the impact ionization rate reflects the drift of the field, which is not surprising because it depends exponentially on the field (sec. 2.4). The field drift was attributed to the accumulation of negative oxide charges. Therefore, it is concluded that the drift of the impact ionization rate is also caused by the generation of negative oxide charges. This is consistent with the findings in chapter 4. In conclusion, the accumulation of negative oxide charges below the field plate leads to an increase of the electric field there, which causes the increase of the impact ionization.

Drift of internal parameters during down degradation

Figure 6.7 shows the spatial distribution of the concentration of negative oxide charges $N_{ox}(x,t)$ and interface traps $N_{it}(x,t)$ in the sensor edge between the n and p contacts. The distance x is measured from the center of the active area. The variation over time is assigned by color.

In the beginning of oxide degradation, negative charges are generated predominantly in the outer edge, which is reflected by the peak occurring at about $183 \mu\text{m}$. With time it increases in height. At the same time, its spur towards the n side becomes larger. After about 20 min the peak reaches the limit of $N_{ox,max} = 6 \times 10^{11} \text{cm}^{-2}$. Somewhat later after about 2.5 h its spur in the x direction reaches the end of the field plate at $x = 155 \mu\text{m}$. Subsequently, a second peak forms below the field plate also reaching the limit concentration $N_{ox,max}$ after around 16 h.

A similar progression is observed in the generation of interface traps. Already after the first 6 min a peak around $x = 182 \mu\text{m}$ has formed and reached the limit of $N_{it,max} = 5 \times 10^{12} \text{cm}^{-2}$. At this time, traps below the field plate and throughout the gap are already generated. As time progresses, the concentration of interface traps N_{it} increases from the outside to the inside in direction of $-x$. In general, it can be observed that the generation of interface traps at the beginning of the stress is much faster than the generation of oxide charges. After about 2 h, however, both proceed

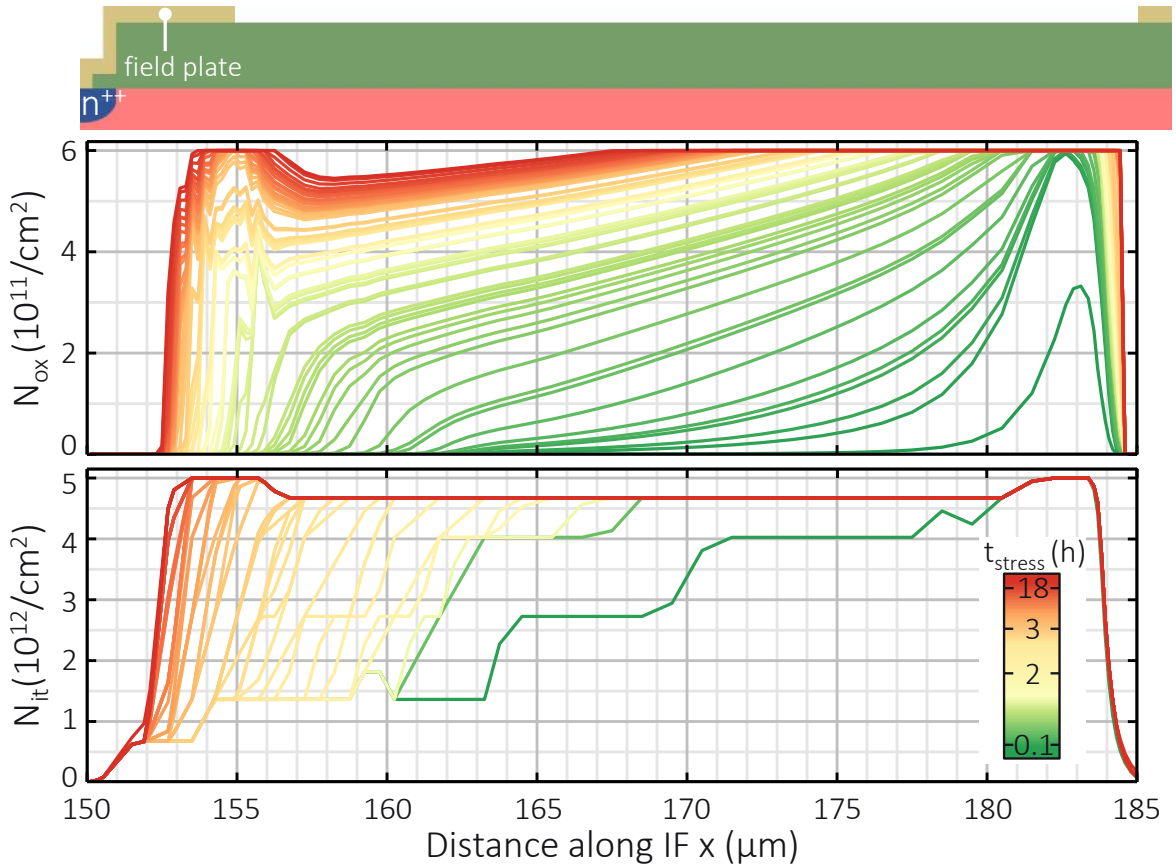


Figure 6.7: Distribution of negative oxide charges N_{ox} and interface traps N_{it} along the interface in the APDs edge extracted from simulation results. The time under stress t_{stress} is assigned by color.

at about the same rate. Presumably, the diffusion of the liberated hydrogen after 2 h is the limiting factor in the generation of further interface traps. Figure 6.8 shows the cross section of the APD in its edge region. The distribution of field strength and impact ionization rate are shown before degradation (t_0) and after the variance of the $\delta-U$ curve with time is saturated (t_{sat}). The coordinates x and y correspond to the distance from the center of the active area along the interface and from the interface into the depth of the sensor. A schematic cross section showing the doping and material profiles is shown for ease of understanding. Before degradation (t_0), the maximum field of about 2.5×10^5 V/cm is at about $x = 185 \mu\text{m}$ at the interface. The peaks below the field plate as in figure 6.8 are not observed here at all. There is only a local maximum of below 1.5×10^5 V/cm at the curvature of the n^{++} doping. After a stress time of $t_{stress} = t_{sat}$, the maximum at $x = 185 \mu\text{m}$ decreased to a value of about 2×10^5 V/cm. The local maximum at the curvature of the n^{++} doping increases somewhat and has a value of about 1.5×10^5 V/cm. A similar picture emerges when regarding the profile of the impact ionization rate G_n . Before stress, its maximum of

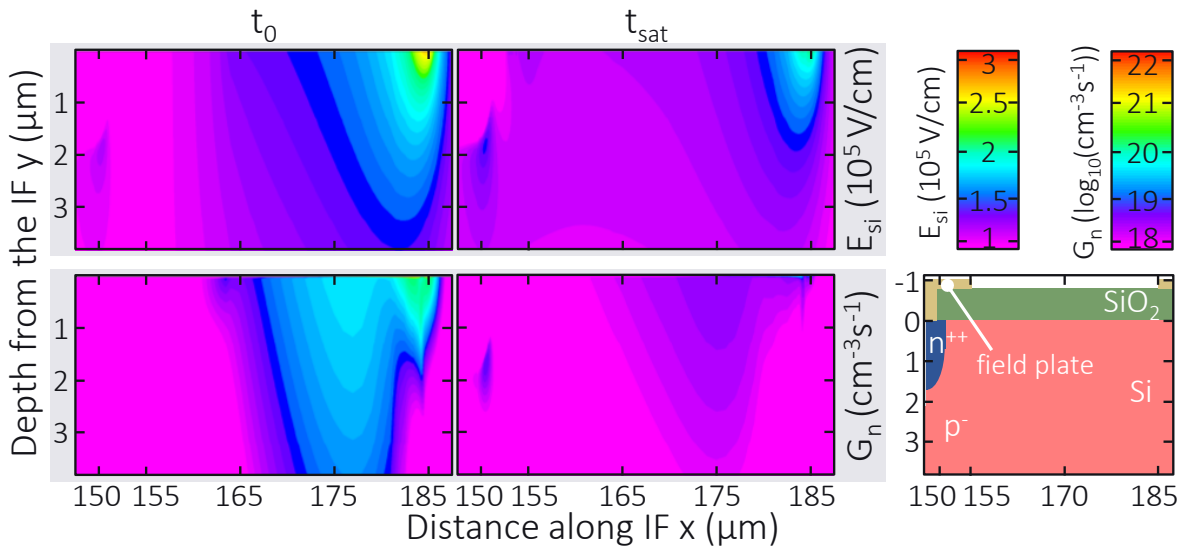


Figure 6.8: Profile of the electric field and the impact ionization rate in the edge region of the LiDAR APD for different times t_0 and t_{sat} . Also, a sketch of the doping and material profile is shown for clarity.

slightly above $10^{20} \text{ cm}^{-3} \text{ s}^{-1}$ is at about $x = 185 \mu\text{m}$ at the interface. However, after a time of $t_{stress} = t_{sat}$, its value decreased to a value below $10^{19} \text{ cm}^{-3} \text{ s}^{-1}$.

The area where the decrease of field and impact ionization rate is very strong corresponds to area where the generation of negative oxide charges is very strong in the first 2 h of degradation. Together with the previous findings it is concluded, that during degradation the generation of oxide charges causes the field in the sensor edge to decrease. This also results in a decrease of the impact ionization rate. Thus, if charge carriers in the gap are slightly multiplied in the unstressed sensor, this multiplication decreases with the aging of the sensors and leads to the observed down trend.

6.1.4 Recap

Stress experiments have been performed on APDs. Sensors of the studied design are currently tested and installed in automotive LiDAR modules. Two different degradation trends have emerged from the investigations. Their occurrence and degradation extent and pace does not correlate with the breakdown voltage. Furthermore, the time scale of APD and PIN test sensor degradation studied in chapter 5 is the same under the same conditions. Both share a similar edge structure. The results of the simulation prove, that the degradation of the sensors occurs exclusively in their edge region. Therefore, it is concluded that degradation is only dependent on the edge design and all the results obtained so far on the basis of the investigations on PIN test sensors can be transferred to APDs. This is important new information, which will be used in the

following. Both trends are self-consistently simulated with the calibrated degradation model in excellent agreement. Moreover, another important new insight is generated: One of the degradation trends, referred to as up-down trend, reflects an increase of the impact ionization rate in the edge region of the APD. Around 40 % of the more than 30 studied sensors showed this degradation behavior. While the second, referred to as down trend, was observed for 60 % of all studied sensors and corresponds to a decrease of the impact ionization rate in their edge.

6.2 Degradation effect on the APD function in automotive LiDAR systems

The signal-noise ratio (SNR) is crucial for the proper functioning of the APD in LiDAR operation (sec. 2.2). At $SNR = 1$, the signal is as large as the noise. This is the theoretical limit below which signals cannot be resolved. In practice, it has to be at least $SNR = 3$ for a signal in order to be resolved [40]. As discussed in section 2.1, the noise of the sensor includes the temperature noise, also called Johnson noise, and the shot noise. The latter is determined by the generation-recombination processes taking place in the sensor. The more pronounced these processes are, the more promoted is the shot noise. It was shown previously, that the up-down degradation trend reflects an increase of the impact ionization rate in the edge region of the sensor. It is predominantly addressed to the generation of negative oxide charges. Furthermore, interface traps are generated which interact as generation-recombination centers (sec. 2.3). In this case, both, the generation of oxide charges and interface traps lead to an increase in shot noise. The Johnson Noise remains unaffected by these processes and is therefore neglected in the following. In order to estimate the strongest possible degradation induced increase of noise in the following, the empirical distribution of sensor properties established in section 5.4 is extrapolated to the tail where sensors are very prone to degradation. Based in this, the calibrated degradation model which already demonstrated excellent agreement with numerous experimental degradation data is used to simulate the degradation effects on functional parameters of these prone sensors which will finally lead to the determination of the noise current.

6.2.1 Extrapolation of sensor properties

For the strongest possible degradation induced increase of noise, the generation-recombination processes need to be maximized in strength during degradation. The processes that lead to the strengthen of generation-recombination processes are sufficiently well described

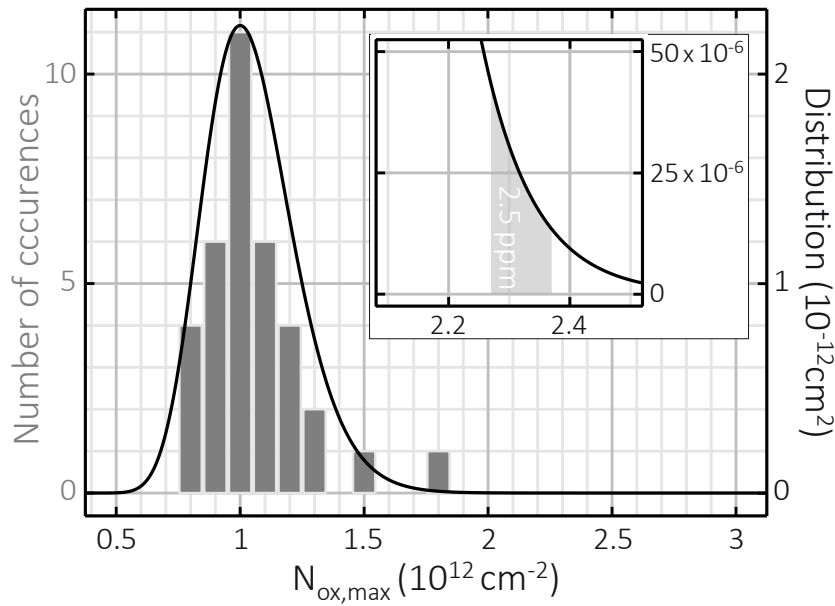


Figure 6.9: Statistical spread between individual sensors. Number of occurred values of $N_{ox,max}$ from the fit of the degradation model on experimental degradation data discussed in section 5.4 (gray bars). Log normal distribution for the mean value $\langle N_{ox,max} \rangle \approx 1 \times 10^{12} \text{ cm}^{-2}$ and the standard deviation $\sigma_{N_{ox,max}} \approx 0.2 \times 10^{12} \text{ cm}^{-2}$ (black curve). The enlarged section shows the normal distribution in the region of high values of $N_{ox,max}$ that account for 2.5 ppm of all up-down sensors (40%) and 1 ppm of the entirety of all sensors.

by the calibrated degradation model, which is flexible only in the parameters of the concentration of preexisting positive fixed charges $N_{ox,init}$ and electron traps $N_{ox,max}$ in the oxide. As discussed in section 5.4, these reflect the individuality of the sensors and govern the generation of oxide charges, which influences the impact ionization rate during degradation (sec. 5.3). An increase of noise generally occurs only in the case of the up-down trend, which occurs for $N_{ox,max} > N_{ox,init}$ (sec. 6.1). In section 5.3, it was discussed that the maximum deviation from the initial characteristic of the sensor δ_{max} that occurs during degradation increases predominantly with $N_{ox,max}$. In the previous section it was revealed, that the increase of the deviation from the initial characteristic is a reflection of the increasing impact ionization rate. Therefore, the higher $N_{ox,max}$, the higher the increase of the impact ionization rate during degradation. However, in order to make significant statements about the effect of an increased impact ionization rate on the function of the LiDAR APD, $N_{ox,max}$ cannot be chosen arbitrarily large. For lifetime determination in the automotive industry, such events are crucial when 1 ppm of all sensors fail at the same time (sec. 2.3.1). It was shown in section 6.1.2 that the up-down trend occurs only for 40% of all sensors and only this fraction leads to an increase of the impact ionization rate. So for a total of 1 ppm of all sensors to fail at the same time, 2.5 ppm of the sensors with up-down trend must fail at the same

time. Therefore, a value of $N_{ox,max}$ need to be determined, which occurs statistically with a frequency of $2.5 \text{ ppm} = 2.5 \times 10^{-6}$ in the case of an appearing up-down trend. A distribution of the number of occurrences of the values of $N_{ox,max}$ was determined in section 5.4 by fitting the model to experimental degradation data. It is shown as a bar plot in figure 6.9. For a discussion of these data, it is referred to section 5.4. The number of sensors studied there is not sufficient to observe fractions of their entirety in the millionths. In order to obtain a distribution nevertheless, the observed numbers of occurrence are fitted with the log normal distribution with mean $\langle N_{ox,max} \rangle \approx 1 \times 10^{12} \text{ cm}^{-2}$ and standard deviation $\sigma_{N_{ox,max}} \approx 0.2 \times 10^{12} \text{ cm}^{-2}$. The corresponding density distribution is also shown in figure 6.9. It rises steeply for values $N_{ox,max} > 0.5 \times 10^{12} \text{ cm}^{-2}$, reaches its maximum of nearly $2.2 \times 10^{-12} \text{ cm}^{-2}$ at $N_{ox,max} = 1 \times 10^{12} \text{ cm}^{-2}$, and then decreases again. At approximately $2 \times 10^{12} \text{ cm}^{-2}$ it becomes very small. As discussed, the part of the density distribution of interest for the following discussion is the tail of high values $N_{ox,max}$. The part of the distribution is needed that encloses an area of 2.5 ppm with the x -axis. This is shown in the enlarged section in the figure. Between $N_{ox,max} = 2.2 \times 10^{12} \text{ cm}^{-2}$ and $N_{ox,max} = 2.5 \times 10^{12} \text{ cm}^{-2}$ the curve drops steeply from above $50 \times 10^{-18} \text{ cm}^{-2}$ to below $5 \times 10^{-18} \text{ cm}^{-2}$. Between $N_{ox,max} = 2.27 \times 10^{12} \text{ cm}^{-2}$ and $N_{ox,max} = 2.37 \times 10^{12} \text{ cm}^{-2}$ it includes an area of about 2.5 ppm with the x axis. Therefore, in the following $N_{ox,max} = N_{1 \text{ ppm}} \approx 2.32 \times 10^{12} \text{ cm}^{-2}$ is chosen as the value reflecting 1 ppm of all sensors failing simultaneously. Those high concentrations of electron traps are still possible in SiO_2 . It was for example found in [95], that values higher than $4 \times 10^{12} \text{ cm}^{-2}$ can occur. The drift of the functional parameters of these very prone sensors during degradation and its impact on the sensor noise characteristics is discussed now.

6.2.2 Impact on device functionality

The shot noise of the APD is determined by all generation-recombination processes (sec. 2.1). Equation 2.4 describes the underlying relationships. However, the consideration only takes into account contributions from the center of the sensor, i.e. the active area and the volume underneath, and neglects contributions from the edge region. In this section, the consideration is extended to the edge contribution. All essential quantities are shown in figure 6.10. A sketch of the cross section of the sensor with its doping and material profiles is depicted. For details on that, it is referred to section 2.1. The incident light consists of the signal with intensity P_S and the background radiation with intensity P_B . There are two areas in the sensor where it can penetrate. That is the volume below the central active area where the actual APD is located and the part of the edge region which is below the gap between n and p contact metals. In

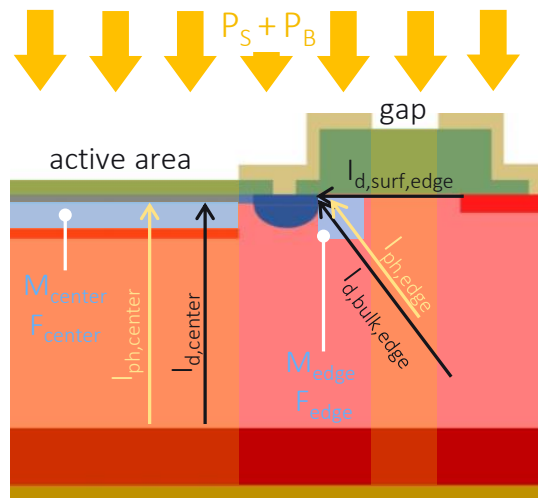


Figure 6.10: Sketch of the cross-section of the APD with doping and material profiles. The relevant quantities for the noise are drawn. They are the dark and photo currents in the sensor center and its edge region ($I_{d,center}$, $I_{d,surf,edge}$, $I_{d,bulk,edge}$, $I_{ph,center}$, $I_{ph,edge}$). In center and edge there are multiplication zones (light blue). High fields there lead to multiplication M_{center} and M_{edge} and correspondingly to excess noise F_{center} and F_{edge} . The incident light includes the signal P_S and the background radiation P_B . The volume that it penetrates in the sensor is shaded in yellow. It corresponds to the volume where carriers are photo generated.

these yellow shaded volumes, charge carriers are generated by the absorption of light and the photo-electric effect. These contribute to the photo current of the sensor center $I_{ph,center}$ and its edge $I_{ph,edge}$. Moreover, the interaction of charge carriers with the lattice leads to thermal generation and recombination by the Shockley-Read-Hall mechanism (sec. 2.4.2). This generates the components of the dark current $I_{d,center}$ and $I_{d,edge}$ in sensor center and edge, respectively. The latter is composed of the bulk current $I_{d,bulk,edge}$ and the surface current $I_{d,surf,edge}$. The surface current $I_{d,surf,edge}$ is a leakage current caused by the formation of a surface conduction channel in silicon at the Si:SiO₂ interface. In addition, impact ionization of charge carriers occurs in the center in the light blue colored region. This results in the gain M_{center} . All charge carriers entering this zone from below are multiplied with it. In section 6.1.3 it was shown that in the considered case of the up-down trend, degradation results in an increase of the impact ionization rate. The corresponding region is colored light blue in the figure. All charge carriers entering it are multiplied with gain M_{edge} . In the sensor center, both photo $I_{ph,center}$ and dark current $I_{d,center}$ are multiplied by M_{center} . In the edge region, photo $I_{ph,edge}$ and dark current $I_{d,edge} = I_{d,bulk,edge} + I_{d,surf,edge}$ are multiplied by M_{edge} . As described in section 2.1, the avalanche multiplication is generally associated with a statistical noise factor, the excess noise F . As defined by equation 2.3, it is determined by gain M and the ratio $k = \frac{\alpha_p}{\alpha_n}$ of the impact ionization coefficients of electrons α_n and holes α_p . As expressed in equation 2.16, the coefficients

α_n and α_p are determined by the electric field from which the charge carriers obtain the necessary energy for impact ionization. As the field increases, the excess noise factor also increases. The multiplication in the center is affected by the excess noise factor F_{center} and in the edge by F_{edge} . The shot noise current from edge and center are determined by:

$$\langle i_{shot}^2 \rangle_j = 2eB_N [I_{d,j} + I_{ph,j}] M_j F_j \quad \text{where } j \in \{edge, center\} \quad (6.1)$$

In eq. 6.1 $I_{d,j}$ and $I_{ph,j}$ are the multiplied dark and photo current terms. Furthermore, e is the elementary charge and B_N is the noise bandwidth of the amplifier connected behind the APD. A circuit as shown in figure 2.8 on the lower left is assumed. For the LiDAR application, $B_N = 50$ MHz was defined in [40]. The $\langle i_{shot}^2 \rangle_j$ add up to the total noise current square:

$$\langle i_{shot}^2 \rangle = \langle i_{shot}^2 \rangle_{edge} + \langle i_{shot}^2 \rangle_{center} \quad (6.2)$$

In order to investigate the effect of degradation on the shot noise of the sensor, an APD with an active area with diameter of $350 \mu\text{m}$ and a breakdown voltage of $U_{br,RT} \approx 200$ V is regarded. Aside of that, it corresponds to the design of the APD from section 6.1. To model degradation, the profile of oxide charges in the edge region that resulted from the simulation in paragraph 6.1.3 are scaled to match a concentration of oxide electron traps of $N_{ox,max} = N_{1ppm} \approx 2.32 \times 10^{12} \text{ cm}^{-2}$. In this way, the degradation under the action of the stressors $T_{stress} = 145^\circ\text{C}$, $U_{stress} = 380$ V and $P_{stress} = 20 \text{ mW/cm}^2$ is simulated with the calibrated degradation model.

Regarding the operation conditions for the noise performance considerations, it has to be noted that an increase in operation temperature due to the temperature coefficient (sec. 2.1) causes the APD to be operated at higher voltages to keep the gain constant (sec. 2.2). This leads to an increase of the internal fields in the sensor which leads to an increase in the excess noise factor. In addition, increased temperature increases the rate of collisions of charge carriers on the grid, generating more dark current. Both lead to an increase in shot noise. Therefore, to consider the worst possible noise performance, an operating temperature of $T_{op} = 125^\circ\text{C}$ is regarded which corresponds to the limit of the temperature in the LiDAR mission profile. According to the temperature coefficient $T_K = 1.5 \text{ V/K}$ (sec. 2.1), the APD then breaks down at $U = U_{br,125} \approx 350$ V. The case when the signal comes from 100 m distant targets is considered. For this purpose, a signal power of $2.2 \times 10^{-4} \text{ mW}$ and a background power of $2.2 \times 10^{-5} \text{ mW}$ are assumed in [40]. Sensor chips were studied there obtaining a total edge length of approximately 1 mm. It is assumed that the incident light is focused on the sensor in such a way that

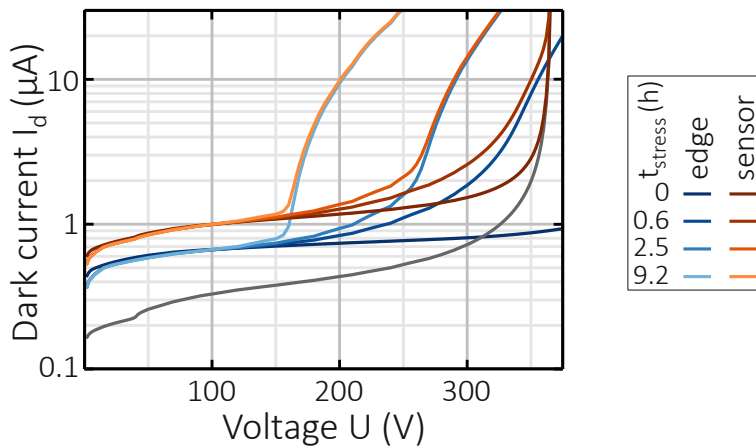


Figure 6.11: Simulation results of the APD most prone to degradation for dark current terms at 125°C from the center of the APD $I_{d,center}$ (gray curve), from the edge $I_{d,edge}$ (blue curves), and the resulting dark currents of the whole sensor I_d (orange curves) for different stress times t_{stress} .

it is completely irradiated with light. That is, the focused beam has a diameter of 1.4 mm and a cross-sectional area of 0.015 cm². From this, the intensities of the signal $P_S \approx 1.5 \times 10^{-2}$ mW/cm² and the background illumination $P_B \approx 1.5 \times 10^{-3}$ mW/cm² are determined. The functional parameters are determined in the following under the mentioned operation conditions, whereas the time scale of degradation is governed by the conditions of the mentioned stressors (T_{stress} , U_{stress} , P_{stress}).

Dark current

First, the dark current terms are investigated. In order to determine the edge contribution $I_{d,edge}$, the sensor is simulated in the dark and without avalanche implant. The resulting dark current is then scaled according to the ratio of the volume of the edge region to the total volume of the sensor and set equal to $I_{d,edge}$. This approach somewhat underestimates the real value of $I_{d,edge}$. The contribution of the center $I_{d,center}$ is determined by simulating the sensor in the dark with avalanche implant. $I_{d,edge}$ is then subtracted from the resulting dark current. The total dark current is the sum of both contributions. The corresponding dark current terms are plotted against voltage U for different times under stress t_{stress} in figure 6.11. The curve of the center dark current $I_{d,center}$ increases rather flatly at low voltages. In this voltage range, the level of dark current is comparatively low with $I_{d,center} < 0.5 \mu\text{A}$. The closer the voltage is to the breakdown voltage $U_{br,125} \approx 350$ V, the steeper the current increases until it abruptly approaches infinity at $U = U_{br,125}$. This typical behavior of an APD is discussed in section 2.1. The dark current from the edge $I_{d,edge}$ is shown for four times t_{stress} . Before degradation ($t_{stress} = 0$), the curve rises relatively flat with voltage such that $0.35 \mu\text{A} \geq I_{d,edge} < 1 \mu\text{A}$. With time, the $I_{d,edge}$ curve changes. After a time of $t_{stress} = 0.6$ h it already rises above a value of $1 \mu\text{A}$ at $U \approx 240$ V and becomes much steeper thereafter. After $t_{stress} = 2.5$ h the curve exceeds over $1 \mu\text{A}$ at about 200 V and runs much steeper afterwards. After $t_{stress} = 9.2$ h the curve kinks above $1 \mu\text{A}$ already

at about 155 V and runs very steeply afterwards. Thereby the slope after the kink becomes steeper with increasing time t_{stress} . The total sensor dark current I_d calculated from the sum of $I_{d,edge}$ and $I_{d,center}$ is shown for the same times. Before degradation $t = 0$, it runs slightly above the dark current from the edge. At $U = U_{br,125}$ it kinks and runs with $I_{d,center}$ towards infinity. After $t_{stress} = 0.6$ h below 150 V the curve is the same as before the stress. Above 150 V its course gradually approaches that of $I_{d,edge}$ after 0.6 h. At $U > U_{br,125}$, it then runs with the current from the center $I_{d,center}$. After $t_{stress} = 2.5$ h the curve already kinks a little above 200 V and then runs together with the edge contribution. After $t_{stress} = 9.2$ h the curve kinks already at about 155 V and runs together with the edge contribution. A behavior similar to that of the edge dark current was observed in section 5.2 and 6.1.2 for the dark current during degradation. It could be attributed to the increase in the impact ionization rate in the edge. So, the kink and steep increase of the current $I_{d,edge}$ is an avalanche multiplication effect of the edge current.

In conclusion, the dark current at the edge of the sensor starts to breakdown during the time under stress. The breakdown voltage $U_{br,edge}$ decreases with an increase of t_{stress} . So that the edge breakdown occurs after long stress times at much lower voltages than the avalanche breakdown in the center of the sensor. If the sensor breaks through at the edge, its dark current contribution dominates the total dark current I_d . Even at voltages below $U_{br,edge}$, the edge provides a larger contribution to the total current I_d . Only in the avalanche breakdown of the center at $U = U_{br,center}$ the center dark current predominates in the early stage of degradation.

Photo current and gain

The contributions to the photo current $I_{ph,center}$ and $I_{ph,edge}$ are determined by illuminating either the optical area or the gap in the simulation. The total photo current I_{ph} is then equal to the sum of both. The resulting photo currents are shown in figure 6.12a plotted against voltage U for different times under stress t_{stress} . The photo current from the edge $I_{ph,edge}$ is very flat before stress ($t_{stress} = 0$) and has predominantly a value of 3 nA. After $t_{stress} = 0.6$ h the curve is the same as before stress at $U < 175$ V. At a voltage of about 175 V it rises more steeply above the curve before the stress. The curves after $t_{stress} = 2.5$ h and $t_{stress} = 9.2$ h are also the same as before the stress at rather low voltages. After $t_{stress} = 2.5$ h it starts to increase more steeply at about 160 V, running above that after $t_{stress} = 0.6$ h. After $t_{stress} = 9.2$ h it already starts to increase at about 150 V. Thereby it runs above the curve after $t_{stress} = 2.5$ h. The photo current from the center $I_{ph,center}$ runs in a way typical for the APD as discussed in section 2.1. The $I_{ph,center}$ - U curve thereby runs above 5 nA and at all times t_{stress}

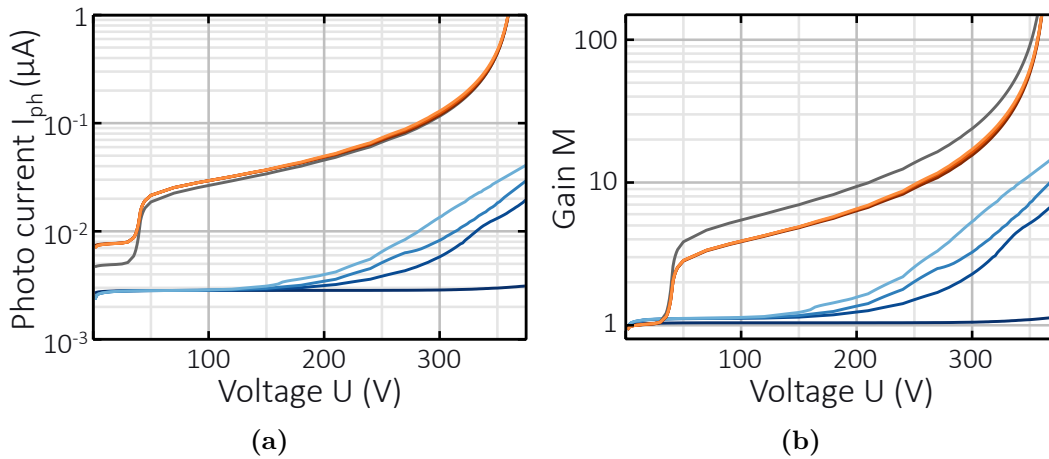


Figure 6.12: Simulation results of the APD most prone to degradation for a: Photo currents from center $I_{ph,center}$ (gray), edge $I_{ph,edge}$ (blue curves) and total photo current I_{ph} (orange curves) for different stress times t_{stress} . b: Gain in center M_{center} (gray), edge M_{edge} (blue curves) and total gain M (orange curves) for different stress times t_{stress} . For the color assignment of the curves, see the legend in figure 6.11.

almost an order of magnitude above the curves of $I_{ph,edge}$. The curves of the total photo current $I_{ph}(U)$ are approximately the same at any time t_{stress} . Above about 200 V they run exactly like the center $I_{ph,center}$ - U curve. Below that, the difference is rather small. The bending and subsequent increase of the photo current with voltage in the edge for $t_{stress} > 0$ is interpreted as a avalanche breakdown of the edge photo current just like the behavior of the dark current in the edge discussed above. With increasing time t_{stress} the breakdown occurs at lower voltages. The increase of the dark current $I_{d,edge}$ is steeper than for the photo current $I_{ph,edge}$, especially after long times t_{stress} . Thus, the breakdown in the edge is different for photo and dark current. It is weaker for the photo current. In conclusion, degradation leads to an avalanche multiplication of the photo current in the edge which is weaker than for the dark current. However, the photo current in the center is dominant and the photo current from the edge has a negligible influence on the total photo current I_{ph} even after degradation. For a diameter of $350 \mu\text{m}$, the active area is about $96000 \mu\text{m}^2$. The gap has a width of $30 \mu\text{m}$ and therefore an area of about $50000 \mu\text{m}^2$. Thus, in the center an area almost twice as large as in the edge is illuminated. In addition, the center is designed to increasingly multiply the photo current above 40 V with increasing voltage. Both lead to the dominance of the photo current in the center $I_{ph,center}$.

The gain of the photo current in center and edge can be determined from the respective photo currents $I_{ph,center}$ and $I_{ph,edge}$ according to equation 2.1. The gain of the whole sensor is also calculated from equation 2.1 and the total photo current, i.e. the orange curves in figure 6.12a. The resulting gain-voltage curves are shown in figure 6.12b for

different times t_{stress} . The gain of the photo current in the edge M_{edge} is very flat before stress ($t_{stress} = 0$) and has predominantly a value of 1. After $t_{stress} = 0.6$ h, M_{edge} is the same as before stress at $U < 175$ V. At $U > 175$ V it increases with voltage above the pre-stress curve. The curves after $t_{stress} = 2.5$ h and $t_{stress} = 9.2$ h are the same as before the stress at voltages below 175 V. After $t_{stress} = 2.5$ h it starts to increase with U at about 160 V and is above that after $t_{stress} = 0.6$ h. After $t_{stress} = 9.2$ h it already starts to increase with U at about 150 V. Thereby it runs above the curve after $t_{stress} = 2.5$ h. After $t_{stress} = 9.2$ h the M_{edge} - U curve reaches values above 10 at high voltages $U > 350$ V. The gain of the photo current in the center M_{center} behaves in the typical way for the APD as discussed in section 2.1. The M_{center} - U curve runs more than half an order of magnitude above the M_{edge} - U curves at voltages $U > 40$ V. At high voltages $U > 350$ V values above 100 are reached. The curves of the total gain $M(U)$ run approximately the same at any time t_{stress} . They are similar to those of the gain in the center $M_{center}(U)$ but slightly below.

In conclusion, the influence of the edge on the total gain M is rather weak as in the case of the photo current. Since the gain is generally based on the photo current, this is not surprising and the dominance of the center can again be attributed to the ratio of the areas of the active area and the gap. An APD most prone to degradation was studied here. Even in this case, the M - U and likewise the I_{ph} - U characteristics are only negligibly affected by the degradation phenomena.

Shot noise

In order to determine the excess noise factor in center F_{center} and edge F_{edge} , the multiplication field $E_{M,j}$ must be determined in the multiplication zones in center and edge as outlined in figure 6.10. It enters the excess noise F_j factor via the k factor as defined in equation 2.3. It is the quotient $k = \alpha_p/\alpha_n$ of the field dependent impact ionization rates of holes and electrons as they are defined in equation 2.16. There is an exponential relationship $F_j \propto \exp(-E_0/E_{M,j})$ where E_0 is a positive constant. Thus, particularly high fields have an exponentially large effect on the excess noise factor. The sensor is designed such that the field in the multiplication zone is approximately constant in the center. So in this area the average of the field is set equal to $E_{M,center}$. In the edge region, the calculation is less clear. Because of the exponential relationship between F and E_M , the average of the 0.01% highest field values was set equal to $E_{M,edge}$. The field distributions in each multiplication zone were extracted from the semiconductor device simulation results. The resulting values for the multiplication fields $E_{M,j}$ are shown in figure 6.13a. Their values in center and edge after different times t_{stress} is plotted against the voltage U . The multiplication field in the center

$E_{M,center}$ increases steeply from 0 to nearly 2.8×10^5 V/cm up to a voltage of 40 V. It then rises more flatly with voltage, reaching a value of about 3.3×10^5 V/cm at 350 V. The design goal is that the multiplication field in the center in the operation range is approximately 3×10^5 V/cm. Therefore, the APD is operated at voltages $U \geq 40$ V. Before stress ($t_{stress} = 0$), the multiplication field in the edge $E_{M,edge}$ increases approximately linearly with voltage from 0 at $U = 0$ to 2.3×10^5 V/cm at $U = 350$ V. After $t_{stress} = 0.6$ h, the field increases rapidly with voltage at voltages below about 30 V, where it already reaches a value of about 1.8×10^5 V/cm. After that, the increase with voltage is somewhat flatter. With 3×10^5 V/cm at $U = 150$ V it is as high as the field in the center. At higher voltages, the field in the edge is higher than in the center and reaches a value of 4.2×10^5 V/cm at $U = 350$ V. After $t_{stress} = 2.5$ h, $E_{M,edge}$ increases sharply with U to about 2×10^5 V/cm at 30 V. Thereafter, the slope with voltage is also flatter. However, the field at any voltage is above that after $t_{stress} = 0.6$ h. At $U \approx 80$ V it is about 2.9×10^5 V/cm and the same as the field in the center. At higher voltages, the field at the edge is higher, reaching a value of 4.3×10^5 V/cm at $U = 350$ V. After a time $t_{stress} = 9.2$ h, $E_{M,edge}$ also increases sharply with U to approximately 2.3×10^5 V/cm at 30 V. Thereafter, the slope is flatter with voltage. However, the field at any voltage is above that after $t_{stress} = 2.5$ h. At $U \approx 50$ V it is about 2.8×10^5 V/cm and equals the field in the center. At higher voltages, the field at the edge is higher, reaching a value of slightly more than 4.3×10^5 V/cm at $U = 350$. In conclusion, the multiplication field at the edge $E_{M,edge}$ increases with time t_{stress} at all voltages. In the operation range ($U \geq 40$ V) it reaches the same value as in the center with increasing time t_{stress} at decreasing voltages U . Subsequently, it runs above $E_{M,center}$ and after $t_{stress} = 9.2$ h it partly exceeds it more than 1×10^5 V/cm. This favors a higher excess noise factor in the edge than in the center, especially after long stress periods.

From the previously determined quantities and equations 6.1 and 6.2, the square of the shot noise current from center $\langle i_{shot}^2 \rangle_{center}$ and edge $\langle i_{shot}^2 \rangle_{edge}$ and finally the entire sensor $\langle i_{shot}^2 \rangle$ are determined. The respective noise current is then determined by calculating the root. The resulting curves are plotted against voltage for different times t_{stress} in figure 6.13b. Starting at $U = 0$ with a value slightly less than 2 nA, the shot noise current from the center $\sqrt{\langle i_{shot}^2 \rangle_{center}}$ increases with voltage. At about $U = 40$ V it increases rapidly to a value above 5 nA. Then it is rather flat, reaching a value of 40 nA at 300 V and increasing rapidly again at voltages $U \geq U_{br,125}$ and approaches infinity. The noise current from the edge $\sqrt{\langle i_{shot}^2 \rangle_{edge}}$ runs very flat before stress ($t_{stress} = 0$). Below 50 V it reaches a value slightly less than 3 nA. At $U = 350$ V it reaches a value of 4 nA. During degradation the curve below 100 V remains the same as before stress. At

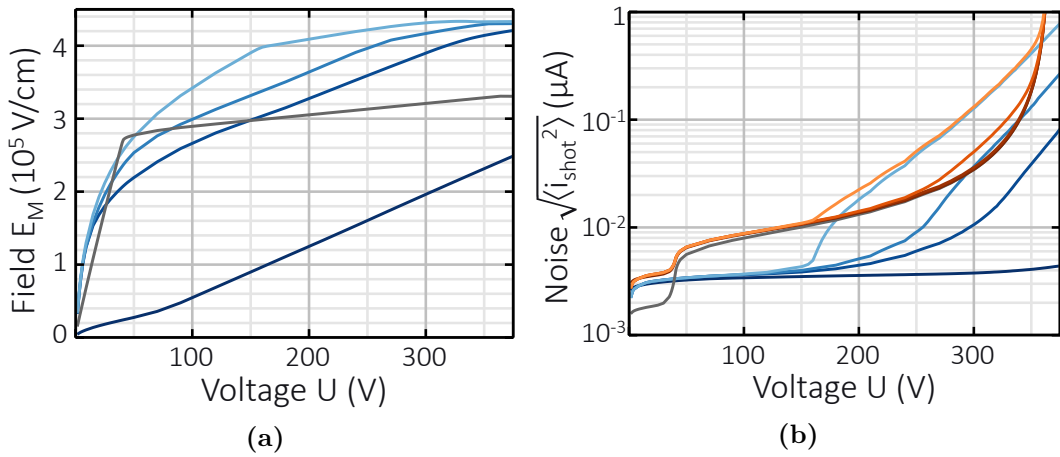


Figure 6.13: Simulation results of the APD most prone to degradation for a: The multiplication field E_M in the center (gray) and at the edge (blue curves) for different times t_{stress} . b: The shot noise current from the center $\sqrt{\langle i_{shot}^2 \rangle_{center}}$ (gray), from the edge $\sqrt{\langle i_{shot}^2 \rangle_{edge}}$ (blue curves) and of the whole sensor $\sqrt{\langle i_{shot}^2 \rangle}$ (orange curves) for different times t_{stress} . For the color assignment of the curves, see the legend in figure 6.11.

about 100 V it begins to rise above the pre-stress values. In this range, the slope becomes steeper with time t_{stress} . At 350 V the noise current is 40 nA after 0.6 h, 150 nA after 2.5 h and around 450 nA after 9.2 h. So, the higher t_{stress} , the higher the noise current at a certain voltage above 100 V. The shot noise current of the entire sensor $\sqrt{\langle i_{shot}^2 \rangle}$ runs slightly above the noise current from the edge at voltages below 40 V. At 40 V it rises rapidly to 5 nA and then runs slightly above the noise current from the center. Before and also after 0.6 h under stress, it thereby approaches the center noise with increasing voltage and is congruent above 150 V. After 2.5 h, the noise current below 250 V is congruent as before stress. At a voltage of 260 V it deviates to larger values. Then, it is slightly above the edge noise current after 2.5 h. Thereby it reaches a value of 200 nA at 350 V and is congruent with the center noise current when the center avalanche breakdown occurs at larger voltages. After 9.2 h, the noise current of the entire sensor is also congruent with the values before stress below 160 V. At a voltage of 160 V it deviates to larger values. It then starts to approach the noise current from the edge. At 250 V it is congruent with it. At 350 V it reaches a value of 480 nA. At voltages above the center avalanche breakdown it goes with the center noise.

In conclusion, the shot noise current of the investigated sensor very prone to degradation is strongly affected by degradation after $t_{stress} = 2.5$ h. It even triples at voltages above 250 V after 9.2 h under stress. The origin can be primarily broken down to the avalanche breakdown of the edge dark current. This is seen from the fact, that the noise current curve increases above the unstressed course for voltages above the

avalanche breakdown voltage of the edge dark current which decreases with increasing time under stress. Therefore, the noise degradation becomes more pronounced with time. Secondary, the multiplication field in the edge increases strongly with time which leads to an increase of the excess noise factor F_{edge} and an additional promotion of the edge noise.

6.2.3 Recap

Noise is a crucial parameter in LiDAR operation. If the noise is too high, small signals are not reliably resolved. It increases when the generation-recombination processes in the sensor become more pronounced during degradation. In the case of the up-down trend, the impact ionization rate increases predominantly due to the generation of oxide charges. The generation of dark current increases due to the generation of interface traps. It was concluded that the higher the concentration of empty electron traps in the oxide $N_{ox,max}$, the more the noise increases during degradation. The 1 ppm of sensors that fail at the same time is crucial for the lifetime in LiDAR application. This raised the problem that a lot more than one million devices would have to be tested. Here, an alternative approach was chosen. The empirical distribution of $N_{ox,max}$ values determined in section 5.4 was extrapolated to the tail of large values and the value corresponding to approximately 1 ppm was extracted. Sensors with this concentration of electron traps in the oxide correspond to those most prone to degradation. Their degradation was then simulated under extreme conditions. For this purpose, the APD degradation model developed in chapter 3 and calibrated in chapter 5 was used in cooperation with the numerical iteration approach tailor-made in chapter 4 to enable the self-consistent simulation of degradation. In this way, many important new insights could be gained. First of all it was revealed, that an avalanche breakdown of the dark current in the edge of the sensor evolves as an effect of degradation. Its breakdown voltage $U_{br,edge}$ decreases with increasing time under stress. The edge breakdown occurs after long stress times at much lower voltages than the avalanche breakdown in the center of the sensor, which leads to an edge contribution exceeding the center contribution by more than one order of magnitude. Furthermore, even for the studied most prone sensor only a negligible effect on the gain and photo current characteristic was observed. The multiplication field in the edge increases due to degradation. In the operation range it reaches the same value as in the center with increasing time at decreasing voltages U and exceeds the center field by up to more than 1×10^5 V/cm. This promotes an increase of the excess noise factor in the edge above that in the center. In literature, only studies considering the noise of the APD chip center are found. Here, the consideration was extended to the contributions from the chip edge

in order to include the effect of degradation. For the first time ever, it was revealed in this section, that the noise of APDs is highly affected by their degradation. It even triples at high voltages and long times under stress. The origin was primarily assigned to the avalanche breakdown of the edge dark current. Secondary, the increase of the multiplication field in the edge region causes an increase of the excess noise factor F_{edge} corresponding to an additional promotion of the edge noise contribution.

6.3 Degradation mode and estimation of life time

From the functional parameters determined in the previous section for an operation temperature of $T_{op} = 125^\circ\text{C}$, the signal-noise-ratio (SNR) for the detection of 100 m distant objects will be calculated. The time scale of degradation of the functional parameters was governed by the stressors (T_{stress} , U_{stress} , P_{stress}). It will be rescaled in order to estimate the life time of the simulated APD, which correspond to 1 ppm of the sensor population obtaining the same high concentration of oxide electron traps $N_{1\text{ppm}}$.

6.3.1 Degradation of signal-noise-ratio

The signal-noise-ratio is generally calculated according to:

$$SNR = \frac{I_S}{\sqrt{\langle i_{shot}^2 \rangle}} \quad (6.3)$$

The optical signal P_S evokes a signal current due to the photo-electric generation of charge carriers. This is generated in the sensor both below the gap and below the active area. At the edge it is multiplied by M_{edge} and at the center by M_{center} . The current I_S in equation 6.3 is the resulting signal current measured at the contacts of the APD. In the noise term in equation 6.3 and 6.1, the photo current includes the current I_B in addition to I_S , which is generated due to background illumination in the same way as I_S . The resulting SNR is plotted in figure 6.14 against voltage U for different times under stress t_{stress} . Starting at $U = 0$ and $SNR \approx 2.3$, it initially decreases with increasing voltage before stress ($t_{stress} = 0$), goes through a local minimum of about 2 at about 30 V, and increases rapidly at about 40 V. At 50 V it reaches a value of 3 and then slowly increases with voltage. At about 250 V it reaches its maximum of about 3.3 and then decreases. At about 320 V it drops below 3 and decreases rapidly with increasing voltage. After 0.6 h under stress, the SNR proceeds mostly as before stress. The only difference is that it is slightly smaller between 150 V and 320 V. After

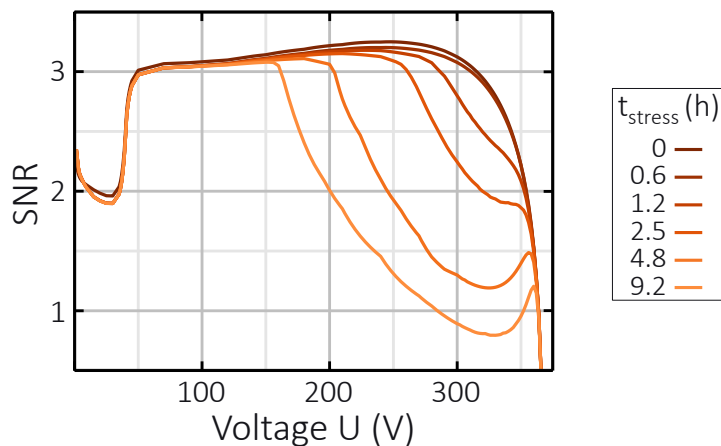


Figure 6.14: Signal-noise-ratio (SNR) simulated for the APD considered in section 6.2 against operation voltage U after different times under stress t_{stress} .

1.2 h the SNR runs the same as after 0.6 h at low voltages. At about 230 V, it kinks downward and is up to 0.5 smaller than before stress. At 350 V it meets the $SNR-U$ curve before stress. After 2.5 h the SNR is the same as after 0.6 h below about 210 V. It then also bends downward. In this case it is almost up to 1 smaller than before stress. At a little above 350 V it meets the $SNR-U$ curve before the stress. After 4.8 h the SNR is congruent with that after 0.6 h below about 180 V. Then it kinks downward and becomes up to about 1.8 smaller than before stress. It also forms a local minimum of about 1.2 at 325 V. At just below 360 V it meets the $SNR-U$ curve before the stress. After 9.2 h, the SNR runs the same as after 0.6 h below about 155 V. It then bends downward and becomes smaller than before the stress up to about 2.2. It also forms a local minimum of about 0.8 at 330 V. At just below 360 V it meets the $SNR-U$ curve before the stress.

A signal can be technically resolved at $SNR \geq 3$ [40]. Therefore, the optical signal P_S from 100 m distant objects, which was regarded here, can be resolved between $U = 50$ V and $U = 320$ V before sensor degradation. As discussed in the previous section, the noise due to degradation increases in this range and thus the SNR decreases with time. Consequently, the SNR in the range of $280 \text{ V} \leq U < 350 \text{ V}$ drops to values below $SNR = 1$ after 9.2 h under stress. In this case, it is both technically and theoretically no longer possible to resolve the signal. This means that the signal from 100 m distant objects cannot be resolved and the sensor no longer functions as required. So it fails as a result of degradation.

6.3.2 Estimation of life time for SNR degradation mode

Previously, the degradation of an automotive LiDAR APD was simulated under the condition of stress level 6 defined in section 5.2 and listed in table 5.1. It corresponds to an operation voltage of $U_{stress} = 380$ V, a temperature of $T_{stress} = 145$ °C, and an

illumination intensity of $P_{stress} = 20 \text{ mW/cm}^{-2}$. The results of the simulation finally led to the results in figure 6.14. It could be shown that the APD fails after 9.2 h under these conditions due to an SNR below 1. In section 5.1, it was discussed that within the mission profile of the automotive LiDAR application, a temperature of maximum $T_{op} = T_{max} = 125^\circ\text{C}$ is specified. The gain curves $M(U)$ in figure 6.12b were calculated for this temperature. In the application, values between $M = 20$ and $M = 50$ are common. This corresponds to voltages between 310 V and 350 V. It is therefore assumed that APDs in LiDAR application at $T_{op} = 125^\circ\text{C}$ operate at $U_{op} = 310 \text{ V}$. Further, it is assumed that the APD is permanently exposed to signal P_S and background radiation P_B during operation. As discussed in section 2.2, the signal P_S is often realized as rectangular pulses with duration of 10 ns. These are modulated with a frequency of 500 kHz. The time average of the signal intensity is then given by:

$$\langle P_S \rangle_t = P_S \cdot 10 \text{ ns} \cdot 500 \text{ kHz} \approx P_S \cdot 0.005$$

In total, the APD is then exposed to an intensity of $P_{op} = P_B + \langle P_S \rangle_t \approx 1.5 \times 10^{-3} \text{ mW/cm}^{-2}$. In order to determine the time after that the APD fails ($SNR < 1$) for the mentioned operation conditions (T_{op}, U_{op}, P_{op}), the quotients δ_T , δ_U and δ_P are determined from the correlations between the stressors and t_{max} in figure 5.7:

$$\delta_T = \frac{t_{max}(T = T_{op})}{t_{max}(T = T_{stress})} \quad \delta_U = \frac{t_{max}(U = U_{op})}{t_{max}(U = U_{stress})} \quad \delta_P = \frac{t_{max}(P = P_{op})}{t_{max}(P = P_{stress})}$$

This is done in parts by an interpolation between the data points. The time scale of degradation of the simulated stress conditions ($U_{stress} = 380 \text{ V}$, $T_{stress} = 145^\circ\text{C}$, $P_{stress} = 20 \text{ mW/cm}^{-2}$) is then rescaled to the assumed operation conditions ($T_{op} = 125^\circ\text{C}$, $U_{op} = 320 \text{ V}$, $P_{op} = 1.5 \times 10^{-3} \text{ mW/cm}^{-2}$) using the factor $\delta_{op} = \delta_T \delta_U \delta_P \approx 108$. Then, the time after which the APD has an $SNR < 1$ under the operations conditions and thus fails is $t_{fail} = 9.2 \text{ h} \cdot \delta_{op} \approx 1000 \text{ h}$. The simulated APD corresponds to the 1 ppm of all sensors most prone to degradation (sec. 6.2.1). So, 1 ppm of all sensors fail simultaneously after 1000 h of operation, because they can no longer detect objects at a distance of 100 m. In conclusion, the life time of this particular APD design under the mentioned most severe LiDAR operation conditions corresponds to $t_{life} \approx 1000 \text{ h}$. After that, signals from objects at a distance of 100 m can no longer be guaranteed to be reliably resolved.

6.3.3 Recap

In the previous section, an APD was modeled corresponding to the 1 ppm of all sensors most prone to degradation. The shot noise has been determined by simulation for the highest temperature in the LiDAR mission profile of 125 °C before and during degradation under extreme conditions. Therefrom, the signal-noise-ratio (SNR) was determined in this section. First time ever, the degradation mode of APDs in LiDAR application was identified. Before stress the SNR exceeds $SNR = 3$ in the voltage range of $50 \text{ V} \leq U < 320 \text{ V}$. The regarded small signal intensities of 100 m distant objects are therefore successfully resolved in this range. During degradation, the SNR decreases and drops below $SNR = 1$ in the range of $280 \text{ V} \leq U < 350 \text{ V}$ and the resolution of the signal becomes impossible in this range. The APD fails. Finally, the lifetime was estimated for this SNR degradation mode. In the case of the most severe operation conditions in LiDAR operation, it amounts to only $t_{life} \approx 1000 \text{ h}$. This is another very important new information as the estimated low lifetime indicates the need of design optimization.

6.4 Summary

Stress experiments have been performed on APDs. Sensors of the studied design are currently tested and installed in automotive LiDAR modules. Two different degradation trends have emerged from the investigations. Both trends were self-consistently simulated with the calibrated degradation model in excellent agreement. Their occurrence and degradation extent and pace does not correlate with the breakdown voltage. Furthermore, the time scale of APD and PIN test sensor degradation studied in chapter 5 is the same under the same conditions. Both share a similar edge structure. The results of the simulation further proved, that the degradation of the sensors occurs exclusively in their edge region. Therefore, it was concluded that degradation is only dependent on the edge design. This is a very important insight into APD degradation, as it indicates that only design improvements of the sensor edge will affect their degradation. In addition all the results obtained so far on the basis of the investigations on PIN test sensors can be transferred to APDs. Moreover, another important new insight is generated: One of the degradation trends reflects an increase of the impact ionization rate in the edge region of the APD. Around 40 % of the more than 30 studied sensors showed this degradation behavior. While the second was observed for 60 % of all studied sensors and corresponds to a decrease of the impact ionization rate in their edge region. This is very significant for the noise which increases when the generation-recombination processes in the sensor become more pronounced during

degradation. High noise currents are devastating in LiDAR operation, because small signals are potentially not reliably resolved.

In order to estimate the impact of the degradation induced increase of noise on the LiDAR application, the empirical distribution of $N_{ox,max}$ values determined in section 5.4 was extrapolated to the tail of high values and the value $N_{1\text{ppm}}$ corresponding to 1 ppm of all sensors was extracted. Sensors obtaining this concentration of electron traps in the oxide are very prone to degradation. Their degradation was then studied under extreme stress conditions. For this purpose, the APD degradation model developed in chapter 3 and calibrated in chapter 5 was used in cooperation with the numerical iteration approach tailor-made in chapter 4 to enable the self-consistent simulation of degradation. In this way, many important new insights could be gained.

First of all it was revealed, that an avalanche breakdown of the dark current in the edge of the sensor evolves as an effect of degradation which causes an edge contribution exceeding the center contribution by more than one order of magnitude. Furthermore, even for the studied very prone sensor only a negligible effect on the gain and photo current characteristic was observed. It is therefore concluded, that the impact of degradation on these characteristics is negligible. The electric field in the sensor edge increases due to degradation and even exceeds the center multiplication field by up to more than 1×10^5 V/cm. This promotes an increase of the excess noise factor in the edge above that in the center. In order to determine the impact of degradation on the noise current, the simplifications in literature considering only the APD center were extended to its edge contributions to include the effect of degradation. It was revealed, that the noise of APDs is highly affected by their degradation. It even triples at high voltages and long times under stress. The origin was exclusively assigned to the edge contribution and primarily to the avalanche breakdown of the edge dark current caused by degradation. Secondary, the field increase in the sensor edge causes an increase of the excess noise factor F_{edge} corresponding to an additional promotion of the edge noise contribution.

Therefrom, the signal-noise-ratio (SNR) was determined. For the first time ever, the SNR degradation mode of APDs in LiDAR application was identified. Before stress it exceeds $SNR = 3$ and the regarded small signal intensities of 100 m distant objects are successfully resolved. During degradation, the SNR decreases and drops below $SNR = 1$. Then, the resolution of the signal is impossible and the APD fails. Finally, the lifetime was estimated for this newly revealed SNR degradation mode. In the case of the most severe operation conditions in LiDAR operation, it amounts to only $t_{life} \approx 1000$ h. This is another very important new information as the estimated low lifetime confirms the need of design optimization.

Chapter 7

Conclusion

Due to the topicality of the research area and conceivably also to the secrecy of industry knowledge, research results concerning APD aging under near-application LiDAR conditions were not available. Also, knowledge about failure mechanisms in APDs was meager, so a quantitative understanding of APD aging especially in LiDAR application did not exist at all, so far. The central results of this thesis establish a fundamental understanding regarding the underlying physics of silicon APD aging and its effects in automotive LiDAR applications.

A novel degradation model was developed, encompassing a wide range of processes, treating fundamental aspects of negative oxide charge generation such as the energy distribution of the electron population at the Si:SiO₂ interface, the derived probability of electrons obtaining enough energy and sufficient momentum towards interface to be injected into the oxide, the capture in preexisting oxide traps, the liberation from them via impact ionization and the relaxation from shallow into deep trap levels. Furthermore, interface trap generation is covered, driven by Si-H bond heating and rupture due to interaction with electrons, opposed by Si-H reformation and finally controlled by diffusion of free hydrogen away from the interface. Each of these two generation processes were casted into a time differential equation that together reflect the degradation process. So far, no model is known covering the kinetics of APD degradation comprehensively in such deep detail.

The degradation process is promoted by electron currents and electric fields inside the device. In turn, oxide charges and interface traps affect internal currents and fields. Initiated by this feedback, a coupled problem arose, which was impossible to be solved analytically. In order to tackle this challenge, a sophisticated numerical iteration approach was tailor-made and successfully solved this problem self-consistently in a tandem procedure combining the simulation of sensor degradation and the device simulator. In a coupled simulation, the device simulator determines currents and fields

inside the device by solving the Poisson and continuity equations. These serve as input to the simulation of the degradation model. It determines the generated oxide charges and interface traps within a defined time window and updates their concentrations. Iteration over this procedure finally yield the time course of degradation. This already led to novel insights into the APD degradation behavior: The generation of negative oxide charges was identified to cause a drift of the impact ionization rate in the sensor edge. The generation of interface traps promotes the accumulation of negative oxide charges by their supply of thermally generated dark current. In this way, degradation is about 14% faster.

In order to reflect not only the causal relations of APD degradation but also to capture its real manifestation, the model was calibrated on real world degradation data obtained from stress experiments conducted under seven stress conditions on five PIN test sensors each. Two parameters reflecting pace and extend of the degradation course of every sensor were defined in order to represent the results. In this way, the essential information of degradation data consisting of hundreds of dark current curves are extracted and compressed into a scatter plot of these two parameters. In this framework, the entire set of experimental results found its complete physical interpretation in conjunction with the degradation model which accomplished excellent agreement. Thereby, the following results were achieved. The time scale of degradation is predominantly governed by the operation conditions. In general, the degradation pace increases with temperature T , voltage U and intensity of illumination P_{opt} whereas the impact of temperature is particularly strong due to the significant participation of the dark current during degradation. The extent of degradation is determined by the properties of the sensor oxide layer including the concentration of preexisting positive charges and electron traps in the oxide. From the correlation between these properties, the oxygen vacancy was concluded to be the dominant trap in the oxide layer of the studied sensors. Even an empirical distribution of oxide properties between individual sensors was provided. These novel research results expand the picture of APD degradation. Moreover, with the calibrated degradation model and its self-consistent simulation approach, an elaborated powerful tool was available to be applied to APDs. Further crucial new insights were extracted from stress experiments on APDs. Sensors of the studied design are currently tested and installed in automotive LiDAR modules. Two different degradation trends have emerged from the investigations. Again, the self-consistent simulation of the calibrated degradation model demonstrated excellent agreement with experimental data. Thereby, it was revealed, that one of the degradation trends reflects an increase of the impact ionization rate in the APD edge. Around 40% of the more than 30 studied sensors showed this degradation behavior. While the

second was observed for 60 % of all studied sensors and corresponds to a decrease of the impact ionization rate in their edge region. The increase of the impact ionization rate indicates a major problem, as noise increases when the generation-recombination processes in the sensor strengthen during degradation. High noise currents are devastating in LiDAR operation, because small signals from very distant objects are potentially not reliably resolved. In order to estimate the impact of the degradation induced increase of noise on the LiDAR application, the previously determined empirical distribution of individual sensor properties was extrapolated to the tail of high electron trap concentrations in the oxide where sensors are very prone to degradation. Furthermore, available noise models considering only the APD center were extended to its edge contribution which includes the effect of degradation. Application of the calibrated APD degradation model and its self-consistent simulation approach disclosed, that the APD noise is highly affected during aging. It even triples at high voltages and long times under stress. The origin was exclusively assigned to the edge contribution. There, the avalanche breakdown of the edge dark current caused by degradation is the main initiator. Consequently, for the first time ever, the signal-noise-ratio (SNR) degradation mode of APDs in LiDAR application was identified. During degradation, the SNR degrades from a value above 3, where small signals from 100 m distant objects are technically well resolved, to a value below 1, where even theoretically a resolution is impossible and the APD fails. Finally, the picture of APD degradation was completed by the estimation of lifetime for this degradation mode. In the case of the most severe conditions in LiDAR operation of 125 °C, it amounts to only 1000 h, which falls much below the requirements of the automotive industry of several decades.

The aforementioned results of aging studies confirm the need of APD design improvement. Moreover, they indicate, that the degradation of the sensors occurs exclusively in their edge region. Therefore, only design improvements of the sensor edge will affect their degradation. When optimizing the robustness of the design against aging, all changes are regarded purposeful that slow degradation by reducing its drivers or reduce its effects. The drivers of degradation are high fields and currents at the Si:SiO₂ interface in the sensor edge. Corresponding concepts are proposed in the following.

The application of deuterium as interface passivator instead of hydrogen would mitigate the generation of interface traps as deuterium is much more massive [65, 75, 81]. It was revealed in this work, that the generation of negative oxide charges which is the reason for the increasing noise during operation would be decelerated by around 14 %. Experimental data indicated the dark current to participate strongly in degradation. Moreover, its multiplication in the edge region is the main reason for the increase in

noise. The edge dark current is fed by a surface leakage current between the p and n side. A sufficiently high p doping processed at the silicon surface between the p and n contacts would prevent its inversion and therefore cancel out the formation of this conduction channel.

The most promising optimization would be so-called guard rings. In the case of the investigated sensors they correspond to an n doping in the form of a ring around the sensor center between the n and p contact. In [242, 243] it was shown that a floating guard ring strongly lowers the fields at the Si:SiO₂ interface. Moreover, the guard rings could be connected to a circuit. This yields the advantage that a large portion of the edge current would drain off into the guard ring. Ideally, there would be no noise contribution from the edge and the degradation would be immensely suppressed.

List of symbols

I_d	Dark current
I_{ph}	Photo current
M	Gain
$\langle i_{shot}^2 \rangle$	Shot noise current square
N_{ox}	Concentration of negative oxide charges, i.e. electrons trapped in the oxide
$N_{ox,max}$	Concentration of preexisting oxide electron traps
$N_{ox,init}$	Concentration of preexisting positive oxide fixed charges
γ_0	Relaxation rate of electrons from shallow into deep oxide trap levels
N_{it}	Concentration of Si:SiO ₂ interface traps
$N_{it,max}$	Concentration limit of Si:SiO ₂ interface traps
$N_{it,init}$	Concentration of Si:SiO ₂ interface traps after H annealing
$N_{H,IF}$	Concentration of free hydrogen at the Si:SiO ₂ interface

Bibliography

- [1] J. WANG, K. LI AND X.-Y. LU: *Chapter 5 - Effect of Human Factors on Driver Behavior*, in *Advances in Intelligent Vehicles*, (Ed. by Y. CHEN AND L. LI), pp. 111–157, Academic Press, Boston, ISBN 978-0-12-397199-9 (2014). doi:<https://doi.org/10.1016/B978-0-12-397199-9.00005-7>
- [2] S. BHARADWAJ, S. BALLARE, ROHIT AND M. K. CHANDEL: *Impact of congestion on greenhouse gas emissions for road transport in Mumbai metropolitan region*, *Transportation Research Procedia*, vol. 25: pp. 3538–3551, world Conference on Transport Research - WCTR 2016 Shanghai. 10-15 July 2016 (2017). doi:<https://doi.org/10.1016/j.trpro.2017.05.282>
- [3] I. KIM, R. J. MARTINS, J. JANG, T. BADLOE, S. KHADIR, H.-Y. JUNG, H. KIM, J. KIM, P. GENEVET AND J. RHO: *Nanophotonics for light detection and ranging technology*, *Nature Nanotechnology*, vol. 16, no. 5: pp. 508–524 (2021). doi:[10.1038/s41565-021-00895-3](https://doi.org/10.1038/s41565-021-00895-3)
- [4] Y. LI AND J. IBANEZ-GUZMAN: *Lidar for Autonomous Driving: The Principles, Challenges, and Trends for Automotive Lidar and Perception Systems*, *IEEE Signal Processing Magazine*, vol. 37, no. 4: pp. 50–61 (2020). doi:[10.1109/MSP.2020.2973615](https://doi.org/10.1109/MSP.2020.2973615)
- [5] B. BEHROOZPOUR, P. A. M. SANDBORN, M. C. WU AND B. E. BOSER: *Lidar System Architectures and Circuits*, *IEEE Communications Magazine*, vol. 55, no. 10: pp. 135–142 (2017). doi:[10.1109/MCOM.2017.1700030](https://doi.org/10.1109/MCOM.2017.1700030)
- [6] D. J. LUM: *Ultrafast time-of-flight 3D LiDAR*, *Nature Photonics*, vol. 14, no. 1: pp. 2–4 (2020). doi:[10.1038/s41566-019-0568-2](https://doi.org/10.1038/s41566-019-0568-2)
- [7] M.-C. AMANN, T. M. BOSCH, M. LESCURE, R. A. MYLLYLAE AND M. RIOUX: *Laser ranging: a critical review of unusual techniques for distance measurement*, *Optical Engineering*, vol. 40, no. 1: pp. 10 – 19 (2001). doi:[10.1117/1.1330700](https://doi.org/10.1117/1.1330700)

- [8] R. O. DUBAYAH AND J. B. DRAKE: *Lidar Remote Sensing for Forestry*, Journal of Forestry, vol. 98, no. 6: pp. 44–46 (2000). doi:10.1093/jof/98.6.44
- [9] S. T. S. HOLMSTROM, U. BARAN AND H. UREY: *MEMS Laser Scanners: A Review*, Journal of Microelectromechanical Systems, vol. 23, no. 2: pp. 259–275 (2014). doi:10.1109/JMEMS.2013.2295470
- [10] H. W. YOO, N. DRUML, D. BRUNNER, C. SCHWARZL, T. THURNER, M. HENNECKE AND G. SCHITTER: *MEMS-based lidar for autonomous driving*, e & i Elektrotechnik und Informationstechnik, vol. 135, no. 6: pp. 408–415 (2018). doi:10.1007/s00502-018-0635-2
- [11] V. MILANOVIĆ, A. KASTURI, H. J. KIM AND F. HU: *Iterative learning control algorithm for greatly increased bandwidth and linearity of MEMS mirrors in LiDAR and related imaging applications*, in *MOEMS and Miniaturized Systems XVII*, (Ed. by W. PIYAWATTANAMETHA, Y.-H. PARK AND H. ZAPPE), vol. 10545, pp. 242 – 256, International Society for Optics and Photonics, SPIE (2018)
- [12] B. L. STANN, J. F. DAMMANN AND M. M. GIZA: *Progress on MEMS-scanned lidar*, in *Laser Radar Technology and Applications XXI*, (Ed. by M. D. TURNER AND G. W. KAMERMAN), vol. 9832, pp. 197 – 205, International Society for Optics and Photonics, SPIE (2016)
- [13] D. WANG, C. WATKINS AND H. XIE: *MEMS Mirrors for LiDAR: A Review*, Micromachines, vol. 11, no. 5 (2020). doi:10.3390/mi11050456
- [14] M. J. HECK: *Highly integrated optical phased arrays: photonic integrated circuits for optical beam shaping and beam steering*, Nanophotonics, vol. 6, no. 1: pp. 93–107 (2017). doi:doi:10.1515/nanoph-2015-0152
- [15] R. FATEMI, B. ABIRI, A. KHACHATURIAN AND A. HAJIMIRI: *High sensitivity active flat optics optical phased array receiver with a two-dimensional aperture*, Opt. Express, vol. 26, no. 23: pp. 29983–29999 (2018). doi:10.1364/OE.26.029983
- [16] C. V. POULTON, M. J. BYRD, P. RUSSO, E. TIMURDOGAN, M. KHANDAKER, D. VERMEULEN AND M. R. WATTS: *Long-Range LiDAR and Free-Space Data Communication With High-Performance Optical Phased Arrays*, IEEE Journal of Selected Topics in Quantum Electronics, vol. 25, no. 5: pp. 1–8 (2019). doi:10.1109/JSTQE.2019.2908555
- [17] C.-P. HSU, B. LI, B. SOLANO-RIVAS, A. R. GOHIL, P. H. CHAN, A. D. MOORE AND V. DONZELLA: *A Review and Perspective on Optical Phased Array*

-
- for *Automotive LiDAR*, IEEE Journal of Selected Topics in Quantum Electronics, vol. 27, no. 1: pp. 1–16 (2021). doi:10.1109/JSTQE.2020.3022948
- [18] S. CHUNG, M. NAKAI, S. IDRES, Y. NI AND H. HASHEMI: *19.1 Optical Phased-Array FMCW LiDAR with On-Chip Calibration*, in *2021 IEEE International Solid-State Circuits Conference (ISSCC)*, vol. 64, pp. 286–288 (2021). doi:10.1109/ISSCC42613.2021.9366004
- [19] J. LAMBERT, A. CARBALLO, A. M. CANO, P. NARKSRI, D. WONG, E. TAKEUCHI AND K. TAKEDA: *Performance Analysis of 10 Models of 3D LiDARs for Automated Driving*, IEEE Access, vol. 8: pp. 131699–131722 (2020). doi:10.1109/ACCESS.2020.3009680
- [20] R. HALTERMAN AND M. BRUCH: *Velodyne HDL-64E lidar for unmanned surface vehicle obstacle detection*, in *Unmanned Systems Technology XII*, (Ed. by G. R. GERHART, D. W. GAGE AND C. M. SHOEMAKER), vol. 7692, pp. 123 – 130, International Society for Optics and Photonics, SPIE (2010)
- [21] B. SCHWARZ: *Mapping the world in 3D*, Nature Photonics, vol. 4, no. 7: pp. 429–430 (2010). doi:10.1038/nphoton.2010.148
- [22] M. KUTILA, P. PYYKÖNEN, H. HOLZHÜTER, M. COLOMB AND P. DUTHON: *Automotive LiDAR performance verification in fog and rain*, in *2018 21st International Conference on Intelligent Transportation Systems (ITSC)*, pp. 1695–1701 (2018). doi:10.1109/ITSC.2018.8569624
- [23] C. RABLAU: *LIDAR - A new (self-driving) vehicle for introducing optics to broader engineering and non-engineering audiences*, in *Fifteenth Conference on Education and Training in Optics and Photonics: ETOP 2019*, Optical Society of America (2019). doi:10.1364/ETOP.2019.11143_138
- [24] J. WOJTANOWSKI, M. ZYGMUNT, M. KASZCZUK, Z. MIERCZYK AND M. MUZAL: *Comparison of 905 nm and 1550 nm semiconductor laser rangefinders' performance deterioration due to adverse environmental conditions*, Opto-Electronics Review, vol. 22, no. 3: pp. 183–190 (2014). doi:10.2478/s11772-014-0190-2
- [25] R. RORIZ, J. CABRAL AND T. GOMES: *Automotive LiDAR Technology: A Survey*, IEEE Transactions on Intelligent Transportation Systems, pp. 1–16 (2021). doi:10.1109/TITS.2021.3086804

- [26] Z. AHMAD, S.-I. KUO, Y.-C. CHANG, R.-L. CHAO, N. NASEEM, Y.-S. LEE, Y.-J. HUNG, H.-M. CHEN, J. CHEN, C. S. GOH AND J.-W. SHI: *Avalanche Photodiodes With Dual Multiplication Layers and Ultra-High Responsivity-Bandwidth Products for FMCW Lidar System Applications*, IEEE Journal of Selected Topics in Quantum Electronics, vol. 28, no. 2: pp. 1–9 (2022). doi:10.1109/JSTQE.2021.3062637
- [27] K. PASQUINELLI, R. LUSSANA, S. TISA, F. VILLA AND F. ZAPPA: *Single-Photon Detectors Modeling and Selection Criteria for High-Background LiDAR*, IEEE Sensors Journal, vol. 20, no. 13: pp. 7021–7032 (2020). doi:10.1109/JSEN.2020.2977775
- [28] P. VINES, K. KUZMENKO, J. KIRDODA, D. C. S. DUMAS, M. M. MIRZA, R. W. MILLAR, D. J. PAUL AND G. S. BULLER: *High performance planar germanium-on-silicon single-photon avalanche diode detectors*, Nature Communications, vol. 10, no. 1: p. 1086 (2019). doi:10.1038/s41467-019-08830-w
- [29] M. WARREN: *Automotive LIDAR Technology*, pp. C254–C255 (2019). doi:10.23919/VLSIC.2019.8777993
- [30] Z. ANTUNOVIC, I. BRITVITCH, K. DEITERS, N. GODINOVIC, Q. INGRAM, A. KUZNETSOV, Y. MUSIENKO, I. PULJAK, D. RENKER, S. REUCROFT, R. RUSACK, T. SAKHELASHVILI, A. SINGOVSKI, I. SORIC AND J. SWAIN: *Radiation hard avalanche photodiodes for the CMS detector*, Nuclear Instruments and Methods in Physics Research Section A: Accelerators, Spectrometers, Detectors and Associated Equipment, vol. 537, no. 1: pp. 379–382, proceedings of the 7th International Conference on Inorganic Scintillators and their Use in Scientific and Industrial Applications (2005). doi:https://doi.org/10.1016/j.nima.2004.08.047
- [31] E. ISHIMURA, E. YAGYU, M. NAKAJI, S. IHARA, K. YOSHIARA, T. AOYAGI, Y. TOKUDA AND T. ISHIKAWA: *Degradation Mode Analysis on Highly Reliable Guardring-Free Planar InAlAs Avalanche Photodiodes*, J. Lightwave Technol., vol. 25, no. 12: pp. 3686–3693 (2007)
- [32] Y. TASHIRO, K. TAGUCHI, Y. SUGIMOTO, T. TORIKAI, K. NISHIDA AND K. TAGUCHI: *Degradation modes in planar structure $In_{0.53}Ga_{0.47}As$ photodetectors*, Journal of Lightwave Technology (1983)
- [33] J. VERDEBOUT AND R. L. BOOKER: *Degradation of native oxide passivated silicon photodiodes by repeated oxide bias*, Journal of Applied Physics, vol. 55, no. 2: pp. 406–412 (1984). doi:10.1063/1.333088

-
- [34] J. J.-S. HUANG, Y.-H. JAN, H. CHEN, H. S. CHANG, C. NI AND E. CHOU: *Predictive Reliability Model of 10G/25G Mesa-Type Avalanche Photodiode Degradation*, Applied Physics Research, vol. 8: p. 66 (2016). doi:10.5539/apr.v8n3p66
- [35] S. SZE AND K. NG: *Physics of Semiconductor Devices*, John Wiley & Sons, Inc. (2008)
- [36] *Opto Semiconductor Handbook*, chapter 2: si photodiodes Edition, Hamamatsu Photonics (2018)
- [37] M. A. GREEN: *Self-consistent optical parameters of intrinsic silicon at 300K including temperature coefficients*, Solar Energy Materials and Solar Cells, vol. 92, no. 11: pp. 1305–1310 (2008). doi:https://doi.org/10.1016/j.solmat.2008.06.009
- [38] FIRST SENSOR AG AS PART OF TE CONNECTIVITY: *Part Description AD230-9 TO*, technical report (Order # 3001344)
- [39] R. MCINTYRE: *Multiplication noise in uniform avalanche diodes*, IEEE Transactions on Electron Devices, vol. ED-13, no. 1: pp. 164–168 (1966). doi:10.1109/T-ED.1966.15651
- [40] A. BUCHNER, S. HADRATH, R. BURKARD, F. M. KOLB, J. RUSKOWSKI, M. LIGGES AND A. GRABMAIER: *Analytical Evaluation of Signal-to-Noise Ratios for Avalanche- and Single-Photon Avalanche Diodes*, Sensors, vol. 21, no. 8 (2021). doi:10.3390/s21082887
- [41] M. ANDERSSON AND J. KJORNBERG: *Design of Lidar system*, Master thesis, Lund University (2014)
- [42] TEXAS INSTRUMENTS: *LiDAR Pulsed Time of Flight Reference Design*, TI Designs
- [43] *How to measure lifetime for Robustness Validation – step by step*, Robustness Validation Forum - ZVEI: German Electrical and Electronic Manufacturers ‘Association e.V. - Electronic Components and Systems (ECS) Division (2012)
- [44] *Handbook for Robustness Validation of Semiconductor Devices in Automotive Applications*, 3. Edition, ZVEI: Zentralverband Elektrotechnik- und Elektronikindustrie e. V. (German Electrical and Electronic Manufacturers‘ Association) - Electronic Components and Systems Division (2015)

- [45] M. BARKE, M. KÄRGEL, W. LU, F. SALFELDER, L. HEDRICH, M. OLBRICH, M. RADETZKI AND U. SCHLICHTMANN: *Robustness validation of integrated circuits and systems*, in *2012 4th Asia Symposium on Quality Electronic Design (ASQED)*. doi:10.1109/ACQED.2012.6320491
- [46] SAE, (Editor): *Handbook for Robustness Validation of Semiconductor Devices in Automotive Applications*, SAE International Standard J1879 (2014)
- [47] *AEC Q100*
- [48] A. BADIHI, B. EITAN, I. COHEN AND J. SHAPPIR: *Current induced trap generation in SiO₂*, Applied Physics Letters, vol. 40, no. 5: pp. 396–398 (1982). doi:10.1063/1.93115
- [49] A. H. EDWARDS: *Interaction of H and H₂ with the silicon dangling orbital at the <111> Si/SiO₂ interface.*, Physical review. B, Condensed matter, vol. 44: pp. 1832–1838 (1991)
- [50] D. J. LEPINE: *Spin-Dependent Recombination on Silicon Surface*, Phys. Rev. B, vol. 6: pp. 436–441 (1972). doi:10.1103/PhysRevB.6.436
- [51] T. KAWAUCHI, H. YONEMURA, S. KISHIMOTO AND K. FUKUTANI: *Hydrogen Redistribution and Performance Improvement of Silicon Avalanche Photodiode by Low-Temperature Annealing*, IEEE Electron Device Letters, vol. 33, no. 8: pp. 1162–1164 (2012). doi:10.1109/led.2012.2200451
- [52] L. A. RAGNARSSON AND P. LUNDGREN: *Electrical characterization of P_b centers in (100) Si-SiO₂ structures: The influence of surface potential on passivation during post metallization anneal*, Journal of Applied Physics, vol. 88, no. 2: pp. 938–942 (2000). doi:10.1063/1.373759
- [53] M. J. UREN, J. H. STATHIS AND E. CARTIER: *Conductance measurements on P_b centers at the (111) Si:SiO₂ interface*, Journal of Applied Physics, vol. 80, no. 7: pp. 3915–3922 (1996). doi:10.1063/1.363349
- [54] J. ALBOHN, W. FUSSEL, N. D. SINH, K. KLIEFOTH AND W. FUHS: *Capture cross sections of defect states at the Si/SiO₂ interface*, Journal of Applied Physics, vol. 88, no. 2: pp. 842–849 (2000). doi:10.1063/1.373746
- [55] E. YABLONOVITCH, R. M. SWANSON, W. D. EADES AND B. R. WEINBERGER: *Electron-hole recombination at the Si-SiO₂ interface*, Applied Physics Letters, vol. 48, no. 3: pp. 245–247 (1986). doi:10.1063/1.96570

-
- [56] D. VUILLAUME, R. BOUCHAKOUR, M. JOURDAIN AND J. C. BOURGOIN: *Capture cross section of Si-SiO₂ interface states generated during electron injection*, Applied Physics Letters, vol. 55, no. 2: pp. 153–155 (1989). doi:10.1063/1.102397
- [57] D. VUILLAUME, D. GOGUENHEIM AND G. VINCENT: *New insights on the electronic-properties of the trivalent silicon defects at oxidized (100) silicon surfaces*, Applied Physics Letters, vol. 57, no. 12: pp. 1206–1208 (1990). doi:10.1063/1.103486
- [58] E. AVNI, L. LOEV AND J. SHAPPIR: *Temperature effects on electron trap generation and occupation in SiO₂*, Journal of Applied Physics, vol. 63, no. 8: pp. 2700–2703 (1988). doi:10.1063/1.340988
- [59] Y. NISSAN-COHEN, J. SHAPPIR AND D. FROHMAN-BENTCHKOWSKY: *Characterization of simultaneous bulk and interface high-field trapping effects in SiO₂*, in *1983 International Electron Devices Meeting*, pp. 182–185. doi:10.1109/IEDM.1983.190471
- [60] B. A. McDONALD: *Avalanche degradation of h_{FE}* , IEEE Transactions on Electron Devices, vol. ED17, no. 10: p. 871 (1970). doi:10.1109/t-ed.1970.17089
- [61] C. M. HU, S. C. TAM, F. C. HSU, P. K. KO, T. Y. CHAN AND K. W. TERRILL: *Hot-electron-induced MOSFET degradation - model, monitor, and improvement*, IEEE Transactions on Electron Devices, vol. 32, no. 2: pp. 375–385 (1985)
- [62] D. A. BUCHANAN, A. D. MARWICK, D. J. DIMARIA AND L. DORI: *Hot-electron-induced hydrogen redistribution and defect generation in metal-oxide-semiconductor capacitors*, Journal of Applied Physics, vol. 76, no. 6: pp. 3595–3608 (1994). doi:10.1063/1.357420
- [63] D. J. DIMARIA: *Defect generation under substrate-hot-electron injection into ultrathin silicon dioxide layers*, Journal of Applied Physics, vol. 86, no. 4: pp. 2100–2109 (1999). doi:10.1063/1.371016
- [64] J. SUNE AND E. WU: *Mechanisms of hydrogen release in the breakdown of SiO₂-based gate oxides*, in *IEEE International Electron Devices Meeting, 2005. IEDM Technical Digest.*, pp. 388–391 (2005). doi:10.1109/IEDM.2005.1609359
- [65] J. W. LYDING, K. HESS AND I. C. KIZILYALLI: *Reduction of hot electron degradation in metal oxide semiconductor transistors by deuterium processing*, Applied Physics Letters, vol. 68, no. 18: pp. 2526–2528 (1996). doi:10.1063/1.116172

- [66] B. R. TUTTLE, W. MCMAHON AND K. HESS: *Hydrogen and hot electron defect creation at the Si(100)/SiO₂ interface of metal-oxide-semiconductor field effect transistors*, Superlattices and Microstructures, vol. 27, no. 2: pp. 229–233 (2000). doi:<https://doi.org/10.1006/spmi.1999.0804>
- [67] C. GUERIN, V. HUARD AND A. BRAVAIX: *General framework about defect creation at the Si/SiO₂ interface*, Journal of Applied Physics, vol. 105, no. 11 (2009). doi:[10.1063/1.3133096](https://doi.org/10.1063/1.3133096)
- [68] S. F. W. M. HATTA, N. SOIN AND J. F. ZHANG: *The effect of gate oxide thickness and drain bias on NBTI degradation in 45nm PMOS*, in *2010 IEEE International Conference on Semiconductor Electronics (ICSE2010)*, pp. 210–213. doi:[10.1109/SMELEC.2010.5549558](https://doi.org/10.1109/SMELEC.2010.5549558)
- [69] G. VAN DEN BOSCH, G. GROESENEKEN AND H. E. MAES: *Direct and post-injection oxide and interface-trap generation resulting from low-temperature hot-electron injection*, Journal of Applied Physics, vol. 74, no. 9: pp. 5582–5586 (1993). doi:[10.1063/1.354219](https://doi.org/10.1063/1.354219)
- [70] S. OGAWA AND N. SHIONO: *Generalized diffusion-reaction model for the low-field charge-buildup instability at the Si-SiO₂ interface*, Physical Review B, vol. 51, no. 7: pp. 4218–4230 (1995). doi:[10.1103/PhysRevB.51.4218](https://doi.org/10.1103/PhysRevB.51.4218)
- [71] S. CHAKRAVARTHI, A. KRISHNAN, V. REDDY, C. MACHALA AND S. KRISHNAN: *A comprehensive framework for predictive modeling of negative bias temperature instability*, in *2004 IEEE International Reliability Physics Symposium. Proceedings*, pp. 273–282. doi:[10.1109/RELPHY.2004.1315337](https://doi.org/10.1109/RELPHY.2004.1315337)
- [72] M. A. ALAM, H. KUFLUOGLU, D. VARGHESE AND S. MAHAPATRA: *A comprehensive model for PMOS NBTI degradation: Recent progress*, Microelectronics Reliability, vol. 47, no. 6: pp. 853–862 (2007). doi:[10.1016/j.microrel.2006.10.012](https://doi.org/10.1016/j.microrel.2006.10.012)
- [73] M. A. ALAM AND S. MAHAPATRA: *A comprehensive model of PMOS NBTI degradation*, Microelectronics Reliability, vol. 45, no. 1: pp. 71–81 (2005). doi:[10.1016/j.microrel.2004.03.019](https://doi.org/10.1016/j.microrel.2004.03.019)
- [74] A. KRISHNAN, C. CHANCELLOR, S. CHAKRAVARTHI, P. NICOLLIAN, V. REDDY, A. VARGHESE, R. KHAMANKAR AND S. KRISHNAN: *Material dependence of hydrogen diffusion: implications for NBTI degradation*, in *IEEE International Electron Devices Meeting, 2005. IEDM Technical Digest.*, pp. 4 pp.–691. doi:[10.1109/IEDM.2005.1609445](https://doi.org/10.1109/IEDM.2005.1609445)

-
- [75] C. G. VAN DE WALLE AND B. R. TUTTLE: *Microscopic theory of hydrogen in silicon devices*, IEEE Transactions on Electron Devices, vol. 47, no. 10: pp. 1779–1786 (2000). doi:10.1109/16.870547
- [76] K. L. BROWER: *Dissociation kinetics of hydrogen-passivated (111) Si-SiO₂ interface defects*, Physical Review B, vol. 42, no. 6: pp. 3444–3453 (1990). doi:10.1103/PhysRevB.42.3444
- [77] H. KUFLUOGLU AND M. A. ALAM: *Theory of interface-trap-induced NBTI degradation for reduced cross section MOSFETs*, IEEE Transactions on Electron Devices, vol. 53, no. 5: pp. 1120–1130 (2006). doi:10.1109/ted.2006.872098
- [78] E. H. POINDEXTER: *MOS interface states - overview and physicochemical perspective*, Semiconductor Science and Technology, vol. 4, no. 12: pp. 961–969 (1989). doi:10.1088/0268-1242/4/12/001
- [79] H. KUFLUOGLU AND M. A. ALAM: *A generalized reaction-diffusion model with explicit H-H₂ dynamics for negative-bias temperature-instability (NBTI) degradation*, IEEE Transactions on Electron Devices, vol. 54, no. 5: pp. 1101–1107 (2007). doi:10.1109/ted.2007.893909
- [80] W. M. A. BIK, R. N. H. LINSSEN, F. HABRAKEN, W. F. VANDERWEG AND A. E. T. KUIPER: *Diffusion of hydrogen in low-pressure chemical vapor-deposited silicon-nitride films*, Applied Physics Letters, vol. 56, no. 25: pp. 2530–2532 (1990). doi:10.1063/1.103261
- [81] Z. CHEN, K. HESS, J. J. LEE, J. W. LYDING, E. ROSENBAUM, I. KIZILYALLI, S. CHETLUR AND R. HUANG: *On the mechanism for interface trap generation in MOS transistors due to channel hot carrier stressing*, IEEE Electron Device Letters, vol. 21, no. 1: pp. 24–26 (2000). doi:10.1109/55.817441
- [82] F. J. FEIGL, D. R. YOUNG, D. J. DIMARIA, S. LAI AND J. CALISE: *The effects of water on oxide and interface trapped charge generation in thermal SiO₂-films*, Journal of Applied Physics, vol. 52, no. 9: pp. 5665–5682 (1981). doi:10.1063/1.329502
- [83] P. COTTRELL, R. TROUTMAN AND T. NING: *Hot-electron emission in n-channel IGFETs*, IEEE Journal of Solid-State Circuits, vol. 14, no. 2: pp. 442–455 (1979). doi:10.1109/JSSC.1979.1051196
- [84] E. TAKEDA, N. SUZUKI AND T. HAGIWARA: *Device performance degradation to hot-carrier injection at energies below the Si-SiO₂ energy barrier*, in

- 1983 *International Electron Devices Meeting*, pp. 396–399 (1983). doi:10.1109/IEDM.1983.190525
- [85] S. AUR, P. YANG, P. PATNAIK AND P. K. CHATTERJEE: *Modeling of Hot Carrier Effects for LDD MOSFETs*, in *1985 Symposium on VLSI Technology. Digest of Technical Papers*, pp. 112–113 (1985)
- [86] T. TSUCHIYA AND J. FREY: *Relationship between hot-electrons/Holes and degradation of p- and n-channel MOSFET's*, IEEE Electron Device Letters, vol. 6, no. 1: pp. 8–11 (1985). doi:10.1109/EDL.1985.26024
- [87] F. F. FANG AND A. B. FOWLER: *Hot Electron Effects and Saturation Velocities in Silicon Inversion Layers*, Journal of Applied Physics, vol. 41, no. 4: pp. 1825–1831 (1970). doi:10.1063/1.1659111
- [88] H. MATSUMOTO, K. SAWADA, S. ASAI, M. HIRAYAMA AND K. NAGASAWA: *Effect of long-term stress on IGFET degradations due to hot electron trapping*, IEEE Transactions on Electron Devices, vol. 28, no. 8: pp. 923–928 (1981). doi:10.1109/T-ED.1981.20460
- [89] J. A. BRACCHITTA, T. L. HONAN AND R. L. ANDERSON: *Hot-electron-induced degradation in MOSFETs at 77K*, IEEE Transactions on Electron Devices, vol. 32, no. 9: pp. 1850–1857 (1985). doi:10.1109/t-ed.1985.22208
- [90] D. J. DIMARIA, D. W. DONG, C. FALCONY, T. N. THEIS, J. R. KIRTLLEY, J. C. TSANG, D. R. YOUNG, F. L. PESAVENTO AND S. D. BRORSON: *Charge transport and trapping phenomena in off-stoichiometric silicon dioxide films*, Journal of Applied Physics, vol. 54, no. 10: pp. 5801–5827 (1983). doi:10.1063/1.331806
- [91] Y. NISSAN-COHEN, J. SHAPPIR AND D. FROHMANBENTCHKOWSKY: *Dynamic-model of trapping-detrapping in SiO₂*, Journal of Applied Physics, vol. 58, no. 6: pp. 2252–2261 (1985). doi:10.1063/1.335942
- [92] P. BALK, M. ASLAM AND D. R. YOUNG: *High-temperature annealing behavior of electron traps in thermal SiO₂*, Solid-State Electronics, vol. 27, no. 8-9: pp. 709–719 (1984). doi:10.1016/0038-1101(84)90019-4
- [93] P. ROBLIN, A. SAMMAN AND S. BIBYK: *Simulation of hot-electron trapping and aging of nMOSFETs*, IEEE Transactions on Electron Devices, vol. 35, no. 12: pp. 2229–2237 (1988). doi:10.1109/16.8797

-
- [94] E. H. NICOLLIAN, C. N. BERGLUND, P. F. SCHMIDT AND J. M. ANDREWS: *Electrochemical charging of thermal SiO₂ films by injected electron currents*, Journal of Applied Physics, vol. 42, no. 13: p. 5654 (1971). doi:10.1063/1.1659996
- [95] S. K. LAI, D. R. YOUNG, J. A. CALISE AND F. J. FEIGL: *Reduction of electron trapping in silicon dioxide by high-temperature nitrogen anneal*, Journal of Applied Physics, vol. 52, no. 9: pp. 5691–5695 (1981). doi:10.1063/1.329505
- [96] R. A. GDULA: *The Effects of Processing on Hot Electron Trapping in SiO₂*, Journal of The Electrochemical Society, vol. 123, no. 1: pp. 42–47 (1976). doi:10.1149/1.2132762
- [97] M. ASLAM: *Common origin for electron and hole traps in MOS devices*, IEEE Transactions on Electron Devices, vol. 34, no. 12: pp. 2535–2539 (1987). doi:10.1109/t-ed.1987.23345
- [98] P. M. LENAHAN AND P. V. DRESSENDORFER: *Hole traps and trivalent silicon centers in metal-oxide silicon devices*, Journal of Applied Physics, vol. 55, no. 10: pp. 3495–3499 (1984). doi:10.1063/1.332937
- [99] S. K. LAI: *Interface trap generation in silicon dioxide when electrons are captured by trapped holes*, Journal of Applied Physics, vol. 54, no. 5: pp. 2540–2546 (1983). doi:10.1063/1.332323
- [100] P. CAPLAN, E. POINDEXTER, B. E. DEAL AND R. RAZOUK: *ESR centers, interface states, and oxide fixed charge in thermally oxidized silicon wafers*, Journal of Applied Physics, vol. 50: pp. 5847–5854 (1979)
- [101] E. POINDEXTER, P. CAPLAN, B. E. DEAL AND R. RAZOUK: *Interface states and electron spin resonance centers in thermally oxidized (111) and (100) silicon wafers*, Journal of Applied Physics, vol. 52: pp. 879–884 (1981)
- [102] L. DOTHANH, M. ASLAM AND P. BALK: *Defect structure and generation of interface states in MOS structures*, Solid-State Electronics, vol. 29, no. 8: pp. 829–840 (1986). doi:10.1016/0038-1101(86)90186-3
- [103] M. ASLAM: *Electron self-trapping in SiO₂*, Journal of Applied Physics, vol. 62, no. 1: pp. 159–162 (1987). doi:10.1063/1.339839
- [104] J. J. LANDER AND J. MORRISON: *Low Voltage Electron Diffraction Study of the Oxidation and Reduction of Silicon*, Journal of Applied Physics, vol. 33, no. 6: pp. 2089–2092 (1962). doi:10.1063/1.1728901

- [105] S. S. COHEN: *Electrical Properties of Post-annealed Thin SiO₂ Films*, Journal of The Electrochemical Society, vol. 130, no. 4: pp. 929–932 (1983). doi:10.1149/1.2119860
- [106] D. L. GRISCOM AND W. B. FOWLER: *ELECTRON-TRANSFER MODEL FOR E'-CENTER OPTICAL ABSORPTION IN SiO₂*, in *The Physics of MOS Insulators*, (Ed. by G. LUCOVSKY, S. T. PANTELIDES AND F. L. GALEENER), pp. 97–101, Pergamon, ISBN 978-0-08-025969-7 (1980). doi:<https://doi.org/10.1016/B978-0-08-025969-7.50022-1>
- [107] K. L. NGAI AND C. T. WHITE: *A model of interface states and charges at the Si-SiO₂ interface - its predictions and comparisons with experiments*, Journal of Applied Physics, vol. 52, no. 1: pp. 320–337 (1981). doi:10.1063/1.328496
- [108] D. R. YOUNG, E. A. IRENE, D. J. DiMARIA, R. F. DE KEERSMAECKER AND H. Z. MASSOUD: *Electron trapping in SiO₂ at 295 and 77K*, Journal of Applied Physics, vol. 50, no. 10: pp. 6366–6372 (1979). doi:10.1063/1.325727
- [109] A. HARTSTEIN AND D. R. YOUNG: *Identification of electron traps in thermal silicon dioxide films*, Applied Physics Letters, vol. 38, no. 8: pp. 631–633 (1981). doi:10.1063/1.92459
- [110] M. V. FISCHETTI: *The importance of the anode field in controlling the generation rate of the donor states at the Si-SiO₂ interface*, Journal of Applied Physics, vol. 56, no. 2: pp. 575–577 (1984). doi:10.1063/1.333953
- [111] D. R. YOUNG: *Characterization of electron traps in SiO₂ as influenced by processing parameters*, Journal of Applied Physics, vol. 52, no. 6: pp. 4090–4094 (1981). doi:10.1063/1.329259
- [112] D. DiMARIA: *The properties of electron and hole traps in thermal silicon dioxide layers grown on silicon*, in *The Physics of SiO₂ and its Interfaces*, (Ed. by S. T. PANTELIDES), pp. 160–178, Pergamon, ISBN 978-0-08-023049-8 (1978). doi:<https://doi.org/10.1016/B978-0-08-023049-8.50034-8>
- [113] G. GROESENEKEN, R. DEGRAEVE, T. NIGAM, G. VAN DEN BOSCH AND H. E. MAES: *Hot carrier degradation and time-dependent dielectric breakdown in oxides*, Microelectronic Engineering, vol. 49, no. 1-2: pp. 27–40 (1999). doi:10.1016/S0167-9317(99)00427-X

-
- [114] R. FOWLER AND L. NORDHEIM: *Electron Emission in Intense Electric Fields*, Proceedings of the Royal Society of London Series A, vol. 119, no. 781: pp. 173–181 (1928). doi:10.1098/rspa.1928.0091
- [115] D. J. DIMARIA, E. CARTIER AND D. ARNOLD: *Impact ionization, trap creation, degradation, and breakdown in silicon dioxide films on silicon*, Journal of Applied Physics, vol. 73, no. 7: pp. 3367–3384 (1993). doi:10.1063/1.352936
- [116] C. R. CROWELL AND S. M. SZE: *Temperature dependence of avalanche multiplication in semiconductors*, Applied Physics Letters, vol. 9, no. 6: p. 242 (1966). doi:10.1063/1.1754731
- [117] C. A. LEE, R. A. LOGAN, R. L. BATDORF, J. J. KLEIMACK AND W. WIEGMANN: *Ionization Rates of Holes and Electrons in Silicon*, Phys. Rev., vol. 134: pp. A761–A773 (1964). doi:10.1103/PhysRev.134.A761
- [118] T. GRASSER: *Hot Carrier Degradation in Semiconductor Devices*, Springer International Publishing, ISBN 9783319089942 (2014)
- [119] J. F. VERWEY: *Nonavalanche injection of hot carriers into SiO₂*, Journal of Applied Physics, vol. 44, no. 6: pp. 2681–2687 (1973). doi:10.1063/1.1662633
- [120] T. NING: *Hot-electron emission from silicon into silicon dioxide*, Solid-State Electronics, vol. 21, no. 1: pp. 273–282 (1978). doi:https://doi.org/10.1016/0038-1101(78)90148-X
- [121] M. DEPAS, B. VERMEIRE, P. MERTENS, R. VAN MEIRHAEGHE AND M. HEYNS: *Determination of tunnelling parameters in ultra-thin oxide layer poly-Si/SiO₂/Si structures*, Solid-State Electronics, vol. 38, no. 8: pp. 1465–1471 (1995). doi:https://doi.org/10.1016/0038-1101(94)00269-L
- [122] H. GESCH, J.-P. LEBURTON AND G. DORDA: *Generation of interface states by hot hole injection in MOSFET's*, IEEE Transactions on Electron Devices, vol. 29, no. 5: pp. 913–918 (1982). doi:10.1109/T-ED.1982.20799
- [123] R. FAIR AND R. SUN: *Threshold-voltage instability in MOSFET's due to channel hot-hole emission*, IEEE Transactions on Electron Devices, vol. 28, no. 1: pp. 83–94 (1981). doi:10.1109/T-ED.1981.20287
- [124] S. K. LAI: *Two-carrier nature of interface-state generation in hole trapping and radiation damage*, Applied Physics Letters, vol. 39, no. 1: pp. 58–60 (1981). doi:10.1063/1.92514

- [125] E. TAKEDA, A. SHIMIZU AND T. HAGIWARA: *Role of hot-hole injection in hot-carrier effects and the small degraded channel region in MOSFET's*, IEEE Electron Device Letters, vol. 4, no. 9: pp. 329–331 (1983). doi:10.1109/EDL.1983.25751
- [126] F.-C. HSU AND S. TAM: *Relationship between MOSFET degradation and hot-electron-induced interface-state generation*, IEEE Electron Device Letters, vol. 5, no. 2: pp. 50–52 (1984). doi:10.1109/EDL.1984.25829
- [127] F.-C. HSU AND K.-Y. CHIU: *Temperature dependence of hot-electron-induced degradation in MOSFET's*, IEEE Electron Device Letters, vol. 5, no. 5: pp. 148–150 (1984). doi:10.1109/EDL.1984.25865
- [128] D. J. DIMARIA AND J. W. STASIAK: *Trap creation in silicon dioxide produced by hot-electrons*, Journal of Applied Physics, vol. 65, no. 6: pp. 2342–2356 (1989). doi:10.1063/1.342824
- [129] Y. NISSAN-COHEN, J. SHAPPIR AND D. FROHMANBENTCHKOWSKY: *Trap generation and occupation dynamics in SiO₂ under charge injection stress*, Journal of Applied Physics, vol. 60, no. 6: pp. 2024–2035 (1986). doi:10.1063/1.337204
- [130] M. SHATZKES AND M. AVRON: *Impact ionization and positive charge in thin SiO₂-films*, Journal of Applied Physics, vol. 47, no. 7: pp. 3192–3202 (1976). doi:10.1063/1.323115
- [131] N. KLEIN AND P. SOLOMON: *Current runaway in insulators affected by impact ionization and recombination*, Journal of Applied Physics, vol. 47, no. 10: pp. 4364–4372 (1976). doi:10.1063/1.322440
- [132] E. HARARI: *Dielectric-breakdown in electrically stressed thin-films of thermal SiO₂*, Journal of Applied Physics, vol. 49, no. 4: pp. 2478–2489 (1978). doi:10.1063/1.325096
- [133] M. H. WOODS AND R. WILLIAMS: *Hole traps in silicon dioxide*, Journal of Applied Physics, vol. 47, no. 3: pp. 1082–1089 (1976). doi:10.1063/1.322730
- [134] R. DEGRAEVE, G. GROESENEKEN, R. BELLENS, J. L. OGIER, M. DEPAS, P. J. ROUSSEL AND H. E. MAES: *New insights in the relation between electron trap generation and the statistical properties of oxide breakdown*, IEEE Transactions on Electron Devices, vol. 45, no. 4: pp. 904–911 (1998). doi:10.1109/16.662800
- [135] E. AVNI AND J. SHAPPIR: *A model for silicon-oxide breakdown under high-field and current stress*, Journal of Applied Physics, vol. 64, no. 2: pp. 743–748 (1988). doi:10.1063/1.342477

-
- [136] J. SUNE, I. PLACENCIA, N. BARNIOL, E. FARRES, F. MARTIN AND X. AYMERICH: *On the breakdown statistics of very thin SiO₂ films*, Thin Solid Films, vol. 185, no. 2: pp. 347–362 (1990). doi:[https://doi.org/10.1016/0040-6090\(90\)90098-X](https://doi.org/10.1016/0040-6090(90)90098-X)
- [137] D. DUMIN, J. MADDUX, R. SCOTT AND R. SUBRAMONIAM: *A model relating wearout to breakdown in thin oxides*, IEEE Transactions on Electron Devices, vol. 41, no. 9: pp. 1570–1580 (1994). doi:[10.1109/16.310108](https://doi.org/10.1109/16.310108)
- [138] P. APTE AND K. SARASWAT: *Modeling ultrathin dielectric breakdown on correlation of charge trap-generation to charge-to-breakdown*, in *Proceedings of 1994 IEEE International Reliability Physics Symposium*, pp. 136–142 (1994). doi:[10.1109/RELPHY.1994.307845](https://doi.org/10.1109/RELPHY.1994.307845)
- [139] H. SATAKE AND A. TORIUMI: *Substrate hole current generation and oxide breakdown in Si MOSFETs under Fowler-Nordheim electron tunneling injection*, in *Proceedings of IEEE International Electron Devices Meeting*, pp. 337–340 (1993). doi:[10.1109/IEDM.1993.347339](https://doi.org/10.1109/IEDM.1993.347339)
- [140] P. HEREMANS, R. BELLENS, G. GROESENEKEN, A. SCHWERIN, H. MAES, M. BROX AND W. WEBER: *Hot Carrier Design Considerations for MOS Devices and Circuits*, chapter The Mechanisms of Hot-Carrier Degradation, pp. 1–119, Springer US (1992)
- [141] J. MCPHERSON AND H. MOGUL: *Disturbed bonding states in SiO₂ thin-films and their impact on time-dependent dielectric breakdown*, in *1998 IEEE International Reliability Physics Symposium Proceedings. 36th Annual (Cat. No.98CH36173)*, pp. 47–56. doi:[10.1109/RELPHY.1998.670441](https://doi.org/10.1109/RELPHY.1998.670441)
- [142] J. W. MCPHERSON AND H. C. MOGUL: *Impact of mixing of disturbed bonding states on time-dependent dielectric breakdown in SiO₂ thin films*, Applied Physics Letters, vol. 71, no. 25: pp. 3721–3723 (1997). doi:[10.1063/1.120493](https://doi.org/10.1063/1.120493)
- [143] J. W. MCPHERSON, V. K. REDDY AND H. C. MOGUL: *Field-enhanced Si-Si bond-breakage mechanism for time-dependent dielectric breakdown in thin-film SiO₂ dielectrics*, Applied Physics Letters, vol. 71, no. 8: pp. 1101–1103 (1997). doi:[10.1063/1.119739](https://doi.org/10.1063/1.119739)
- [144] J. W. MCPHERSON AND H. C. MOGUL: *Underlying physics of the thermochemical E model in describing low-field time-dependent dielectric breakdown in SiO₂ thin films*, Journal of Applied Physics, vol. 84, no. 3: pp. 1513–1523 (1998). doi:[10.1063/1.368217](https://doi.org/10.1063/1.368217)

- [145] J. W. MCPHERSON: *Time dependent dielectric breakdown physics - Models revisited*, Microelectronics Reliability, vol. 52, no. 9-10: pp. 1753–1760 (2012). doi:10.1016/j.microrel.2012.06.007
- [146] D. J. DIMARIA: *Temperature dependence of trap creation in silicon dioxide*, Journal of Applied Physics, vol. 68, no. 10: pp. 5234–5246 (1990). doi:10.1063/1.347040
- [147] A. SCHWERIN AND M. HEYNS: *Insulating Films on Semiconductors*, chapter Oxide field dependence of bulk and interface trap generation in SiO₂ due to hot electron injection, pp. 263–266, CRC Press (1991)
- [148] H. SATAKE AND A. TORIUMI: *Common origin for stress-induced leakage current and electron trap generation in SiO₂*, Applied Physics Letters, vol. 67, no. 23: pp. 3489–3490 (1995). doi:10.1063/1.115256
- [149] J. S. STATE TECHNOLOGY ASSOCIATION: *Failure mechanisms and models for semiconductor devices*, JEDEC Publication 122H (2016)
- [150] Y. NISSAN-COHEN AND T. GORCZYCA: *The effect of hydrogen on trap generation, positive charge trapping, and time-dependent dielectric-breakdown of gate oxides*, IEEE Electron Device Letters, vol. 9, no. 6: pp. 287–289 (1988). doi:10.1109/55.719
- [151] C. C. H. HSU, T. NISHIDA AND C. T. SAH: *Observation of threshold oxide electric-field for trap generation in oxide-films on silicon*, Journal of Applied Physics, vol. 63, no. 12: pp. 5882–5884 (1988). doi:10.1063/1.340281
- [152] D. J. DIMARIA, M. V. FISCHETTI, M. ARIENZO AND E. TIERNEY: *Electron heating studies in silicon dioxide - low fields and thick-films*, Journal of Applied Physics, vol. 60, no. 5: pp. 1719–1726 (1986). doi:10.1063/1.337264
- [153] D. J. DIMARIA: *Electron energy dependence of metal-oxide-semiconductor degradation*, Applied Physics Letters, vol. 75, no. 16: pp. 2427–2428 (1999). doi:10.1063/1.125036
- [154] Z. A. WEINBERG, W. C. JOHNSON AND M. A. LAMPERT: *High-field transport in SiO₂ on silicon induced by corona charging of unmetallized surface*, Journal of Applied Physics, vol. 47, no. 1: pp. 248–255 (1976). doi:10.1063/1.322307
- [155] E. S. ANOLICK AND G. R. NELSON: *Low-field time-dependent dielectric integrity*, IEEE Transactions on Reliability, vol. 29, no. 3: pp. 217–221 (1980). doi:10.1109/tr.1980.5220804

-
- [156] B. LINDER, J. STATHIS, R. WACHNIK, E. WU, S. COHEN, A. RAY AND A. VAYSHENKER: *Gate oxide breakdown under Current Limited Constant Voltage Stress*, in *2000 Symposium on VLSI Technology. Digest of Technical Papers (Cat. No.00CH37104)*, pp. 214–215. doi:10.1109/VLSIT.2000.852830
- [157] T. NISHIDA AND S. E. THOMPSON: *Oxide field and thickness dependence of trap generation in 9-30 nm dry and dry wet dry oxides*, *Journal of Applied Physics*, vol. 69, no. 7: pp. 3986–3994 (1991). doi:10.1063/1.348914
- [158] S. D. BRORSON, D. J. DIMARIA, M. V. FISCHETTI, F. L. PESAVENTO, P. M. SOLOMON AND D. W. DONG: *Direct measurement of the energy-distribution of hot-electrons in silicon dioxide*, *Journal of Applied Physics*, vol. 58, no. 3: pp. 1302–1313 (1985). doi:10.1063/1.336098
- [159] M. M. HEYNS, R. F. DEKEERSMAECKER AND M. W. HILLEN: *Trap generation and electron detrapping in SiO₂ during high-field stressing of metal-oxide-semiconductor structures*, *Applied Physics Letters*, vol. 44, no. 2: pp. 202–204 (1984). doi:10.1063/1.94709
- [160] D. J. DIMARIA AND J. R. ABERNATHEY: *Electron heating in silicon-nitride and silicon oxynitride films*, *Journal of Applied Physics*, vol. 60, no. 5: pp. 1727–1729 (1986). doi:10.1063/1.337265
- [161] D. J. DIMARIA: *Correlation of trap creation with electron heating in silicon dioxide*, *Applied Physics Letters*, vol. 51, no. 9: pp. 655–657 (1987). doi:10.1063/1.98324
- [162] D. J. DIMARIA AND J. H. STATHIS: *Ultimate limit for defect generation in ultra-thin silicon dioxide*, *Applied Physics Letters*, vol. 71, no. 22: pp. 3230–3232 (1997). doi:10.1063/1.120299
- [163] D. J. DIMARIA: *Explanation for the polarity dependence of breakdown in ultra-thin silicon dioxide films*, *Applied Physics Letters*, vol. 68, no. 21: pp. 3004–3006 (1996). doi:10.1063/1.116678
- [164] D. J. DIMARIA AND J. H. STATHIS: *Explanation for the oxide thickness dependence of breakdown characteristics of metal-oxide-semiconductor structures*, *Applied Physics Letters*, vol. 70, no. 20: pp. 2708–2710 (1997). doi:10.1063/1.118999

- [165] M. FUJII, Y. INOUE, S. HAYASHI AND K. YAMAMOTO: *Hopping conduction in SiO₂ films containing C, Si, and Ge clusters*, Applied Physics Letters, vol. 68, no. 26: pp. 3749–3751 (1996). doi:10.1063/1.115994
- [166] K. C. CHANG, C. H. PAN, T. C. CHANG, T. M. TSAI, R. ZHANG, J. C. LOU, T. F. YOUNG, J. H. CHEN, C. C. SHIH, T. J. CHU, J. Y. CHEN, Y. T. SU, J. P. JIANG, K. H. CHEN, H. C. HUANG, Y. E. SYU, D. S. GAN AND S. M. SZE: *Hopping Effect of Hydrogen-Doped Silicon Oxide Insert RRAM by Supercritical CO₂ Fluid Treatment*, IEEE Electron Device Letters, vol. 34, no. 5: pp. 617–619 (2013). doi:10.1109/led.2013.2251995
- [167] I. SILVACO: *Atlas User's Manual - DEVICE SIMULATION SOFTWARE*, Silvaco, Inc. (2016)
- [168] J. C. MAXWELL: *VIII. A dynamical theory of the electromagnetic field*, Philosophical Transactions of the Royal Society of London, vol. 155: pp. 459–512 (1865). doi:10.1098/rstl.1865.0008
- [169] S. SELBERHERR: *Analysis and Simulation of Semiconductor Devices*, Springer-Verlag Wien (1984)
- [170] J. SLOTBOOM: *The pn-product in silicon*, Solid-State Electronics, vol. 20, no. 4: pp. 279–283 (1977). doi:https://doi.org/10.1016/0038-1101(77)90108-3
- [171] J. SLOTBOOM AND H. DE GRAAFF: *Measurements of bandgap narrowing in Si bipolar transistors*, Solid-State Electronics, vol. 19, no. 10: pp. 857–862 (1976). doi:https://doi.org/10.1016/0038-1101(76)90043-5
- [172] W. VAN ROOSBROECK: *Theory of the flow of electrons and holes in germanium and other semiconductors*, The Bell System Technical Journal, vol. 29, no. 4: pp. 560–607 (1950). doi:10.1002/j.1538-7305.1950.tb03653.x
- [173] D. CAUGHEY AND R. THOMAS: *Carrier mobilities in silicon empirically related to doping and field*, Proceedings of the IEEE, vol. 55, no. 12: pp. 2192–2193 (1967). doi:10.1109/PROC.1967.6123
- [174] V. UHNEVIONAK, A. BURENKOV, C. STRENGER, G. ORTIZ, E. BEDELPEREIRA, V. MORTET, F. CRISTIANO, A. J. BAUER AND P. PICHLER: *Comprehensive Study of the Electron Scattering Mechanisms in 4H-SiC MOSFETs*, IEEE Transactions on Electron Devices, vol. 62, no. 8: pp. 2562–2570 (2015). doi:10.1109/TED.2015.2447216

-
- [175] W. SHOCKLEY AND W. T. READ: *Statistics of the Recombinations of Holes and Electrons*, Phys. Rev., vol. 87: pp. 835–842 (1952). doi:10.1103/PhysRev.87.835
- [176] R. N. HALL: *Electron-Hole Recombination in Germanium*, Phys. Rev., vol. 87: pp. 387–387 (1952). doi:10.1103/PhysRev.87.387
- [177] R. A. RYMZHANOV, N. A. MEDVEDEV AND A. E. VOLKOV: *Effects of model approximations for electron, hole, and photon transport in swift heavy ion tracks*, Nuclear Instruments & Methods in Physics Research Section B-Beam Interactions with Materials and Atoms, vol. 388: pp. 41–52 (2016). doi:10.1016/j.nimb.2016.11.002
- [178] Z. J. DING AND R. SHIMIZU: *Inelastic-collisions of kV electrons in solids*, Surface Science, vol. 222, no. 2-3: pp. 313–331 (1989). doi:10.1016/0039-6028(89)90362-2
- [179] A. AKKERMAN AND M. MURAT: *Electron-phonon interactions in silicon: Mean free paths, related distributions and transport characteristics*, Nuclear Instruments & Methods in Physics Research Section B-Beam Interactions with Materials and Atoms, vol. 350: pp. 49–54 (2015). doi:10.1016/j.nimb.2015.03.024
- [180] W. SHOCKLEY: *Hot electrons in germanium and Ohms law*, Bell System Technical Journal, vol. 30, no. 4: pp. 990–1034 (1951). doi:10.1002/j.1538-7305.1951.tb03692.x
- [181] M. ASCHE AND O. G. SARBEI: *Electric conductivity of hot carriers in si and ge*, Physica Status Solidi, vol. 33, no. 1: pp. 9–+ (1969). doi:10.1002/pssb.19690330102
- [182] G. BAUER, G. BORSTEL, H. FALGE AND A. OTTO: *Tracts in Modern Physics: Solid-State Physics*, chapter Determination of electron temperatures and of hot electron distribution functions in semiconductors, pp. 1–106, Springer-Verlag Berlin Heidelberg (1974)
- [183] L. REGGIANI: *Hot-Electron Transport in Semiconductors*, Springer (1985)
- [184] W. SHOCKLEY: *Problems related to p-n junctions in silicon*, Solid-State Electronics, vol. 2, no. 1: pp. 35–+ (1961). doi:10.1016/0038-1101(61)90054-5
- [185] B. ZIAJA, R. A. LONDON AND J. HAJDU: *Ionization by impact electrons in solids: Electron mean free path fitted over a wide energy range*, Journal of Applied Physics, vol. 99, no. 3 (2006). doi:10.1063/1.2161821

- [186] D. CASSI AND B. RICCO: *An analytical model of the energy-distribution of hot-electrons*, IEEE Transactions on Electron Devices, vol. 37, no. 6: pp. 1514–1521 (1990). doi:10.1109/16.106247
- [187] E. PAIGE: *Progress in Semiconductors, Volume 8*, chapter The Electrical Conductivity of Germanium, p. 1, John Wiley & Sons (1964)
- [188] B. R. NAG: *Hot-carrier dc conduction in elemental semiconductors*, Solid-State Electronics, vol. 10, no. 5: p. 385 (1967). doi:10.1016/0038-1101(67)90038-x
- [189] D. BARTELINK, J. L. MOLL AND N. I. MEYER: *Hot-electron emission from shallow p-n junctions in silicon*, Physical Review, vol. 130, no. 3: pp. 972–+ (1963). doi:10.1103/PhysRev.130.972
- [190] T. GRASSER, H. KOSINA, C. HEITZINGER AND S. SELBERHERR: *Characterization of the hot electron distribution function using six moments*, Journal of Applied Physics, vol. 91, no. 6: pp. 3869–3879 (2002). doi:10.1063/1.1450257
- [191] C. BULUCEA: *Avalanche injection into oxide in silicon gate-controlled devices .1. theory*, Solid-State Electronics, vol. 18, no. 4: pp. 363–374 (1975). doi:10.1016/0038-1101(75)90092-1
- [192] M. GRUNDMANN: *The Physics of Semiconductors - An Introduction Including Devices and Nanophysics*, Springer (2006)
- [193] J. LEE, I.-C. CHEN AND C. HU: *Statistical modeling of silicon dioxide reliability*, in *26th Annual Proceedings Reliability Physics Symposium 1988*, pp. 131–138 (1988). doi:10.1109/RELPHY.1988.23440
- [194] G. ARNOLD: *Ion implantation in silicate glasses*, Journal of Non-Crystalline Solids, vol. 179: pp. 288–299, proceedings of the First PAC RIM Meeting on Glass and Optical Materials (1994). doi:https://doi.org/10.1016/0022-3093(94)90707-2
- [195] E. W. J. MITCHELL AND E. G. S. PAIGE: *The optical effects of radiation induced atomic damage in quartz*, Philosophical Magazine, vol. 1, no. 12: pp. 1085–1115 (1956). doi:10.1080/14786435608238193
- [196] R. A. WEEKS AND C. M. NELSON: *Trapped electrons in irradiated quartz and silica - 2. Electron spin resonance*, Journal of the American Ceramic Society, vol. 43, no. 8: pp. 399–404 (1960). doi:10.1111/j.1151-2916.1960.tb13682.x

-
- [197] C. NELSON AND J. CRAWFORD: *Optical absorption in irradiated quartz and fused silica*, Journal of Physics and Chemistry of Solids, vol. 13, no. 3: pp. 296–305 (1960). doi:[https://doi.org/10.1016/0022-3697\(60\)90014-7](https://doi.org/10.1016/0022-3697(60)90014-7)
- [198] C. R. HELMS AND E. H. POINDEXTER: *The silicon-silicon dioxide system: Its microstructure and imperfections*, Reports on Progress in Physics, vol. 57, no. 8: pp. 791–852 (1994). doi:[10.1088/0034-4885/57/8/002](https://doi.org/10.1088/0034-4885/57/8/002)
- [199] W. HANSCH, A. VON SCHWERIN AND F. HOFMANN: *A new self-consistent modeling approach to investigating MOSFET degradation*, IEEE Electron Device Letters, vol. 11, no. 9: pp. 362–364 (1990). doi:[10.1109/55.62956](https://doi.org/10.1109/55.62956)
- [200] R. L. KAMOCSAI AND W. POROD: *Hot-electrons and traps in a-SiO₂*, Solid-State Electronics, vol. 32, no. 12: pp. 1825–1829 (1989). doi:[10.1016/0038-1101\(89\)90319-5](https://doi.org/10.1016/0038-1101(89)90319-5)
- [201] R. L. KAMOCSAI AND W. POROD: *A monte-carlo model of hot-electron trapping and detrapping in SiO₂*, Journal of Applied Physics, vol. 69, no. 4: pp. 2264–2275 (1991). doi:[10.1063/1.348706](https://doi.org/10.1063/1.348706)
- [202] A. B. BHATTACHARYYA, L. MANCHANDA AND J. VASI: *Electron traps in SiO₂ grown in the presence of trichloroethylene*, Journal of the Electrochemical Society, vol. 129, no. 12: pp. 2772–2778 (1982). doi:[10.1149/1.2123677](https://doi.org/10.1149/1.2123677)
- [203] R. DOERING AND Y. NISHI, (Editors): *Handbook of Semiconductor Manufacturing Technology*, Taylor and Francis Group (2008)
- [204] K. HESS, L. F. REGISTER, B. TUTTLE, J. LYDING AND I. C. KIZILYALLI: *Impact of nanostructure research on conventional solid-state electronics: The giant isotope effect in hydrogen desorption and CMOS lifetime*, Physica E-Low-Dimensional Systems & Nanostructures, vol. 3, no. 1-3: pp. 1–7 (1998). doi:[10.1016/s1386-9477\(98\)00211-2](https://doi.org/10.1016/s1386-9477(98)00211-2)
- [205] M. BINA, S. TYAGINOV, J. FRANCO, K. RUPP, Y. WIMMER, D. OSINTSEV, B. KACZER AND T. GRASSER: *Predictive Hot-Carrier Modeling of n-Channel MOSFETs*, IEEE Transactions on Electron Devices, vol. 61, no. 9: pp. 3103–3110 (2014). doi:[10.1109/ted.2014.2340575](https://doi.org/10.1109/ted.2014.2340575)
- [206] S. REGGIANI, G. BARONE, S. POLI, E. GNANI, A. GNUDI, G. BACCARANI, M. Y. CHUANG, W. D. TIAN AND R. WISE: *TCAD Simulation of Hot-Carrier and Thermal Degradation in STI-LDMOS Transistors*, IEEE Transactions on Electron Devices, vol. 60, no. 2: pp. 691–698 (2013). doi:[10.1109/ted.2012.2227321](https://doi.org/10.1109/ted.2012.2227321)

- [207] I. STARKOV, S. TYAGINOV, H. ENICHLMAIR, J. CERVENKA, C. JUNGEMANN, S. CARNIELLO, J. M. PARK, H. CERIC AND T. GRASSER: *Hot-carrier degradation caused interface state profile-Simulation versus experiment*, Journal of Vacuum Science & Technology B, vol. 29, no. 1 (2011). doi:10.1116/1.3534021
- [208] B. N. J. PERSSON AND P. AVOURIS: *Local bond breaking via STM-induced excitations: the role of temperature*, Surface Science, vol. 390, no. 1-3: pp. 45–54 (1997). doi:10.1016/s0039-6028(97)00507-4
- [209] S. TYAGINOV AND T. GRASSER: *Modeling of hot-carrier degradation: Physics and controversial issues*, in *2012 IEEE International Integrated Reliability Workshop Final Report*, pp. 206–215. doi:10.1109/IIRW.2012.6468962
- [210] T. C. SHEN, C. WANG, G. C. ABELN, J. R. TUCKER, J. W. LYDING, P. AVOURIS AND R. E. WALKUP: *Atomic-Scale Desorption Through Electronic and Vibrational Excitation Mechanisms*, Science, vol. 268, no. 5217: pp. 1590–1592 (1995). doi:10.1126/science.268.5217.1590
- [211] E. T. FOLEY, A. F. KAM, J. W. LYDING AND P. AVOURIS: *Cryogenic UHV-STM Study of Hydrogen and Deuterium Desorption from Si(100)*, Phys. Rev. Lett., vol. 80: pp. 1336–1339 (1998). doi:10.1103/PhysRevLett.80.1336
- [212] S. TYAGINOV, I. STARKOV, O. TRIEBL, H. CERIC, T. GRASSER, H. ENICHLMAIR, J.-M. PARK AND C. JUNGEMANN: *Secondary generated holes as a crucial component for modeling of HC degradation in high-voltage n-MOSFET*, pp. 123–126 (2011). doi:10.1109/SISPAD.2011.6035065
- [213] S. E. TYAGINOV, I. STARKOV, H. ENICHLMAIR, J. M. PARK, C. JUNGEMANN AND T. GRASSER: *Physics-Based Hot-Carrier Degradation Modeling*, ECS Transactions, vol. 35, no. 4: pp. 321–352 (2019). doi:10.1149/1.3572292
- [214] W. MCMAHON, A. HAGGAG AND K. HESS: *Reliability scaling issues for nanoscale devices*, IEEE Transactions on Nanotechnology, vol. 2, no. 1: pp. 33–38 (2003). doi:10.1109/tnano.2003.808515
- [215] M. BINA, K. RUPP, S. TYAGINOV, O. TRIEBL AND T. GRASSER: *Modeling of hot carrier degradation using a spherical harmonics expansion of the bipolar Boltzmann transport equation*, in *IEEE IEDM 2012* (2012)
- [216] W. MCMAHON AND K. HESS: *A Multi-Carrier Model for Interface Trap Generation*, Journal of Computational Electronics, vol. 1, no. 3: pp. 395–398 (2002). doi:10.1023/A:1020716111756

-
- [217] J. BUDE AND K. HESS: *Thresholds of impact ionization in semiconductors*, Journal of Applied Physics, vol. 72, no. 8: pp. 3554–3561 (1992). doi:10.1063/1.351434
- [218] C. KANETA, T. YAMASAKI AND Y. KOSAKA: *Nano-scale simulation for advanced gate dielectrics*, Fujitsu Scientific and Technical Journal, vol. 39, no. 1: pp. 106–118 (2003)
- [219] C. G. VAN DE WALLE AND R. A. STREET: *Structure, energetics, and dissociation of Si-H bonds at dangling bonds in silicon*, Phys. Rev. B, vol. 49: pp. 14766–14769 (1994). doi:10.1103/PhysRevB.49.14766
- [220] B. TUTTLE AND C. G. VAN DE WALLE: *Structure, energetics, and vibrational properties of Si-H bond dissociation in silicon*, Physical Review B, vol. 59, no. 20: pp. 12884–12889 (1999). doi:10.1103/PhysRevB.59.12884
- [221] K. HESS, L. F. REGISTER, W. MCMAHON, B. TUTTLE, O. AKTAS, U. RAVAIOLI, J. W. LYDING AND I. C. KIZILYALLI: *Theory of channel hot-carrier degradation in MOSFETs*, Physica B-Condensed Matter, vol. 272, no. 1-4: pp. 527–531 (1999). doi:10.1016/s0921-4526(99)00363-4
- [222] K. HESS, P. VON ALLMEN, M. GRUPEN AND L. F. REGISTER: *Simulating Electronic Transport in Semiconductor Nanostructures*, pp. 215–225, Springer Netherlands, Dordrecht, ISBN 978-94-009-1746-0 (1996). doi:10.1007/978-94-009-1746-0_19
- [223] E. CARTIER, J. H. STATHIS AND D. A. BUCHANAN: *Passivation and depassivation of silicon dangling bonds at the Si/SiO₂ interface by atomic hydrogen*, Applied Physics Letters, vol. 63, no. 11: pp. 1510–1512 (1993). doi:10.1063/1.110758
- [224] M. V. FISCHETTI, R. GASTALDI, F. MAGGIONI AND A. MODELLI: *Slow and fast states induced by hot-electrons at Si-SiO₂ interface*, Journal of Applied Physics, vol. 53, no. 4: pp. 3136–3144 (1982). doi:10.1063/1.331010
- [225] C. M. SVENSSON: *The defect structure of the Si-SiO₂ interface, a model based on trivalent silicon and its hydrogen 'compounds'*, in *The Physics of SiO₂ and its Interfaces*, pp. 328–332, Pergamon, ISBN 978-0-08-023049-8 (1978). doi:https://doi.org/10.1016/B978-0-08-023049-8.50061-0
- [226] J. H. STATHIS AND E. CARTIER: *Atomic hydrogen reactions with P_b centers at the (100) Si/SiO₂ interface*, Phys. Rev. Lett., vol. 72: pp. 2745–2748 (1994). doi:10.1103/PhysRevLett.72.2745

- [227] M. L. REED AND J. D. PLUMMER: *Si-SiO₂ interface trap production by low-temperature thermal processing*, Applied Physics Letters, vol. 51, no. 7: pp. 514–516 (1987). doi:10.1063/1.98383
- [228] K. L. BROWER: *Passivation of paramagnetic Si-SiO₂ interface states with molecular hydrogen*, Applied Physics Letters, vol. 53, no. 6: pp. 508–510 (1988). doi:10.1063/1.100620
- [229] D. L. GRISCOM: *Diffusion of radiolytic molecular hydrogen as a mechanism for the post-irradiation buildup of interface states in SiO₂-on-Si structures*, Journal of Applied Physics, vol. 58, no. 7: pp. 2524–2533 (1985). doi:10.1063/1.335931
- [230] M. REED AND J. PLUMMER: *Chemistry of Si-SiO₂ interface trap annealing*, Journal of Applied Physics, vol. 63, no. 12: pp. 5776–5793 (1988). doi:10.1063/1.340317
- [231] B. TUTTLE: *Energetics and diffusion of hydrogen in SiO₂*, Phys. Rev. B, vol. 61 (2000). doi:10.1103/PhysRevB.61.4417
- [232] K. O. JEPPSON AND C. M. SVENSSON: *Negative bias stress of MOS devices at high electric fields and degradation of MNOS devices*, Journal of Applied Physics, vol. 48, no. 5: pp. 2004–2014 (1977). doi:10.1063/1.323909
- [233] J. YUE, Y. XIAO, Y. LI, G. HAN, Y. ZHANG AND W. HOU: *Enhanced photovoltaic performances of the dye-sensitized solar cell by utilizing rare-earth modified tin oxide compact layer*, Organic Electronics, vol. 43: pp. 121–129 (2017). doi:https://doi.org/10.1016/j.orgel.2017.01.018
- [234] V. KOTU AND B. DESHPANDE: *Data Science - Concepts and Practrice*, 2. Edition, Elsevier (2019)
- [235] M. RAO AND C. RAO, (Editors): *Handbook of Statistics Vol. 32 - Computational Statistics with R*, Elsevier (2014)
- [236] A. ZAI AND B. BROWN: *Deep Reinforcement Learning in Action*, Manning Publications (2020)
- [237] M. PAWLUS AND R. DEVINE: *Hands-On Deep Learning with R*, Packt Publishing (2020)
- [238] S. E. THOMPSON AND T. NISHIDA: *A new measurement method for trap properties in insulators and semiconductors - using electric-field stimulated trap-to-band*

-
- tunneling transitions in SiO₂*, Journal of Applied Physics, vol. 70, no. 11: pp. 6864–6876 (1991). doi:10.1063/1.349810
- [239] J. R. JAMESON, W. HARRISON, P. B. GRIFFIN AND J. D. PLUMMER: *Double-well model of dielectric relaxation current*, Applied Physics Letters, vol. 84, no. 18: pp. 3489–3491 (2004). doi:10.1063/1.1738177
- [240] M. J. GILLAN: *Quantum-classical crossover of the transition rate in the damped double well*, Journal of Physics C: Solid State Physics, vol. 20, no. 24: pp. 3621–3641 (1987). doi:10.1088/0022-3719/20/24/005
- [241] L. MIHAILOV, M. KIRTICHEVA AND A. MANOV: *An Improved Method of Relaxation Rate Calculation in Double-Well Potential Systems*, Molecular Engineering, vol. 7, no. 1: pp. 149–160 (1997). doi:10.1023/A:1008226330007
- [242] Y. LIU, S. FORREST, J. HLADKY, M. LANGE, G. OLSEN AND D. ACKLEY: *A planar InP/InGaAs avalanche photodiode with floating guard ring and double diffused junction*, Journal of Lightwave Technology, vol. 10, no. 2: pp. 182–193 (1992). doi:10.1109/50.120573
- [243] S. CHO, S. YANG, J. MA, S. LEE, J. YU, A. CHOO, T. KIM AND J. BURM: *Suppression of avalanche multiplication at the periphery of diffused junction by floating guard rings in a planar InGaAs-InP avalanche photodiode*, IEEE Photonics Technology Letters, vol. 12, no. 5: pp. 534–536 (2000). doi:10.1109/68.841277

Zusammenfassung nach Promotionsordnung §11 (4)

Zusammenfassung der Dissertation

Underlying physics and effects of silicon APD aging in automotive LiDAR applications

Der Fakultät für Physik und Geowissenschaften der Universität Leipzig
eingereicht von

M. Sc. Stefan Christoph Kammer

angefertigt bei der

First Sensor AG (Teil von TE connectivity), Abteilung Entwicklung und Chip Design
11/2021

Over 90 % of traffic accidents are caused by human error [1]. Therefore, the realization of autonomous driving could save countless lives and drastically reduce the associated financial expenses. Moreover, the collective behavior of self-driving cars would avoid traffic jams and thus reduce fuel consumption and greenhouse gas emissions [2]. The majority of concepts is based on LIGHT DETECTION AND RANGING (LiDAR) [3], which is the most precise method to measure distances [4]. Matched to the 95 % of commercial LiDAR systems based on laser wavelengths of mostly 905 nm [4,5], silicon-based photo sensors are used. Avalanche photo diodes (APD) are the only sensor solution in mass production [6]. Due to an internal multiplication mechanism based on impact ionization, high signal-noise-ratios (SNR) are achieved and provide the required resolution of low signals from more than 100 m distant targets [4]. Currently none of the LiDAR technologies meet the reliability requirements of the automotive industry concerning the aging of installed components [7]. Consequently, autonomous driving cannot yet be realized for public use.

Very little is known about the aging of APDs in general and nothing at all in the field of automotive LiDAR. In order to provide novel insights into APD aging that help designers to achieve more robust sensors and thus to enable a step closer to the realization of autonomous driving, it was the aim of this thesis prepared in the industrial environment to reveal the underlying physical aging mechanisms and their effects on the function of APDs in automotive LiDAR application. At first, a novel APD degradation model was developed encompassing a wide range of processes, treating numerous fundamental aspects of negative oxide charge generation and Si:SiO₂ interface trap generation. So far, no model is known covering the kinetics of APD degradation comprehensively in such deep detail. Due to the feedback between degradation phenomena and sensor internal fields and currents, a coupled problem arose. It was tackled by a sophisticated numerical iteration approach which was tailor-made and solved this problem self-consistently

in a tandem procedure combining the simulation of sensor degradation and the SILVACO ATLAS device simulator. This led to novel insights into the APD degradation behavior. The generation of negative oxide charges was identified to cause a drift of the impact ionization rate in the sensor edge. The generation of interface traps promotes the accumulation of negative oxide charges by their supply of thermally generated dark current. In this way, degradation is about 14% faster. In order to reflect not only the causal relations of APD degradation, the model was calibrated on experimental degradation data. With the calibrated degradation model and its self-consistent simulation approach an elaborated powerful tool was available. Stress experiments have been performed on test sensors under a variation of operation conditions and on APDs. APDs of the studied design are currently tested and installed in automotive LiDAR modules. The entire set of experimental results found its complete physical interpretation in conjunction with the degradation model which achieved an excellent agreement. Thereby, numerous novel insights were revealed: The extent of degradation is induced by the properties of the sensors oxide layer. The degradation pace increases with temperature, voltage and intensity of illumination whereas the impact of temperature is particularly strong due to the significant participation of the dark current during degradation. The oxygen vacancy was proven to be the dominant trap in the oxide layer of the studied sensors. An empirical distribution of individual sensor properties was achieved. In some cases, the impact ionization rate in the sensor edge increased which indicates a major problem, as noise increases when the generation-recombination processes in the sensor become more pronounced during degradation. In order to estimate the impact of the degradation induced increase of noise on the LiDAR application, the empirical distribution of individual sensor properties was extrapolated to the tail where sensors are very prone to degradation. Furthermore, the available noise models were extended to cover the effect of degradation. Application of the calibrated APD degradation model revealed, that the APD noise is highly affected and even triples during aging. The origin was exclusively assigned to the edge contribution. There, the avalanche breakdown of the edge dark current caused by degradation is the main initiator. Consequently, for the first time ever, the signal-noise-ratio (SNR) degradation mode of APDs in LiDAR application was identified. During degradation, the SNR of small signals from 100 m distant objects degrades to a value below 1, where even theoretically a resolution is impossible. Finally, the picture of APD degradation was completed by the estimation of lifetime. In the case of the most severe conditions in LiDAR operation, it amounts to only $t_{life} \approx 1000$ h, which falls much below the requirements of the automotive industry of several decades.

Bibliography

- [1] J. Wang, K. Li and X.-Y. Lu: Effect of Human Factors on Driver Behavior, in *Advances in Intelligent Vehicles* pp. 111–157, Academic Press, Boston (2014).
- [2] S. Bharadwaj, S. Ballare, Rohit and M. K. Chandel: Impact of congestion on greenhouse gas emissions for road transport in Mumbai metropolitan region, *Transportation Research Procedia* **25**, pp. 3538–3551 (2017).
- [3] I. Kim *et al.*: Nanophotonics for light detection and ranging technology, *Nature Nanotechnology*, **16**, 5, 508–524 (2021).
- [4] Y. Li and J. Ibanez-Guzman: Lidar for Autonomous Driving: The Principles, Challenges, and Trends for Automotive Lidar and Perception Systems, *IEEE Signal Processing Magazine*, **37**, 4, 50–61 (2020).
- [5] M. Kutila *et al.*: Automotive LiDAR performance verification in fog and rain, in 2018 21st International Conference on Intelligent Transportation Systems (ITSC), 1695–1701 (2018).
- [6] M. Warren: Automotive LIDAR Technology, C254–C255 (2019).
- [7] C.-P. Hsu *et al.*: A Review and Perspective on Optical Phased Array for Automotive LiDAR, *IEEE Journal of Selected Topics in Quantum Electronics*, **27**, 1, 1–16 (2021).

Danksagung

An dieser Stelle möchte ich mich bei allen Personen bedanken, die zum Gelingen dieser Arbeit beigetragen und mich unterstützt haben. Zuerst möchte ich meinen Dank Herrn Prof. Dr. Marius Grundmann aussprechen für die Betreuung während meiner Promotionszeit und die Wegweisenden Diskussionen.

Außerdem bedanke ich mich bei der First Sensor AG als Teil von TE Connectivity und ganz besonders bei Herrn Dr. Martin Wilke und Herrn Dr. Marc Schillgalies für die Betreuung, die Möglichkeit im aufregenden industriellen Kontext zu promovieren, für ihr Vertrauen und dass sie mir jederzeit mit Rat zur Seite standen. Bedanken möchte ich mich auch bei Frau Dr. Jennifer Mertens für die Betreuung in der ersten Zeit meiner Arbeit.

Weiterer Dank gebühren Herrn Dr. Michael Pierschel und Herrn Dr. Evgeny Chernyavskiy für die Unterweisung in das Sensor Chip Design, die Sensor Chip Simulation und insbesondere in die Funktionsweise der untersuchten APD Chips - ein faszinierendes Feld, das ich gerne weiter verfolge. Bei Herrn Gerd Lange, Herrn Robert Quade und Herrn Dr. Jona Kurpiers bedanke ich mich für die Unterstützung bei den experimentellen Aufbauten und ihren offenen und lockeren Umgang. Der Metrology Gruppe unter der Führung von Gerd Lange danke ich für die Bereitstellung des Datensatzes im Grundlagenkapitel. Herrn Holger Arndt danke ich für die grundlegende Einführung in die Funktionsweise von LiDAR - ein weitreichendes und aufregendes Gebiet, welches ich zukünftig hoffentlich weiter erschließe.

Für die beständige Unterstützung bei allen organisatorischen und bürokratischen Hürden danke ich im speziellen Anja Heck und Birgit Wendisch.

Begonnen hat mein Weg als Physiker lange vor dem Physikstudium, als mich mein Onkel Siegfried Neuber mit der Relativitätsphysik in Berührung brachte. Von diesem Moment an war meine Faszination entfacht und jedes mal, wenn ich den Nachthimmel blickte, war mir klar: Ich werde Physik studieren und verstehen wie die Welt funktioniert. Daher möchte ich mich von tiefstem Herzen auch bei ihm für diesen initialen Funken bedanken!

Vielen Dank auch an meine FreundInnen, die mich schon mein Leben lang unterstützen

und mich während der Promotionszeit mit schönen Momenten abgelenkt haben. Ich bin sehr froh und dankbar, dass ich sie habe.

Dank gebührt auch meinen Brüdern Markus und Fabian dafür, dass sie immer ein offenes Ohr hatten wenn ich mich über die Stagnation der Arbeit beschweren wollte. Bei ihnen fühle ich mich immer wohl!

Außerdem bedanke ich mich bei meiner Frau Laura dafür, dass ich mich gegen Ende der Promotionszeit immer häufiger beschweren durfte, wenn die Arbeit nicht so wollte wie ich. Manchmal war es sicherlich nicht einfach mit mir. Die wunderschönen Momente mit ihr haben mich dennoch immer wieder aufgebaut und Kraft schöpfen lassen. Zusammen schaffen wir alles!

Großer Dank gebührt meinen Eltern, die die Grundlage dafür geschaffen haben, wer ich heute bin und mir durch ihre bedingungslose Unterstützung meine Ausbildung und meinen Lebensweg geebnet haben. Ich bin sehr stolz auf sie.

Lebenslauf

Persönliche Daten

Name	Stefan Christoph Kammer
Geburtstag	09. August 1990
Geburtsort	Gehrden
Adresse	Seumestraße 15 10245 Berlin
Nationalität	deutsch

Ausbildung

03/2018	Abschluss: Master of Science Titel der Abschlussarbeit: <i>"Investigation of electronic transport properties in Si-doped AlGaN"</i>
2014 – 2018	Masterstudiengang Physik an der Technischen Universität Berlin
06/2014	Abschluss: Bachelor of Science Titel der Abschlussarbeit: <i>"Nanoimprint Lithographie für selektives Wachstum in der MBE"</i>
2010 – 2014	Bachelorstudiengang Physik an der Georg-August-Universität Göttingen
06/2010	Abschluss: Abitur
2003 – 2010	Schulbesuch des Matthias-Claudius Gymnasiums Gehrden
2001 – 2003	Schulbesuch der KGS Ronnenberg
1997 – 2001	Schulbesuch der Regenbogenschule Weetzen

Selbstständigkeitserklärung

Hiermit erkläre ich, dass ich die von mir vorgelegte Dissertation mit dem Titel:

"Underlying physics and effects of silicon APD aging
in automotive LiDAR applications"

ohne unzulässige Hilfe und ohne Benutzung anderer als der angegebenen Hilfsmittel angefertigt und dass die aus fremden Quellen direkt oder indirekt übernommenen Gedanken in der Arbeit als solche kenntlich gemacht wurden. Ich versichere, dass außer den von mir in der Dissertation genannten keine weiteren Personen bei der geistigen Herstellung der vorliegenden Arbeit beteiligt waren und ich insbesondere nicht die Hilfe eines Promotionsberaters in Anspruch genommen habe. Weiterhin erkläre ich, dass keine weiteren Personen von mir oder in meinem Auftrag weder unmittelbar noch mittelbar geldwerte Leistungen für Arbeiten erhalten haben, die im Zusammenhang mit dem Inhalt der vorgelegten Dissertation stehen. Ich versichere, dass die vorgelegte Arbeit weder im Inland noch im Ausland in gleicher oder in ähnlicher Form in einer anderen Prüfungsbehörde zum Zwecke einer Promotion oder eines anderen Prüfungsverfahrens vorgelegt und in ihrer Gesamtheit noch nicht veröffentlicht wurde. Ich erkläre, dass ich bisher keine erfolglosen Promotionsversuche unternommen habe.

Berlin, den 19.11.2021

Stefan Kammer